SYNTHESIS, IN VITRO AND IN VIVO EVALUATION OF NANOPARTICLES AND METAL COMPLEXES FOR THE TREATMENT OF BRAIN DISEASES

TIFFANY GWEN KAY CHAN

A thesis submitted for the degree of Doctor of Philosophy

DEPARTMENT OF CHEMISTRY
IMPERIAL COLLEGE LONDON
FEBRUARY 2020

CONTENTS

DECLARATION 6

ACKNOWLEDGMENTS 7

ABSTRACT 8

LIST OF FIGURES 9

LIST OF TABLES 18

ABBREVIATIONS 19

1 INTRODUCTION 21

1.1 The Blood-Brain Barrier - an obstacle for drug delivery . . . 21

1.1.1 The Neurovascular Unit . . . 21

1.1.2 Endothelial Cell Junctions . . . 22

1.2 Transport across the Blood-Brain Barrier . . . 24

1.2.1 Existing Methods to Overcome the Blood-Brain Barrier . . . 25

1.2.2 Focused Ultrasound-Mediated Blood-Brain Barrier Opening . . . 28

1.3 Thesis Aims . . . 30

2 DNA-COATED NANOPARTICLES FOR BRAIN DISEASES 31

2.1 Background . . . 31

2.1.1 Spherical Nucleic Acids . . . 31

2.2 Aims and Objectives . . . 33

2.3 Results and Discussion . . . 33

2.3.1 Nanoparticle Synthesis and Characterisation . . . 33

2.3.2 Delivering Nanoparticles across the BBB with Ultrasound . . . 39

2.3.3 Size-Dependency of Ultrasound-Mediated Delivery . . . 46

2.3.4 Safety of Focused Ultrasound-Mediated BBB Opening . . . 46

2.4 Conclusions and Future Directions . . . 49

3 METAL COMPLEXES FOR THE TREATMENT OF ALZHEIMER'S DISEASE 53

3.1 Background . . . 53

3.1.1 The Amyloid Beta Hypothesis . . . 53
3.1.2 The Role of Metal Ions in Alzheimer's Disease . . . 57
3.1.3 Metal-Targeted Therapeutic Strategies for Alzheimer's Disease . . . 59
3.2 Aims and Objectives . . . 62
3.3 Results and Discussion . . . 62
3.3.1 Designing Potential Inhibitors of Amyloid Beta Aggregation . . . 62
3.3.2 Investigating the Ability to Inhibit Aβ Aggregation using the Thioflavin-T Assay . . . 66
3.3.3 Probing the Binding Mode to Amyloid Beta . . . 73
3.3.4 Assessing Cytotoxicity of the Synthesised Metal Complexes . . . 77
3.3.5 Assessing the Effect on Amyloid Beta Neurotoxicity . . . 78
3.4 Conclusions and Future Directions . . . 82

4 ASSESSING THERAPEUTIC EFFICACY OF METAL COMPLEXES IN VIVO 84
4.1 Background . . . 84
4.1.1 The Effects of Focused Ultrasound on Alzheimer's Disease Pathology . . . 84
4.2 Aims and Objectives . . . 86
4.3 Results and Discussion . . . 86
4.3.1 Improving Ultrasound-Mediated BBB Opening . . . 86
4.3.2 Delivering Metal Salphens and Salnaphs across the BBB using Ultrasound . . . 91
4.3.3 Safety of Repeated Treatments . . . 94
4.3.4 Assessing Efficacy in an Alzheimer's Disease Mouse Model . . . 96
4.4 Conclusions and Future Directions . . . 107

5 CONCLUSIONS 109

6 METHODS - DNA-COATED NANOPARTICLES FOR BRAIN DISEASES 111
6.1 Synthesis of DNA-Coated Gold Nanoparticles . . . 111
6.1.1 Surface Functionalisation with Oligonucleotides . . . 111
6.2 Characterisation of DNA-Coated Gold Nanoparticles . . . 112
6.2.1 UV-Vis Spectroscopy . . . 112
6.2.2 Transmission Electron Microscopy . . . 112
6.2.3 Dynamic Light Scattering and Electrophoretic Light Scattering . . . 113
6.2.4 Determination of Oligonucleotide Loading . . . 113
6.3 Ultrasound-Mediated Delivery of Nanoparticles into the Brain . . . 113
6.3.1 Delivery of DNA-coated Gold Nanoparticles across the BBB . . . 114

6.3.2 Fluorescence Microscopy . . . 115
6.3.3 Assessing Safety with H&E Staining . . . 115

7 METHODS - METAL COMPLEXES FOR ALZHEIMER'S DISEASE 117
7.1 Synthesis of Metal Complexes . . . 117
7.1.1 4-(2-bromoethoxy)-2-hydroxybenzaldehyde . . . 118
7.1.2 4-(4-formyl-3-hydroxyphenoxy)-*N*,*N*,*N*-trimethylethan-1-ammonium bromide . . . 118
7.1.3 Salnaph Ligand . . . 119
7.1.4 Cobalt Salnaph Complexes (4a-4e) . . . 120
7.1.5 [Pt(5-methyl-2-phenylpyridine)(DMSO)Cl] (5) . . . 122
7.1.6 [Pt(4,7-diphenyl-1,10-phenanthroline)Cl_2] (6) . . . 122
7.1.7 Stability of Cobalt Salnaphs in Aqueous Solution . . . 123
7.2 Preparation of Amyloid Beta Peptide . . . 123
7.3 In vitro Experiments . . . 124
7.3.1 Thioflavin-T Assay . . . 124
7.3.2 Transmission Electron Microscopy . . . 124
7.3.3 Fluorescence Spectroscopy . . . 125
7.3.4 ^{1}H NMR Spectroscopy of Aβ . . . 125
7.3.5 Circular Dichroism . . . 125
7.4 Cellular Studies . . . 125
7.4.1 Cytotoxicity of Complexes . . . 126
7.4.2 Cytotoxicity of 4b . . . 126
7.4.3 Cytotoxicity of Aβ1-42 . . . 126

8 METHODS - ASSESSING THERAPEUTIC EFFICACY IN VIVO 128
8.1 Ultrasound Setup . . . 128
8.2 Rapid Short Pulse Sequences . . . 129
8.3 Laser Ablation Inductively Coupled Plasma Mass Spectrometry . . . 129
8.3.1 LA-ICP-MS . . . 130
8.4 Safety of Repeated Treatments . . . 130
8.5 Preliminary Study in 5xFAD Mice . . . 131
8.5.1 Albumin Staining . . . 132
8.5.2 Thioflavin-S Staining . . . 133
8.5.3 MOAB-2 Staining . . . 133

8.5.4 Image Analysis: ThS & MOAB-2 Staining . . . 133

BIBLIOGRAPHY 134

APPENDIX 151

9.6 Chapter 2: DNA-Coated Nanoparticles for Brain Diseases . . . 151

9.6.1 CTAB-Capped Au NPs . . . 151

9.6.2 UV-Vis Spectra of Synthesised Au NPs . . . 152

9.6.3 Emission Intensities of Synthesised Cy5-DNA-Au NPs . . . 152

9.6.4 Pressure Threshold . . . 153

9.6.5 Cy5-DNA-Au NP Delivery at 350 kPa . . . 154

9.6.6 H&E Staining . . . 155

9.7 Chapter 3: Metal Complexes for Alzheimer's Disease . . . 156

9.7.1 Characterisation Data - Metal Complexes . . . 156

9.8 Chapter 4: Assessing Therapeutic Efficacy *In Vivo* . . . 166

9.8.1 Delivery of Complex 1 across the BBB using Ultrasound . . . 166

9.8.2 Thioflavin-S Staining: Group 1 (No Treatment) . . . 167

9.8.3 Thioflavin-S Staining: Group 2 (Ultrasound Only) . . . 168

9.8.4 Thioflavin-S Staining: Group 3 (Ultrasound + 4b) . . . 169

9.8.5 MOAB-2 Staining: Group 1 (No Treatment) . . . 170

9.8.6 MOAB-2 Staining: Group 2 (Ultrasound Only) . . . 171

9.8.7 MOAB-2 Staining: Group 3 (Ultrasound + 4b) . . . 172

DECLARATION

Declaration of Originality

I confirm that all of the work presented in this thesis is my own, except where stated. Contributions from collaborators have been clearly identified. All source materials have been appropriately referenced and acknowledged.

Declaration of Copyright

The copyright of this thesis rests with the author. Unless otherwise indicated, its contents are licensed under a Creative Commons Attribution-Non Commercial-No Derivatives 4.0 International Licence (CC BY-NC-ND). Under this licence, you may copy and redistribute the material in any medium or format on the condition that you credit the author, do not use it for commercial purposes and do not distribute modified versions of the work. When reusing or sharing this work, ensure you make the licence terms clear to others by naming the licence and linking to the licence text. Please seek permission from the copyright holder for uses of this work that are not included in this licence or permitted under UK Copyright Law.

ACKNOWLEDGMENTS

First and foremost, I would like to thank my supervisors, Prof. Ramon Vilar and Dr. James Choi, for their unwavering support and advice over these last four years - none of this work would have been possible without their guidance.

Second, I would like to thank all of the members of the Vilar Group and the NSB Lab, both past and present, who I have been fortunate enough to work alongside during my PhD. Many of them have become close friends and this journey would have been significantly less enjoyable without them. Special thanks to Carmen Ruehl (*'cobalt salphens are the future!'*), Dr. Viktoria Rakers and Tim Kench from the Vilar Group for kindly allowing me to use their complexes as part of my Alzheimer's disease screen, as well as Dr. Aaron Torres-Huerta for embarking on the development of functionalised nanoparticles with me. From the NSB Lab, I would like to thank Sophie Morse in particular, without whom none of the *in vivo* work reported in this thesis would have been possible. Our (almost) daily Slack conversations will be missed! In addition, thanks to Matthew Copping, Dr. Gerard Hernandez-Mir and Dr. Ellie Watts for our useful discussions regarding everything Alzheimer's disease-related over the past few years, as well as the rest of the capillary cluster. I would also like to thank my proof-readers, Sophie Morse and Ben Lewis, for their help in catching typos and making this thesis better.

Third, I would like to thank our collaborators for their assistance with certain parts of this thesis: Barry Sampson for his help with LA-ICP-MS and Dr. Magdalena Sastre for providing the 5xFAD mice used in this work and general Alzheimer's disease-related expertise. In addition, I would like to thank the Facility for Imaging by Light Microscopy (FILM), particularly Stephen Rothery and Dr. David Gaboriau, for microscopy advice, Dr. Claire Higgins for allowing me access to her cryostat, Dr. Joseph Barrit for running TEM samples and Dr. Yingqi Xu for his guidance on running peptide NMRs.

Last, but not least, I would like to thank all of my friends and family for their support and encouragement over the past four years and the EPSRC CDT in Neurotechnology for funding this work.

ABSTRACT

An intact blood-brain barrier is essential in order to maintain brain homeostasis and preserve neuronal function. However, its presence prevents over 98% of conventional small molecule drugs from entering the brain, making the treatment of brain diseases such as Alzheimer's disease extremely challenging. Due to this, there has been great interest in designing methods to overcome the blood-brain barrier, but many of these are either highly invasive, non-targeted or show poor efficiency. Over the past twenty years, the use of focused ultrasound in combination with circulating microbubbles has emerged as a promising strategy, allowing the blood-brain barrier to be disrupted in a completely non-invasive, targeted and transient manner.

In this thesis, we have developed two systems to take advantage of this technology: DNA-coated nanoparticles as potential delivery platforms for combination therapies and a series of metal complexes as potential inhibitors of amyloid beta aggregation for the treatment of Alzheimer's disease. In Chapter 2, we began by synthesising a series of fluorescently-labelled DNA-coated nanoparticles and showed that they can be successfully delivered to a target location across the blood-brain barrier in mice using ultrasound. Ongoing work is seeking to evaluate drug-loaded derivatives of these nanoparticles *in vitro* and *in vivo*. In Chapters 3 and 4, a series of metal salphens and salnaphs were investigated for their ability to inhibit the aggregation of the amyloid beta peptide, which is one of the key hallmarks of Alzheimer's disease. Through a series of *in vitro* assays, we showed that the synthesised metal complexes are able to inhibit amyloid beta aggregation and are non-cytotoxic. Using ultrasound-mediated blood-brain barrier opening methods, these complexes were successfully delivered into the brains of mice, allowing their therapeutic efficacy to be assessed *in vivo*. Preliminary findings obtained with our complexes in an Alzheimer's disease mouse model are presented.

LIST OF FIGURES

Figure 1.1 Schematic representation of the key components of the neurovascular unit, redrawn from [1]. The blood-brain barrier tightly regulates the paracellular and transcellular transport of substances from the blood to the brain and vice versa. 21

Figure 1.2 The two main types of endothelial cell junctions - tight junctions and adherens junctions - and the key proteins that they are composed of, redrawn from [1, 33]. The blue boxes show the estimated distances and spaces within the BBB that therapeutic agents have to overcome in order to enter the brain.[1] 23

Figure 1.3 Possible transport routes across the blood-brain barrier, redrawn from [4]. Due to the presence of narrow tight junctions between adjacent endothelial cells (left), the majority of substances can only enter the brain *via* a transcellular pathway (middle). Actively opposing the influx of substances into the brain are efflux transporters such as P-gp, which sit on the apical side of the BBB (right). 25

Figure 1.4 Schematic representation of focused ultrasound-mediated BBB opening. In this method, intravenously administered microbubbles are exposed to focused ultrasound. This induces the microbubbles to radially oscillate and exert mechanical stress on the blood vessel walls, resulting in increased permeability. 29

Figure 2.1 Structure of a spherical nucleic acid. 32

Figure 2.2 Proposed mechanism of gold nanoparticle formation, redrawn from [124]. The gold precursor is reduced to give primary particles, which grow into larger particles *via* coalescence. 34

Figure 2.3 **a)** Representative TEM images of the synthesised Cy5-DNA-Au NPs **A**, **B** and **C**. Particles are monodisperse and quasi-spherical. **b)** Size distribution of Cy5-DNA-Au NPs **A, B** and **C**, determined by measuring the particles using ImageJ (n > 100 for each set). 36

Figure 2.4 **a)** The Stokes-Einstein and Henry's equation used in DLS and ELS. (D: diffusion coefficient, k_B: Boltzmann constant, T: temperature, η: solvent viscosity, R_h: hydrodynamic radius, U_E: electrophoretic mobility, ε: dielectric constant of the solution, ζ : zeta potential, $F(\kappa\alpha)$: Henry function) **b)** Zeta potential is the potential at the boundary between the slipping plane and the bulk solution. 37

Figure 2.5 Experimental setup for *in vivo* experiments and a screenshot of the GUI used to control the system. The setup and GUI were developed by Dr. A. Pouliopoulos (PhD student, NSB Lab). 40
Figure 2.6 Experimental workflow for *in vivo* experiments. 41
Figure 2.7 **a)** Aerial view of the ultrasound setup. To target specific regions of the brain, a metal cross is placed on top of the lambdoid and sagittal sutures of the mouse skull, which are visible through the intact skin of the mouse head. **b)** Example raster scan. 42
Figure 2.8 Fluorescence microscopy image of successful targeting of the left hippocampus. Ultrasound-mediated BBB opening can be clearly seen in the left hippocampus (purple; injected tracer: 3 kDa Texas Red-labelled dextran), with no evidence of BBB opening observed in the non-sonicated right hippocampus. 44
Figure 2.9 Ultrasound parameters used for BBB opening. The left thalamus region was targeted in all Cy5-DNA-Au NP experiments, leaving the right thalamus as the non-sonicated control. 44
Figure 2.10 Bright-field and fluorescence microscopy images showing the successful delivery of Cy5-DNA-Au NPs to the left thalamus of the brain. Signal corresponding to the Au NP cores can be observed in bright-field images (green box) and is found at the same location as signal from the attached Cy5-labelled DNA strands (orange box). . 45
Figure 2.11 **a)** Representative fluorescence microscopy images showing the successful delivery of Cy5-DNA-Au NPs **A**, **B** and **C** to the left thalamus. No evidence of nanoparticle delivery was observed in the right thalamus in all experiments. **b)** Normalised optical density, calculated over five sections per brain. Using the same ultrasound parameters, Cy5-DNA-Au NPs **A** were delivered across the BBB six times more efficiently than Cy5-DNA-Au NPs **C** ($p < 0.05$, $n = 5$ for each set of nanoparticles). 47
Figure 2.12 Representative fluorescence microscopy images showing the successful delivery of a 3 kDa Texas Red-labelled dextran to the left thalamus (top). H&E staining shows a few sites of red blood cell extravasation in the targeted region (bottom; left), which are not present in the control (bottom; right). No other tissue effects were observed. 49
Figure 2.13 **Top:** A novel bimetallic zinc receptor was loaded with two bisphosphonate-based drugs, etidronate and aledronate. The synthesis depicted was carried out by Dr. A. Torres-Huerta (Postdoc, Vilar Group). **Bottom:** Etidronate- and aledronate-loaded DNA-Au NPs **D** and **E** were synthesised following similar methods to those reported above. . 52

Figure 3.1 Alzheimer's disease is characterised by the presence of amyloid beta plaques in the extracellular space and neurofibrillary tangles inside neurons. The abnormal build-up of these protein deposits over time ultimately results in brain atrophy. 54
Figure 3.2 In a healthy brain, the amyloid precursor protein is cleaved once by α-secretase, In contrast, in Alzheimer's disease, it is cleaved twice: first by β-secretase and then by γ-secretase. This results in the release of the so-called amyloid beta peptide, which, over time, aggregates to form oligomers and plaques. The amyloid beta hypothesis states that it is the presence of these aggregates that triggers Alzheimer's disease pathology. 55
Figure 3.3 **a)** Sequence of Aβ1-42. The N-terminal metal binding site has been highlighted in orange. **b)** Proposed binding modes of Cu^{+} and Cu^{2+} ions to the Aβ peptide, redrawn from *[219]*. 58
Figure 3.4 **a)** Generation of ROS *via* Fenton and Haber-Weiss reactions. **b)** Proposed catalytic cycle for ROS generation by Cu-Aβ, redrawn from *[235]*. Cu^{2+}-Aβ is first reduced to Cu^{+}-Aβ by a naturally occurring reducing agent and is then able to initiate ROS production. Key ROS are highlighted in blue. 59
Figure 3.5 **a)** Examples of metal complexes that have been designed to target the N-terminal metal binding site of Aβ.[246,250–252] **b)** Proposed binding modes of metal complexes to the N-terminal of Aβ. All metal complexes reported for this application are believed to interact *via* non-covalent π-π stacking interactions with aromatic amino acids, as well as coordination to Aβ. 61
Figure 3.6 Structures of metal salphens and salnaphs **1-4e** used in this study. Salphens **1** and **2** were synthesised by Dr. V. Rakers (PhD student, Vilar Group) whilst cobalt salphens **3a-3e** were synthesised by C. Ruehl. Experimental details for the synthesis of these complexes can be found in their theses.[257–259] 63
Figure 3.7 Aromatic region (5.0 to 15.0 ppm) of the ^{1}H NMR spectrum (400 MHz, DMSO-d_6) of the salnaph ligand recorded before and after cobalt complexation. The bottom spectrum is of complex **4d** (L = NH_3), which has axial ligands that do not give signals in the aromatic region. Disappearance of the -O<u>H</u> (H_H) signal is observed upon complexation, as well as shifts in the aromatic protons. 65
Figure 3.8 ^{1}H NMR spectra (400 MHz, DMSO-d_6) of octahedral cobalt salnaphs **4a-4e**. 65

Figure 3.9 ^{1}H NMR spectrum (400 MHz) of complex **4e** (L = $BzNH_2$) recorded in 1:9 D_2O:phosphate-buffered saline (pH 7.4; 137 mM NaCl, 2.7 mM KCl, 8 mM Na_2HPO_4 and 2 mM KH_2PO_4) over time. As the axial ligands are displaced, a second set of NMR signals appear. Key changes in the NMR spectrum of complex **4e** over time are highlighted. 66

Figure 3.10 Stabilities of cobalt salnaphs **4a-4e** over time in 1:9 D_2O:phosphate-buffered saline (pH 7.4; 137 mM NaCl, 2.7 mM KCl, 8 mM Na_2HPO_4 and 2 mM KH_2PO_4). 67

Figure 3.11 **a)** Structure of ThT and its proposed binding mode to amyloid fibrils. **b)** Example of a ThT emission curve recorded for Aβ1-42 incubated by itself and with an inhibitor of Aβ aggregation at 37 °C with shaking. For samples of Aβ1-42 incubated by itself, a sigmoidal curve is obtained in which a sharp increase in the emission intensity is observed upon fibril formation. 68

Figure 3.12 Inhibition of Aβ1-42 aggregation (%) induced by metal complexes **1**, **2**, **3c** and **4c** determined using the ThT assay. Complexes **5** and **6** are literature compounds and are included as positive controls.[246,249] Complexes were tested at [Aβ42]:[complex] = 1:0.2, 1:0.1, 1:0.07, 1:0.05 and 1:0.04, and all samples were incubated at 37 °C with shaking. The dotted line represents the half-inhibition point and all data is reported as the mean ± standard deviation of three independent experiments. 69

Figure 3.13 Inhibition of Aβ1-42 aggregation (%) induced by cobalt salphens **3a-3e** (top) and cobalt salnaphs **4a-4e** (bottom) determined using the ThT assay. Complexes were tested at [Aβ42]:[complex] = 1:0.2, 1:0.1, 1:0.07, 1:0.05 and 1:0.04, and all samples were incubated at 37 °C with shaking. The dotted line represents the half-inhibition point and all data is reported as the mean ± standard deviation of three independent experiments. 71

Figure 3.14 Representative TEM images of Aβ1-42 incubated by itself or with metal complexes **1**, **2**, **3c** or **4c** for 48 hr at 37 °C (1:1 ratio). Clear fibril formation can be observed in the sample of Aβ1-42 incubated by itself. Little fibril formation is observed when Aβ1-42 is incubated with complex **1**, whilst no evidence of fibril formation is observed with complexes **2, 3c** and **4c**. 72

Figure 3.15 Normalised fluorescence emission of the Tyr10 residue of Aβ1-16 on addition of cisplatin (negative control; black), **2**, **3c** and **4c** (0 to 0.75 eq.) in phosphate-buffered saline (pH 7.4; 137 mM NaCl, 2.7 mM KCl, 8 mM Na_2HPO_4 and 2 mM KH_2PO_4). The highest degree of quenching is seen with salnaph complex **4c** (square). All data is reported as the mean ± standard deviation of three independent experiments. . . 74

Figure 3.16 **a)** ^{1}H NMR spectrum of Aβ1-28 incubated by itself (black) or with complexes **1, 2, 3c** or **4c** at 0 and 24 hrs. **b)** ^{1}H NMR spectrum of H6R Aβ1-28 incubated by itself (black) or with complexes **1, 2, 3c** or **4c** at 0 and 24 hrs. All spectra were recorded at 400 MHz in 1:9 D_2O:phosphate-buffered saline (pH 7.4; 137 mM NaCl, 2.7 mM KCl, 8 mM Na_2HPO_4 and 2 mM KH_2PO_4) at 37 °C. Peaks corresponding to the Aβ histidine residues have been assigned based on literature.[249,270] 75

Figure 3.17 **a)** Light can be circularly polarised in the left- and right-handed directions. Linearly polarised light is the superimposition of left- and right-handed circularly polarised light of the same amplitude. Optically active chiral molecules will absorb left- and right-handed circularly polarised light by different extents, resulting in elliptically polarised light. θ denotes the degrees of ellipticity. **b)** Circular dichroism spectra of Aβ1-42 after incubation with complexes **1, 2, 3c** and **4c** at 37 °C for 48 hrs in phosphate-buffered saline (pH 7.4; 137 mM NaCl, 2.7 mM KCl, 8 mM Na_2HPO_4 and 2 mM KH_2PO_4). A blue shift is observed on addition of all complexes. Spectra shown are the average of two independent experiments. 76

Figure 3.18 Mechanism of the MTS assay. In the presence of viable cells, MTS is reduced to form a purple formazan product. Measuring the absorbance at 490 nm allows the cell viability to be determined. 78

Figure 3.19 **a)** Cytotoxicity of metal complexes **1, 2, 3c** and **4c** against human neuroblastoma (SH-SY5Y) cells determined using the MTS assay after 24 hrs incubation at 37 °C. **b)** Minimal cytotoxic effects were observed with all octahedral cobalt complexes **3** and **4**, regardless of the axial ligand used. All data is reported as the mean ± standard deviation of three independent experiments. 79

Figure 3.20 Cytotoxicity of complex **4b** against human neuroblastoma (SH-SY5Y) and prostate cancer (PC3) cells after 24 hrs incubation at 37 °C. Minimal cytotoxicity was observed in both cell lines. All data is reported as the mean ± standard deviation of three independent experiments. 80

Figure 3.21 Cytotoxicity of metal complexes **2a-2c** against human neuroblastoma (SH-SY5Y) cells after 24 hrs incubation at 37 °C. Greater cytotoxicity is observed by attaching a cell-penetrating peptide to the backbone (**2b**) or changing the side-arms to piperidine (**2c**). All data is reported as the mean ± standard deviation of three independent experiments. 80

Figure 3.22 Cytotoxicity of fresh and aged Aβ1-42 against human neuroblastoma (SH-SY5Y) cells. No significant cytotoxicity is observed. All data is reported as the mean ± standard deviation of three independent experiments. 81

Figure 4.1 Long pulse and rapid short pulse (RaSP) sequences. Figure adapted from reference *[86]*. 87

Figure 4.2 **a)** Representative fluorescence microscopy images obtained after delivering a Texas Red-labelled 3 kDa dextran across the BBB to the left hippocampus using long pulse and RaSP sequences. No evidence of delivery is observed in the right hippocampus (non-sonicated control; insets) in all experiments. **b)** Calculated normalised optical density (NOD; a measure of the dose delivered) and coefficient of variation (COV; a measure of the distribution heterogeneity). No difference in the NOD was observed, but there was a significant difference in the COV (n = 5 for each pulse sequence; $p < 0.001$). All quantitative analysis was conducted by S. Morse (PhD student, NSB Lab). 89

Figure 4.3 **a)** Representative fluorescence microscopy images of the left hippocampus obtained after injecting a Texas Red-labelled 3 kDa dextran 0, 10 or 20 mins after ultrasound-mediated BBB opening using long pulse and RaSP sequences. No evidence of the 3 kDa dextran is seen in the right hippocampus (non-sonicated control; insets) at all time-points. **b)** Calculated normalised optical density at all time-points (n = 3 for each time-point). With RaSP sequences, the BBB closes within 10 mins. The shaded region is the mean normalised optical density ± standard deviation of control non-sonicated mice (n = 3). All quantitative analysis was conducted by S. Morse (PhD student, NSB Lab). 90

Figure 4.4 Successful delivery of platinum salphen **1** across the BBB to the left hippocampus. Element distribution map for Pt195 (yellow/red) is overlaid on P31 map (grey; provides brain outline) for clarity. No evidence of complex **1** is detected in the right hippocampus (control), indicating that it does not cross the BBB by itself. LA-ICP-MS experiments were run with Mr. B. Sampson (Imperial College London). 92

Figure 4.5 **a)** Fluorescence microscopy image of successful ultrasound-mediated BBB opening in the left hippocampus, detected by co-injecting a Texas Red-labelled 3 kDa dextran (purple). **b)** Element distribution map for Co59 obtained after delivering cobalt complex **4c** across the BBB to the left hippocampus using ultrasound. Missing lines are due to a software malfunction that took place during the LA-ICP-MS run. LA-ICP-MS runs were conducted with Mr. B. Sampson (Imperial College London). . 93

Figure 4.6 Summary of treatment schedule and treatment conditions. Wild type C57BL/6J mice were treated with ultrasound (US) and complex **4b** at either 30 mg/kg or 23 mg/kg once a week for four weeks (n = 2 for each group). Body weight and behaviour were monitored every week in accordance with Home Office regulations and institutional guidelines. 94

Figure 4.7 **a)** No signs of weight loss were observed when complex **4b** (30 mg/kg or 23 mg/kg; n = 2 for each dose) was delivered across the BBB in C57BL/6J mice. Treatment was conducted on days 0, 7, 14 and 21. **b)** Representative example of H&E staining. No differences were observed between the targeted and control regions. 95

Figure 4.8 Summary of treatment schedule and treatment conditions. A total of n = 9 transgenic 5xFAD mice were used in this study, n = 3 mice per group. Group 1 received no treatment, Group 2 received only ultrasound treatment and Group 3 received both complex **4b** and ultrasound treatment. The dose of cobalt complex **4b** used was 30 mg/kg. 97

Figure 4.9 Examples of successful Thioflavin-S (green) and MOAB-2 (cyan) staining in transgenic 5xFAD mice. Thioflavin-S is a dye which stains for Aβ fibrils, whilst MOAB-2 is an antibody which stains for all forms of Aβ. The left hippocampal region is shown in both images. 97

Figure 4.10 **a)** Direct and indirect immunofluorescence staining methods, redrawn from *[313]*. Only one antibody is used in direct methods, whilst two are used in indirect methods. Indirect methods are more complicated to perform, but they are more sensitive than direct methods. **b)** General steps involved in indirect immunohistochemical staining. 99

Figure 4.11 Albumin staining across five sections at the hippocampal level. The albumin extravasation seen is directly related to the extent of BBB opening induced by the focused ultrasound and microbubbles.[86] Under the experimental conditions used, the extent of BBB opening differs throughout the brain, with BBB opening observed at the level in which sections **b** and **c** were taken from. Less BBB opening is seen in sections **a, d** and **e**. It should be noted that we do not expect major extravasation of albumin with these ultrasound parameters.[86] 101

Figure 4.12 **Top:** Sample processing workflow. Brains were sectioned into 20 µm horizontal sections. For ultrasound-treated brains (Groups 2 and 3), five sections across the hippocampal region were stained with albumin to identify the site of BBB opening. Ten sections from each brain around the site of BBB opening were stained with ThS and another ten with MOAB-2. **Bottom:** Image analysis workflow. The region of interest, the left hippocampus, was defined. Images were then thresholded and the particle burden, number of particles and average particle area was calculated automatically using ImageJ. All analysis was conducted blind and repeated three times to prevent bias. 102

Figure 4.13 Representative ThS-stained sections from each brain studied (n = 3 mice per treatment condition). The image shown is the section that best represents the average plaque burden of that brain sample. All quantitative analysis was conducted on ten sections from each brain. Additional images from each brain can be found in the Appendix. 104

Figure 4.14 Representative MOAB-2-stained sections from each brain studied (n = 3 mice per treatment condition). The image shown is the section that best represents the average particle burden of that brain sample. All quantitative analysis was conducted on ten sections from each brain. Additional images from each brain can be found in the Appendix. 105

Figure 4.15 Particle burden, number of particles and average particle area determined from brain sections stained with ThS **(a)** and MOAB-2 **(b)**. A reduction in the particle burden and number of particles ($p < 0.05$) was observed between Group 1 (no treatment) and Group 3 (ultrasound + **4b**). Quantitative analysis was conducted blind and repeated three times to minimise errors (n = 3 mice for each treatment condition; 10 sections per brain). 106

Figure 7.1 Structures of the metal complexes used in this study. Metal salphens **1** and **2** were synthesised by Dr. V. Rakers (PhD student, Vilar Group), whilst cobalt salphens **3a-e** were synthesised by C. Ruehl (PhD student, Vilar Group).[257,258] Complexes **5** and **6** were used as controls and synthesised based on literature protocols.[248,319–321] . . . 117
Figure 8.1 Summary of treatment schedule and treatment conditions. Wild-type C57BL/6J mice were treated with ultrasound and cobalt salnaph **4b** at either 30 mg/kg or 23 mg/kg once a week for four weeks (*n* = 2 mice per group). Body weight was recorded every week. . . . 131
Figure 8.2 Summary of treatment schedule and treatment conditions. A total of *n* = 9 transgenic 5xFAD mice were used in this study, *n* = 3 mice per group. . . . 132
Figure 9.3 **Top:** Synthesis route to CTAB-capped Au NPs.[129] **Bottom:** TEM images of CTAB-capped NPs synthesised (diameter = 19.8 ± 3.1 nm) during MRes work. Non-spherical particles can be seen due to CTAB preferentially binding to the {100} faces.[133] . . . 151
Figure 9.4 Absorbance spectrum of the synthesised Au NPs. An increase in the intensity and wavelength of the absorption band as the NP size is increased is seen.[135] . . . 152
Figure 9.5 Fluorescence emission spectra of Cy5-DNA-Au NPs **A**, **B** and **C**. . . . 152
Figure 9.6 Representative images of the delivery of Texas Red-labelled 3 kDa dextran across the BBB at different peak-negative pressures. The pressure threshold was determined to be between 180 and 350 $kPa_{pk\text{-}neg}$. These experiments were conducted with Dr. A. Pouliopoulos and S. Morse (PhD students, NSB Lab). . . . 153
Figure 9.7 Delivery of Cy5-DNA-Au NPs **A** at a peak-negative pressure of 350 kPa. Minimal fluorescence signal in the Cy5 channel is observed, indicating limited delivery of the NPs across the BBB. . . . 154
Figure 9.8 Representative image of a H&E-stained section. Haematoxylin stains nuclei blue, whilst eosin stains proteins pink. . . . 155
Figure 9.9 Delivery of complex **1** across the BBB using ultrasound (frequency: 1 MHz, peak-negative pressure: 350 kPa, pulse length: 0.005 ms, PRF: 1.25 kHz, burst length: 10 ms, BRF: 0.5 Hz, duration: 250 s). Complex **1** is weakly emissive at 580 nm when excited at 445 nm and thus, sections were imaged in the GFP channel in an attempt to locate the presence of the complex. Little evidence of delivery was observed *via* fluorescence-based methods. . . . 166

LIST OF TABLES

Table 1.1 Existing methods of overcoming the blood-brain barrier. 26

Table 2.1 Properties of the synthesised gold nanoparticles before and after functionalisation with oligonucleotides (λ_{SPR} = surface plasmon resonance wavelength; d_{TEM} = TEM diameter; d_h = hydrodynamic diameter; ζ = zeta potential). 38

Table 2.2 Different metal crosses that were used to try and improve the targeting accuracy. The stainless steel cross gave the best results and was used in all subsequent *in vivo* experiments. Acoustic impedances, *Z*, are taken from references [144, 145]. 43

Table 3.1 Examples of disease-modifying drugs targeted towards Aβ and the clinical study phase that was reached. 56

Table 7.1 Peptide sequences used. 124

ABBREVIATIONS

A	**Aβ**	amyloid beta
	Ab	antibody
	APP	amyloid precursor protein
B	**BBB**	blood-brain barrier
	BL	burst length
	BRF	burst repetition frequency
	BSA	bovine serum albumin
C	**COV**	coefficient of variation
	CTAB	cetyltrimethylammonium bromide
	Cy5	cyanine 5
D	**DCM**	dichloromethane
	DLS	dynamic light scattering
	DMEM	dulbecco's modified eagle medium
	DMSO	dimethyl sulphoxide
E	**ELS**	electrophoretic light scattering
F	**FBS**	foetal calf serum
G	**GUI**	graphical user interface
H	**H&E**	haematoxylin & eosin
	HFIP	1,1,1,3,3,3-hexafluoro-2-propanol
I	**IgG**	immunoglobulin G
J	**JAM**	junctional adhesion molecule
L	**LA-ICP-MS**	laser ablation inductively-coupled plasma mass spectrometry
M	**MOAB-2**	anti-beta amyloid antibody
	mPEG	methoxypolyethylene glycol
	MS-ES$^+$	mass spectrometry electrospray positive ion mode

	MTS	3-(4,5-dimethylthiazol-2-yl)-5-(3-carboxymethoxyphenyl)-2-(4-sulphophenyl)-2*H*-tetrazolium, inner salt
N	**NFT**	neurofibrillary tangle
	NMR	nuclear magnetic resonance
	NOD	normalised optical density
	NP	nanoparticle
	NVU	neurovascular unit
O	**OCT**	optimal cutting temperature
P	**P-gp**	P-glycoprotein
	PBS	phosphate-buffered saline
	PBST	phosphate-buffered saline with 0.1% Tween 20
	PL	pulse length
	PMS	phenazine methosulphate
	PRF	pulse repetition frequency
	PSEN1	presenilin 1
R	**RaSP**	rapid short pulse
	ROS	reactive oxygen species
S	**SNA**	spherical nucleic acid
	SPR	surface plasmon resonance
T	**TBS**	tris-buffered saline
	TCEP	tris(2-carboxyethyl)phosphine
	TEM	transmission electron microscopy
	tg	transgenic
	ThS	thioflavin-S
	ThT	thioflavin-T
U	**US**	ultrasound
V	**VE**	vascular endothelial
W	**wt**	wild type

1 INTRODUCTION

1.1 THE BLOOD-BRAIN BARRIER - AN OBSTACLE FOR DRUG DELIVERY

The blood-brain barrier (BBB) is a highly selective, semi-permeable barrier which maintains brain homeostasis and preserves neuronal function by carefully regulating the passage of substances that enter and exit the brain.[1] It is formed by the endothelial cells that line cerebral vasculature, surrounded by the basement membrane, pericytes and astrocytes (Figure 1.1). Together with microglia and neurons, these components constitute what is known as the neurovascular unit (NVU).

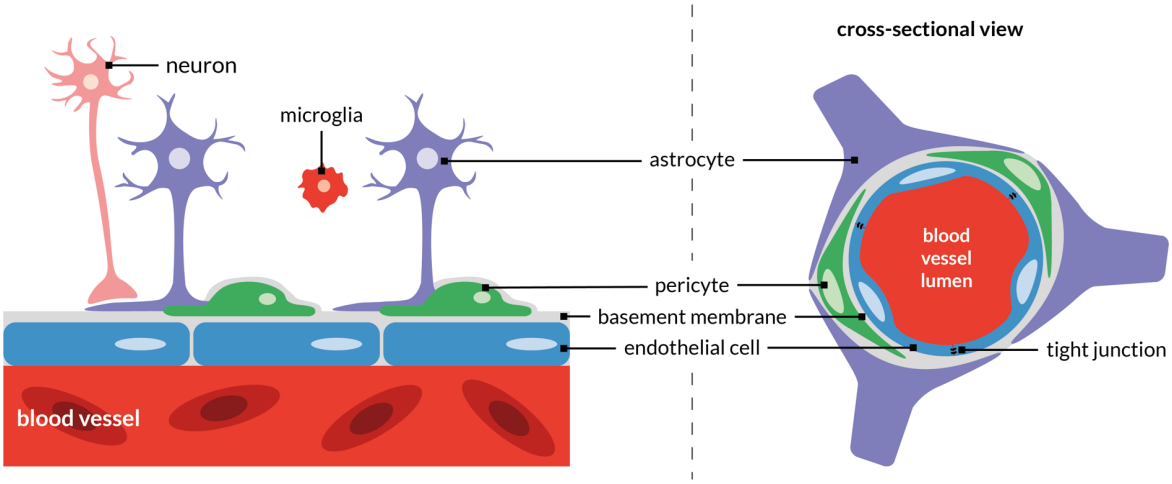


Figure 1.1: Schematic representation of the key components of the neurovascular unit, redrawn from [1]. The blood-brain barrier tightly regulates the paracellular and transcellular transport of substances from the blood to the brain and vice versa.

1.1.1 The Neurovascular Unit

Endothelial cells line the interior surface of all blood vessels in the body. Unlike the endothelial cells found in the rest of the body, cerebral endothelial cells are unique in that they contain few pores and vesicles and are connected by narrow junctions of < 1 nm in diameter.[1–3] These features act to restrict both the paracellular and transcellular transport of substances across the BBB and into the brain; in fact, it has

been stated that brain capillaries are approximately 50 to 100 times tighter than peripheral microvessels.[4] Endothelial cells are surrounded by the vascular basement membrane, which is formed from layers of extracellular matrix proteins such as collagen IV and laminin.[5] The basement membrane is believed to be important for maintaining BBB integrity, with the knockout of collagen IV or laminin leading to deformed BBBs and cerebral haemorrhages *in vivo*.[6,7]

Embedded in the basement membrane are cells known as pericytes, which wrap around cerebral endothelial cells and are known to play key roles in the formation and regulation of the BBB.[8] Studies have shown that both mice deficient in pericytes and mice with high pericyte density have leaky BBBs due to enhanced transcytosis; it is therefore believed that a precise ratio of pericytes to endothelial cells is essential in order to maintain barrier function.[9–12] Pericytes are in contact with the end-feet of astrocytes, which, in turn, are in contact with the synapses of neurons. Astrocytes are the most abundant cells in the brain and have been implicated in a number of critical processes, including the maintenance and repair of the BBB, water and ion regulation, clearance of toxins and the provision of nutrients to neurons.[13–15] The close proximity of astrocytes and neurons allows signalling between the two cell types to take place, enabling the modulation of cerebral blood flow and neuronal activation.[16–18]

The last component of the neurovascular unit is the microglia, which are the primary immune cells of the brain. In response to brain injury, microglia become activated and secrete inflammatory factors that induce BBB disruption, allowing serum components and other immune cells to enter the brain.[19,20] Activated microglia also rapidly migrate to sites of damage and clear cellular debris and bacteria *via* phagocytosis.[21,22] The presence of activated microglia has been observed in a number of brain diseases, including Alzheimer's disease, Parkinson's disease and multiple sclerosis.[23–25]

1.1.2 Endothelial Cell Junctions

There are two types of junctions that exist between adjacent cerebral endothelial cells: tight junctions and adherens junctions (Figure 1.2). These junctions act to severely restrict the paracellular transport of substances from the blood to the brain and vice versa.

Tight junctions are located on the apical side of endothelial cells and consist of three main families of transmembrane proteins: claudins (~20 to 30 kDa), occludins (~60 kDa) and junctional adhesion molecules (~30 to 40 kDa). It is believed that the claudin proteins are essential for maintaining the tightness of tight junctions through the formation of both homophilic and heterophilic intercellular contacts between their extracellular loops.[26,27] To date, several types of claudins have been found in cerebral endothelial cells:

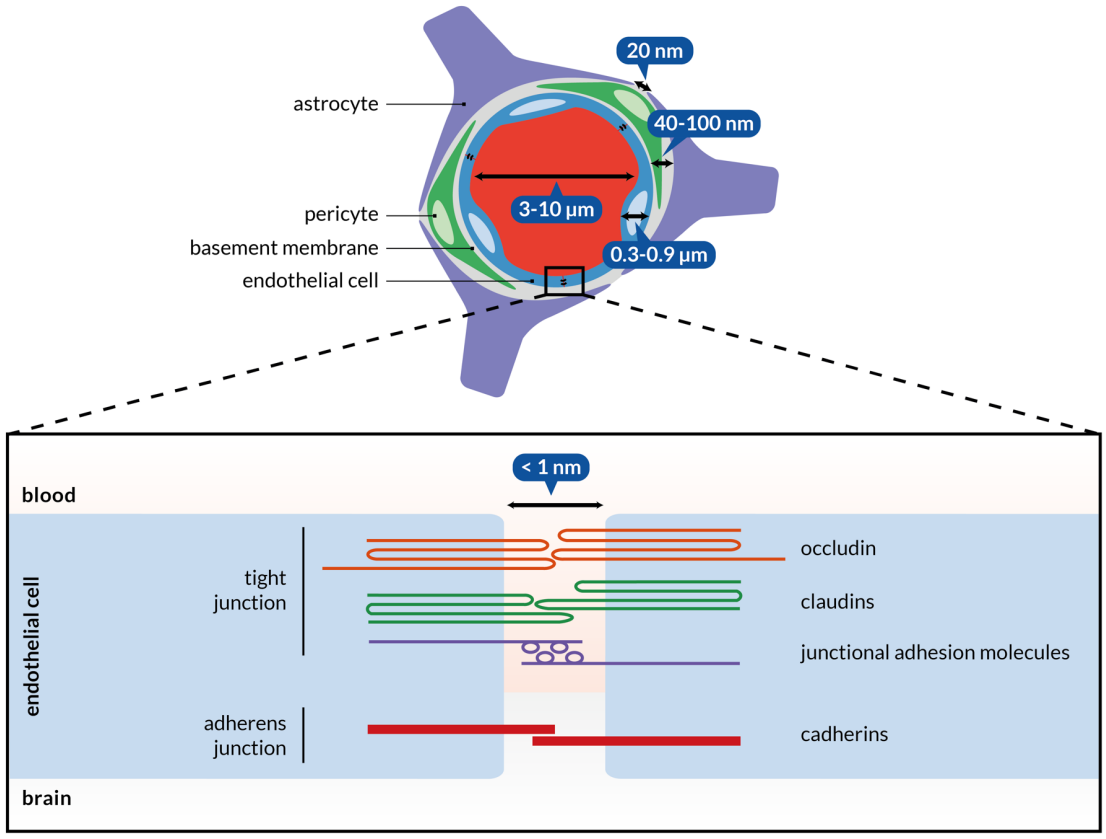


Figure 1.2: The two main types of endothelial cell junctions - tight junctions and adherens junctions - and the key proteins that they are composed of, redrawn from [1, 33]. The blue boxes show the estimated distances and spaces within the BBB that therapeutic agents have to overcome in order to enter the brain.[1]

claudins-3, -5 and -12.[28,29] Claudin-5 is expressed at significantly higher levels than the other claudins in cerebral capillaries and has therefore been the most widely studied in the context of the BBB.[30,31] Knockout of claudin-5 in mice results in severely leaky BBBs that molecules of up to 800 Da can successfully permeate.[32] Moreover, these mice were found to die within just ten hours of birth, highlighting the importance of having a tight BBB.[32]

In contrast to claudin-deficient mice, mice deficient in occludin are viable and show tight junctions that are morphologically identical to those in wild type mice.[34] However, these mice show chronic inflammation, brain calcification and growth retardation.[34] It has been proposed that occludin primarily has a regulatory role in the BBB; for instance, occludin phosphorylation is reported to play a critical role in the regulation of tight junction permeability.[35] Occludin is also known to be redox-sensitive and is believed to act as a redox sensor at tight junctions: under hypoxic conditions, occludin oligomers dissociate to induce tight junction disruption, whilst under normoxic conditions, occludin oligomerisation and tight junction assembly is promoted.[36,37]

The third component of tight junctions consists of junctional adhesion molecules (JAM), such as JAM-1, JAM-2 and JAM-3. The role of JAMs is yet to be fully elucidated, but it has been proposed that JAMs may be involved in tight junction assembly through interactions with other tight junction proteins.[38] JAMs are also believed to contribute towards BBB integrity as decreased JAM-1 expression is observed in *in vivo* models of BBB breakdown.[39]

On the basal side of the BBB are the adherens junctions, which are mainly composed of vascular endothelial (VE)-cadherin proteins (Figure 1.2). The cytoplasmic domain of VE-cadherin is connected to the intracellular actin cytoskeleton *via* catenin proteins.[40] Multiple functions have been associated with adherens junctions, including the stabilisation of intercellular contacts, regulation of the actin cytoskeleton and intracellular signalling.[40,41] In fact, it has been suggested that VE-cadherin can directly regulate the expression of the key tight junction protein claudin-5.[42]

1.2 TRANSPORT ACROSS THE BLOOD-BRAIN BARRIER

The presence of tight junctions and adherens junctions between adjacent endothelial cells greatly restricts the movement of substances *via* a paracellular route, with only small ions and molecules able to enter the brain this way (Figure 1.3).[4,43] As a consequence, the majority of substances can only pass from the blood to the brain and vice versa through transcellular routes. However, transport across the BBB *via* transcellular pathways is also somewhat restricted; although small, lipophilic molecules (*e.g.* O_2 and ethanol) can pass through endothelial cells by passive diffusion, larger or more lipophilic molecules (*e.g.* glucose and insulin) must pass *via* a transport route involving specialised receptors.[4,43] A number of efflux transporters such as P-glycoprotein (P-gp) are also located at the apical side of the endothelial cell membrane and serve to actively extrude harmful substances from the brain.[44] The presence of the BBB therefore allows the brain to regulate the influx of essential nutrients whilst simultaneously excluding or effluxing harmful pathogens and neurotoxins.

Whilst an intact BBB is essential for the maintenance of brain homeostasis, its presence makes the treatment of brain diseases extremely challenging; the majority of small molecule drugs are too large to cross the BBB *via* a paracellular route and cannot be easily modified to cross *via* a transcellular route. Moreover, a wide range of structurally-diverse drugs are known substrates of the efflux transporters located at the BBB.[45–47] Due to this, even drugs which should be able to cross the BBB *via* transcellular routes may not be able to enter the brain at therapeutic concentrations; for example, Schinkel *et al.* reported that mice deficient in P-gp showed significantly increased sensitivity to the neurotoxin ivermectin (100-fold) and

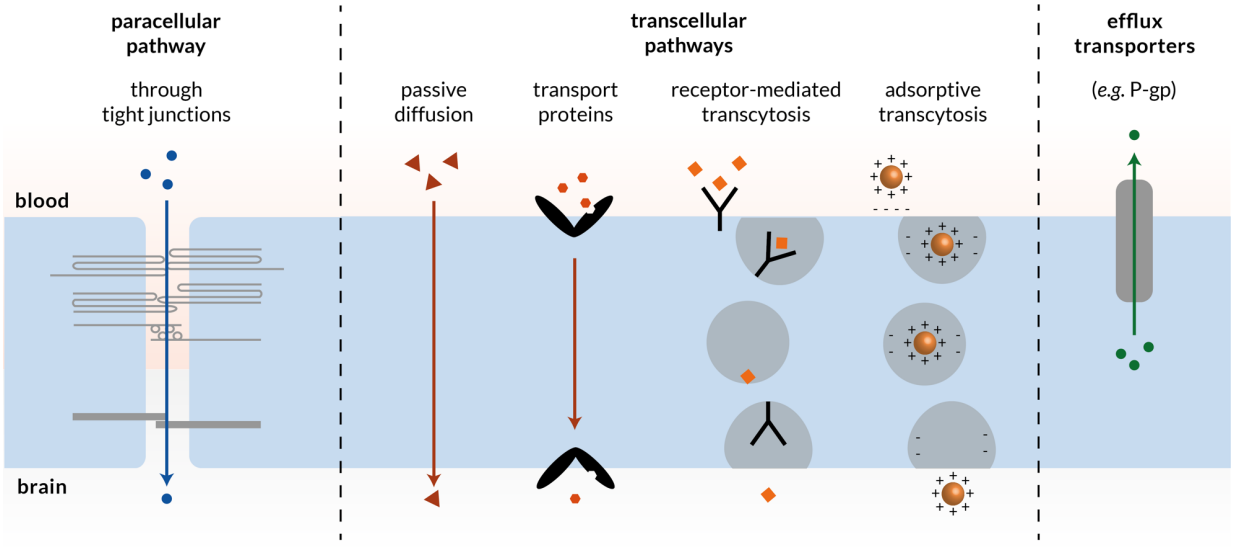


Figure 1.3: Possible transport routes across the blood-brain barrier, redrawn from [4]. Due to the presence of narrow tight junctions between adjacent endothelial cells (left), the majority of substances can only enter the brain *via* a transcellular pathway (middle). Actively opposing the influx of substances into the brain are efflux transporters such as P-gp, which sit on the apical side of the BBB (right).

chemotherapeutic vinblastine (3-fold), suggesting that the action of P-gp severely restricts their entry into the brain.[45–47] It has been claimed that over 98% of conventional small molecule drugs are unable to cross the BBB, making it one of the biggest obstacles for the treatment of brain diseases such as glioblastoma and Alzheimer's disease.[48]

1.2.1 Existing Methods to Overcome the Blood-Brain Barrier

Numerous studies have tried to elucidate the exact physiochemical properties required for therapeutic agents to efficiently cross the BBB. Characteristics such as low molecular weight, low polarity, moderate lipophilicity and a low propensity for hydrogen bond formation have all been suggested to lead to improved BBB penetration.[49–51] However, designing effective therapeutics that successfully fulfil all of these criteria is non-trivial and thus, the development of methods to overcome the BBB has been of great interest in recent years. As of now, there are a variety of methods that have been developed to do this, a selection of which are presented in Table 1.1.

The most straightforward approaches to overcome the BBB involve bypassing the BBB altogether by delivering therapeutics directly into the central nervous system using intrathecal (*i.e.* into the lumbar spine) or intracerebroventricular (*i.e.* into the lateral ventricles of the brain) injections.[52,53] However, aside from

Method	Advantages	Disadvantages
direct injection	targeted; low off-target toxicity	highly invasive; poor drug penetration beyond injection site
intranasal delivery	non-invasive; reduction of systemic side-effects; easy administration	non-targeted; limited dosing volume possible: drugs must be potent; frequent use can damage nasal mucosa
interstitial wafers	targeted; sustained and controllable drug release; reduction of systemic side-effects	invasive: implants increase chances of infection; can only deliver a limited amount of therapeutic per implant; poor drug penetration beyond implant site
osmotic disruption	less invasive than direct injections; induces transient BBB disruption	invasive; induces transient cerebral edema; non-targeted: linked to neurological deficits, strokes, seizures
enhanced transcellular transport	non-invasive; easy administration	non-targeted; non-trivial: must consider first pass clearance, immune response, off-target effects *etc*; often poor efficiency

Table 1.1: Existing methods of overcoming the blood-brain barrier.

being highly invasive, the concentration of the administered drug is often very low in regions far away from the injection site, limiting the use of these methods in the treatment of brain diseases.[54]

In recent years, intranasal delivery has emerged as a non-invasive alternative to bypass the BBB. Therapeutics administered intranasally can reach the central nervous system *via* the olfactory and trigeminal neural pathways, reducing the risk of any side-effects associated with systemic exposure.[55–57] As of now, this method has been used to successfully deliver a wide range of substances to the brain, including small molecule drugs and peptides.[55–57] However, only small volumes of the drug can be administered at a time, meaning that this method is only suitable for highly potent therapeutics.[58,59] Furthermore, frequent usage can lead to damage of the nasal mucosa.[58,59]

In addition to intrathecal, intracerebroventricular and intranasal drug delivery methods, interstitial delivery methods have also been investigated as a way of bypassing the BBB. An example of this is the use of interstitial wafers, in which the therapeutics to be delivered are incorporated into a polymeric wafer and implanted into the brain.[60] Successful drug delivery to the brain has been shown with this method, but the need to surgically implant objects in the brain results in an increased chance for infection.[61] Low drug concentrations are also found in brain regions located far away from the implant site, limiting their use.[62]

An alternative strategy to bypassing the BBB is to transiently disrupt the BBB *via* the intraarterial administration of osmotic agents such as mannitol.[63] Osmotic agents induce endothelial cell dehydration, resulting in cell shrinkage, widening of the tight junctions and, in turn, increased BBB permeability.[64] The BBB disruption induced is transient, with a return to normal permeability observed within approximately ten minutes.[64,65] To date, osmotic BBB disruption methods have been used in a number of pre-clinical and clinical trials; for example, in 2000, Doolittle *et al.* used osmotic BBB disruption in conjunction with intraarterial chemotherapy in over two hundred brain tumour patients and observed high rates of tumour response.[66–68] However, despite promising results being obtained, this technique has not been widely adopted as it is non-specific and leads to BBB disruption throughout the entire brain. As a consequence, adverse side-effects such as strokes, neurological deficits and seizures have been reported using this method.[66,69] Osmotic BBB disruption is also known to lead to transient cerebral edema, with an increase of ~1.5% in brain water reported after application.[66,70]

The chemical modification of existing therapeutics to facilitate transcellular passage across the BBB has also been attempted. One of the most widely used strategies to date involves the targeting of endogenous receptors, such as the transferrin receptor (TfR), which are involved in receptor-mediated transcytosis across the BBB; for example, Mishra *et al.* developed a series of TfR-targeted nanoparticles as carriers for the antiviral drug azidothymidine and showed that their accumulation in the brain was significantly higher (~21%) than non-targeted nanoparticles (~9%) four hours post-administration.[71] Whilst promising

results have been obtained using this strategy, it should be noted that this is a non-targeted method and is difficult to achieve with high efficiency. In the case of the transferrin pathway, TfR is known to be expressed in many cell types, including red blood cells, hepatocytes and intestinal cells.[72–74] Moreover, its natural ligand, transferrin, is present in the bloodstream at µM concentrations and may therefore actively compete with TfR-targeted therapeutics.[75–77]

1.2.2 Focused Ultrasound-Mediated Blood-Brain Barrier Opening

Over the past twenty years, the use of focused ultrasound combined with intravenously administered microbubbles has emerged as a promising method to disrupt the BBB in a non-invasive, targeted and transient manner.[78] Microbubbles are typically composed of a gas core encapsulated by a protein or lipid shell, commercially available for use as contrast agents in ultrasound imaging.[79,80] The diameter of microbubbles used for biomedical applications is between 0.5 to 10 µm, making them approximately equal to the size of red blood cells.[79–81] In ultrasound-mediated BBB opening methods, microbubbles are administered intravenously and exposed to a focused ultrasound field (Figure 1.4).[78] Microbubbles in an ultrasound field radially oscillate, exerting mechanical stress on the blood vessel walls.[82,83] This, in turn, leads to an increase in vessel permeability, enhancing the delivery of therapeutic agents to the brain.[78,84–87] Ultrasound-mediated BBB disruption is a transient effect, with the BBB reported to return to its normal permeability level within 4 to 48 hrs after ultrasound exposure in rodent models.[88–90]

To date, a wide range of small molecules, nanoparticles and antibodies have been successfully delivered across the BBB in animal models using focused ultrasound.[78,84–87] Moreover, McDannold *et al.* have shown that it is possible to repeatedly open the BBB with ultrasound in monkeys without any significant changes in behaviour or tissue morphology.[91] The magnitude of ultrasound-induced BBB opening can be controlled by the acoustic pressure amplitudes used, with the use of higher acoustic pressures leading to greater BBB opening and allowing the delivery of larger substances across the BBB.[92] However, the choice of acoustic pressure is also believed to be strongly correlated to the safety profile achieved, with safer BBB opening obtained at lower acoustic pressures; for example, Baseri *et al.* observed minimal tissue effects at low acoustic pressures, but saw multiple sites of red blood cell extravasation or large-scale haemorrhages when higher acoustic pressures were used.[92,93] Varying the other parameters such as the ultrasound frequency, pulse length, pulse repetition frequency or microbubble concentration has also been shown to lead to differences in the magnitude of BBB disruption induced.[94–98]

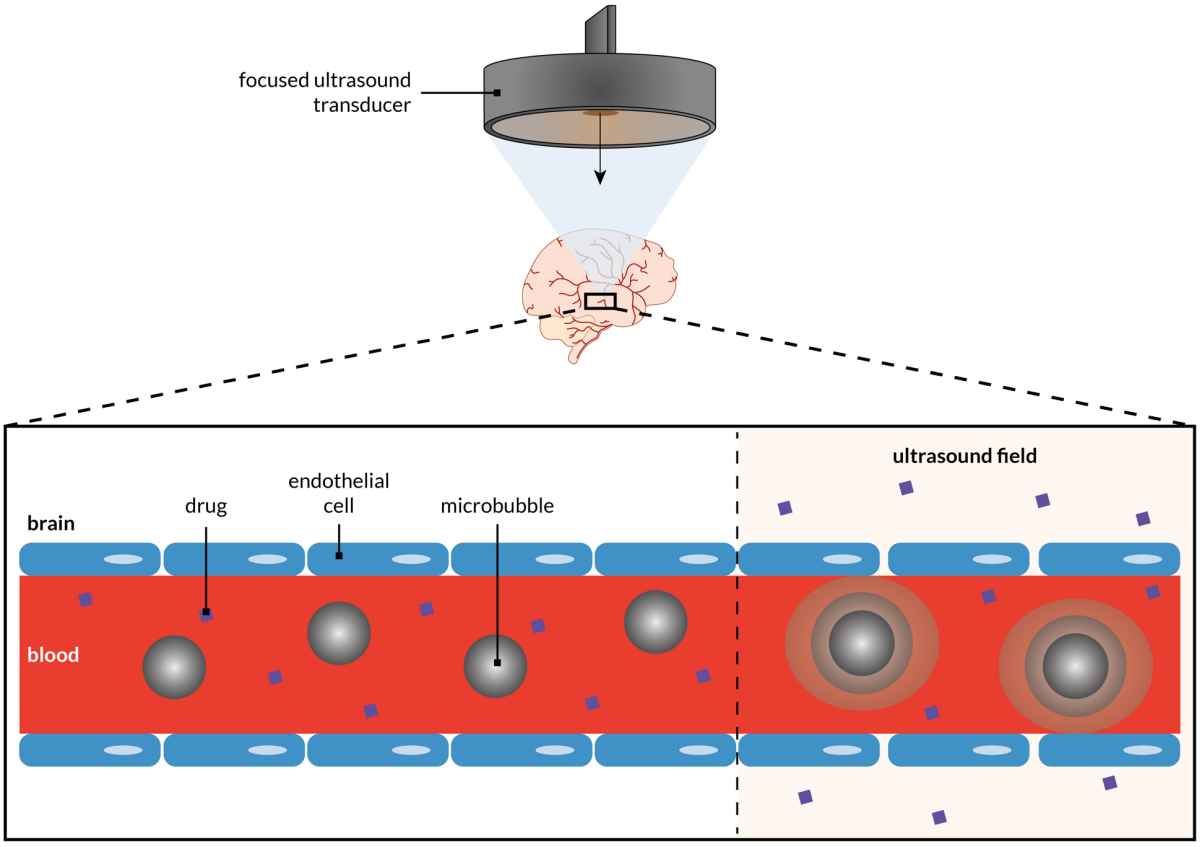


Figure 1.4: Schematic representation of focused ultrasound-mediated BBB opening. In this method, intravenously administered microbubbles are exposed to focused ultrasound. This induces the microbubbles to radially oscillate and exert mechanical stress on the blood vessel walls, resulting in increased permeability.

Precise determination of the acoustic parameters required for safe and reliable ultrasound-mediated BBB opening has been of great interest in recent years; however, as of now, the optimal parameter set has not been identified. One of the main reasons for this is that the exact biological mechanisms underlying focused ultrasound-mediated BBB opening have yet to be fully elucidated. Various studies have provided evidence that ultrasound-mediated BBB opening leads to both enhanced paracellular and transcellular transport across the BBB, with a widening of the tight junctions between endothelial cells, an increase in the number of vesicles and vacuoles present, endothelial cell fenestration and suppression of P-gp expression being observed in the sonicated region.[84,88,99] Interestingly, a size-threshold has been associated with ultrasound-mediated BBB opening, with smaller molecules being delivered more efficiently across the BBB than larger molecules using the same set of ultrasound parameters.[92,100] Since the size of vesicles is greater than that of the model drugs used in these studies, it has been suggested that the presence of a size-threshold indicates that the widening of tight junctions is the predominant mechanism of ultrasound-mediated BBB opening.[92,100]

In spite of the incomplete understanding regarding the mechanisms of ultrasound-mediated BBB opening, a number of Phase I clinical trials are currently being conducted in an attempt to assess the safety and feasibility of this method in human patients. Promising results have been achieved to date, with Lipsman *et al.* and Abrahao *et al.* reporting that the BBB can be opened safely, reversibly and reliably in patients with early to moderate Alzheimer's disease and amyotrophic lateral sclerosis respectively.[101,102]

1.3 THESIS AIMS

Being able to deliver drugs across the BBB in a non-invasive and targeted manner without requiring additional chemical modifications greatly expands the scope for the development of therapeutics for brain diseases. The overall aim of this thesis was to develop chemical systems that can take advantage of ultrasound-mediated drug delivery methods and to assess their therapeutic efficacy *in vivo* by delivering them across the BBB in relevant mouse models. Two systems have been investigated in this work: nanoparticles as delivery platforms for combination therapies (Chapter 2) and metal complexes for the treatment of Alzheimer's disease (Chapters 3 and 4).

2 DNA-COATED NANOPARTICLES FOR BRAIN DISEASES

2.1 BACKGROUND

Conventional methods employed to administer small molecule drugs are typically systemic, involving oral, gastrointestinal or intravenous administration. Drawbacks of systemic administration methods include a lack of specificity, low accumulation of the drug at the target location and the potential for adverse side-effects. In recent years, functionalised nanoparticles have attracted significant interest for therapeutic applications as they can facilitate targeted and site-specific drug delivery. The most commonly used nanosystems for drug delivery are based on either organic (*e.g.* micelles and liposomes), polymeric (*e.g.* dendrimers) or inorganic (*e.g.* quantum dots, gold nanoparticles and superparamagnetic iron oxide nanoparticles) systems.[103–106]

2.1.1 Spherical Nucleic Acids

Spherical nanoparticles coated with a dense layer of oligonucleotides, also known as spherical nucleic acids (SNAs), have emerged as promising nanoplatforms for drug delivery applications due to their high versatility.[107] To date, a variety of core materials have been used to form them, including gold nanoparticles and quantum dots, and almost any oligonucleotide sequence can be attached to the surface (Figure 2.1).[108,109] Numerous studies have shown that these nanoparticles can be easily adapted for diagnostic, therapeutic and material synthesis purposes; for example, Jensen *et al.* designed a system consisting of a gold nanoparticle core functionalised with small interfering RNA targeted towards the *Bcl2L12* oncogene, which is upregulated in glioblastoma, the most common form of primary brain cancer.[108,110–112] Administration of these nanoparticles in glioblastoma mouse models led to the reduced expression of Bcl2L12 and a decline in tumour progression.[108]

In addition to their versatility, the dense, highly orientated oligonucleotide shell that coats these nanoparticles has been shown to convey desirable properties to the nanoparticles regardless of the core material used; for instance, despite possessing a highly negatively charged oligonucleotide shell, these nanoparticles have been shown to rapidly enter over fifty different cell types without the need for external transfecting agents.[111,113] Conversely, linear oligonucleotides of the same sequence are unable to

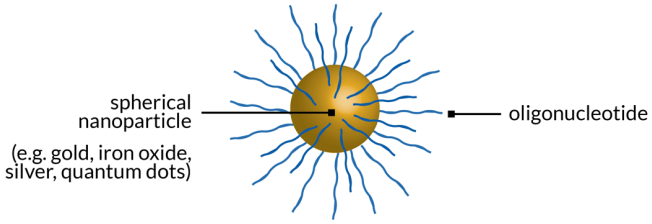


Figure 2.1: Structure of a spherical nucleic acid.

enter cells without the use of cationic transfecting agents due to electrostatic repulsion between the cell membrane and their negatively charged phosphate backbones.[113] The efficient cellular uptake of SNAs is thought to occur through specific binding of the oligonucleotide shell to Class A scavenger receptors on the cell membrane and subsequent internalisation *via* a caveolae-mediated pathway.[113,114] The difference in cell uptake abilities between SNAs and linear single-stranded oligonucleotides is believed to be due to the 3D arrangement of oligonucleotides on the nanoparticle surface; through studies in mouse endothelial (C166) cells, Choi *et al.* showed that it is the 3D oligonucleotide shell - and not the core material - that is responsible for the nanoparticles' high binding affinity to cell surface receptors.[113] Other desirable properties that are associated with SNAs include resistance to enzymatic degradation, minimal triggering of cellular immune responses and no observed toxicity when administered *in vivo*.[115–117]

As of now, a number of different variations of SNAs have been developed, with a wide range of core materials and oligonucleotide sequences being employed; however, there are very few examples of their use - and more broadly, other nanoparticle systems - in the treatment of brain diseases as their size typically prevents them from efficiently crossing the BBB.[48,108,118] Interestingly, the *Bcl2L12*-targeted SNAs developed by Jensen *et al.* have been reported to cross the BBB by themselves, with SNAs being detected in the brains of both healthy and glioma-bearing mice 48 hrs after their administration.[108] However, significantly greater SNA accumulation was found in the tumours of glioma-bearing mice than in normal brain tissue.[108] In glioblastoma, the BBB is known to be leaky at the tumour core, but intact at the tumour margins and surrounding tissue; as a consequence, many of the strategies to treat glioblastoma are aimed at overcoming the intact BBB at the tumour margins to prevent tumour recurrences.[119] Thus, whilst the results obtained by Jensen *et al.* are promising, the significantly higher accumulation of SNAs that was detected in the tumour tissue compared to in healthy tissue suggests that the intact BBB remains an obstacle for the efficient delivery of these types of nanoparticles to the brain.

2.2 AIMS AND OBJECTIVES

The overall aims of the work presented in this chapter were to investigate the feasibility of delivering SNAs across the BBB using focused ultrasound and to probe the size-dependency of focused ultrasound-mediated BBB opening. To achieve these aims, the following objectives had to be fulfilled:

- Synthesise and characterise a range of SNAs of different sizes.
- Deliver the synthesised nanoparticles across the BBB *in vivo* using ultrasound and microbubbles.
- Assess whether the nanoparticles remain intact upon delivery to the brain using microscopy.
- Investigate the size-dependency of focused ultrasound-mediated BBB opening by comparing the delivery of the different sized nanoparticles to the brain.
- Assess the safety of the experimental conditions used with H&E staining.

2.3 RESULTS AND DISCUSSION

2.3.1 Nanoparticle Synthesis and Characterisation

In spite of the fact that the majority of clinically approved nanoparticles to date have sizes of approximately 100-200 nm (*e.g.* Doxil®, 80 to 100 nm; Myocet®, 150 to 250 nm), there is growing interest in developing smaller nanoparticles, particularly for anti-cancer applications. Nanoparticles of 50 nm diameter or smaller have been shown to exhibit increased tumour penetration over their larger counterparts.[120–122] Moreover, prior work suggests that there is a size-threshold associated with focused ultrasound-mediated delivery across the BBB, with smaller molecular weight dextrans being delivered more efficiently than larger molecular weight dextrans under the same experimental conditions.[92,100] Due to this observation, it has been suggested that the predominant mechanism of focused ultrasound-mediated drug delivery across the BBB is increased paracellular transport due to a widening of the tight junctions between adjacent endothelial cells.[92] As a consequence, smaller nanoparticles are likely to be delivered more efficiently using this method than larger nanoparticles. With this in mind, it was decided that sub-25 nm oligonucleotide-coated nanoparticles would be investigated in this initial study.

Synthesis of Monodisperse Gold Nanoparticles

To date, SNAs have been made using a variety of different core materials, including gold nanoparticles (Au NPs), quantum dots and iron oxide nanoparticles.[108,109,123] For this study, a Au NP core was chosen as Au NPs have been widely investigated in the past and there are well-established methods to synthesise them in a monodisperse manner (Figure 2.2). The majority of routes used to synthesise Au NPs involve the reduction of a gold source, $HAuCl_4$, from a +3 oxidation state to 0.[124] A capping agent, such as citrate, is typically added to prevent nanoparticle aggregation or further growth.

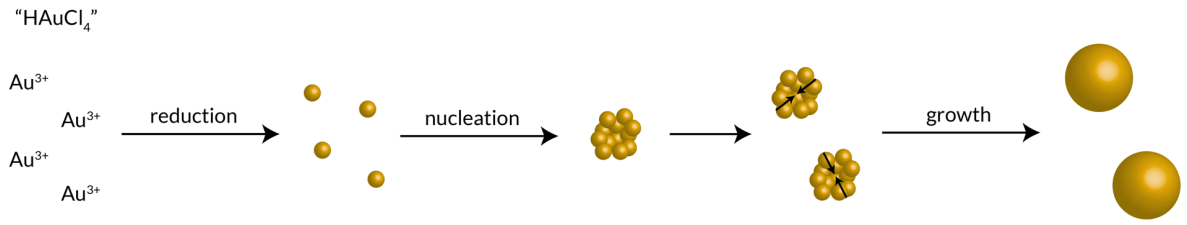
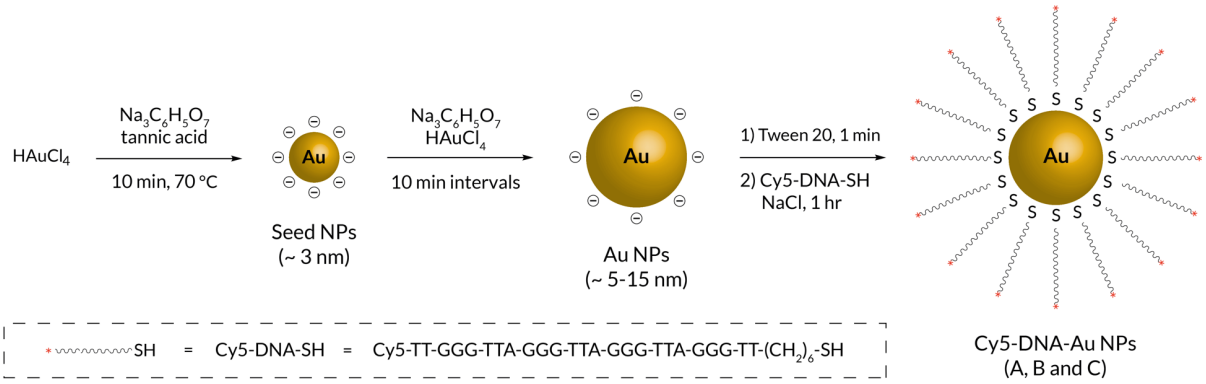


Figure 2.2: Proposed mechanism of gold nanoparticle formation, redrawn from [124]. The gold precursor is reduced to give primary particles, which grow into larger particles *via* coalescence.

The direct reduction of $HAuCl_4$ by sodium citrate is the most widely used method to synthesise Au NPs, giving nanoparticles of 5 to 150 nm in diameter.[125,126] Whilst a certain level of size control can be obtained by adjusting the pH, solvent and $HAuCl_4$:citrate ratio, the resulting particles are typically polydisperse and of varying morphology due to a lack of control over the nucleation and growth steps.[126–128] To overcome this, seeded growth methods have been developed. These involve the initial synthesis of small seed particles, which are then grown larger through successive growth steps.[129,130] The use of multiple growth steps allows for a high seed particle:metal salt ratio to be maintained, favouring the growth process over additional nucleation.[129,130] However, to date, most seeded growth protocols rely on the use of strong reducing agents and capping agents, resulting in highly passivated particles that are difficult to functionalise further; for example, one of the most well-established seeded growth methods to synthesise monodisperse Au NPs of 5-40 nm involves the use of cetyltrimethylammonium bromide (CTAB) as both the reducing and capping agent.[129] Not only is CTAB difficult to displace due to its bulky nature, making subsequent surface functionalisation reactions difficult, but free CTAB is toxic at sub-micromolar concentrations. Stringent purification steps must therefore be carried out if the nanoparticles are to be used for *in vitro* or *in vivo* applications.[131] As was shown during MRes work, the addition of CTAB can also lead to the formation of non-spherical particle populations as CTAB preferentially binds to the {100} faces of Au NPs, leading to greater Au^0 deposition on the {111} faces (Appendix: Figure 9.3).[132,133]

To avoid these issues, a CTAB-free seeded growth protocol was used in this work, involving the reduction of a gold(III) source with a combination of tannic acid and sodium citrate (Scheme 1).[130] The synthesised Au NPs were then coated with a 25-base length oligonucleotide, containing a thiol tag on the 3' end to allow for attachment to the Au NP surface and a Cy5 tag on the 5' end to allow for fluorescence detection. A 25-base length oligonucleotide was chosen as this is the typical length of gene therapies. To functionalise the nanoparticles, a method adapted from Li *et al.* was followed.[134] First, a solution of Tween20 was added to the nanoparticles in order to protect their surface and prevent aggregation. The thiolated oligonucleotides and NaCl were then added. The addition of NaCl is used to screen the charges between oligonucleotide strands and allow for more efficient loading. In contrast to the method reported by Li *et al.*, the addition of methoxypolyethylene glycol thiol (mPEG-SH; 6000 kDa) was found to be unnecessary to form stable particles and was not included so that higher loading of oligonucleotides on the particle surface could be achieved.



Scheme 1: Synthesis of DNA-coated gold nanoparticles *via* a seeded growth protocol.[130,134] Ten successive growth steps were performed, resulting in five gold nanoparticle solutions of increasing particle size.

Characterisation of DNA-coated Gold Nanoparticles

Following the method depicted above, three sets of Cy5-DNA-Au NPs (**A**, **B** and **C**) of different sizes were synthesised. All nanoparticles were fully characterised using UV-Vis spectroscopy, transmission electron microscopy (TEM), dynamic light scattering (DLS) and electrophoretic light scattering (ELS). We have previously reported the characterisation of the nanoparticles used in this study in extensive detail and will therefore only briefly discuss this here.[87,133]

Absorption spectra of the synthesised Au NPs show a strong absorption band at ~515 nm for all sets of nanoparticles, indicating the formation of small Au NPs with diameters less than 30 nm (Table 2.1;

Appendix: Figure 9.4).[135,136] This was confirmed by TEM, which showed that the three sets of Cy5-DNA-Au NPs synthesised were monodisperse, quasi-spherical and had diameters less than 15 nm (Figure 2.3). Quantification was performed using ImageJ by measuring at least 100 nanoparticles per set, with the core Au NP diameters determined to 6.3 ± 0.7 nm (**A**), 9.5 ± 1.4 nm (**B**) and 14.2 ± 1.2 nm (**C**).

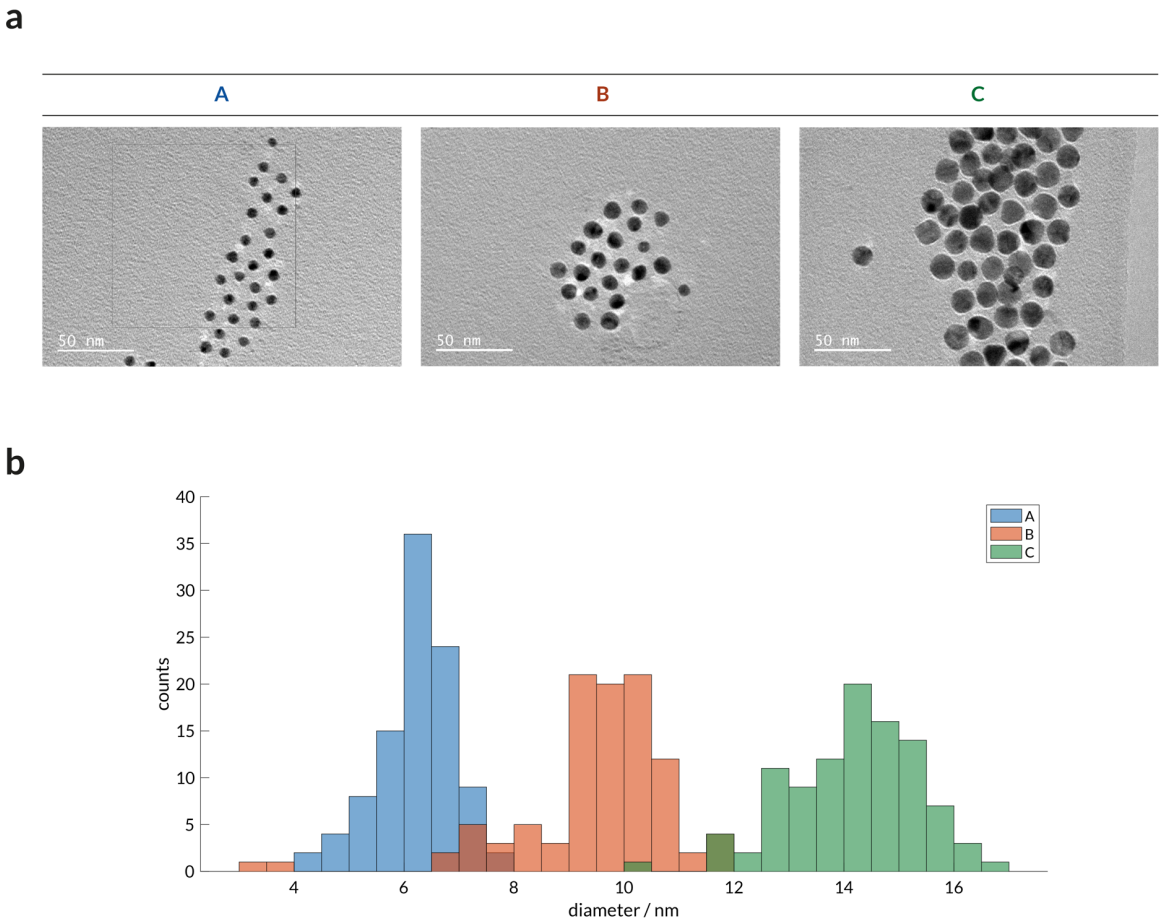


Figure 2.3: **a)** Representative TEM images of the synthesised Cy5-DNA-Au NPs **A**, **B** and **C**. Particles are monodisperse and quasi-spherical. **b)** Size distribution of Cy5-DNA-Au NPs **A, B** and **C**, determined by measuring the particles using ImageJ (n > 100 for each set).

Further characterisation of the synthesised nanoparticles was carried out using DLS and ELS. DLS allows the determination of the hydrodynamic diameters of the particles, which takes into account both the size of the particles as well as any solvent effects. In DLS, a single frequency laser beam is directed through the nanoparticle sample. Upon hitting the particles, the incident light is scattered. Due to the effects of Brownian motion, the intensity of the scattered light fluctuates over time; this fluctuation is dependent on the particle size, with larger particles - which move at slower speeds - causing less fluctuations than smal-

ler particles.[137] The rate at which the intensity of the scattered light fluctuates can be used to determine the diffusion coefficient of the particles and, in turn, the hydrodynamic diameter *via* the Stokes-Einstein equation (Figure 2.4).[137]

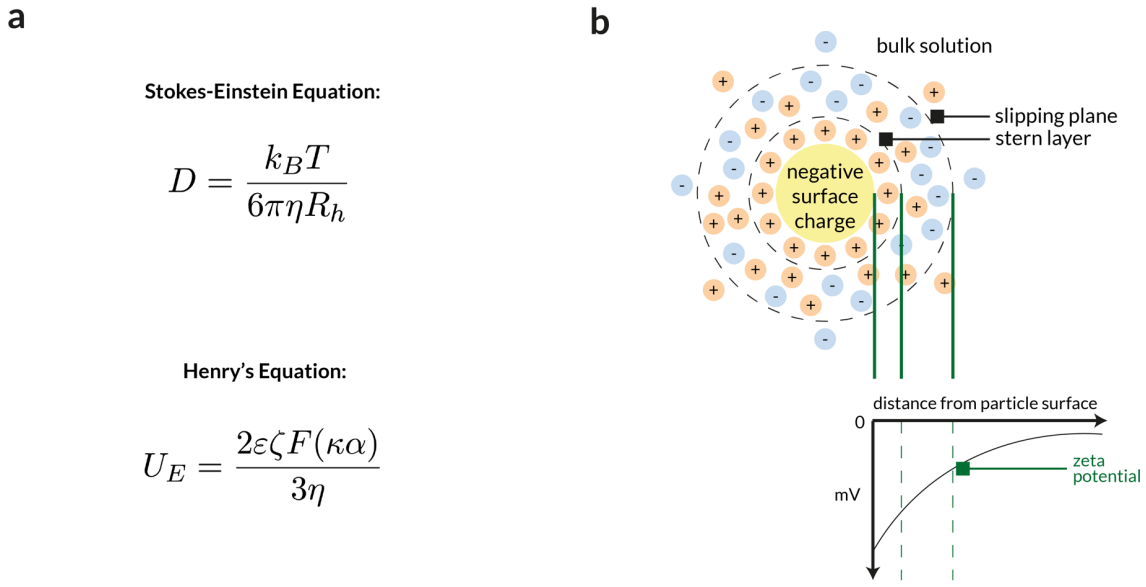


Figure 2.4: **a)** The Stokes-Einstein and Henry's equation used in DLS and ELS. (*D*: diffusion coefficient, k_B: Boltzmann constant, *T*: temperature, η: solvent viscosity, R_h: hydrodynamic radius, U_E: electrophoretic mobility, ε: dielectric constant of the solution, ζ : zeta potential, $F(\kappa\alpha)$: Henry function) **b)** Zeta potential is the potential at the boundary between the slipping plane and the bulk solution.

In contrast, ELS is used to determine the zeta potential of the particles, the electric potential at the boundary between the bulk solution and the slipping plane, which can give information about the particle surface charge (Figure 2.4).[138] Voltage is applied across the nanoparticle sample, causing any charged particles to be attracted to the oppositely charged side. In a similar way to DLS, a laser beam is applied to the sample and the frequency shifts in the scattered light due to the movement of the particles in the applied electric field are measured.[138] This allows the electrophoretic mobility of the particles to be calculated, which can be used to determine the zeta potential with Henry's equation (Figure 2.4).

Upon functionalisation of the Au NPs with thiolated oligonucleotides, the hydrodynamic diameters of the Au NPs were seen to increase from less than 12 nm to greater than 20 nm, indicating successful surface attachment (Table 2.1). Changes in the zeta potentials were also observed, with all zeta potentials found to be negative due to the negatively charged citrate (Au NPs) or oligonucleotides (Cy5-DNA-Au NPs) bound to the nanoparticle surface (Table 2.1). The number of oligonucleotide strands attached to each set of nanoparticles was also estimated following methods reported by Demers *et al.*[139] Briefly, the synthesised

		λ_{SPR}/ nm	d_{TEM}/ nm	d_h/ nm	ζ / mV	Oligo Strands / NP
Au NPs	**A**	511	6.3 ± 0.7	5.3 ± 0.5	-50.4 ± 5.5	-
	B	517	9.5 ± 1.4	7.9 ± 1.3	-42.0 ± 4.2	-
	C	519	14.2 ± 1.2	11.9 ± 1.3	-50.3 ± 4.3	-
Cy5-DNA-Au NPs	**A**	-	-	21.6 ± 3.3	-42.5 ± 3.1	40.7 ± 1.8
	B	-	-	23.3 ± 2.6	-35.0 ± 3.5	49.2 ± 2.1
	C	-	-	25.2 ± 1.9	-21.1 ± 1.6	77.0 ± 2.3

Table 2.1: Properties of the synthesised gold nanoparticles before and after functionalisation with oligonucleotides (λ_{SPR} = surface plasmon resonance wavelength; d_{TEM} = TEM diameter; d_h = hydrodynamic diameter; ζ = zeta potential).

Cy5-DNA-Au NPs were incubated with mercaptoethanol, which is able to displace the surface-bound oligonucleotides. Following centrifugation, the fluorescence intensity of the supernatant (containing the displaced oligonucleotides) was compared to a calibration curve to determine the concentration of oligonucleotides present. The average number of oligonucleotides that was attached per particle was then estimated by dividing the measured oligonucleotide concentration by the initial Au NP concentration. Over a series of experiments conducted as part of the MRes project, the oligonucleotide loading was adjusted to ensure that Cy5-DNA-Au NPs **A**, **B** and **C** had similar emission intensities so that their delivery across the BBB with ultrasound could be compared using fluorescence detection methods (Table 2.1; Appendix: Figure 9.5).[87,133] Whilst the fluorescence emission of Cy5-DNA-Au NPs **A**, **B** and **C** are not significantly different from each other, allowing us to conduct the proposed *in vivo* experiments, the precise surface coverage of the synthesised NPs should be determined in future work. Several studies have shown that the properties of SNAs are largely governed by the 3D architecture of the oligonucleotide shell; thus, any differences in the density of the oligonucleotides on the NP surface could lead to different cellular uptake and biodistribution of the Cy5-DNA-Au NPs *in vivo*.[113,140] Ways in which the surface oligonucleotide density could be tuned include adjusting the oligonucleotide concentration present in the reaction mixture, displacing excess oligonucleotide strands with mercaptoethanol and using a mPEG-SH backfill.[133,134,139]

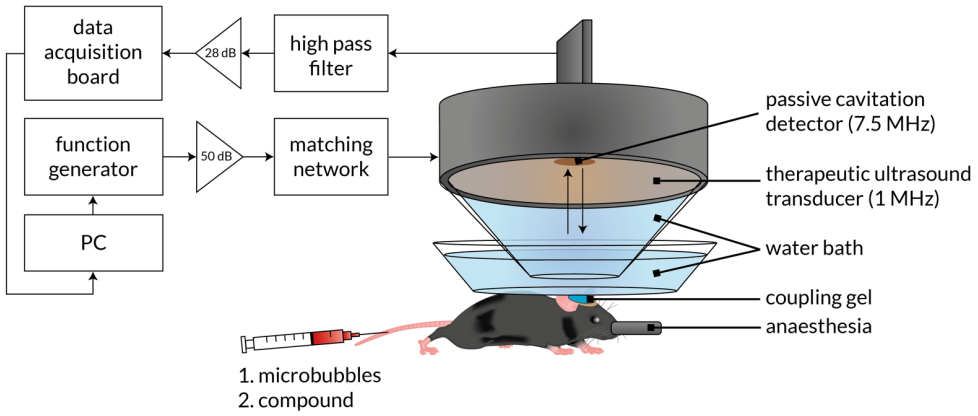
2.3.2 Delivering Nanoparticles across the BBB with Ultrasound

Focused ultrasound and microbubbles have been previously used to deliver a number of nanoparticle systems into the brain *in vivo*, but oligonucleotide-coated nanoparticles have not been delivered before. Thus, we first sought to investigate whether it would be feasible to deliver this type of nanoparticle system across the BBB with ultrasound and whether the DNA-Au NPs would remain intact upon successful delivery.

Ultrasound Setup

All *in vivo* focused ultrasound experiments were performed using the system shown in Figure 2.5, controlled on MATLAB *via* a custom graphical user interface (GUI). Both the system and GUI were developed by Dr. A. Pouliopoulos (PhD student, NSB Lab). Briefly, the desired ultrasound pulse sequence and shape were defined using a function generator, passed through an amplifier and then emitted from a 1 MHz focused ultrasound transducer. The 1 MHz focused ultrasound transducer was mounted onto a programmable 3D positioning system to allow the transducer to be moved to the target location. A 7.5 MHz passive cavitation detector was used during ultrasound treatment to detect the presence of the microbubbles in the sonicated region. To avoid significant attenuation or distortion of the emitted ultrasound, water baths and coupling gel were used in between the skull of the mouse and the transducer.

The general experimental workflow that was followed for all *in vivo* experiments is shown in Figure 2.6. Before every experiment, the fur from the head of the mouse was removed using an electric razor and depilatory cream to allow the skull sutures to be visualised. The mouse was then anaesthetised and its head was fixed using a stereotaxic frame. Next, the transducer was moved to target the desired location; in all experiments, this was either the left hippocampus or left thalamus regions, leaving the right side of the brain as the control. Once the transducer was in place, SonoVue microbubbles, followed by the compound of choice, were injected intravenously into the bloodstream *via* the tail vein. The brain was then sonicated over a period of approximately four minutes. Following sonication, the mouse was transcardially perfused with saline to flush out the blood and fixed by perfusing with 4% paraformaldehyde. The brain was extracted and cryosectioned into horizontal sections for fluorescence imaging (30 µm thickness). Cryosectioning involves embedding the tissue in OCT (optimal cutting temperature; a mixture of polyvinyl alcohol and polyethylene glycol that has the same density as frozen tissue when frozen), snap-freezing the sample in an isopentane/dry ice cold bath and then slicing using a cryostat at temperatures of -10 to -15 °C. Prior to cryosectioning, all samples were cryoprotected by immersing them in graded sucrose



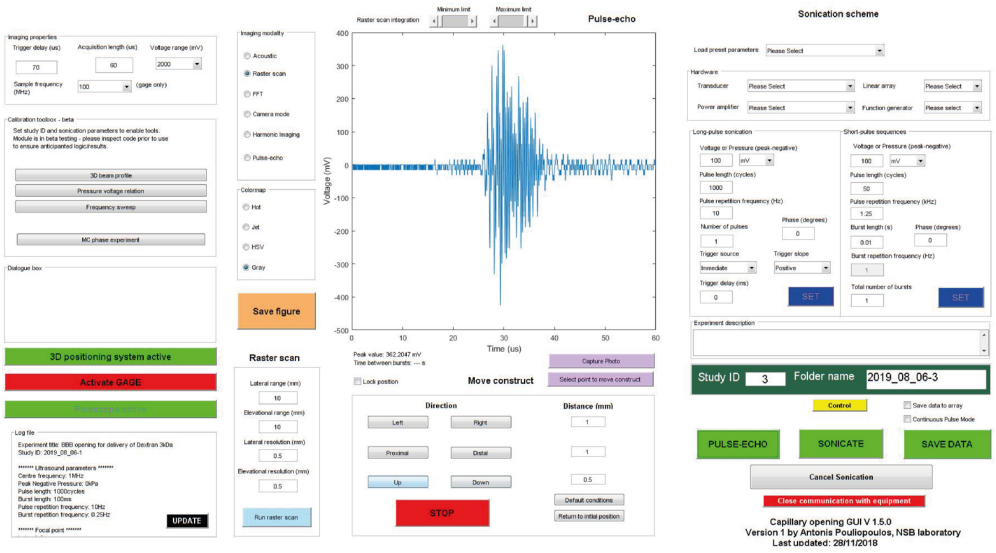


Figure 2.5: Experimental setup for *in vivo* experiments and a screenshot of the GUI used to control the system. The setup and GUI were developed by Dr. A. Pouliopoulos (PhD student, NSB Lab).

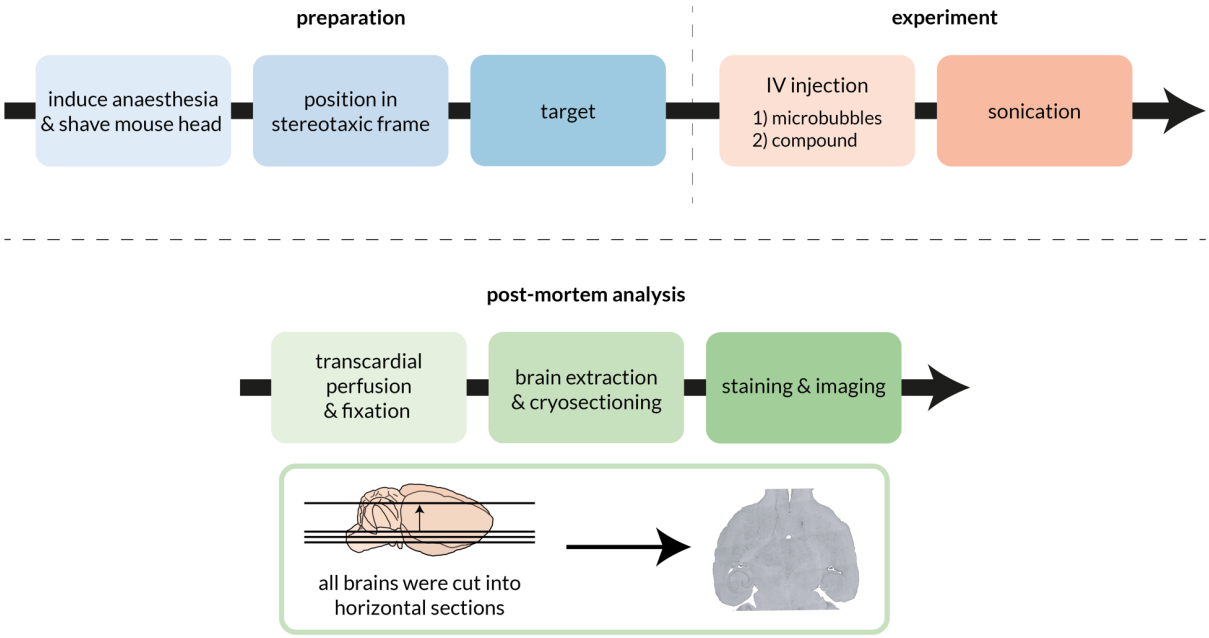


Figure 2.6: Experimental workflow for *in vivo* experiments.

solutions (15% to 30%) over the course of 24 hrs. Sucrose acts as a dehydrant and helps to preserve cellular morphology by preventing ice crystal formation in the tissue during freezing.

Targeting Methods

To target the desired location in the brain, we began by following the grid positioning protocol reported by Choi *et al.*[141] In this method, the fur from the head of the mouse is removed and a metal cross is placed on top of the lambdoid and sagittal sutures of the mouse skull (Figure 2.7). These sutures are visible through the intact skin of the head. A raster scan of 10 mm x 10 mm is then performed using the transducer in pulse-echo mode and connected to a pulser-receiver. Integration of the echos received over time for each point allows the position of the transducer relative to the metal cross to be determined. This information can then be used to target specific regions of the brain.

Initially, we tried to target the hippocampal region of the brain because this has been implicated in a number of diseases, as well as being easily identifiable anatomically. A 3 kDa Texas Red-labelled dextran molecule, which is known to not cross the BBB by itself due to its size, was intravenously injected to allow identification of the site of BBB opening.[86,92] Initial attempts to target with this protocol were unsuccessful due to two main issues: 1) the C57BL/6J mice used often had black skin, making the lambdoid and sagittal sutures impossible to see and 2) the metal cross was not always clearly visible on the raster scans. As a consequence, the targeting procedure was optimised with S. Morse (PhD student, NSB Lab) over the

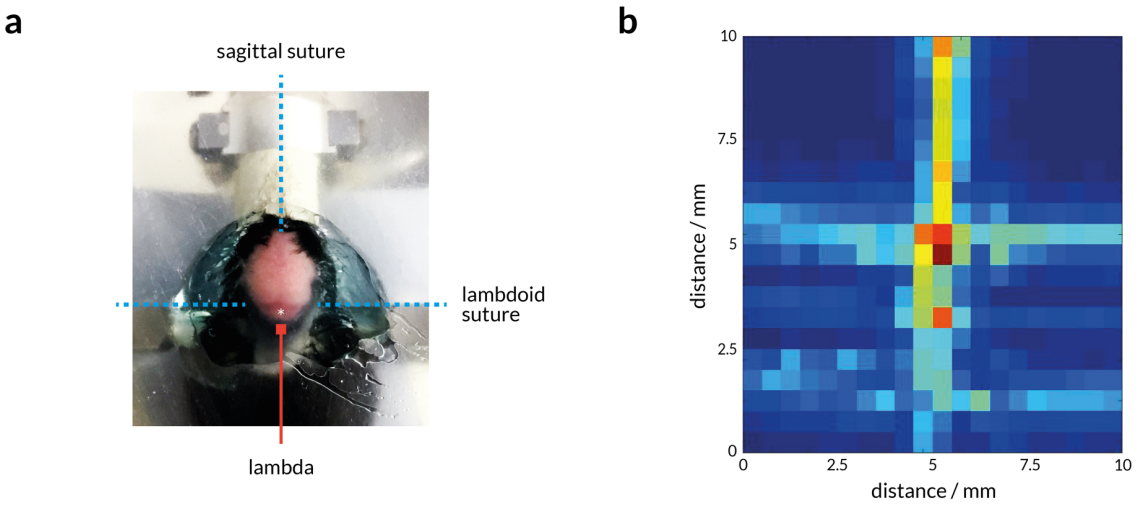


Figure 2.7: **a)** Aerial view of the ultrasound setup. To target specific regions of the brain, a metal cross is placed on top of the lambdoid and sagittal sutures of the mouse skull, which are visible through the intact skin of the mouse head. **b)** Example raster scan.

course of several months. The former issue was found to be due to the hair growth cycle of C57BL/6J mice and was ultimately solved by ordering older mice (10 week old mice versus 8 week old mice).[142] To address the latter problem, a series of *in vivo* experiments were conducted using metal crosses made from different materials. To obtain the best reflection of the emitted ultrasound off the metal cross during the raster scan and, in turn, generate a clearer image, the difference in acoustic impedance between the metal cross and water (Z = 1.5 x 10^6 kg$(m^2s)^{-1}$) should be as high as possible. A summary of the different crosses that were tried can be found in Table 2.2, with the stainless steel cross proving to be most effective. The code was also edited by S. Morse (PhD student, NSB Lab) to further improve targeting accuracy; the details of this can be found in her thesis.[143] Figure 2.8 shows an example of successful hippocampal targeting, made possible after optimisation. Ultrasound-mediated BBB opening can be clearly observed in the left hippocampal region, with no BBB opening observed in the non-sonicated right hippocampal region.

Delivering Nanoparticles across the BBB using Ultrasound

Initially, Cy5-DNA-Au NPs **A, B** or **C** were delivered across the BBB using the ultrasound setup and workflow depicted above (Figure 2.5, Figure 2.6). Briefly, in these experiments, the left thalamus region of the brain was targeted, leaving the right thalamus as the non-sonicated control (Figure 2.9). The mouse was then sonicated using conventional therapeutic ultrasound pulses (frequency: 1 MHz, peak-negative pres-

Metal Cross	Z / kg(m^{2}s)$^{-1}$	Comments
Two 1 mm thick rods made from paper clips	~40 x 10^6	Rods are not flat
3D printed plastic cross covered with aluminium foil	17.3 x 10^6	Poor reflector
3D printed plastic cross covered with a thin layer of tungsten	98 x 10^6	Tungsten layer too thin
Stainless steel cross cut from metal sheet	45.5 x 10^6	Flat; good results

Table 2.2: Different metal crosses that were used to try and improve the targeting accuracy. The stainless steel cross gave the best results and was used in all subsequent *in vivo* experiments. Acoustic impedances, Z, are taken from references [144, 145].

sure: 530 kPa, pulse length: 10 ms, pulse repetition frequency (PRF): 0.5 Hz, sonication duration: 250 s). Experiments conducted with Dr. A. Pouliopoulos, S. Morse and J. Lin (PhD and MRes students, NSB Lab) determined the pressure threshold for successful BBB opening with this pulse sequence to be between 180 $kPa_{pk\text{-}neg}$ and 350 $kPa_{pk\text{-}neg}$ (Appendix: Figure 9.6); reproducible BBB opening was therefore expected using higher peak-negative pressures of 530 kPa. After five ultrasound pulses, SonoVue microbubbles followed by Cy5-DNA-Au NPs **A, B** or **C** were injected intravenously *via* the tail vein. Following sonication, mice were transcardially perfused and fixed. Harvested brains were cryosectioned and imaged using bright-field and fluorescence microscopy in order to detect the presence of the nanoparticles in the brain.

Evidence of successful BBB opening and delivery of Cy5-DNA-Au NPs to the brain was observed in all experiments performed. Due to the characteristic dark red colour of Au NPs, the presence of the Au NP cores was clearly detected in the left thalamus in bright-field images of brain sections (Figure 2.10). Signal from the attached Cy5-labelled oligonucleotides was detected using fluorescence microscopy. These signals were found to be co-localised with the bright-field signals, indicating that the Cy5-DNA-Au NPs remained intact as they crossed the BBB. Negligible nanoparticle signal was observed in the non-sonicated right thalamus in all experiments; thus, whilst Jensen *et al.* reported that their 30 nm DNA-Au NPs were able to cross the BBB by themselves, it is evident that the use of focused ultrasound and microbubbles can significantly increase the accumulation of DNA-Au NPs in the brain.[108]

Delivery of the Cy5-DNA-Au NPs was also attempted at lower pressures of 350 $kPa_{pk\text{-}neg}$, but low fluorescence signal was detected in the targeted region, indicating limited delivery (Appendix: Figure 9.7). As will be discussed in the next section, ultrasound-mediated BBB opening has been associated with a size-threshold in the past, with reports showing more efficient delivery of smaller molecules compared to larger molecules using the same ultrasound parameters.[92,100] Thus, whilst we have shown that we are able to

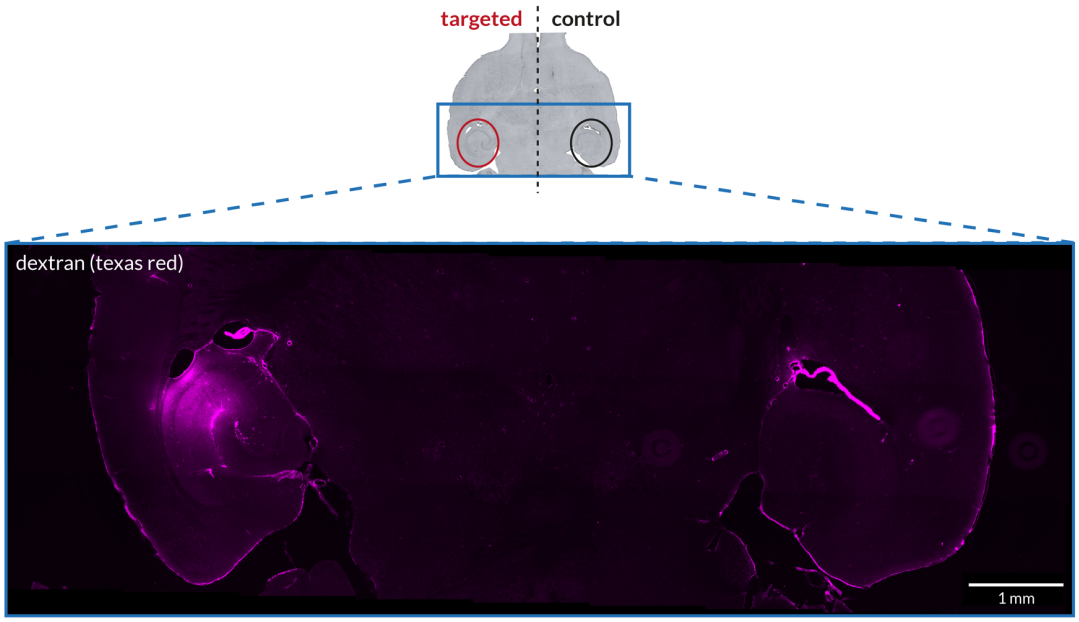
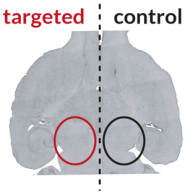


Figure 2.8: Fluorescence microscopy image of successful targeting of the left hippocampus. Ultrasound-mediated BBB opening can be clearly seen in the left hippocampus (purple; injected tracer: 3 kDa Texas Red-labelled dextran), with no evidence of BBB opening observed in the non-sonicated right hippocampus.



ultrasound parameters	
peak negative pressure	530 kPa
frequency	1 MHz
pulse length	10 ms
pulse repetition frequency	0.5 Hz
sonication duration	250 s

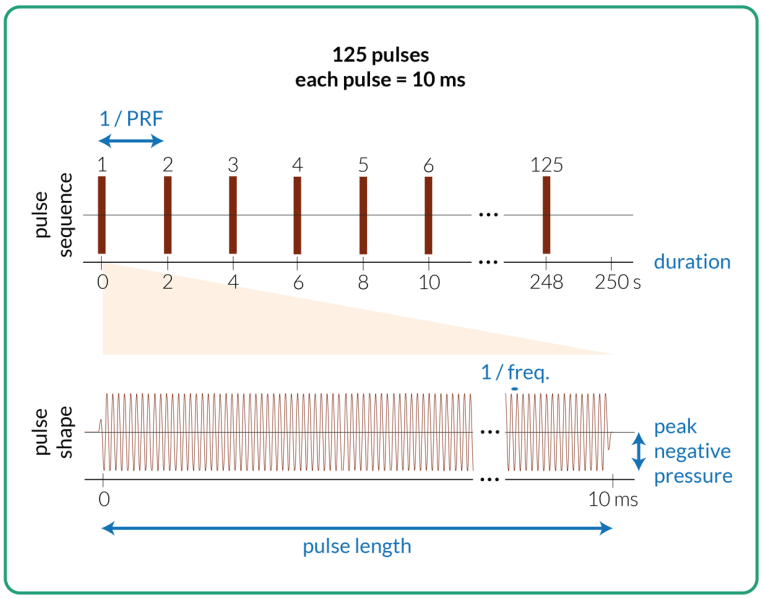


Figure 2.9: Ultrasound parameters used for BBB opening. The left thalamus region was targeted in all Cy5-DNA-Au NP experiments, leaving the right thalamus as the non-sonicated control.

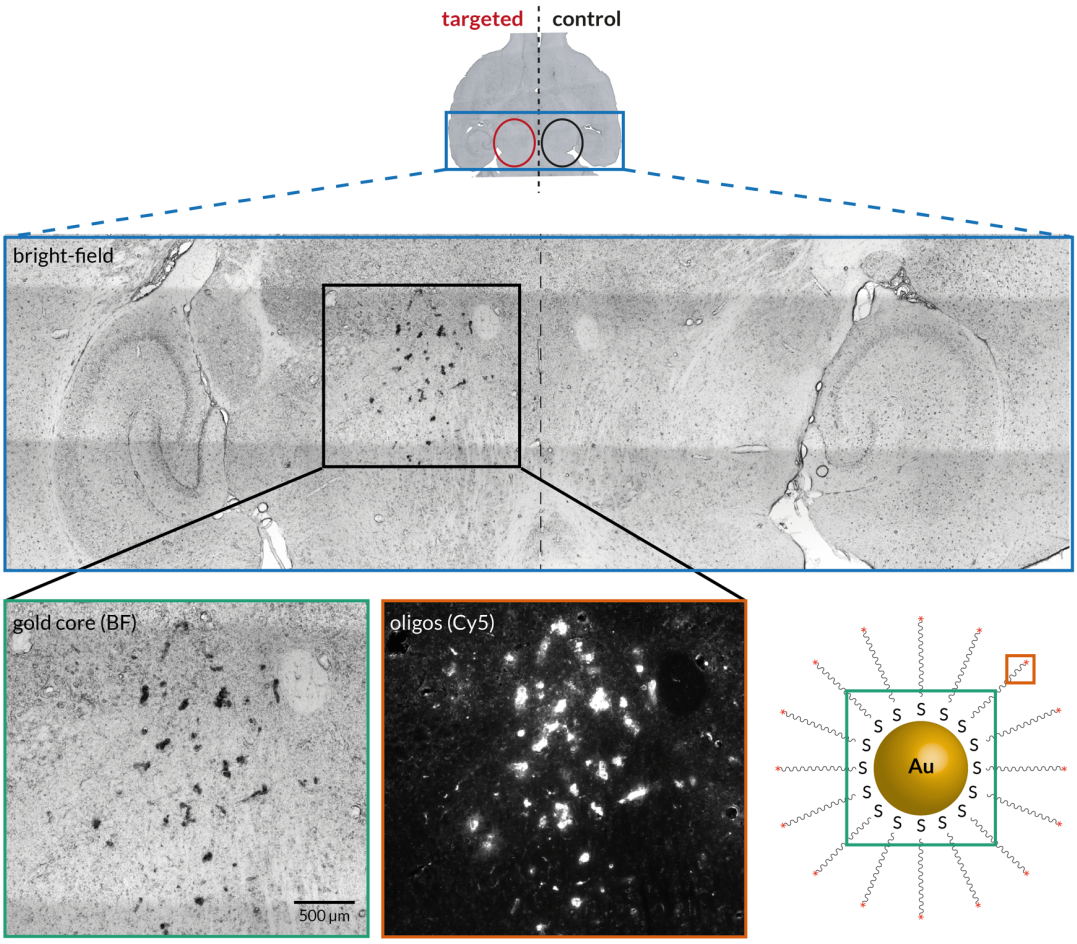


Figure 2.10: Bright-field and fluorescence microscopy images showing the successful delivery of Cy5-DNA-Au NPs to the left thalamus of the brain. Signal corresponding to the Au NP cores can be observed in bright-field images (green box) and is found at the same location as signal from the attached Cy5-labelled DNA strands (orange box).

deliver small molecule probes (*e.g.* 3 kDa dextran, hydrodynamic diameter = ~2 nm; Appendix: Figure 9.6) across the BBB using pressures of 350 $kPa_{pk\text{-}neg}$, efficient delivery of the synthesised Cy5-DNA-Au NPs requires the use of higher acoustic pressures.[86,100] As shown in Appendix: Figure 9.6, the use of higher acoustic pressures induces greater ultrasound-mediated BBB opening; however, this, in turn, leads to an increased probability for tissue damage.[92,93]

2.3.3 Size-Dependency of Ultrasound-Mediated Delivery

To investigate the size-dependency of focused ultrasound-mediated BBB delivery in more detail, Cy5-DNA-Au NPs **A** (d_h = 21.6 ± 3.3 nm), **B** (d_h = 23.3 ± 2.6 nm) and **C** (d_h = 25.2 ± 1.9 nm) were delivered across the BBB using focused ultrasound. The normalised optical density (NOD), the average fluorescence intensity of the targeted region normalised by the control, was then calculated from fluorescence images. A total of n = 5 C57BL/6J mice were used for each set of nanoparticles delivered and all NOD quantification was performed using an in-house MATLAB script written by S. Morse (PhD student, NSB Lab). Briefly, the regions of interest, the left and right thalamus, were selected on MATLAB and any artefacts (*e.g.* folds in tissue) were removed. The images were then thresholded to remove any signal due to tissue autofluoresence. Pixel intensities above the threshold were summed in both sides and the NOD was obtained by subtracting the value obtained for the left thalamus region (targeted) by that of the right thalamus region (non-sonicated control). Five brain sections were analysed per brain and all analysis was conducted at least three times to minimise errors.

As shown in Figure 2.11, the smallest Cy5-DNA-Au NPs (**A**) investigated in this study were delivered six times more efficiently than the largest Cy5-DNA-Au NPs (**C**). This has important implications for ultrasound-mediated nanoparticle delivery as whilst larger nanoparticles offer a greater surface area upon which therapeutic and/or imaging agents can be attached, they are delivered less efficiently across the BBB using focused ultrasound. The observation of a size-dependency also supports the hypothesis that focused ultrasound-mediated BBB opening proceeds predominantly through the widening of the tight junctions that exist between the endothelial cells that make up the blood vessel walls.[92]

2.3.4 Safety of Focused Ultrasound-Mediated BBB Opening

To date, the safety of focused ultrasound-mediated BBB opening has been widely investigated using a range of ultrasound parameters. In general, the use of higher acoustic pressures has been correlated

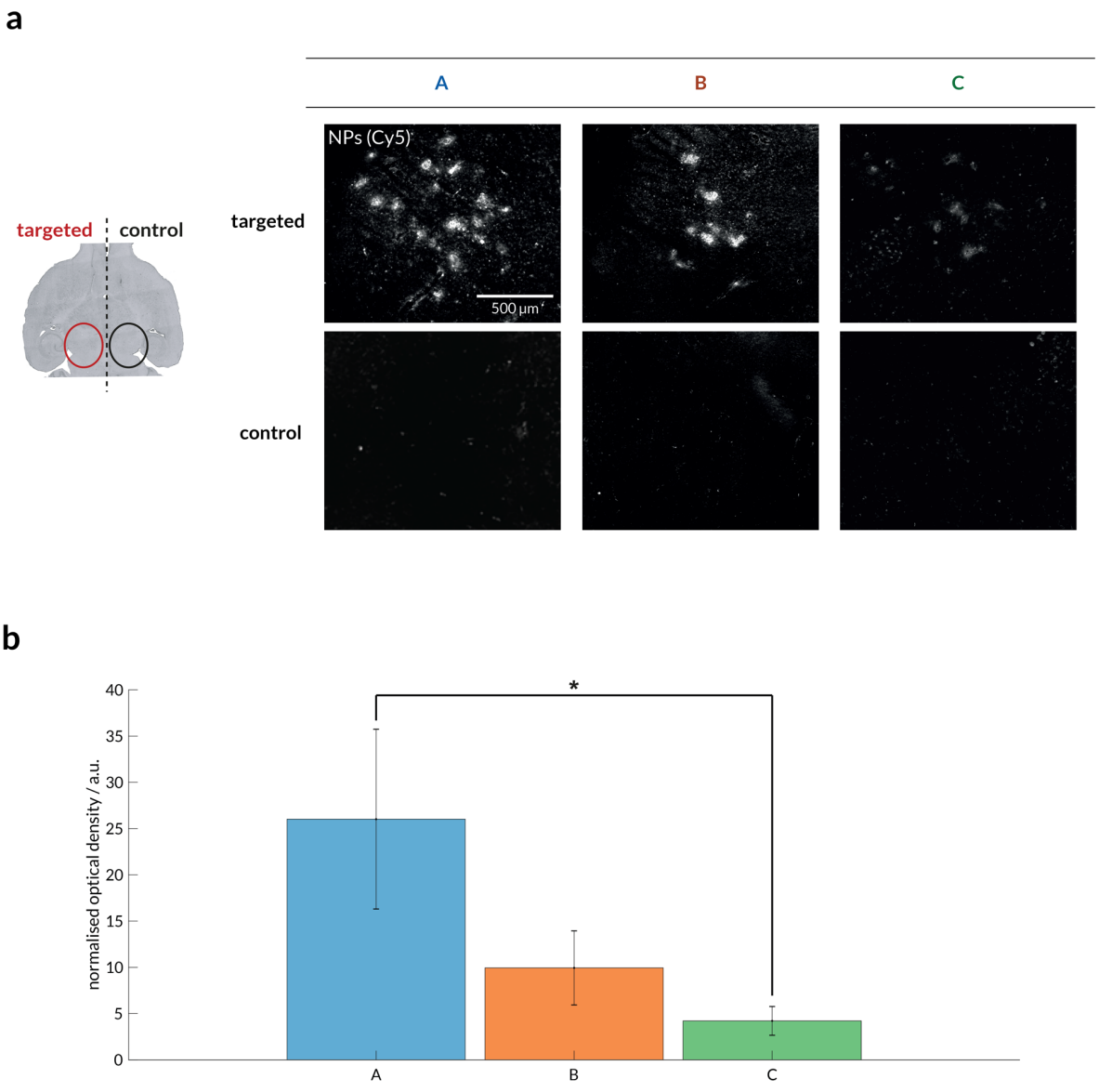


Figure 2.11: **a)** Representative fluorescence microscopy images showing the successful delivery of Cy5-DNA-Au NPs **A**, **B** and **C** to the left thalamus. No evidence of nanoparticle delivery was observed in the right thalamus in all experiments. **b)** Normalised optical density, calculated over five sections per brain. Using the same ultrasound parameters, Cy5-DNA-Au NPs **A** were delivered across the BBB six times more efficiently than Cy5-DNA-Au NPs **C** ($p < 0.05$, $n = 5$ for each set of nanoparticles).

with greater tissue damage; for example, Baseri *et al.* sonicated the left hippocampus of mice at acoustic pressures of 300 to 980 $kPa_{pk\text{-}neg}$ and observed large-scale haemorrhage and extensive tissue damage at acoustic pressures of 980 $kPa_{pk\text{-}neg}$.[93] Conversely, no histological damage was found in the targeted region of brains sonicated at 300 $kPa_{pk\text{-}neg}$.[93]

The most commonly used method to assess tissue damage caused by ultrasound-mediated BBB opening is haematoxylin and eosin (H&E) staining. This stain depends on the contrast between two dyes, haematoxylin and eosin, and allows the identification of any changes in cell morphology, sites of red blood cell extravasation, neuronal death and microvacoulation, all of which have been associated with focused ultrasound-mediated BBB opening in the past.[93,146] Haematoxylin is purple-blue and stains nucleic acids, whilst eosin is pink and stains proteins non-specifically (Appendix: Figure 9.8).[146] Red blood cells are stained bright red in H&E-stained sections.

To assess the safety of the ultrasound parameters used to deliver the synthesised Cy5-DNA-Au NPs across the BBB in this study, C57BL/6J mice (n = 3) were sonicated using the same ultrasound parameter set as above. A Texas Red-labelled 3 kDa dextran was injected to easily identify the site of BBB opening. Brains were paraffin-embedded and sectioned at 5 µm by the UCL IQPath laboratory; paraffin sections were used here, rather than frozen sections, as paraffin-embedding leads to better preservation of morphological detail. Frozen sections have been used elsewhere in this thesis because the process of paraffin-embedding quenches fluorescence signal and does not preserve antigen expression as well, making fluorescence imaging and immunohistochemistry procedures more difficult.[147]

To determine the site of BBB opening, paraffin sections were imaged in the Texas Red channel. Eight sections covering the focal volume were stained with H&E following standard procedures. As shown in Figure 2.12, only minimal tissue effects were observed using the ultrasound parameters applied in this study, with just a few sites of red blood cell extravasation located in the targeted region. For diseases such as glioblastoma in which the life expectancy is short, the benefits of being able to successfully deliver the therapeutic agent to the targeted region may outweigh any minor tissue damage caused. It is, however, believed that these tissue effects could be completely eliminated with further optimisation of the ultrasound parameters. As will be discussed later in this thesis, our laboratory has designed an alternative pulse sequence that results in more efficient and safer drug delivery across the BBB compared to the conventional therapeutic ultrasound sequences used in this study.[86]

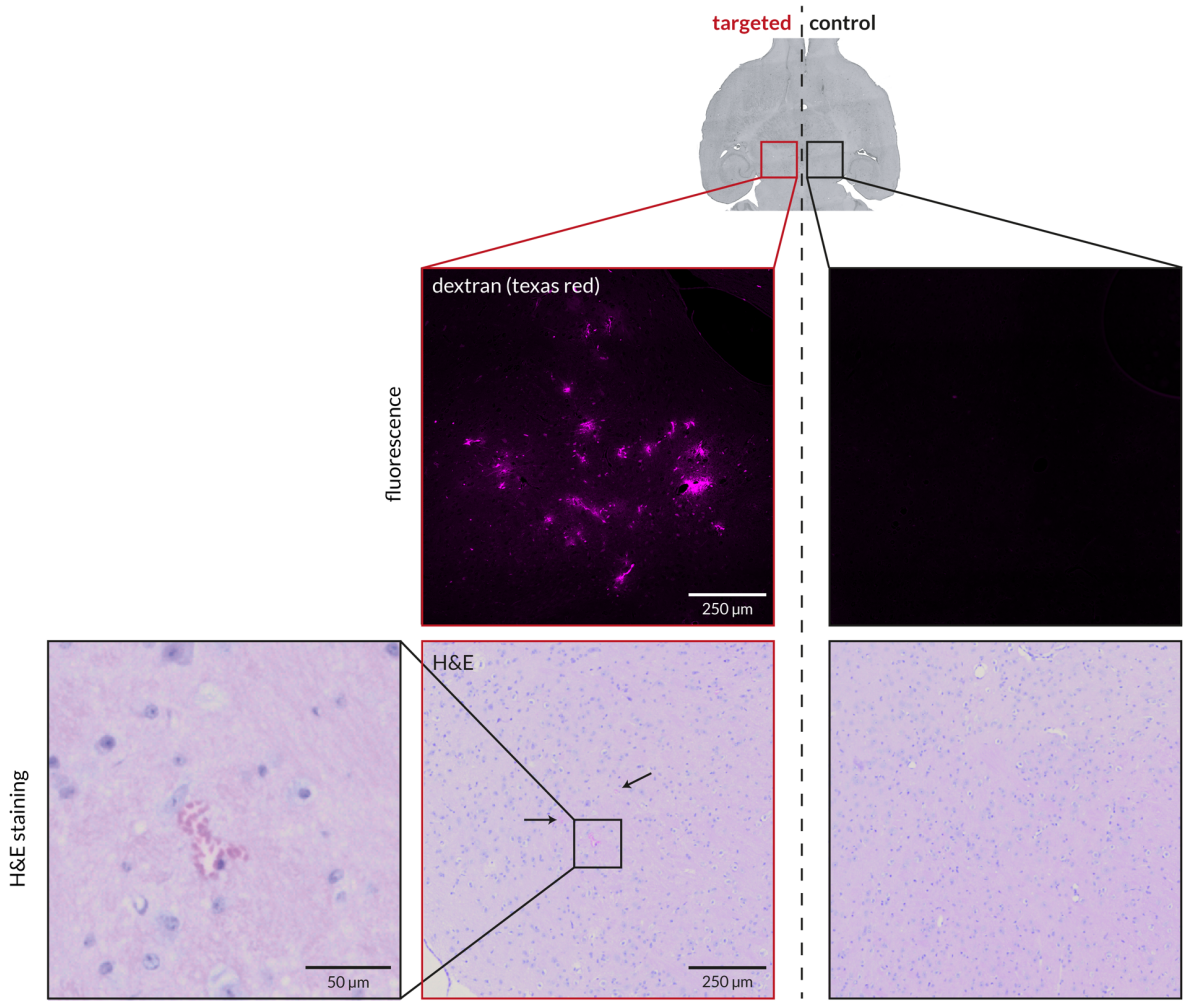


Figure 2.12: Representative fluorescence microscopy images showing the successful delivery of a 3 kDa Texas Red-labelled dextran to the left thalamus (top). H&E staining shows a few sites of red blood cell extravasation in the targeted region (bottom; left), which are not present in the control (bottom; right). No other tissue effects were observed.

2.4 CONCLUSIONS AND FUTURE DIRECTIONS

In this chapter, a series of fluorescent DNA-coated gold nanoparticles of different sizes were synthesised and characterised. These nanoparticles were successfully delivered across the BBB *in vivo* using focused ultrasound and microbubbles; this marks the first time that oligonucleotide-coated nanoparticles have been delivered across the BBB with ultrasound. An investigation into the effect of nanoparticle diameter on the efficiency of ultrasound-mediated delivery was also conducted, with the smallest nanoparticles syn-

thesised (hydrodynamic diameter: ~21 nm) being delivered more efficiently than the largest nanoparticles synthesised (hydrodynamic diameter: ~25 nm). H&E staining showed minor tissue effects as a result of the conventional therapeutic ultrasound sequences used. The observation of a size-dependency supports prior hypotheses that the increased permeability seen as a result of focused ultrasound-mediated BBB opening is predominantly due to a widening of tight junctions between adjacent endothelial cells.[92]

Showing that sub-30 nm nanoparticles can be successfully delivered across the BBB using focused ultrasound opens up many avenues for drug development. Different combinations of therapeutics and/or imaging agents could be loaded onto the nanoparticle surface and used for the treatment and diagnosis of brain diseases such as glioblastoma. In collaboration with Dr. A. Torres-Huerta (Postdoc, Vilar Group), a number of bisphosphonate drug-loaded DNA-Au NPs have since been prepared. Bisphosphonate drugs, such as etidronate, aledronate and zoledronate, are clinically used to treat osteoporosis due to their ability to inhibit bone resorption. However, recent evidence suggests that this class of drug may also possess anti-cancer properties; for example, in the three year ABCSG-12 clinical trial, the addition of zoledronate to breast cancer hormone therapy treatment was seen to lead to a 36% reduction in disease progression in breast cancer patients.[148–150] Moreover, aledronate treatment was shown to promote apoptosis in a human primary glioblastoma cell line (U-87 MG) *in vitro*, suggesting that it may be therapeutically useful for the treatment of brain cancers.[151] However, bisphosphonate drugs typically suffer from poor cellular uptake in non-osteoclast cells and thus, require the use of high concentrations (μM) in order to induce anti-cancer effects.[152,153]

Due to the efficient cellular uptake that has been reported with oligonucleotide-coated nanoparticle systems, we hypothesised that nanoparticles co-loaded with bisphosphonate drugs and oligonucleotides could induce greater anti-cancer effects than those observed with the bisphosphonate drugs on their own.[111,113] Prior work conducted in the group has led to the successful development of a novel bimetallic zinc receptor that selectively binds bisphosphonate drugs. A version of this receptor containing a dithiocarbamate group for facile attachment to the surface of Au NPs was synthesised by Dr. A. Torres-Huerta (Postdoc, Vilar Group). This receptor was loaded with either etidronate (**D**) or aledronate (**E**) and was used to synthesise etidronate- or aledronate-loaded DNA-Au NPs following similar protocols as those discussed above (Figure 2.13). Successful co-functionalisation of the Au NPs with the drug-loaded receptors and oligonucleotide strands was confirmed using ICP-MS and fluorescence spectroscopy. Ongoing work is focused on assessing the efficacy of these platforms in cells and *in vivo*.

For future *in vivo* applications, a move towards the use of fully biocompatible DNA-coated nanoparticles would be ideal in order to circumvent any concerns that there might be regarding the accumulation of metallic nanoparticles in the body. One way this could be achieved is by using so-called 'hollow'

oligonucleotide-coated NPs, which are based on biocompatible silica shells: the gold nanoparticles are first coated with a shell of silica, coated with oligonucleotides and then the gold is dissolved away using I_2.[154]

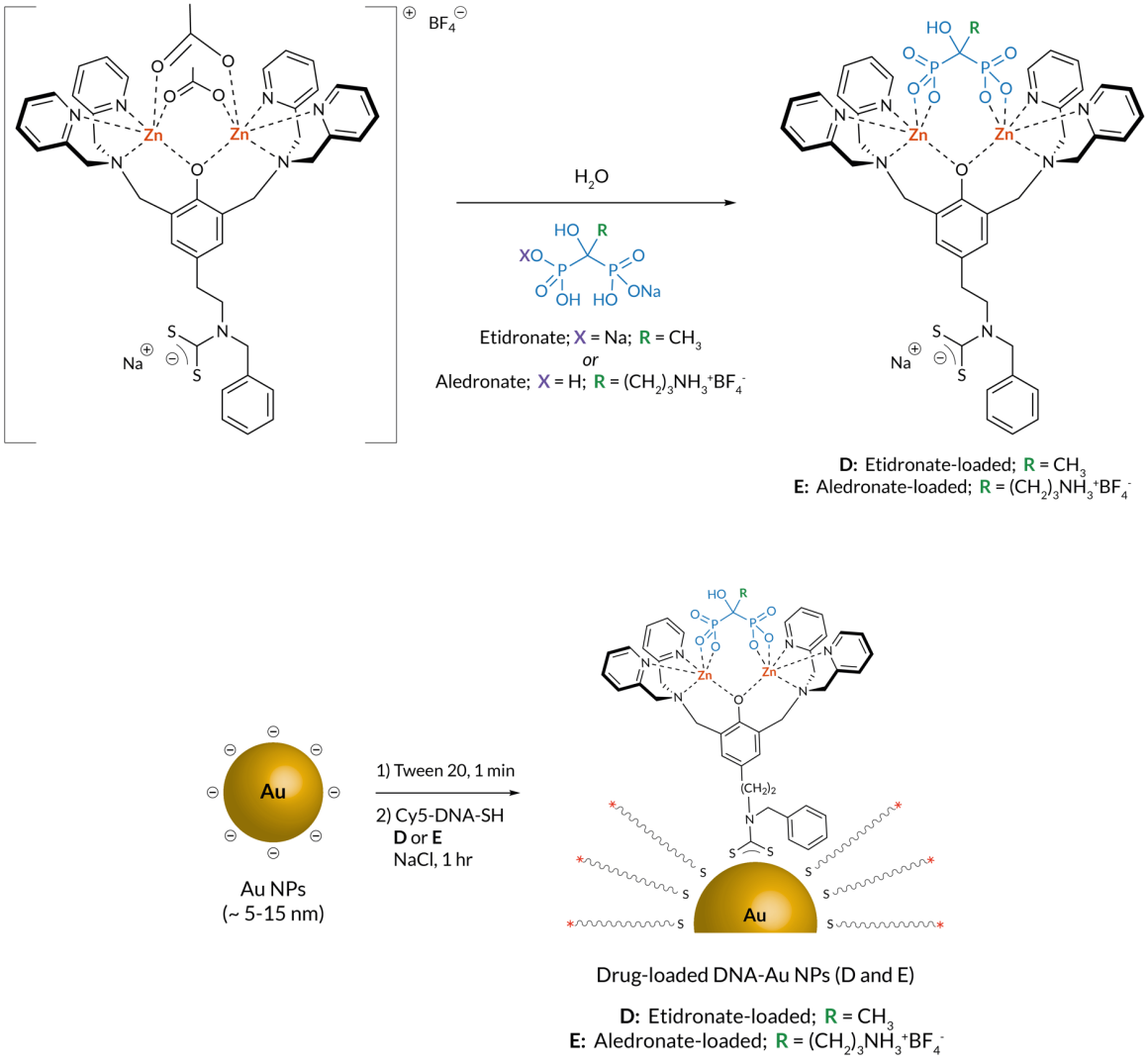


Figure 2.13: **Top:** A novel bimetallic zinc receptor was loaded with two bisphosphonate-based drugs, etidronate and aledronate. The synthesis depicted was carried out by Dr. A. Torres-Huerta (Postdoc, Vilar Group). **Bottom:** Etidronate- and aledronate-loaded DNA-Au NPs **D** and **E** were synthesised following similar methods to those reported above.

3 METAL COMPLEXES FOR THE TREATMENT OF ALZHEIMER'S DISEASE

3.1 BACKGROUND

Alzheimer's disease is the most common form of dementia, accounting for over 50% of all dementia cases. It currently affects approximately 30 million people worldwide, with this number expected to reach over 100 million by the year 2050.[155] The prevalence of the disease increases significantly with age and it is estimated that 25% to 45% of individuals older than 85 years old suffer from dementia.[156] Alzheimer's disease is divided into two subtypes depending on the age of onset: early onset (< 60 years old) and late onset (> 60 years old). Over 90% of Alzheimer's disease cases are classed as being late onset and sporadic, in which genetic mutations are not believed to be the underlying cause.[157]

The first clinical symptom of Alzheimer's disease is usually short-term memory loss. As the disease progresses, cognitive impairment of other areas begins to develop, resulting in difficulties in communication and judgement, mood-swings and disorientation. Late-stage Alzheimer's disease can also lead to neurological symptoms such as seizures, hallucinations, hypertonia, incontinence and mutism.[158,159] To date, three cholinesterase inhibitors (donepezil, rivastigmine and galantamine) have been approved for use in mild to moderate Alzheimer's disease, whilst memantine has been approved for use in moderate to severe Alzheimer's disease.[160–162] Cholinesterase inhibitors enhance cholinergic neurotransmission by blocking the hydrolysis of acetylcholine at the synapses, a neurotransmitter which plays a key role in the encoding, consolidation and retrieval of memory.[163–166] In contrast, memantine is an antagonist of the *N*-methyl-*D*-aspartate (NMDA) receptor and prevents neuronal damage caused by glutamatergic overstimulation.[167,168] Both of these treatments can provide mild to modest symptomatic relief, but they are unable to halt disease progression or modify the disease pathway.[161,169] There have been no new approved drugs for Alzheimer's disease since 2003 and as a consequence, patients with Alzheimer's disease typically survive for eight to ten years after diagnosis.[170]

3.1.1 The Amyloid Beta Hypothesis

Alzheimer's disease is histopathologically characterised by the presence of amyloid beta (Aβ)-containing plaques and neurofibrillary tangles (NFTs) (Figure 3.1).[171] Aβ plaques are aggregates of the Aβ peptide

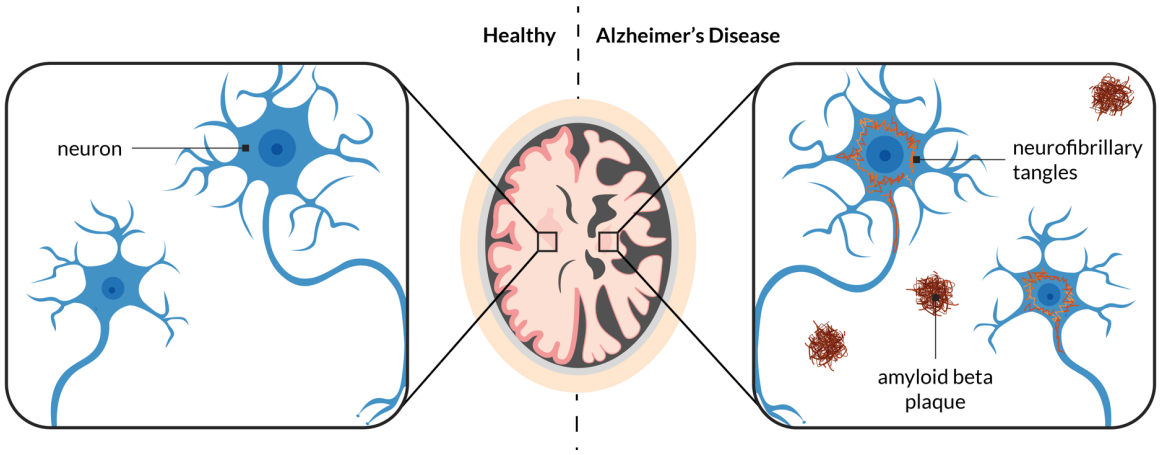


Figure 3.1: Alzheimer's disease is characterised by the presence of amyloid beta plaques in the extracellular space and neurofibrillary tangles inside neurons. The abnormal build-up of these protein deposits over time ultimately results in brain atrophy.

and are found in the extracellular space of the brain, whilst NFTs are aggregates of hyperphosphorylated tau protein and are found inside neurons. The presence of these protein deposits inside the brain leads to impaired cell signalling, neuronal death and, ultimately, brain atrophy.[172,173]

As of now, the exact cause of Alzheimer's disease has not been elucidated. The most prevalent theory is known as the Aβ hypothesis, which states that the accumulation of Aβ peptide inside the brain is the initiating factor for the development of Alzheimer's disease pathogenesis.[174–176] Aβ is produced by the endoproteolysis of the amyloid precursor protein (APP), an integral membrane protein which is concentrated in the synapses of neurons (Figure 3.2).[177,178] In the non-amyloidogenic pathway, APP is cleaved by the enzyme α-secretase to give a soluble extracellular fragment known as sAPPα.[179] In contrast, in the amyloidogenic pathway, APP is sequentially cleaved by β-secretase and γ-secretase to generate Aβ peptides, which are released into the extracellular space.[179,180]

Aβ peptides are usually 40 (Aβ1-40) or 42 (Aβ1-42) amino acids in length. The Aβ1-42 peptide is found at 10-fold lower levels than the Aβ1-40 peptide, but it is more prone towards aggregation.[181] Monomeric Aβ1-40 and Aβ1-42 peptides are known to aggregate to form soluble non-fibrillar oligomers and insoluble fibrillar plaques (Figure 3.2). It was originally believed that the insoluble Aβ plaques were responsible for inducing neurotoxicity, but increasing evidence is suggesting that it is, in fact, the soluble oligomers that are the neurotoxic species. This is supported by the fact that there is a much stronger correlation between the cerebral load of soluble Aβ oligomers and cognitive status than there is with fibrillar Aβ.[182,183] Furthermore, it has been shown that the administration of soluble forms of Aβ to healthy rodents can impair their cognitive function and induce synaptic dysfunction.[184,185] Despite the ongoing controversy about

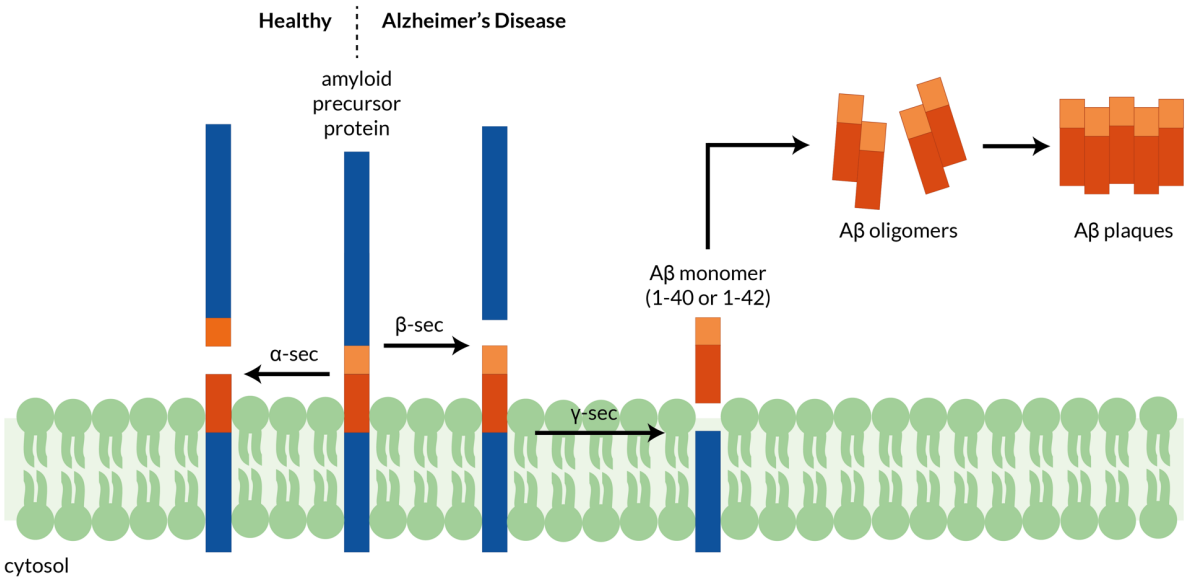


Figure 3.2: In a healthy brain, the amyloid precursor protein is cleaved once by α-secretase, In contrast, in Alzheimer's disease, it is cleaved twice: first by β-secretase and then by γ-secretase. This results in the release of the so-called amyloid beta peptide, which, over time, aggregates to form oligomers and plaques. The amyloid beta hypothesis states that it is the presence of these aggregates that triggers Alzheimer's disease pathology.

whether it is the oligomers or the fibrils that are the toxic species in Alzheimer's disease, there is no known toxicity associated with monomeric Aβ; in fact, there is evidence that monomeric Aβ1-42 could provide neuroprotective effects through activation of the phosphatidylinositol-3-kinase pathway.[186]

In the Aβ hypothesis, the gradual accumulation of aggregated Aβ is thought to initiate a neurodegenerative cascade, involving the triggering of inflammatory responses, oxidative stress, disruption of neuronal homeostasis and NFT formation.[175,176,181] Evidence supporting the Aβ hypothesis includes the fact that familial Alzheimer's disease, a type of aggressive and early onset Alzheimer's disease, is caused by mutations in the genes coding for APP and the γ-secretase complex proteins presenilin 1 and 2.[187] An inherited missense mutation in the APP gene that reduces Aβ production and appears to provide protective effects against Alzheimer's disease has also been identified.[188] Moreover, transgenic mouse models containing mutations in the APP gene are able to reproduce some of the key aspects of Alzheimer's disease, such as plaque development, synaptic dysfunction and memory deficits.[189,190] Numerous *in vitro* and *in vivo* studies in rodents have also shown that immunisation with Aβ can prevent Alzheimer's disease pathology.[191,192]

In recent years, the validity of the Aβ hypothesis has been called into question. If the Aβ hypothesis is true, then any patient with significant Aβ burden in their brains should develop Alzheimer's disease. However, cognitively normal individuals with abundant Aβ deposits in their brains have been identified.[193–196] This implies that Aβ deposition by itself is not enough to cause Alzheimer's disease and there must therefore be other factors involved. Furthermore, if Aβ aggregation is the root cause of Alzheimer's disease, it follows that inhibiting the Aβ pathway in human patients should have a positive effect on disease progression. The three main therapeutic strategies that have been attempted to address this are: 1) the reduction of Aβ production *via* the inhibition of β-secretase or γ-secretase, 2) the inhibition of Aβ aggregation and 3) the promotion of Aβ clearance.[197–203] However, as shown in Table 3.1, minimal clinical benefit has been observed with the majority of anti-amyloid agents investigated thus far. Due to this, it has been proposed that Alzheimer's disease cannot be solely triggered by the aggregation of Aβ; instead, it is likely caused by a complex combination of factors, which could include viral and bacterial infections, the aggregation of tau protein, sleep deprivation and metal dyshomeostasis.[204–208]

Mechanism of Action	Name	Clinical Study Phase	Result	Reference
Reduction of Aβ production	rosiglitazone	3	ineffective	197
	semagacestat	3	ineffective	198
Inhibition of Aβ aggregation	tramiprosate	3	ineffective	199
	scyllo-inositol	2	ineffective	200
Promotion of Aβ clearance	bapineuzumab	3	ineffective	201
	solaneuzumab	3	ineffective	202
	nilvadipine	3	ineffective	203

Table 3.1: Examples of disease-modifying drugs targeted towards Aβ and the clinical study phase that was reached.

Regardless of whether the sequence of events outlined in the Aβ hypothesis is correct, there is significant evidence to suggest that the Aβ peptide plays a central role in the progression of Alzheimer's disease, particularly when in its soluble oligomeric form. Consequently, the development of effective strategies to prevent Aβ aggregation remains of great interest. As of 2019, there are 132 agents currently being investigated in clinical trials for Alzheimer's disease, of which over 70% are aimed at disease modification.[170] 40% of these disease-modifying treatments are targeted towards the Aβ pathway and consist of a range of small molecules, monoclonal antibodies and biological therapies.[170]

3.1.2 The Role of Metal Ions in Alzheimer's Disease

Careful regulation of metal ion levels is crucial in order to maintain healthy brain function. In particular, the homeostasis of copper, iron and zinc ions is thought to be particularly important as they have been implicated in essential biological processes such as neuronal proliferation and signalling, apoptosis, inflammation and the generation of oxidative stress.[209–211] Numerous studies have indicated that cerebral metal ion levels are altered in Alzheimer's disease; for example, through studying the levels of copper, iron and zinc in five different brain regions, Deibel *et al.* reported that the hippocampus and amygdala regions of Alzheimer's disease brains, two regions that have been strongly implicated in the disease, show significantly different levels of copper, iron and zinc.[212] In contrast, minimal changes were observed in the cerebellum region, which is only weakly affected in Alzheimer's disease.[212] As well as this, post-mortem analyses on human patients have shown that the core and rim of Aβ plaques contain significantly higher levels of copper, iron and zinc ions than are found in the brains of neurologically normal patients.[213–215] A correlation between the severity of Alzheimer's disease symptoms and the extent of copper accumulation in Aβ plaques has also been found in mouse models of Alzheimer's disease.[216] As a consequence, it has been proposed that metal ions could play an important role in the development of Alzheimer's disease pathology.

Structural investigations have determined that the N-terminal of the Aβ peptide (residues 1 to 16) contains a high affinity metal binding site to which endogenous metal ions can bind (Figure 3.3). As of now, the binding of copper ions to Aβ is the most well-studied metal ion-Aβ interaction. In the proposed binding modes, Cu^{+} is believed to bind to Aβ in a linear two-coordinate fashion through interactions with the histidine residues (His6, His13 and His14), whilst the binding of Cu^{2+} to Aβ is thought to be square planar in geometry, involving two histidine residues and additional interactions from Asp1 or Ala2 (Figure 3.3).[217–221] The exact species involved in Cu^{2+} binding depends on the pH of the surrounding media.[219,221] Contributions from His6, His13 and His14 have also been implicated in the binding of iron and zinc ions to Aβ, but the precise mode of binding remains unclear.[222,223]

Numerous studies have shown that the binding of metal ions to Aβ can promote aggregation, resulting in increased neurotoxic effects.[224–226] The exact fate of the Aβ peptide upon metal ion binding appears to be highly dependent on the metal ion, pH and stoichiometry; for example, Smith *et al.* showed that at sub-equimolar Cu^{2+} concentrations, the formation of Aβ plaques is favoured, whilst at supra-equimolar concentrations, the formation of small spherical oligomers and large amorphous aggregates is favoured.[224] In addition to their effect on Aβ aggregation, copper and iron ions are redox-active and can promote the production of reactive oxygen species (ROS) and generate oxidative stress. The presence of excess ROS

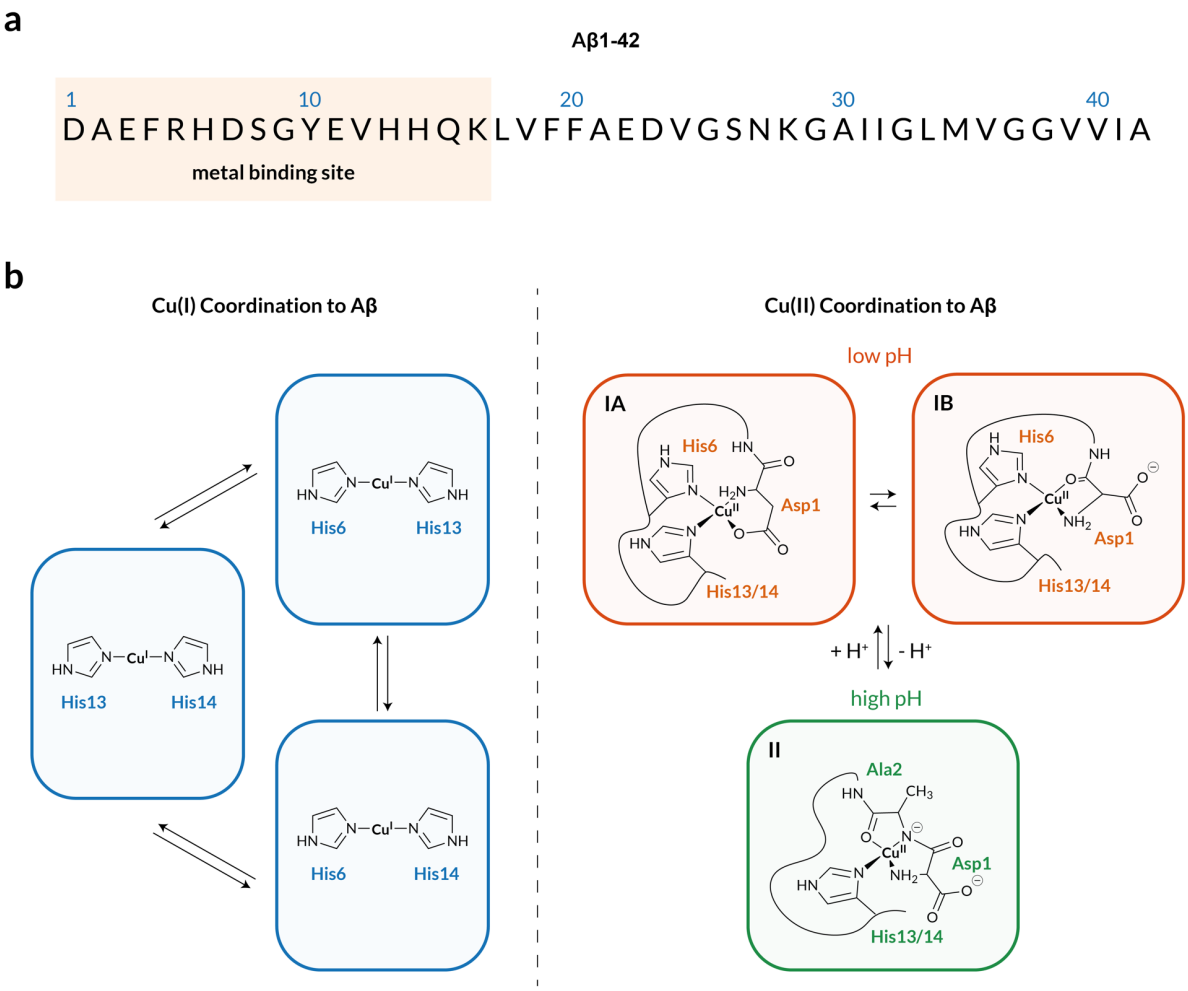


Figure 3.3: **a)** Sequence of Aβ1-42. The N-terminal metal binding site has been highlighted in orange. **b)** Proposed binding modes of Cu^{+} and Cu^{2+} ions to the Aβ peptide, redrawn from *[219]*.

can cause oxidative damage to nucleic acids, proteins and lipids, leading to mutagenesis, carcinogenesis, impaired metabolic activity and altered membrane integrity.[227,228]

ROS generation by copper and iron ions is thought to occur *via* the Fenton and Haber-Weiss reactions depicted in Figure 3.4.[229,230] In theory, these reactions can proceed from both the free metal ions and coordinated metal ion-Aβ complexes; however, despite the former process being more efficient, the latter is more relevant as free metal ion levels in the brain are typically kept very low by a series of metal transporters and chaperones that act to prevent the accumulation of free metal ions.[231] The majority of studies so far have predominantly focused on the contribution of Cu-Aβ to Alzheimer's disease as it has greater redox activity than Fe-Aβ.[232] *In vitro* studies have proposed that Cu-Aβ is able to catalyse

the production of ROS in the presence of a naturally occurring reducing agent, such as glutathione or ascorbate (Figure 3.4).[233,234] A similar process is expected to occur with Fe-Aβ (Fe^{3+}/ Fe^{2+}).

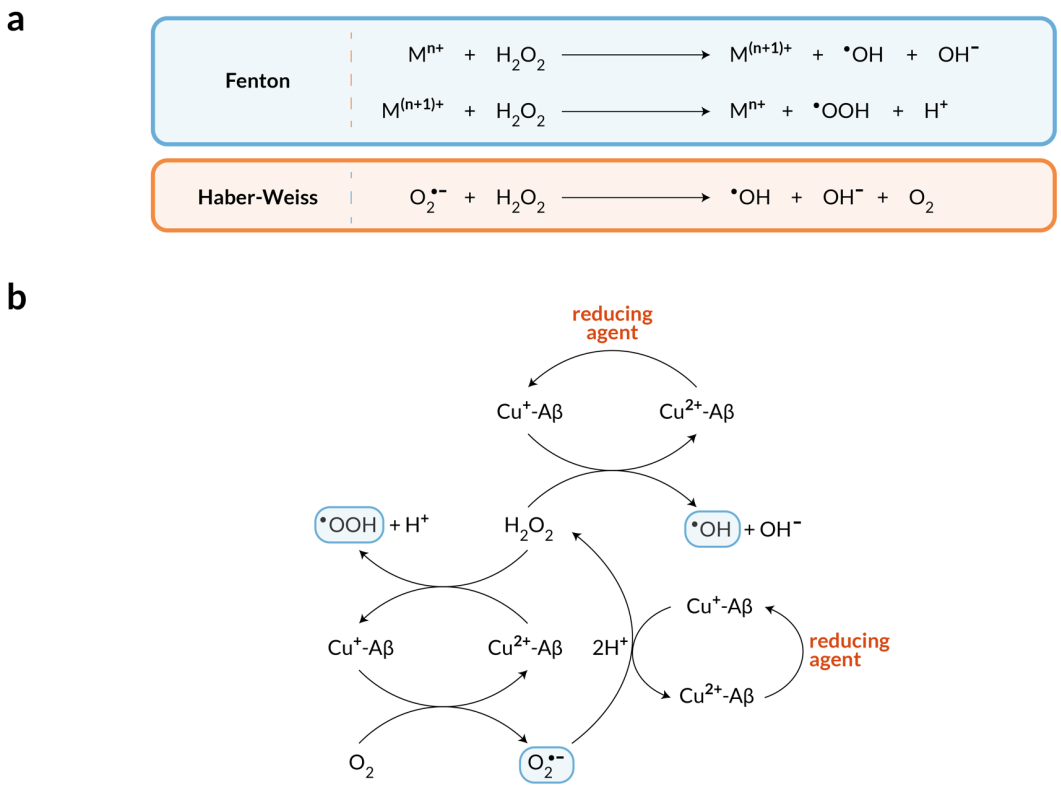


Figure 3.4: **a)** Generation of ROS *via* Fenton and Haber-Weiss reactions. **b)** Proposed catalytic cycle for ROS generation by Cu-Aβ, redrawn from *[235]*. Cu^{2+}-Aβ is first reduced to Cu^+-Aβ by a naturally occurring reducing agent and is then able to initiate ROS production. Key ROS are highlighted in blue.

Biomarkers of oxidative damage are found to be elevated in Alzheimer's disease, particularly in brain regions that are rich in Aβ plaques such as the hippocampus.[236,237] Moreover, oxidative stress has been reported to increase the expression and activity of the β-secretase enzyme, which, in turn, increases the production of Aβ.[238,239] Due to this, it is believed that metal-induced oxidative stress is a key factor that contributes towards the development of Alzheimer's disease.

3.1.3 Metal-Targeted Therapeutic Strategies for Alzheimer's Disease

Two therapeutic strategies that have emerged to tackle the role of metal ions in Alzheimer's disease are: 1) the use of chelators that can remove excess metals and 2) the use of metal complexes that can

preferentially bind to the N-terminal metal binding site. The first strategy has been widely explored in the literature and has resulted in a number of metal ion chelators being tested in clinical trials, such as desferrioxamine.[240] In 1991, McLachlan *et al.* reported that the administration of desferrioxamine to human patients over the course of two years led to a significant decline in the progression of Alzheimer's disease.[240] However, desferrioxamine is known to chelate a number of different metal ions and it is therefore unclear whether the decline observed was due to the removal of aluminium, iron, copper or zinc ions, or a combination of several metal ions.[241,242] The long-term use of desferrioxamine and other metal chelators can also lead to adverse side-effects such as anaemia or infections due to non-specific systemic metal ion depletion.[243,244] In addition, as with all therapeutic agents targeted towards brain diseases, many chelators that have shown promise *in vitro* have limited efficacy *in vivo* due to their inability to cross the BBB and are associated with invasive administration procedures.[48,240,245]

In contrast to chelation therapy, there have been very few examples of metal complexes that are able to modulate Aβ toxicity by binding to the N-terminal metal binding site. The first metal complexes that were designed for this application - and which remain the most well-investigated to date - are a range of platinum-based complexes containing 1,10-phenanthroline-based ligands (Figure 3.5).[246] Barnham *et al.* showed that these complexes were able to bind to Aβ, inhibit its neurotoxicity *in vitro* and also rescue Aβ-induced toxicity in mouse hippocampal slices *ex vivo*.[246] Through a combination of experimental and theoretical studies, the binding mode of these square planar platinum complexes to Aβ was determined to be *via* π-π stacking interactions with aromatic residues such as His, Phe and Tyr, as well as coordination (Figure 3.5).[247] The preferred coordination mode is typically to His6, His13 or His14.[247–249]

To date, a handful of other metal complexes have been designed to target the metal binding site of Aβ.[249–252] Most of these are platinum complexes, but there are a few examples of other metal centres, such as iridium, cobalt and ruthenium, being used.[250–252] A notable example is the octahedral cobalt(III) Schiff base complex reported by Heffern *et al.*, which is able to coordinate to the histidine residues of Aβ through dissociative ligand exchange at the axial positions (Figure 3.5).[250] Using a combination of SDS-PAGE western blot and silver stain analysis, this complex was shown to be able to disrupt the Aβ aggregation pathway and promote the formation of large (> 30 kDa) Aβ oligomers over small toxic oligomers.[250] Moreover, in the presence of the cobalt(III) Schiff base complex, Aβ oligomers displayed reduced binding to the synapses of hippocampal neurons.[250] Recent molecular dynamics simulations have demonstrated that cobalt(III) Schiff base complexes are able to prevent the formation of Aβ fibrils by sterically hindering the formation of hydrogen bonds between Aβ side-chains.[253] Similar to the platinum complexes discussed above, binding to His6 and His13/His14 is thought to be the most favourable coordination mode (Figure 3.5).[250,253]

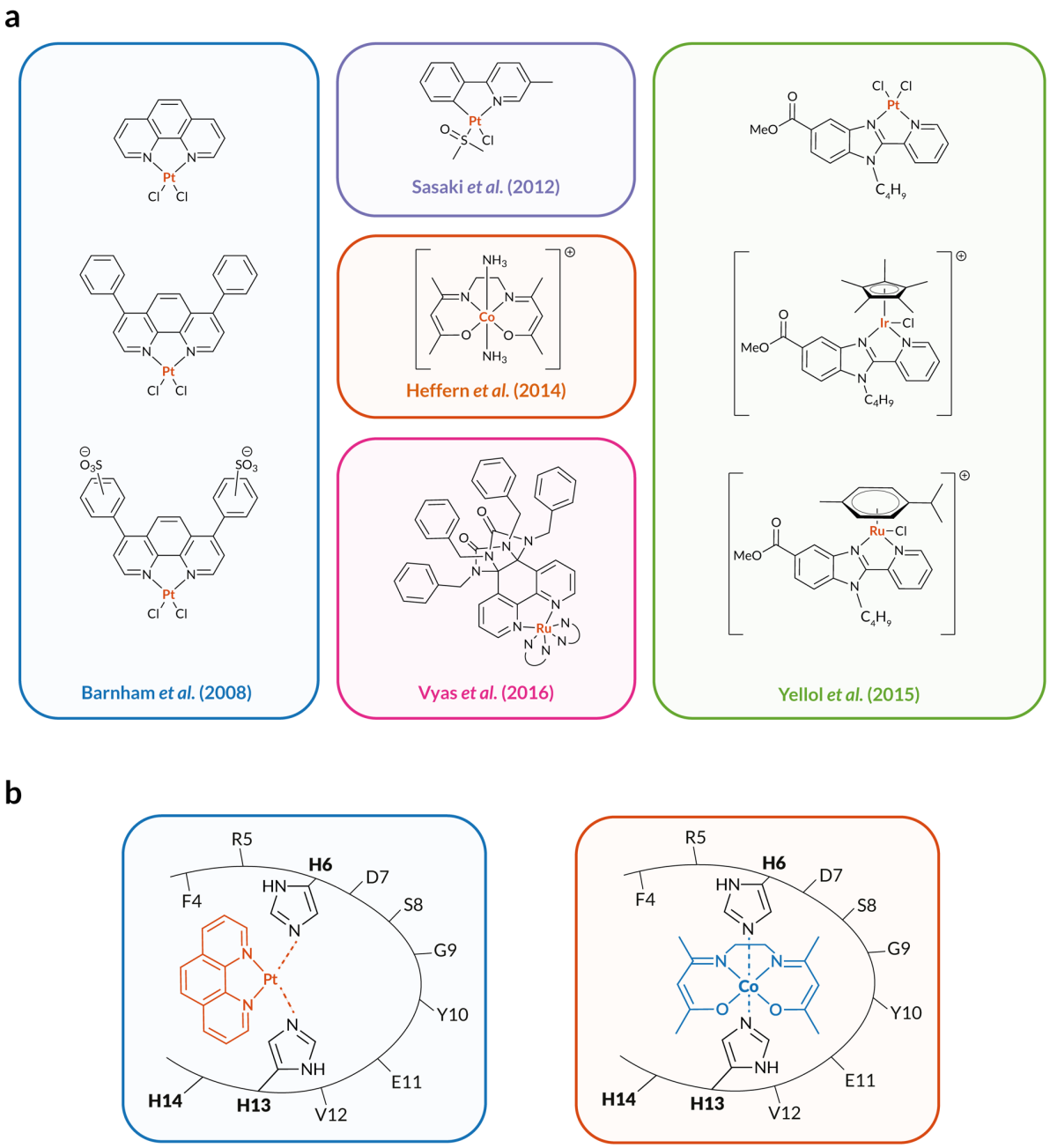


Figure 3.5: **a)** Examples of metal complexes that have been designed to target the N-terminal metal binding site of Aβ.[246,250–252] **b)** Proposed binding modes of metal complexes to the N-terminal of Aβ. All metal complexes reported for this application are believed to interact *via* non-covalent π-π stacking interactions with aromatic amino acids, as well as coordination to Aβ.

As of now, there is only one example of this therapeutic approach being evaluated *in vivo*, presumably due to the difficulty in delivering complexes of this size across the BBB: in 2013, Kenche *et al.* reported a 25% reduction in the number of Aβ plaques in a transgenic mouse model of Alzheimer's disease after administering an orally bioavailable platinum complex with an 8-(1*H*-benzoimidazol-2-yl)-quinoline scaffold over a period of 18 weeks.[48,254] Whilst this data is promising, significant work still needs to be done to establish the feasibility and efficacy of this therapeutic strategy *in vivo*.

3.2 AIMS AND OBJECTIVES

The overall aim of the work presented in this chapter was to design a metal complex capable of inhibiting the aggregation of the Aβ peptide by binding to its N-terminal metal binding site. To prevent off-target effects, we sought to identify a complex that showed good activity against Aβ whilst being non-cytotoxic. In addition to this, we also wanted to investigate the effect of complex geometry and electronic structure on the ability of the complexes to inhibit Aβ aggregation in order to aid the development of second generation complexes.

To achieve these aims, the following objectives had to be fulfilled:

- Design a series of metal complexes to allow factors such as complex geometry and electronic structure on the ability of the complexes to inhibit Aβ aggregation to be investigated.
- Screen the complexes for their ability to inhibit Aβ aggregation using the Thioflavin-T (ThT) assay and transmission electron microscopy.
- Probe the binding mode of the complexes to Aβ using fluorescence spectroscopy, ^{1}H NMR spectroscopy and circular dichroism experiments.
- Establish the cytotoxicity of the synthesised complexes.

3.3 RESULTS AND DISCUSSION

3.3.1 Designing Potential Inhibitors of Amyloid Beta Aggregation

Studies have shown that metal complexes that are able to interact with the high affinity metal ion binding pocket of Aβ are those that are able to π-π stack with aromatic residues and/or coordinate with His6,

His13 or His14.[246,247,250] In this chapter, we investigate a series of metal salphens and salnaphs as potential inhibitors of Aβ aggregation (Figure 3.6). Derivatives of the salphen ligand have previously been shown to possess a moderate ability to inhibit Aβ aggregation and thus, all complexes **1-4** are expected to show inhibitory activity.[255] Salphens **1** and **2** are square planar salphens, synthesised by Dr. V. Rakers (PhD student, Vilar Group), which would only be expected to interact with the N-terminal of Aβ *via* π-π stacking interactions. In contrast, salphens **3a-3e**, synthesised by C. Ruehl (PhD student, Vilar Group), and salnaphs **4a-4e** are octahedral cobalt complexes, which should be able to coordinate to Aβ upon release of their axial ligands in addition to undergoing π-π stacking. These cobalt complexes are expected to interact with Aβ *via* a similar mechanism as the cobalt(III) Schiff base complexes reported by Heffern *et al.* and Iscen *et al.*[250,253] Comparison between square planar complexes **1** and **2** with octahedral complexes **3a-3e** allows probing of coordination effects, whilst comparison between cobalt salphens **3a-3e** and salnaphs **4a-4e** allow probing of π-π stacking. We have also synthesised octahedral complexes **3** and **4** with a variety of axial ligands in order to investigate any effects of having different release kinetics. An analogous series of cobalt salen complexes were investigated for their ability to coordinate to Aβ by E. Ma (MSci student, Vilar Group): the results of this study have been reported in her thesis and will not be discussed here.[256]

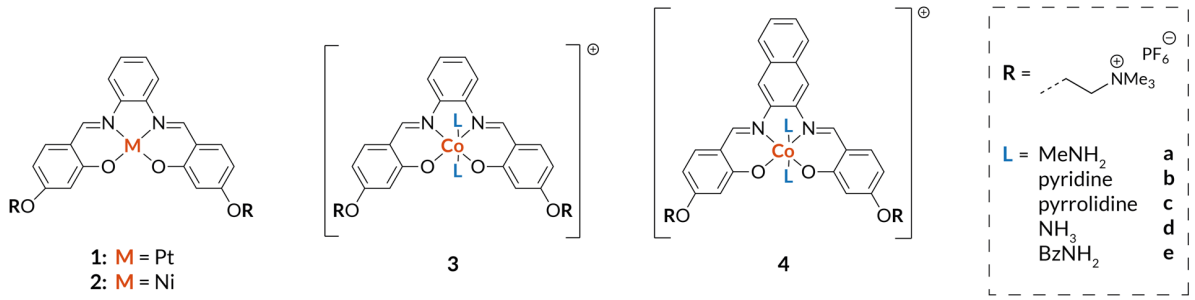
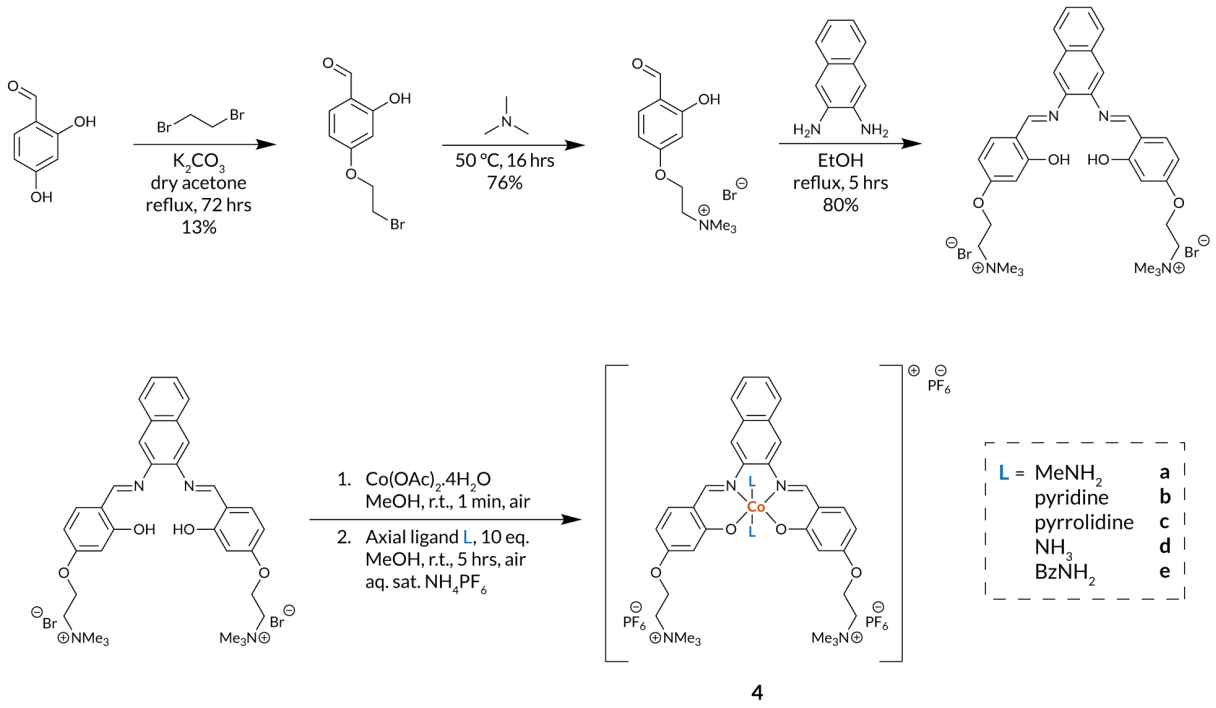


Figure 3.6: Structures of metal salphens and salnaphs **1-4e** used in this study. Salphens **1** and **2** were synthesised by Dr. V. Rakers (PhD student, Vilar Group) whilst cobalt salphens **3a-3e** were synthesised by C. Ruehl. Experimental details for the synthesis of these complexes can be found in their theses.[257–259]

Synthesis of Cobalt Salnaphs

The synthesis route used to obtain complexes **4a-4e** is shown in Scheme 2. Initially, 4-(2-bromoethoxy)-2-hydroxybenzaldehyde was synthesised by reacting 1,2-dibromoethane with 2,4-dihydroxybenzaldehyde under basic conditions.[260] This was then added to trimethylamine to give 4-(4-formyl-3-hydroxyphenoxy)-*N*,*N*,*N*-trimethylethan-1-ammonium bromide.[257] The salnaph ligand was obtained through a condensa-



Scheme 2: Synthesis route to cobalt salnaphs **4a-4e**.

tion reaction with 2,3-diaminonaphthalene. Finally, the desired octahedral cobalt complexes were synthesised by adding the isolated salnaph ligand to $Co(OAc)_2$ and the axial ligand of choice ($MeNH_2$, pyridine, pyrrolidine, NH_3 or $BzNH_2$). Complexation reactions were conducted in air in order to oxidise the Co^{2+} centre to Co^{3+}. All complexes were fully characterised by ^{1}H NMR spectroscopy, mass spectrometry and elemental analysis.

The aromatic region of the ^{1}H NMR spectrum of the salnaph ligand before and after cobalt complexation is shown in Figure 3.7. On formation of the desired octahedral cobalt salnaph complex, the -OH peak disappears, indicating successful complex formation. Shifts in the salnaph aromatic protons, as well as new peaks that correspond to the attached axial ligands, are also observed (Figure 3.7, Figure 3.8). In addition to this, the mass spectra recorded for complexes **4a-4e** showed the expected molecular peaks. Complex purity was confirmed by elemental analyses.

Aqueous Stabilities of Synthesised Cobalt Complexes

For use in *in vivo* applications, it is important to study the lability of the axial ligands in aqueous solution. To assess this, complexes **3a-3e** and **4a-4e** were incubated in aqueous buffer (pH 7.4) and the ^{1}H NMR spectra of the complexes were recorded at various time-points. As the axial ligands are displaced, a second

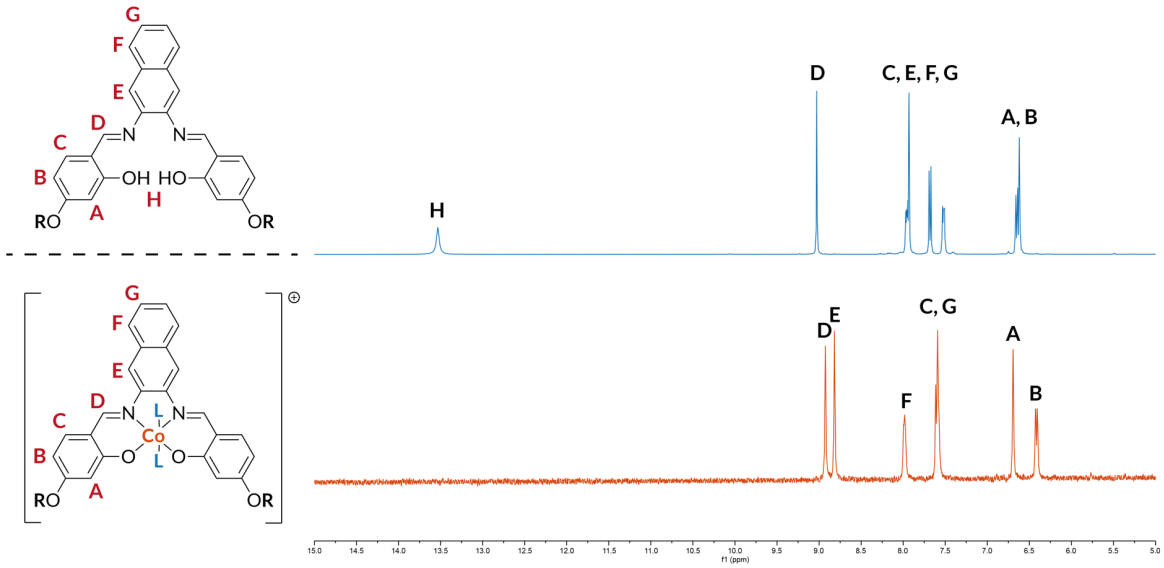


Figure 3.7: Aromatic region (5.0 to 15.0 ppm) of the ^{1}H NMR spectrum (400 MHz, DMSO-d_6) of the salnaph ligand recorded before and after cobalt complexation. The bottom spectrum is of complex **4d** (L = NH_3), which has axial ligands that do not give signals in the aromatic region. Disappearance of the -O<u>H</u> (H_H) signal is observed upon complexation, as well as shifts in the aromatic protons.

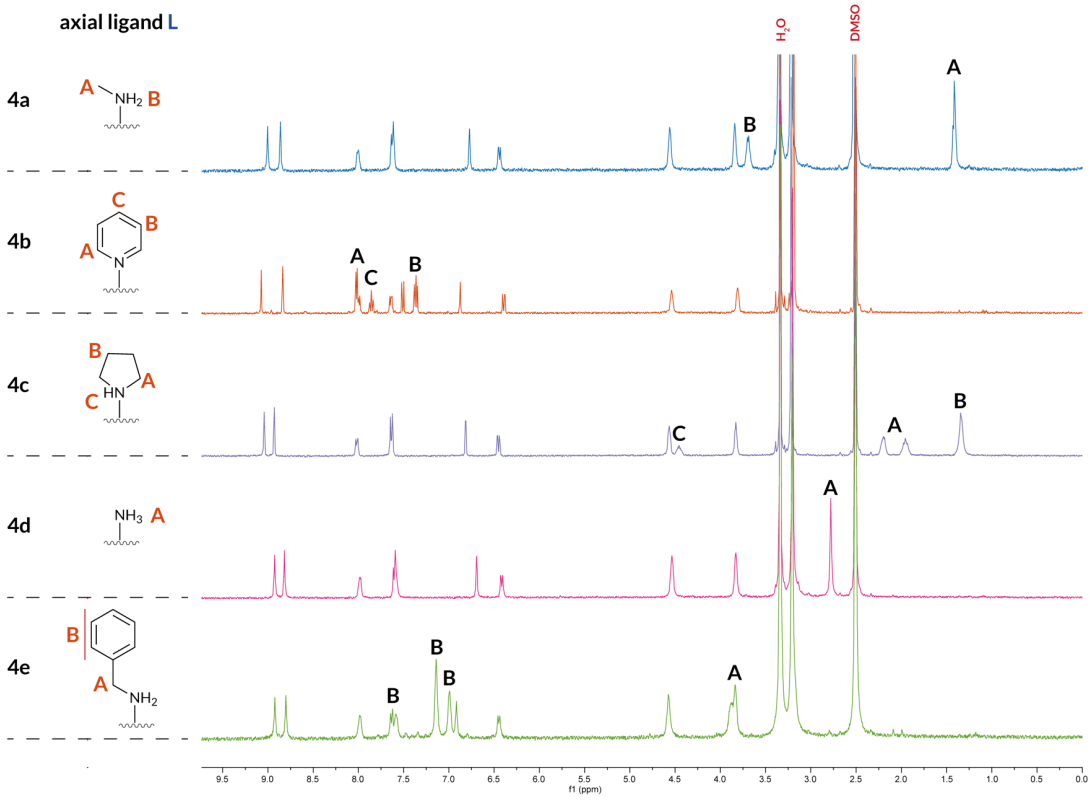


Figure 3.8: ^{1}H NMR spectra (400 MHz, DMSO-d_6) of octahedral cobalt salnaphs **4a-4e**.

set of NMR signals appear, showing that a mixture of products is present (Figure 3.9). By comparing the integrations of the two sets of peaks, the % abundance of the starting octahedral cobalt complex can be calculated, giving an indication of its stability in aqueous solution.

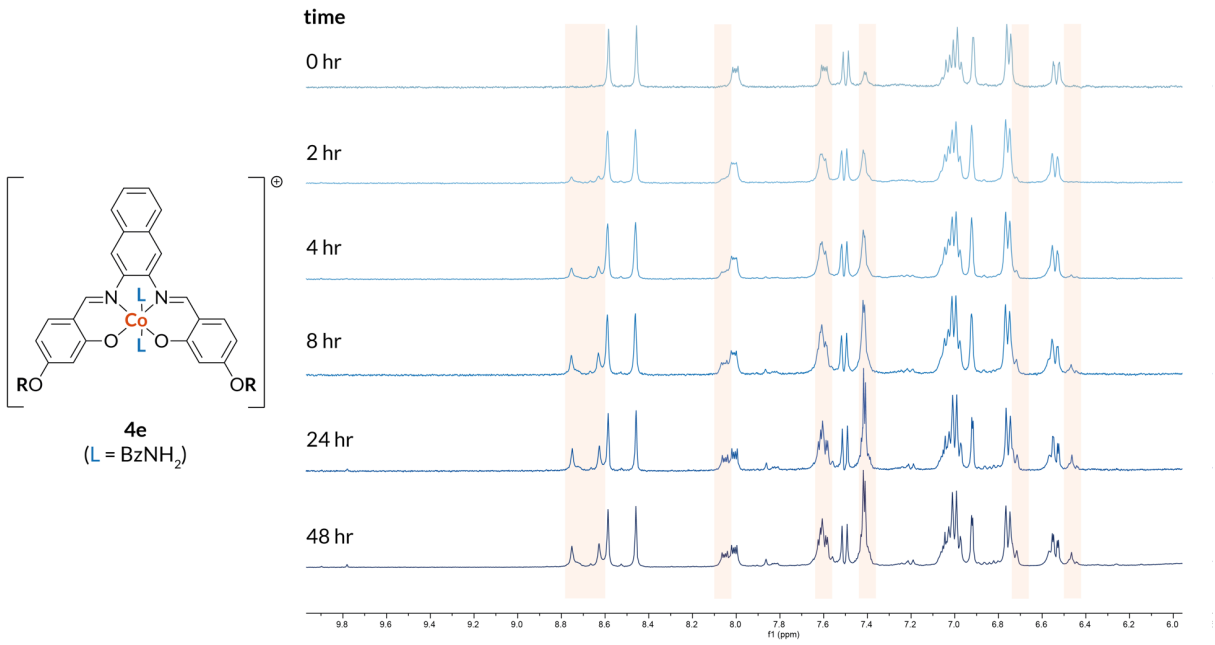


Figure 3.9: ^{1}H NMR spectrum (400 MHz) of complex **4e** (L = $BzNH_2$) recorded in 1:9 D_2O:phosphate-buffered saline (pH 7.4; 137 mM NaCl, 2.7 mM KCl, 8 mM Na_2HPO_4 and 2 mM KH_2PO_4) over time. As the axial ligands are displaced, a second set of NMR signals appear. Key changes in the NMR spectrum of complex **4e** over time are highlighted.

The complete stability data obtained for cobalt salnaphs **4a-4e** can be seen in Figure 3.10. From this data, it is evident that by modifying the attached axial ligands, a range of aqueous stabilities can be obtained. Complexes **4a-4e** remain moderately stable within a 48 hour period, making them suitable for *in vivo* applications. Analogous stability data for cobalt salphens **3a-3e** was collected by C. Ruehl (PhD student, Vilar Group) and shows similar trends as for the salnaph complexes.[259]

3.3.2 Investigating the Ability to Inhibit Aβ Aggregation using the Thioflavin-T Assay

The thioflavin-T assay involves the benzothiazole salt thioflavin-T (ThT) and is routinely used to probe Aβ aggregation *in vitro*. ThT shows weak fluorescence emission at 438 nm when excited at 350 nm in solution, but it shows strong fluorescence emission at 482 nm when excited at 450 nm upon binding to amyloid

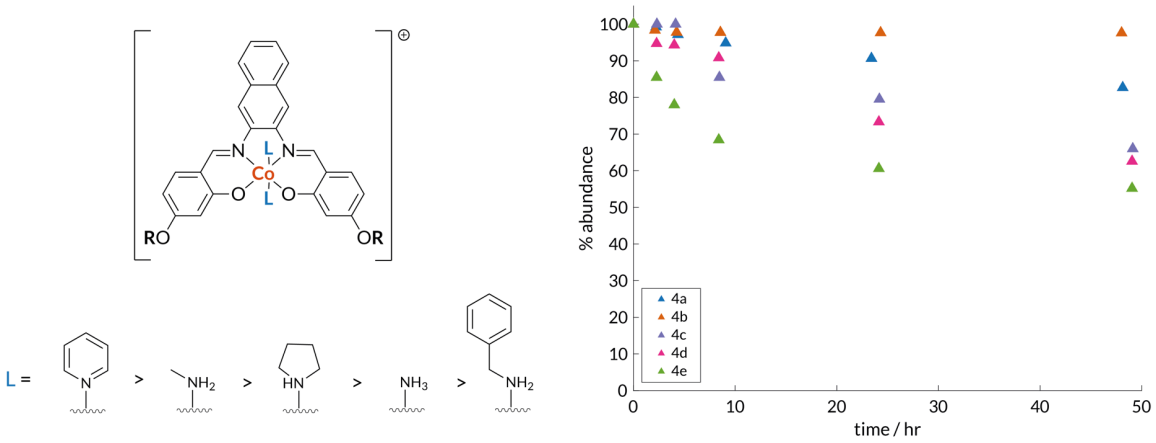


Figure 3.10: Stabilities of cobalt salnaphs **4a-4e** over time in 1:9 D_2O:phosphate-buffered saline (pH 7.4; 137 mM NaCl, 2.7 mM KCl, 8 mM Na_2HPO_4 and 2 mM KH_2PO_4).

fibrils.[261] The fluorescence properties of ThT are due to it acting as a molecular rotor: in the absence of amyloid fibrils, the benzylthiazole and benzylamine rings of ThT are able to rotate freely about their shared C-C bond, resulting in the quenching of any excited states and thus, low fluorescence emission.[261,262] However, in the presence of amyloid fibrils, ThT becomes rotationally immobilised by binding along the side-chain grooves that exist parallel to the long-axis of the fibrils (Figure 3.11).[261,262] This leads to the preservation of excited states and as a consequence, high fluorescence emission is observed upon photon excitation.

Due to the difference in fluorescence intensities that are observed in the absence and presence of amyloid fibrils, ThT is widely used to study Aβ aggregation *in vitro*. In the ThT assay, monomeric Aβ1-42 is incubated with ThT and the fluorescence emission of ThT is recorded over time: as the peptide aggregates from being monomeric to forming fibrillar structures, a sharp increase in the emission of ThT is observed (Figure 3.11). Potential inhibitors of Aβ1-42 aggregation can be screened for their ability to inhibit Aβ aggregation by incubating them with samples of Aβ1-42 and ThT. The fluorescence intensity at the end-point for Aβ1-42 by itself is taken as 0% inhibition, whilst the baseline is taken as 100% inhibition.

Before running an assay such as the ThT assay, it is important to ensure that the starting Aβ solution is entirely monomeric and does not contain any fibrillar structures. The most commonly used method to do this involves incubating Aβ with the fluorinated solvent 1,1,1,3,3,3-hexafluoro-2-propanol (HFIP), followed by lyophilisation and resuspension in a secondary solvent such as DMSO.[263,264] The addition of HFIP is believed to break up β-sheet structures and induce α-helical conformations.[263,264] However, recent evidence has suggested that this method is not able to fully dissociate Aβ peptides; in fact, the presence of low concentrations of HFIP has been reported to enhance fibril formation.[265,266] An alternat-

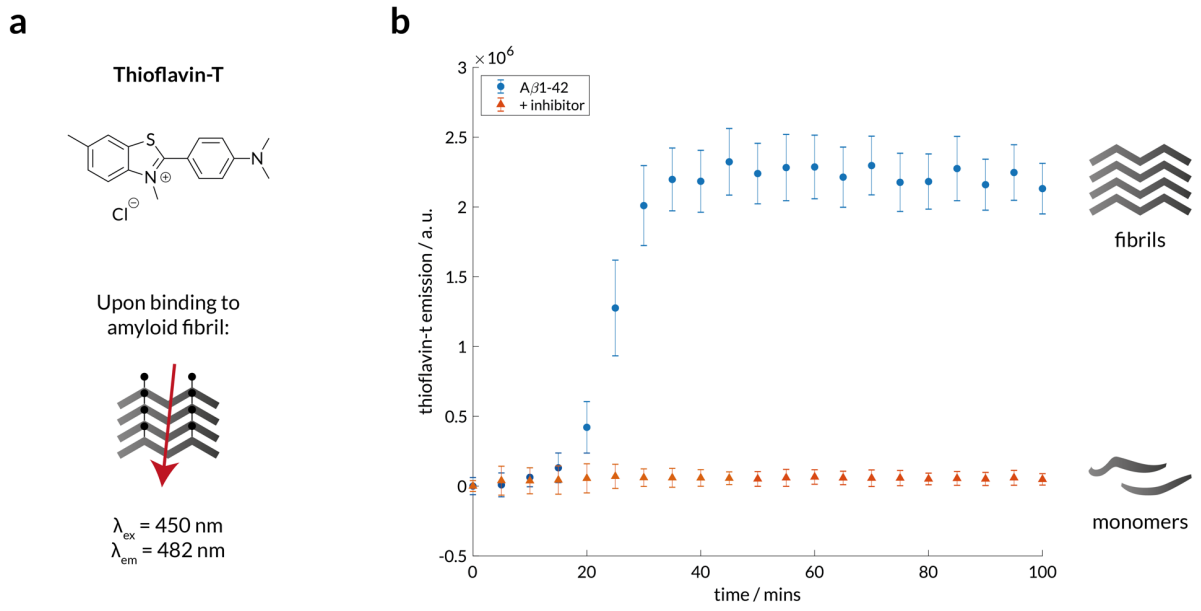


Figure 3.11: **a)** Structure of ThT and its proposed binding mode to amyloid fibrils. **b)** Example of a ThT emission curve recorded for Aβ1-42 incubated by itself and with an inhibitor of Aβ aggregation at 37 °C with shaking. For samples of Aβ1-42 incubated by itself, a sigmoidal curve is obtained in which a sharp increase in the emission intensity is observed upon fibril formation.

ive pretreatment involving the addition of a strong alkali such as ammonium hydroxide was proposed by Ryan *et al.* in 2013.[265] Through a combination of dynamic light scattering, size-exclusion chromatography and small angle X-ray scattering, this pretreatment protocol was shown to be more effective at producing monomeric Aβ solutions and was therefore applied prior to all biophysical and toxicity assays run in this study.[265]

Initially, metal complexes **1, 2, 3c** and **4c** were screened using the ThT assay. Platinum complexes **5** and **6** are two of the most well-studied metal complexes that have been developed to target the N-terminal of Aβ and were included as positive controls.[246,249] Briefly, complexes were tested at [Aβ1-42]:[complex] ratios of 1:0.2, 1:0.1, 1:0.07, 1:0.05, 1:0.04, with final Aβ1-42 and ThT concentrations of 5 μM and 20 μM respectively. All samples were prepared in phosphate-buffered saline (pH 7.4; 137 mM NaCl, 2.7 mM KCl, 8 mM Na_2HPO_4 and 2 mM KH_2PO_4) and incubated at 37 °C with shaking until the end-point of aggregation was reached. As shown in Figure 3.12, complexes **1**, **2**, **3c** and **4c** all show higher inhibitory activity against Aβ aggregation than literature complexes **5** and **6**, with greater inhibition observed with octahedral complexes **3c** and **4c** compared to square planar **1** and **2**. This suggests that complexes **3** and **4** are able to form additional coordination interactions with Aβ as we predicted from their structures. It should also be noted that the [Aβ1-42]:[complex] ratios tested are very low, with complexes **3c** and **4c** showing

> 50% inhibitory activity at ratios of 1:0.04. The ability of the complexes to inhibit Aβ aggregation at such low [Aβ1-42]:[complex] ratios indicates that the interaction between the complexes and Aβ must be sufficient enough to affect neighbouring Aβ monomers, as well as the Aβ monomer being directly bound to. This is in line with the conclusions made by Iscen *et al.* on the binding of their cobalt(III) Schiff base complexes to Aβ, in which successful inhibition of Aβ aggregation was observed at sub-1:1 equivalency in both experimental and computational studies.[253]

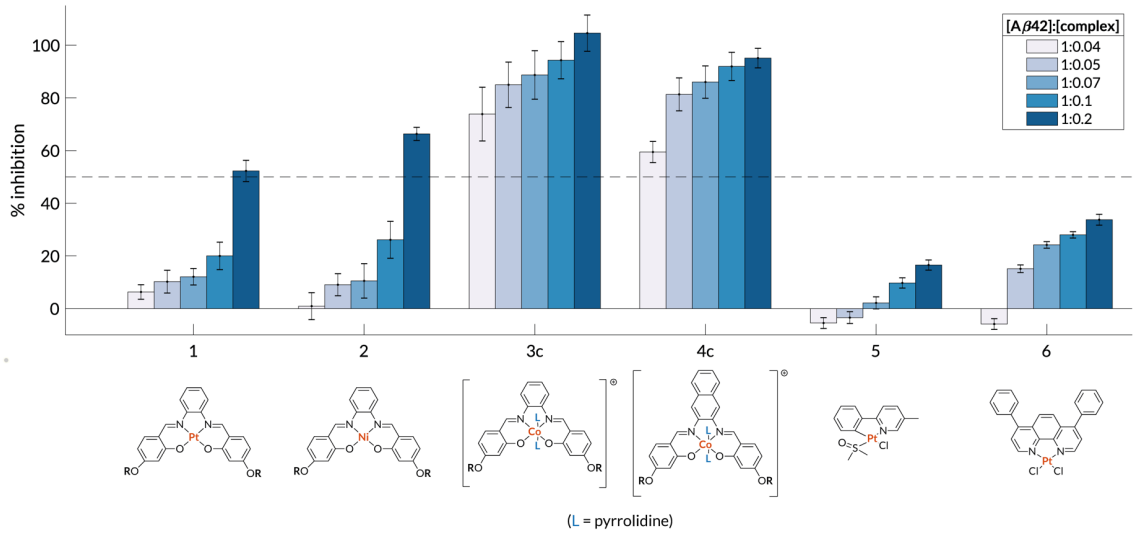


Figure 3.12: Inhibition of Aβ1-42 aggregation (%) induced by metal complexes **1**, **2**, **3c** and **4c** determined using the ThT assay. Complexes **5** and **6** are literature compounds and are included as positive controls.[246,249] Complexes were tested at [Aβ42]:[complex] = 1:0.2, 1:0.1, 1:0.07, 1:0.05 and 1:0.04, and all samples were incubated at 37 °C with shaking. The dotted line represents the half-inhibition point and all data is reported as the mean ± standard deviation of three independent experiments.

If complexes **3** and **4** are indeed coordinating to Aβ in the axial positions as expected, then varying the attached axial ligands should not affect the inhibitory activity, provided that the axial ligands are labile enough to be displaced by Aβ. To investigate this, cobalt complexes with different axial ligands **3a-3e** and **4a-4e** were screened for their activity using the ThT assay. As shown in Figure 3.13, all cobalt complexes outperform their nickel and platinum counterparts (**1** and **2**). Due to the lack of available data points at lower complex concentrations, precise IC_{50} values cannot be calculated for the cobalt complexes, but they are estimated to be between 100 to 300 nM under the experimental conditions used. Complex **4e** appears to have a higher IC_{50} than the other cobalt complexes, despite undergoing dissociative exchange most readily in aqueous solution (Figure 3.10). This suggests that the presence of Aβ and/or ThT makes dissociative exchange less favourable; future work will need to investigate this possibility further, as well

as whether the variations in IC_{50} values between all the other complexes is significant. To do this, the ThT assay should be repeated at lower complex concentrations to allow dose-response curves to be obtained and conducted in a 96-well plate format - rather than in 384-well plates as performed here - to minimise any experimental errors that could arise from the use of small volumes and concentrations. All IC_{50} values should also be validated using alternative assays, such as the Congo Red assay.[267] Due to time constraints, we could not investigate all of our cobalt complexes in the subsequent structural studies and have focused solely on complexes **3c** and **4c**; however, all complexes are expected to interact with Aβ *via* the same general mechanism.

Validating the ThT Assay using Transmission Electron Microscopy

Whilst the ThT assay is routinely used to screen for compounds that are able to inhibit Aβ aggregation, it has its limitations; for example, ThT is only able to recognise fibrillar Aβ assemblies and not soluble oligomeric species, which have also been linked to toxicity.[268] It is therefore important to validate the results obtained from the ThT assay using a secondary method, such as negative stain transmission electron microscopy (TEM). In negative stain TEM, the sample - in this case, Aβ peptide - is applied onto an amorphous carbon grid and then stained with a negative stain such as uranyl acetate. Ideal negative stains are electron dense and accumulate around the sample of interest due to electrostatic repulsion.[269] This leads to a high relative contrast between the background and the sample of interest, allowing the sample to be more easily visualised.

To confirm that the synthesised metal complexes are able to inhibit Aβ aggregation, samples of Aβ1-42 were incubated with metal complexes **1, 2, 3c** and **4c** (1:1 ratio) at 37 °C for 48 hr. The mixtures were then drop-casted onto a carbon-coated grid, negatively stained with uranyl acetate and allowed to dry. TEM images were acquired blind by Dr. J. Barritt (Imperial College London) to avoid bias. As shown in Figure 3.14, the formation of Aβ fibrils is clearly observed in the control sample containing Aβ1-42 incubated by itself. Significantly less fibril formation was observed in all samples containing metal complexes: no evidence of fibril formation was observed in Aβ1-42 samples incubated with complexes **2, 3c** and **4c,** whilst a few fibrils were seen in the Aβ1-42 sample incubated with complex **1**. The formation of oligomers was not detected in any sample. These images support the ThT results reported above and suggest that the metal complexes, particularly octahedral cobalt complexes **3c** and **4c**, are able to suppress Aβ aggregation.

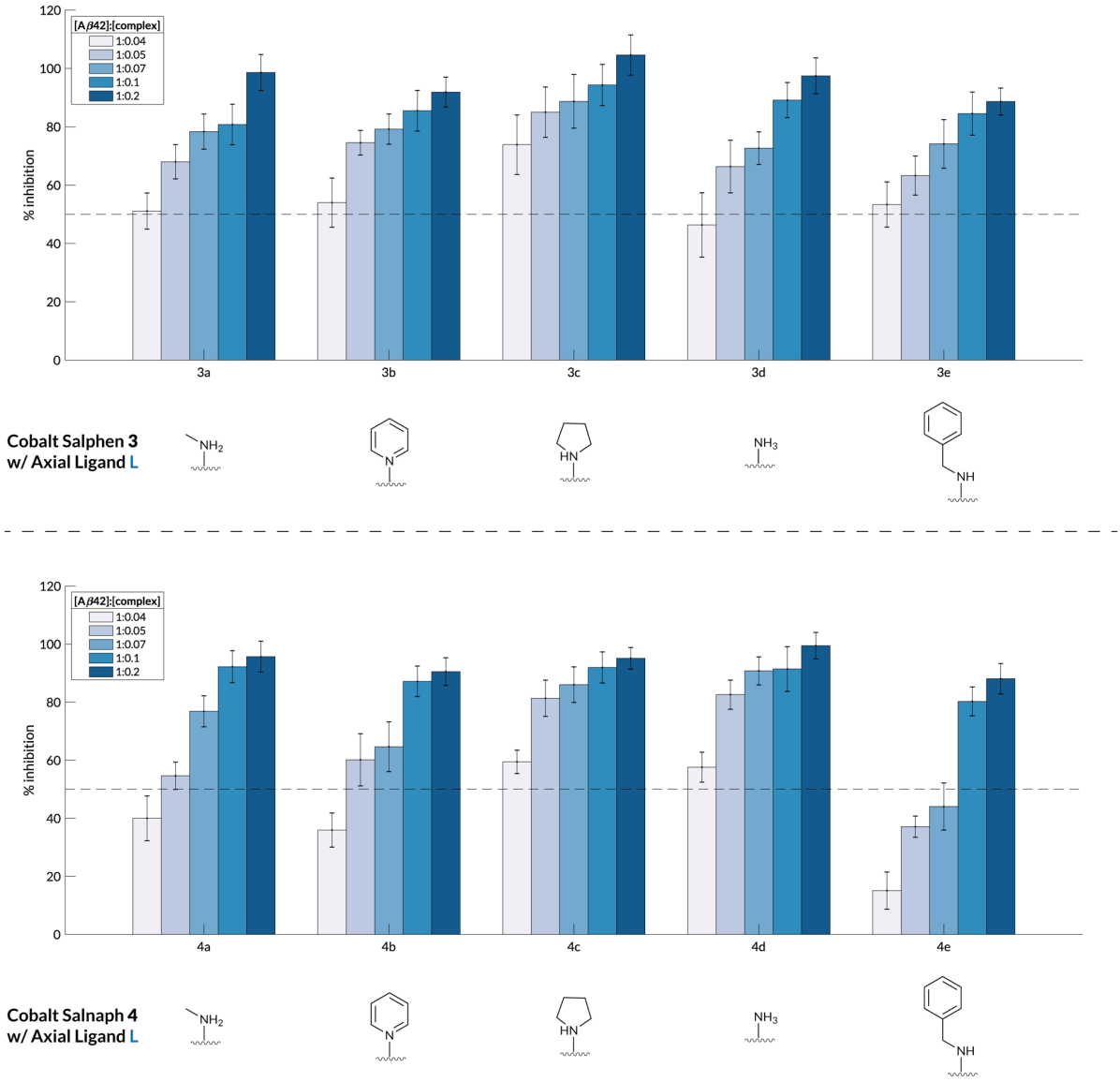


Figure 3.13: Inhibition of Aβ1-42 aggregation (%) induced by cobalt salphens **3a-3e** (top) and cobalt salnaphs **4a-4e** (bottom) determined using the ThT assay. Complexes were tested at [Aβ42]:[complex] = 1:0.2, 1:0.1, 1:0.07, 1:0.05 and 1:0.04, and all samples were incubated at 37 °C with shaking. The dotted line represents the half-inhibition point and all data is reported as the mean ± standard deviation of three independent experiments.

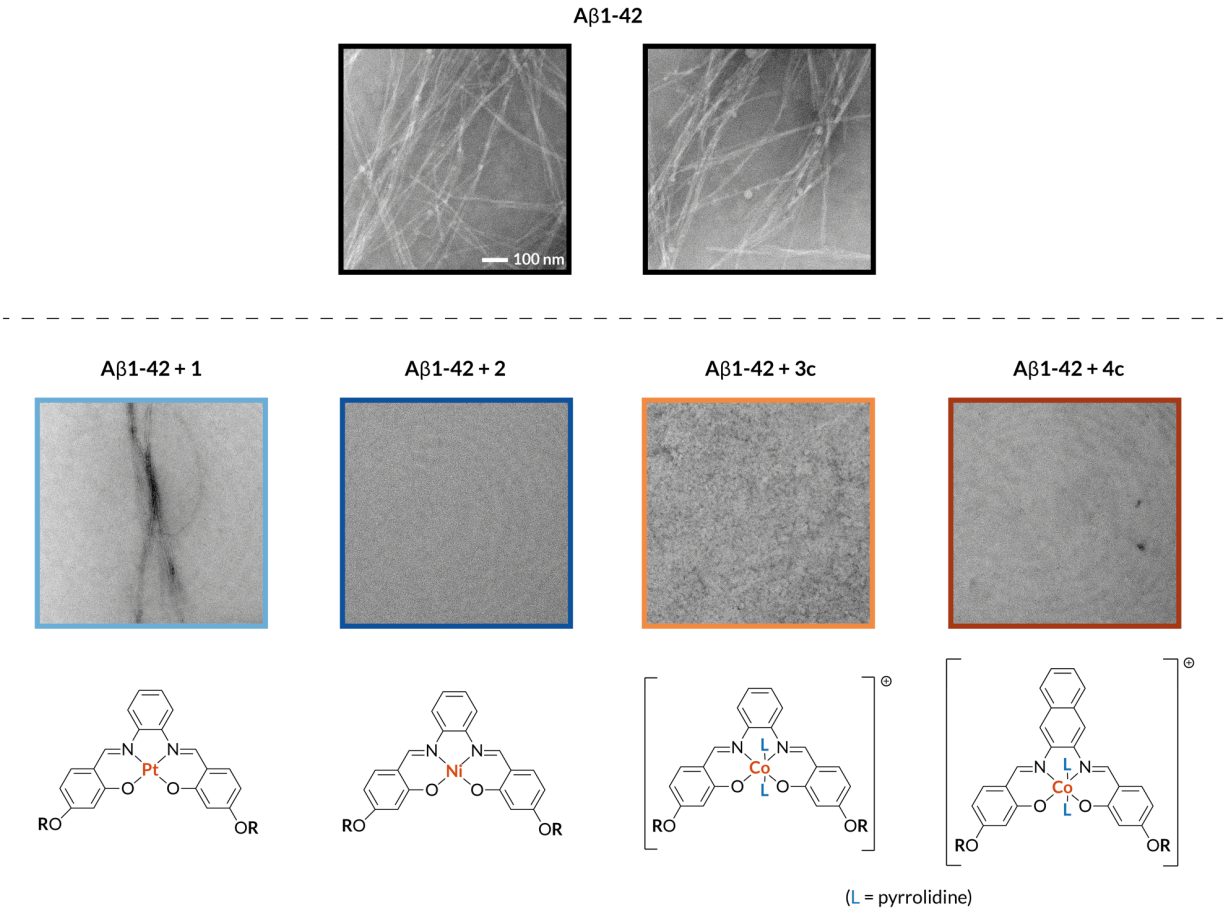


Figure 3.14: Representative TEM images of Aβ1-42 incubated by itself or with metal complexes **1**, **2**, **3c** or **4c** for 48 hr at 37 °C (1:1 ratio). Clear fibril formation can be observed in the sample of Aβ1-42 incubated by itself. Little fibril formation is observed when Aβ1-42 is incubated with complex **1**, whilst no evidence of fibril formation is observed with complexes **2, 3c** and **4c**.

3.3.3 Probing the Binding Mode to Amyloid Beta

Having established that the synthesised metal complexes are able to reduce Aβ aggregation, fluorescence spectroscopy, ^{1}H NMR spectroscopy and circular dichroism spectroscopy were conducted to probe the binding mode to Aβ. Based on prior literature, the complexes were expected to interact with Aβ *via* π-π stacking and, for octahedral cobalt complexes **3** and **4**, coordination with histidine residues.[247,250]

Fluorescence Spectroscopy

The truncated peptide Aβ1-16 is intrinsically fluorescent due to its Tyr10 residue. Metal complexes that are able to interact non-covalently with Aβ1-16 through π-π stacking interactions are expected to quench this intrinsic fluorescence.[247] To investigate this, increasing amounts of metal complexes **2, 3c** and **4c** were titrated against Aβ1-16 (0 to 0.75 equiv.) and the emission spectra was recorded. Cisplatin, which is not expected to form π-π stacking interactions with Aβ, was used as a negative control.

From the fluorescence spectra recorded, significant quenching of the Tyr10 residue of Aβ can be observed for complexes **2**, **3c** and **4c**, whilst only minimal quenching is observed for cisplatin (Figure 3.15). Moreover, greater fluorescence quenching is observed for salnaph complex **4c** compared to its analogous salphen derivative **3c**, suggesting the presence of increased π-π stacking interactions as would be expected from its extended aromatic scaffold. No significant change in fluorescence quenching is observed between square planar salphen **2** and octahedral salphen **3c**, indicating that the quenching effects observed are predominantly due to π-π stacking interactions.

^{1}H NMR Spectroscopy

To investigate any coordination to Aβ, a series of ^{1}H NMR experiments were conducted as any coordination would be expected to strongly perturb the NMR signals of Aβ.[247,249] A truncated Aβ1-28 sequence was used in all NMR experiments to simplify analyses. Samples of Aβ1-28 were incubated with or without the metal complexes in phosphate-buffered saline (pH 7.4; 137 mM NaCl, 2.7 mM KCl, 8 mM Na_2HPO_4 and 2 mM KH_2PO_4) at 37 °C, and the resulting ^{1}H NMR spectra were recorded at various time-points (Figure 3.16). Peaks corresponding to histidine residues were assigned based on literature references.[249,270] When incubated with square planar complexes **1** or **2**, minor perturbations are observed in the ^{1}H NMR spectrum of Aβ1-28, which are likely due to π-π stacking interactions. Conversely, when incubated with octahedral complexes **3c** and **4c**, significant broadening of the Aβ histidine signals is observed, indicating the presence of coordination.

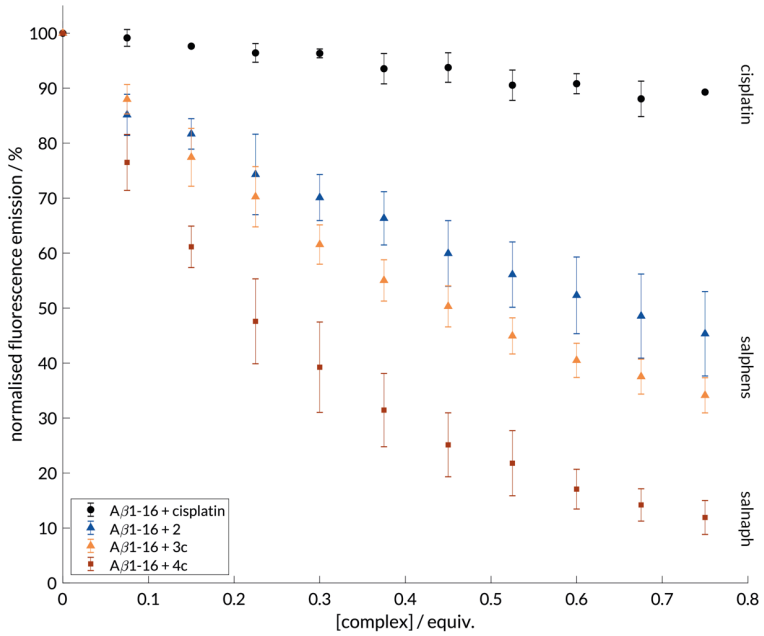


Figure 3.15: Normalised fluorescence emission of the Tyr10 residue of Aβ1-16 on addition of cisplatin (negative control; black), **2**, **3c** and **4c** (0 to 0.75 eq.) in phosphate-buffered saline (pH 7.4; 137 mM NaCl, 2.7 mM KCl, 8 mM Na_2HPO_4 and 2 mM KH_2PO_4). The highest degree of quenching is seen with salnaph complex **4c** (square). All data is reported as the mean ± standard deviation of three independent experiments.

To probe this further, the ^{1}H NMR experiments were repeated with a point-mutated Aβ1-28 peptide, in which the His6 residue was mutated to an arginine (H6R Aβ1-28). In this case, only minor perturbations of the NMR spectrum of Aβ1-28 are observed when it is incubated with all of the complexes, suggesting that for the octahedral cobalt complexes, the His6 residue is key for binding (Figure 3.16). This finding agrees with theoretical density functional theory (DFT) and molecular dynamics studies conducted by Heffern *et al.* and Iscen *et al.* on the use of octahedral cobalt(III) Schiff base complexes as inhibitors of Aβ aggregation.[250,253] Future work should seek to establish the exact binding mode of the complexes to Aβ, a feat which could be achieved using tandem mass spectrometry as described by Ma *et al.*[247]

Circular Dichroism

Circular dichroism (CD) is a spectroscopy technique which involves the absorption of circularly polarised light. Light can be circularly polarised in two directions: left and right (Figure 3.17). Chiral molecules that are optically active will absorb left- and right-handed light by different extents, resulting in light that is elliptically polarised.[271] CD measures the differences in left- and right-handed light absorption as the wavelength is varied and is often reported in degrees of ellipticity, θ, the tangent of the ratio of the minor

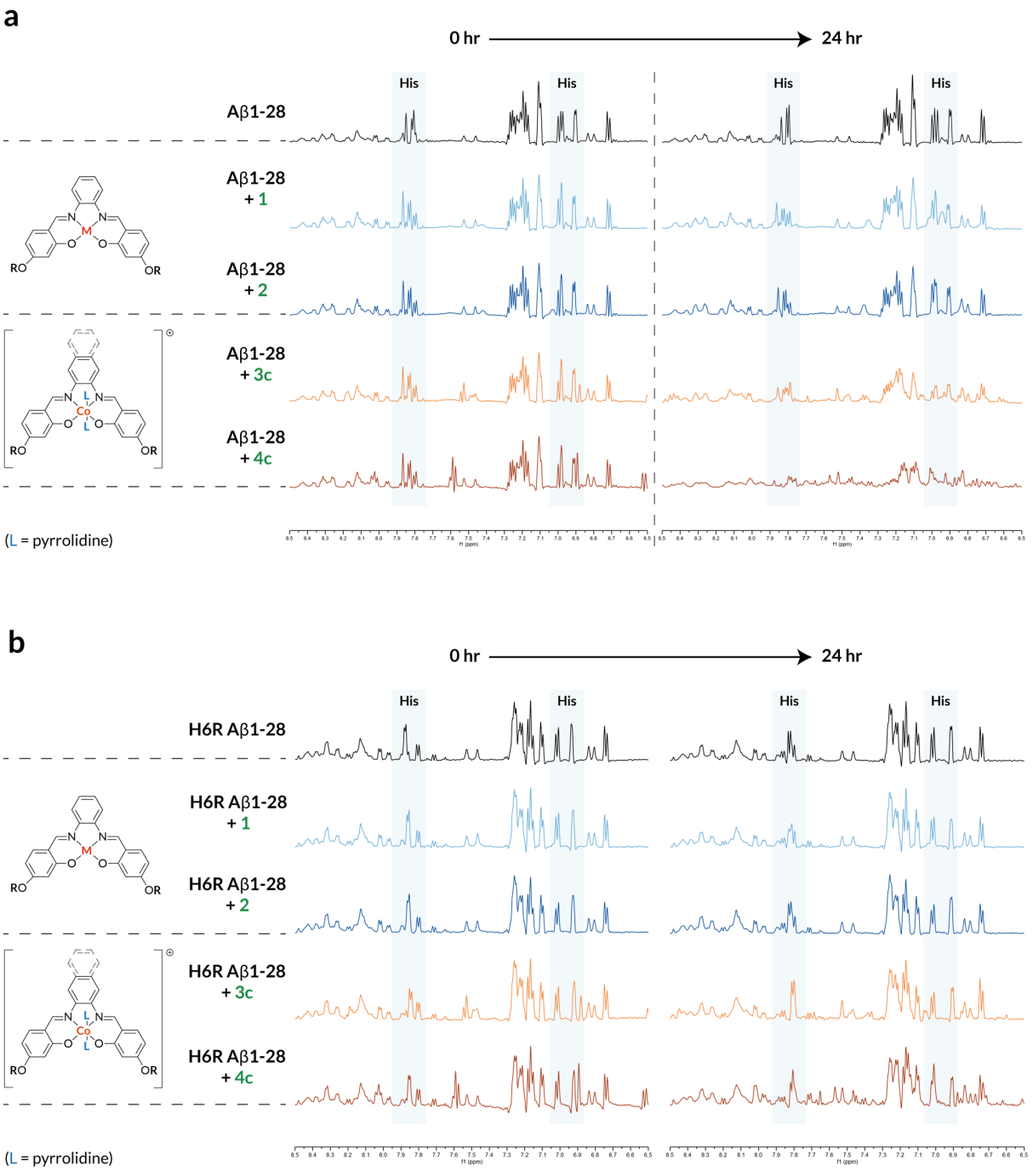


Figure 3.16: **a)** ^{1}H NMR spectrum of Aβ1-28 incubated by itself (black) or with complexes **1, 2, 3c** or **4c** at 0 and 24 hrs**. b)** ^{1}H NMR spectrum of H6R Aβ1-28 incubated by itself (black) or with complexes **1, 2, 3c** or **4c** at 0 and 24 hrs. All spectra were recorded at 400 MHz in 1:9 D_2O:phosphate-buffered saline (pH 7.4; 137 mM NaCl, 2.7 mM KCl, 8 mM Na_2HPO_4 and 2 mM KH_2PO_4) at 37 °C. Peaks corresponding to the Aβ histidine residues have been assigned based on literature.[249,270]

to major elliptical axis. Different protein secondary structures have characteristic CD absorption bands: for example, α-helices give a negative band at 222 nm and 208 nm and a positive band at 193 nm, whilst β-sheets give a negative band at 218 nm and a positive band at 195 nm.[271–273] Disordered proteins show a weak positive band above 210 nm and a negative band at 195 nm.[271,273] CD can therefore be used to assess any changes in protein conformation that may occur as a result of binding interactions.

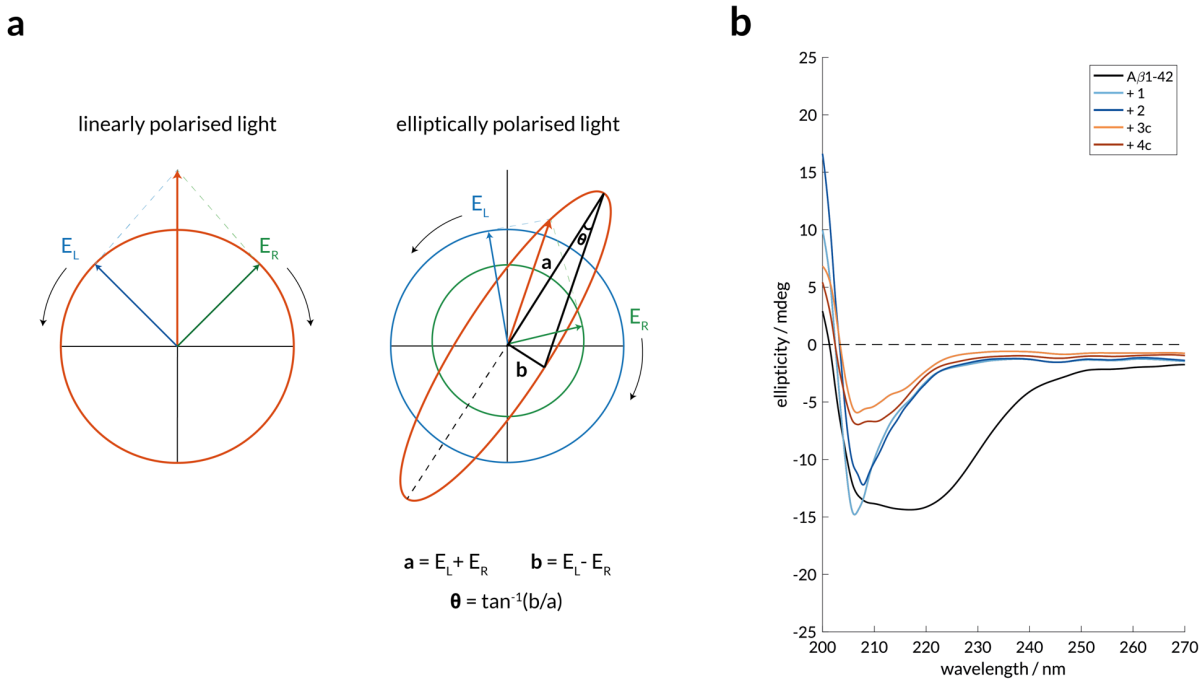


Figure 3.17: **a)** Light can be circularly polarised in the left- and right-handed directions. Linearly polarised light is the superimposition of left- and right-handed circularly polarised light of the same amplitude. Optically active chiral molecules will absorb left- and right-handed circularly polarised light by different extents, resulting in elliptically polarised light. θ denotes the degrees of ellipticity. **b)** Circular dichroism spectra of Aβ1-42 after incubation with complexes **1, 2, 3c** and **4c** at 37 °C for 48 hrs in phosphate-buffered saline (pH 7.4; 137 mM NaCl, 2.7 mM KCl, 8 mM Na_2HPO_4 and 2 mM KH_2PO_4). A blue shift is observed on addition of all complexes. Spectra shown are the average of two independent experiments.

Figure 3.17 shows the CD spectra of Aβ1-42 incubated in the presence and absence of metal complexes **1**, **2**, **3c** and **4c** for 37 °C for 48 hrs (1:1 ratio). For the sample of Aβ1-42 incubated by itself, a clear band at 218 nm is observed, indicative of a β-sheet conformation as would be expected from fully aggregated Aβ peptide. In contrast, a blue shift is observed for all samples incubated with the metal complexes. These peaks cannot be assigned to any of the classic protein secondary structures, but they indicate that the complexes are capable of inducing conformational changes in the Aβ peptide. Theoretical studies conducted by Mutter *et al.* and Iscen *et al.* have suggested that the binding of metals such as Cu, Pt and Co

to Aβ1-42 leads to the stabilisation of helical character over β-sheet formation; thus, the conformational changes that are induced in the Aβ1-42 peptide upon the binding of complexes **1-4** could be responsible for the inhibitory activity that was observed in the ThT assay discussed above.[253,274]

3.3.4 Assessing Cytotoxicity of the Synthesised Metal Complexes

On average, patients with Alzheimer's disease survive for eight to ten years after their symptoms begin; it is therefore important that any proposed treatment for Alzheimer's disease is non-toxic towards healthy cells.[275] Moreover, since Aβ is known to aggregate in the extracellular space, the complexes we develop should ideally show poor cell penetration in order to avoid any off-target effects. To investigate this, the cytotoxicity of the synthesised complexes towards human neuroblastoma cells (SH-SY5Y) was assessed using the MTS assay. The SH-SY5Y cell line shows neuronal characteristics and is widely used as an *in vitro* model for a number of neurodegenerative diseases, including Alzheimer's disease.[276–279]

In the MTS assay, the tetrazolium dye MTS (3-(4,5-dimethylthiazol-2-yl)-5-(3-carboxymethoxyphenyl-2-(4-sulphophenyl)-2*H*-tetrazolium, inner salt) is ultimately reduced to give a purple formazan product in the presence of viable cells (Figure 3.18).[280] Due to its negative charge, MTS possesses poor cell permeability and must be used in combination with intermediate electron carriers such as phenazine methosulphate (PMS).[280,281] These electron carriers enter viable cells, are reduced in the cytoplasm and then exit to reduce MTS to its formazan product in the surrounding cell culture media. By measuring the absorbance at 490 nm, the cell viability can be assessed.

To investigate the cytotoxicity of the synthesised complexes, SH-SY5Y cells were seeded at a density of 2,500 cells/well and incubated for 24 hrs. The cells were then incubated with complexes **1, 2, 3** or **4** at concentrations ranging from 0 to 20 μM for 24 hrs before determining cell viability. As shown in Figure 3.19, all complexes, particularly cobalt complexes **3** and **4**, show low cytotoxicity toward SH-SY5Y cells (IC_{50} > 20 μM). In addition to this, changing the axial ligand attached to **3** or **4** has minimal effects on the observed cytotoxicity, with the IC_{50} remaining > 20 μM in all cases.

Complex **4b** is the most stable of the synthesised octahedral cobalt complexes in aqueous solution and thus, the most promising candidate for *in vivo* studies (Figure 3.10). As a consequence, this complex was screened for any cytotoxic effects at higher concentrations up to 100 μM. As shown in Figure 3.20, minimal cytotoxicity was observed in both human neuroblastoma (SH-SY5Y) and prostate cancer (PC3) cell lines at all concentrations tested (IC_{50} > 100 μM). No associated cytotoxicity was observed in two other

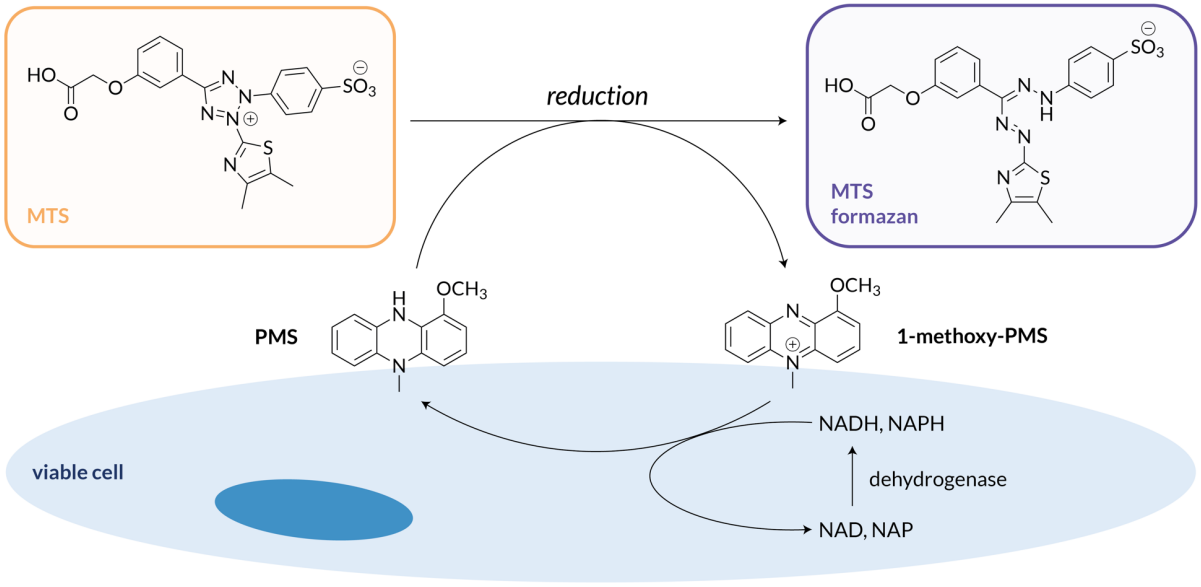


Figure 3.18: Mechanism of the MTS assay. In the presence of viable cells, MTS is reduced to form a purple formazan product. Measuring the absorbance at 490 nm allows the cell viability to be determined.

human cell lines, U2OS (human bone osteosarcoma epithelial cells) and MCF-7 (human breast adenocarcinoma), by C. Ruehl (PhD student, Vilar Group).[259]

A possible explanation for the lack of cytotoxicity observed with the complexes is that the attached trimethylammonium side-arms restrict cell uptake due to their positive charges. This hypothesis is supported by the observation that greater cytotoxicity can be achieved by either attaching a cell-penetrating peptide to the backbone or changing the side-arms for piperidine. An example of this for nickel salphen **2** is shown in Figure 3.21. Complex **2b** (with cell-penetrating peptide) was synthesised by T. Kench (PhD student, Vilar Group) and complex **2c** (with piperidine side-arms) was synthesised by Dr. V. Rakers (PhD student, Vilar Group). As stated above, poor cell uptake is ideal for our proposed application as Aβ is known to aggregate in the extracellular space.

3.3.5 Assessing the Effect on Amyloid Beta Neurotoxicity

Before assessing the efficacy of the complexes *in vivo*, we first wanted to test the complexes *in vitro* in order to establish suitable dosages and timescales. Historically, human neuroblastoma (SH-SY5Y) cells have been commonly used to assess Aβ toxicity.[276–279] In these experiments, Aβ1-42 and the compound of interest are incubated with the cells and a cytotoxicity assay such as the MTS assay is conducted at the desired time-point. Aβ1-42 is expected to induce toxicity to SH-SY5Y cells and thus, this assay can be used

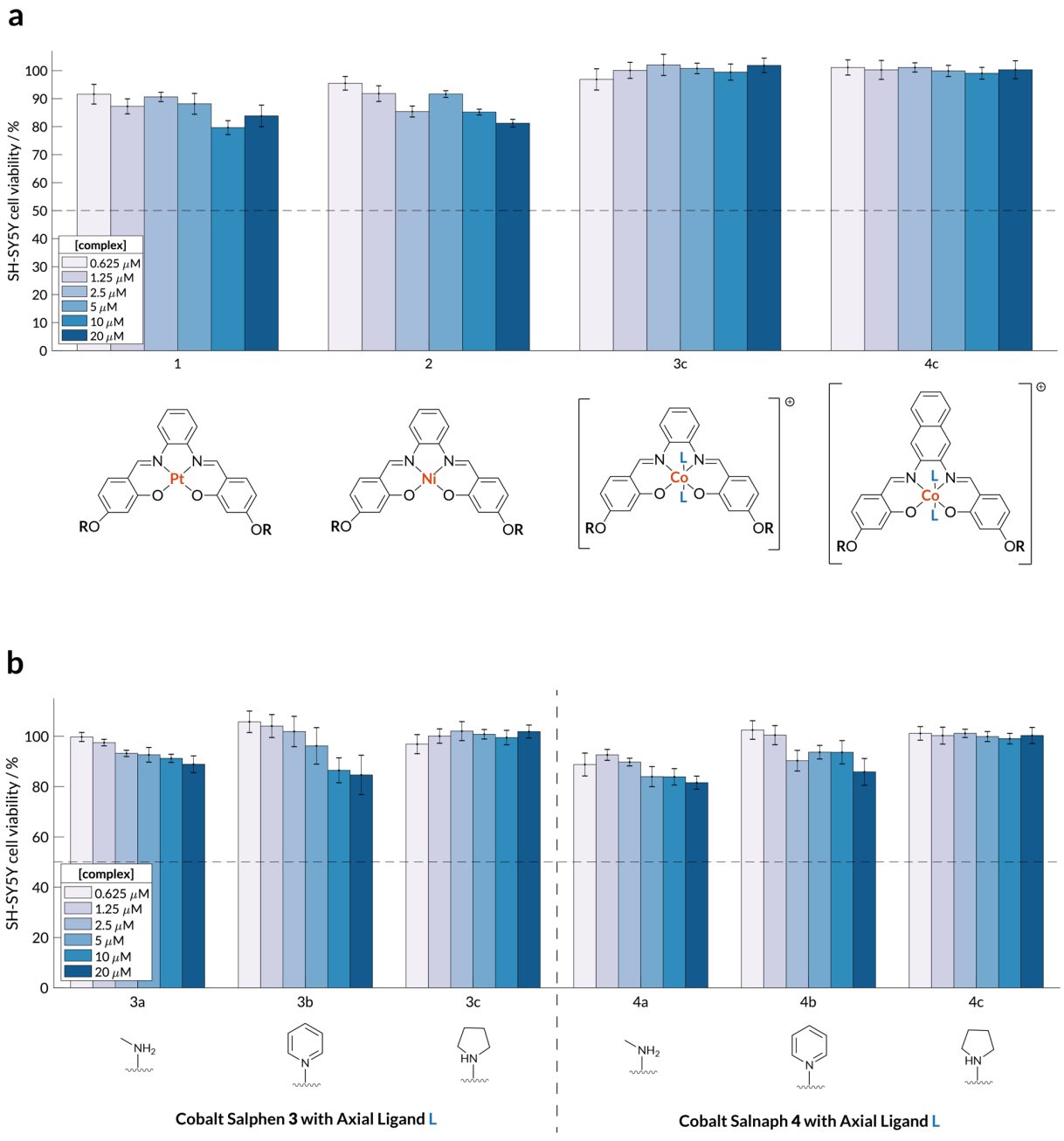


Figure 3.19: **a)** Cytotoxicity of metal complexes **1**, **2**, **3c** and **4c** against human neuroblastoma (SH-SY5Y) cells determined using the MTS assay after 24 hrs incubation at 37 °C. **b)** Minimal cytotoxic effects were observed with all octahedral cobalt complexes **3** and **4**, regardless of the axial ligand used. All data is reported as the mean ± standard deviation of three independent experiments.

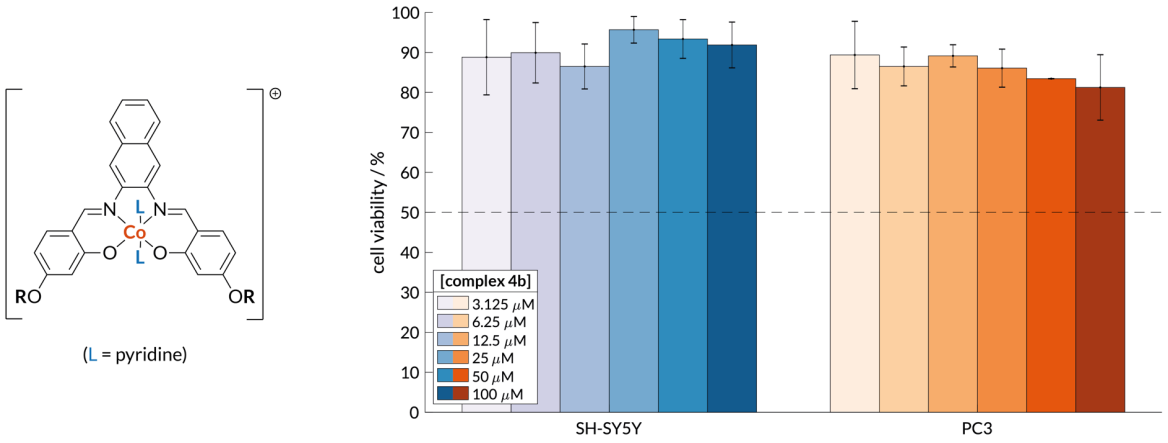


Figure 3.20: Cytotoxicity of complex **4b** against human neuroblastoma (SH-SY5Y) and prostate cancer (PC3) cells after 24 hrs incubation at 37 °C. Minimal cytotoxicity was observed in both cell lines. All data is reported as the mean ± standard deviation of three independent experiments.

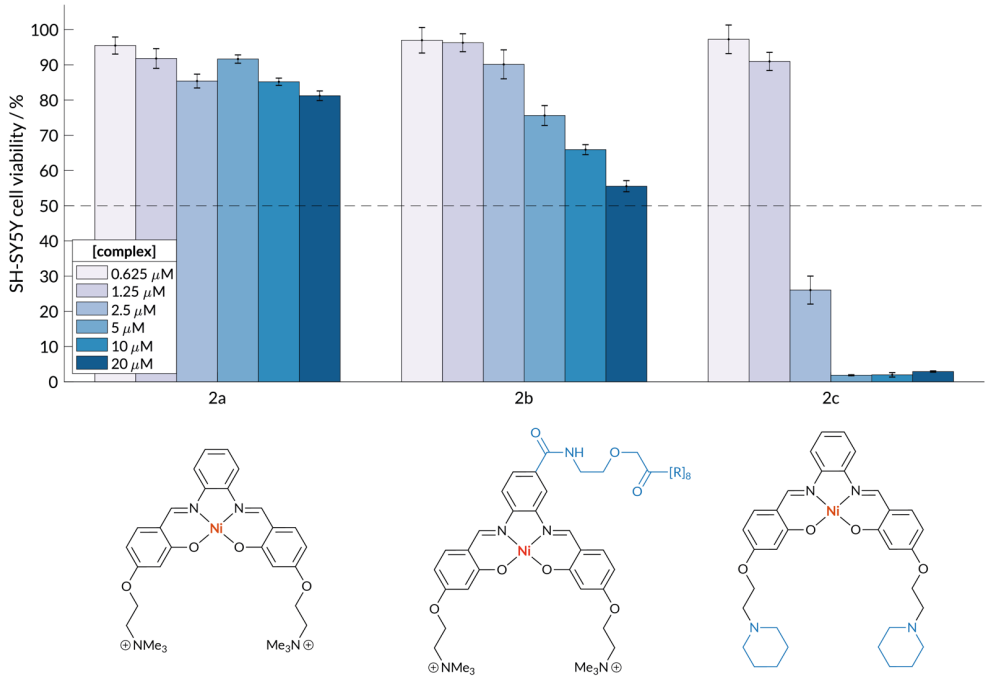


Figure 3.21: Cytotoxicity of metal complexes **2a-2c** against human neuroblastoma (SH-SY5Y) cells after 24 hrs incubation at 37 °C. Greater cytotoxicity is observed by attaching a cell-penetrating peptide to the backbone (**2b**) or changing the side-arms to piperidine (**2c**). All data is reported as the mean ± standard deviation of three independent experiments.

to assess the ability of compounds to prevent Aβ cytotoxicity. However, to date, these assays have been run using a variety of experimental conditions, with vastly different Aβ1-42 concentrations, incubation times and peptide preparation protocols being used. Krishtal *et al.* have also reported that Aβ1-42 only induces toxicity in differentiated SH-SY5Y cell cultures, despite many Aβ/SH-SY5Y neurotoxicity assays being run in undifferentiated cells.[276,278,279]

To investigate this further, we first tried to optimise the conditions required to induce Aβ cytotoxicity. Human neuroblastoma cells were treated with either fresh or aged samples of Aβ1-42, ranging in concentration from 5 µM to 15 µM. After incubating for 4-48 hrs, a MTS assay was conducted to assess cell viability. As shown in Figure 3.22, no evidence of cytotoxicity was observed with both fresh and aged Aβ at all concentrations tested. This is in line with the results obtained by Krishtal *et al.* in undifferentiated SH-SY5Y cells.[276] Due to time-constraints, we did not continue optimising this assay any further and proceeded directly to *in vivo* experiments instead (see Chapter 4 for *in vivo* results). However, in the future, the use of differentiated SH-SY5Y cells or more sophisticated *in vitro* models, such as primary rat hippocampal neurons or organotypic cultures, could allow appropriate test conditions to be identified.

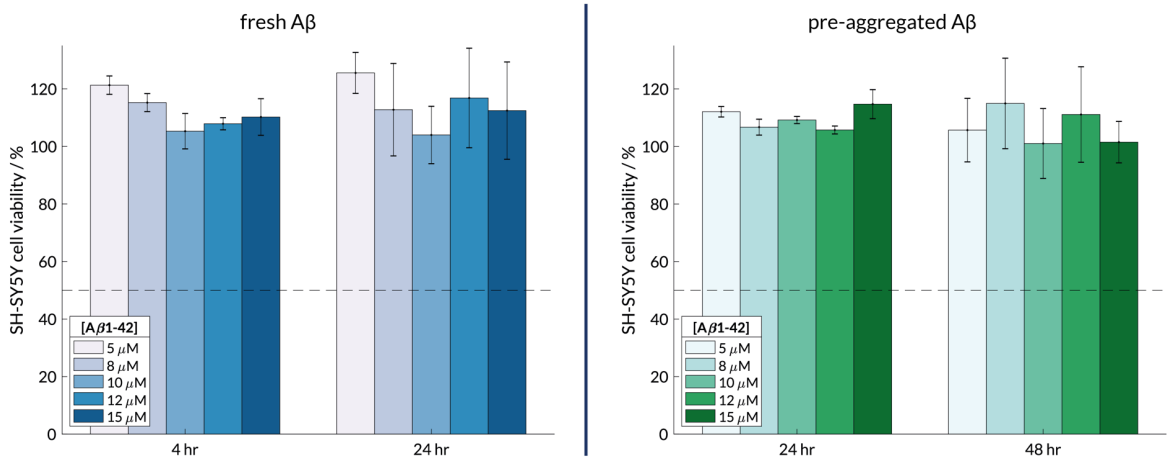


Figure 3.22: Cytotoxicity of fresh and aged Aβ1-42 against human neuroblastoma (SH-SY5Y) cells. No significant cytotoxicity is observed. All data is reported as the mean ± standard deviation of three independent experiments.

3.4 CONCLUSIONS AND FUTURE DIRECTIONS

One of the key pathological hallmarks of Alzheimer's disease is the aggregation of the Aβ peptide to form soluble oligomers and plaques. Studies have shown that the Aβ peptide has a high affinity metal binding site at its N-terminal which is able to modulate Aβ aggregation upon binding of endogenous metal ions such as Cu^{2+}. The binding of Cu^{2+} and Fe^{3+} ions to Aβ is also believed to exacerbate the progression of Alzheimer's disease by triggering the generation of reactive oxygen species and, in turn, oxidative stress. Due to this link between metal ions and Aβ toxicity, it has been hypothesised that metal complexes that are able to preferentially bind to the N-terminal metal binding site of Aβ could prove to be therapeutically useful. To date, less than fifteen metal complexes have been reported for this application, the majority of which are platinum-based complexes, and there is just one example of this approach being tested *in vivo*.[254]

In this chapter, we have sought to expand on this work by investigating a series of metal salphens and salnaphs as potential inhibitors of Aβ aggregation. These complexes were first synthesised and characterised, and their ability to suppress Aβ aggregation was assessed using the Thioflavin-T assay and transmission electron microscopy. Octahedral cobalt complexes **3** and **4** were found to outperform square planar complexes **1** and **2** due to their ability to coordinate to Aβ upon release of their axial ligands. Promisingly, these complexes were also found to show significantly higher activity than the two most well-studied complexes reported in the literature for this application.[246,249] Fluorescence spectroscopy and ^{1}H NMR experiments indicate that cobalt complexes **3** and **4** interact with Aβ *via* π-π stacking and coordination to histidines, which is in line with the observations reported by Heffern *et al.* and Iscen *et al.* on their cobalt(III) Schiff base complexes.[250,253] Inhibition of Aβ aggregation is likely to proceed through a change in Aβ conformation induced by the complexes.

Since Alzheimer's disease patients typically survive for eight to ten years after diagnosis, it is important that any proposed treatment is non-toxic towards healthy cells. To check this, we have tested all the synthesised complexes against two human cell lines and have shown that they possess minimal cytotoxicity (IC50 > 100 μM in both SH-SY5Y and PC3 cell lines). The lack of cytotoxicity observed, particularly for cobalt complexes **3** and **4**, is believed to be due to poor cell penetration. The following chapter describes preliminary *in vivo* studies carried out in 5xFAD mice with complex **4b**, the most stable cobalt complex synthesised. To our knowledge, this represents the second time that metal complexes targeted towards the N-terminal of Aβ have been investigated as potential treatments for Alzheimer's disease *in vivo*.

In terms of future work that should be carried out with complexes **1-4**, it would be useful to establish whether the complexes are able to disassemble pre-formed amyloid fibrils, in addition to preventing fibril formation from monomeric Aβ as shown here. To date, experiments studying this process have rarely been conducted as the ability of many of the commonly used assays, such as the ThT assay, to study the reverse aggregation process is questionable; for example, Moss *et al.* noted a decrease in ThT emission on the addition of nordihydroguaiaretic acid to Aβ1-40 fibrils, which would indicate fibril disassembly, but no changes in fibril size or morphology was observed using a combination of dynamic light scattering, transmission electron microscopy and size-exclusion chromatography.[282] In spite of this, a mixture of microscopy and circular dichroism experiments could allow this information to be determined. Having a better understanding of the exact effect of the investigated complexes on the Aβ aggregation pathway will help to guide future *in vivo* studies; for instance, if the complexes are shown only to be able to act on monomeric Aβ, then administering the complexes early on in the Alzheimer's disease timeline is crucial.

Moreover, whilst this work has solely focused on the ability of complexes **1-4** to inhibit Aβ aggregation, it would be interesting to investigate if the complexes are also able to prevent ROS generation induced by endogenous Cu^{2+} and Fe^{3+} ions binding to Aβ. A simple way to study this would be to use fluorescence-based methods such as the Amplex Red or 2',7'-dichlorodihydrofluorescein diacetate (DCFH-DA) assays, both of which involve the oxidation of non-fluorescent dyes to fluorescent products in the presence of ROS.[283] This is particularly important to study for complexes **2, 3** and **4** as nickel and cobalt ions have been reported to participate in ROS-generating Fenton-type reactions themselves.[284]

From a synthetic perspective, the design of complexes with higher selectivity for Aβ would be of interest. The current series of complexes are not specific for Aβ and could theoretically bind to any protein containing a similar histidine motif. This is likely to be problematic *in vivo* as the complexes will need to traverse through the bloodstream before they reach their target location. Possible approaches to circumvent this are to synthesise complexes that are only activated when they reach the brain or to encapsulate the complexes within triggerable nanoparticle carriers; for example, a number of groups have developed nanoparticle carriers, such as mesoporous silica nanoparticles, that release their cargo upon the application of ultrasound.[285] This strategy could work synergistically with the ultrasound-mediated delivery method employed in this study and limit any off-target effects.

4 ASSESSING THERAPEUTIC EFFICACY OF METAL COMPLEXES IN VIVO

4.1 BACKGROUND

As discussed in Chapter 3, limited research exists on the use of metal complexes targeted to the N-terminal of Aβ as potential therapeutic agents for Alzheimer's disease; to date, there is just one example of this therapeutic strategy being tested *in vivo* and only a handful of complexes that have been tested *in vitro*.[246,249,250,252–254] In spite of the promising *in vitro* data obtained by Heffen *et al.* and Iscen *et al.* with their octahedral cobalt(III) Schiff base complexes, octahedral cobalt complexes have never been investigated *in vivo* for the treatment of Alzheimer's disease.[250,253]

4.1.1 The Effects of Focused Ultrasound on Alzheimer's Disease Pathology

As of now, almost all of the metal complexes that have been developed to inhibit Aβ aggregation by binding to the Aβ N-terminal have molecular weights greater than 400 Da. Due to their size, these complexes are likely to show poor penetration across the BBB, preventing *in vivo* studies from being easily carried out.[48] As discussed in Chapter 2, focused ultrasound and microbubbles can be used to non-invasively deliver small molecules, antibodies and nanoparticles across the BBB *in vivo*, making it an attractive tool for the treatment of brain diseases such as Alzheimer's disease. In 2010, Jordão *et al.* delivered anti-Aβ antibodies into the brains of Alzheimer's disease mice using focused ultrasound and microbubbles and observed a significant reduction in Aβ pathology just four days after a single treatment.[286–288]

Interestingly, therapeutic effects have also been observed from the use of focused ultrasound and microbubbles in the absence of therapeutic agents: a follow-up study conducted by Jordão *et al.* showed that focused ultrasound-mediated BBB opening facilitates the entry of endogenous antibodies into the brain, such as immunoglobulin G (IgG) and immunoglobulin M (IgM).[288] In Alzheimer's disease mice treated with focused ultrasound and microbubbles, IgG and IgM were found to be co-localised with Aβ plaques in the brain.[288] As a consequence, these endogenous antibodies were proposed to play a role in reducing Aβ plaque burden by promoting the clearance of Aβ from the brain.[288] Increased Aβ clearance due to the action of antibodies has been reported to occur *via* a number of mechanisms, including increasing the levels of soluble Aβ, antibody-mediated phagocytosis and enhanced microglial phagocytosis.[192,289,290]

In line with these hypotheses, focused ultrasound-mediated BBB opening has been observed to lead to the transient activation of glial cells such as microglia and astrocytes, both of which have been reported to play central roles in the clearance and degradation of Aβ.[288,291,292] There exists a number of mechanisms by which glial cells are believed to contribute towards Aβ clearance: 1) Aβ can be directly internalised by glial cells *via* pinocytosis, phagocytosis or receptor-mediated endocytosis and then degraded, 2) glial cells secrete proteases (*e.g.* metalloendopeptidases) and extracellular chaperones (*e.g.* apolipoproteins E and J) that are able to degrade Aβ and 3) astrocytes possess projections that wrap around cerebral blood vessels and have been proposed to play a role in the removal of Aβ and waste products from the brain *via* the glymphatic clearance pathway.[204,293–295] Higher levels of Aβ have been detected within glial cells after focused ultrasound-mediated BBB opening, suggesting that this technique can indeed promote the internalisation and clearance of Aβ from the brain.[288,292,296] Promisingly, it has been reported that treatment with focused ultrasound and microbubbles alone can not only reduce the Aβ plaque burden and plaque size in Alzheimer's disease mice, but it can also restore memory function.[292,297] These effects were not observed when focused ultrasound was used in the absence of microbubbles, implying that BBB opening is necessary for these anti-Aβ effects to occur.[298] It follows that the glial cell activation induced by ultrasound-mediated BBB opening is likely to be a consequence of disrupting the structural integrity of the BBB and/or allowing increased levels of endogenous antibodies to enter the brain.[288]

Recent evidence has suggested that the application of focused ultrasound and microbubbles can affect the tau pathway as well, with Pandit *et al.* observing a significant reduction in both early- and late-stage hyperphosphorylated tau in Alzheimer's disease mice treated with ultrasound.[299] The reduction in hyperphosphorylated tau seen after focused ultrasound-mediated BBB opening was associated with an increased clearance of tau through neuronal autophagy.[299] Similar to the studies conducted by Leinenga *et al.*, improvements in both motor and memory function in Alzheimer's disease mice were observed after ultrasound treatment.[299]

All of these studies highlight that focused ultrasound-mediated BBB opening can not only be used to non-invasively deliver therapeutic agents to the brain for the treatment of Alzheimer's disease, but it may also provide additional therapeutic effects itself; for example, Hsu *et al.* recently used focused ultrasound-mediated BBB opening to deliver an inhibitor of glycogen synthase kinase 3 (GSK-3; a protein kinase known to play a key role in modulating γ-secretase activity and thus, Aβ production) to the brain and observed an additive effect, in which the observed reduction in Aβ plaque burden in the brain (40%) was greater than with focused ultrasound (15%) or GSK-3 inhibitor (23%) treatment alone.[300,301] The use of focused ultrasound-mediated delivery methods in Alzheimer's disease treatment is therefore an attractive

therapeutic strategy and could work synergistically to enhance the action of administered therapeutic agents.

4.2 AIMS AND OBJECTIVES

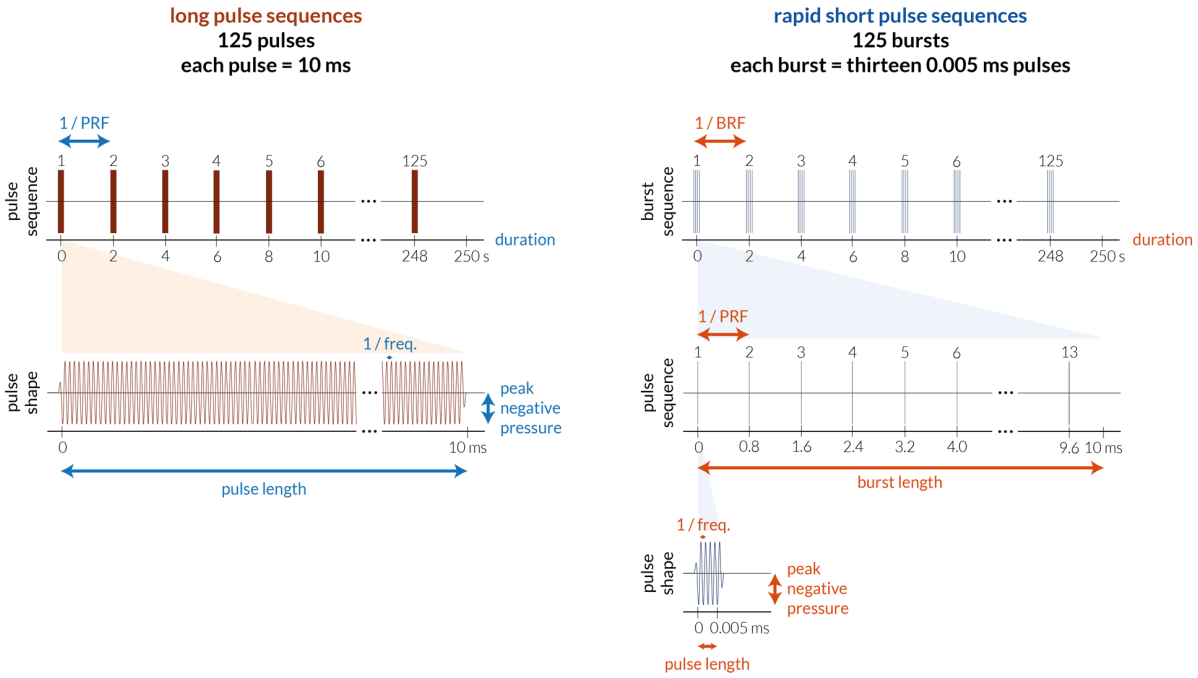
The overall aim of the studies presented in this chapter was to investigate the therapeutic efficacy of the metal complexes described in Chapter 3 in an Alzheimer's disease mouse model. To achieve this aim, the following objectives had to be fulfilled:

- Optimise the parameters used for ultrasound-mediated drug delivery to improve the safety and efficiency of the technique.
- Show that the synthesised metal complexes can be delivered across the BBB using focused ultrasound and microbubbles.
- Investigate the toxicity of delivering the complexes across the BBB using ultrasound over an extended period of time *in vivo*.
- Conduct a preliminary efficacy study with the complexes in an Alzheimer's disease mouse model.
- Determine any effects of the complexes on Aβ burden in the brain using histological methods such as immunohistochemistry.

4.3 RESULTS AND DISCUSSION

4.3.1 Improving Ultrasound-Mediated BBB Opening

Ultrasound sequences used for BBB opening typically consist of a series of long millisecond pulses emitted at low pulse repetition frequencies (~Hz), such as those employed in the nanoparticle work presented in Chapter 2. These types of ultrasound sequences will be referred to here as 'long pulse sequences' (Figure 4.1). Whilst it has been demonstrated that long pulse sequences combined with microbubbles can be used to deliver a wide range of small molecules, antibodies and nanoparticles across the BBB *in vivo*, they have been associated with adverse side-effects such as red blood cell extravasation, microvascular rupture and heterogeneous drug delivery in the targeted region.[87,96,97] *In vitro* studies investigating this observation have shown that long pulse sequences act to promote microbubble clustering and fast mi-



	peak negative pressure	frequency	pulse length	pulse repetition frequency	burst length	burst repetition frequency	duration
long pulses	350 kPa	1 MHz	10 ms	0.5 Hz	-	-	250 s
RaSP			0.005 ms	1.25 kHz	10 ms	0.5 Hz	

Figure 4.1: Long pulse and rapid short pulse (RaSP) sequences. Figure adapted from reference *[86]*.

crobubble destruction.[302–304] In an *in vivo* scenario, this could lead to varying microbubble activity within the ultrasound beam and result in heterogeneous BBB opening being induced along the vessels.

To improve the safety and efficiency of ultrasound-mediated drug delivery to the brain, we have designed a new pulse sequence called **ra**pid **s**hort **p**ulse (RaSP) sequence, which consists of a series of short microsecond pulses separated by microsecond off-times (Figure 4.1). By switching to a series of short pulses and introducing periods of off-times, it was hypothesised that the microbubbles would be able to move freely along the blood vessels in between consecutive pulses, reducing the likelihood of microbubble clustering and destruction. This was supported by *in vitro* experiments performed by Dr. A. Pouliopoulos (PhD student, NSB Lab), in which enhanced microbubble mobility and microbubble lifetime were observed when RaSP sequences were used.[303,304]

To investigate whether we could achieve safer and more efficient BBB opening with RaSP sequences *in vivo*, a Texas Red-labelled 3 kDa dextran was delivered across the BBB in C57BL/6J mice using long

pulse or RaSP sequences (n = 5 for each sequence; ultrasound parameters used are shown in Figure 4.1). Fluorescence images of the brain sections were analysed to evaluate the dose and distribution of the delivered dextran. The former was determined by calculating the normalised optical density (NOD), the average fluorescence intensity in the targeted region normalised by the control region, whilst the latter was determined by calculating the coefficient of variation (COV), the ratio of the standard deviation to the mean fluorescence pixel intensity in the targeted region. All animal experiments in this section were conducted with S. Morse, Dr. A. Pouliopoulos, M. Copping and J. Lin (PhD and MRes students, NSB Lab) and all quantitative analysis was done by S. Morse. A full discussion of the RaSP study can be found in reference *[86]*.

As shown in Figure 4.2, the use of RaSP sequences was able to deliver the 3 kDa dextran across the BBB in a more uniform manner than that observed when using long pulse sequences; in fact, with the long pulse sequences, the delivered dextran was found to accumulate in and around blood vessels, whilst with RaSP sequences, homogeneous distribution of the dextran throughout the brain parenchyma was seen.[86] No significant difference in the NOD was detected between the two pulse sequences, indicating that despite the improved distribution observed using RaSP sequences, the dose of dextran delivered to the brain was similar. Using immunohistochemistry, we have shown that the use of RaSP sequences also results in significantly less extravasation of serum albumin from the blood vessels, which has been linked to neurotoxicity.[86,305,306] Furthermore, no signs of tissue damage in the sonicated regions were observed when using RaSP sequences, whilst sites of red blood cell extravasation and microvacuolations were detected when long pulse sequences were used.[86] The use of RaSP sequences therefore allows for safer and more efficient ultrasound-mediated drug delivery to the brain.

To determine the length of time that the BBB remains disrupted with both long pulse and RaSP sequences, a Texas Red-labelled 3 kDa dextran was injected 0, 10 or 20 mins after ultrasound exposure in C57BL/6J mice (for t = 0 mins, n = 5; for t = 10 or 20 mins, n = 3). With RaSP, the BBB permeability was found to return back to its normal level within 10 mins, whilst increased BBB permeability was still observed at 20 mins after ultrasound exposure when long pulse sequences were used (Figure 4.3).[86] This is in agreement with prior reports of the BBB remaining open for 4 to 48 hrs when analogous long pulse sequences were used.[90,307] The shorter duration of BBB opening induced with RaSP sequences should reduce the risk of other blood-borne substances from entering the brain and thus, result in increased safety. As the use of RaSP sequences appears to result in safer and more efficient BBB opening than the use of conventional long pulse sequences, RaSP sequences were used for all subsequent ultrasound experiments reported in this chapter to reduce the likelihood of tissue damage.

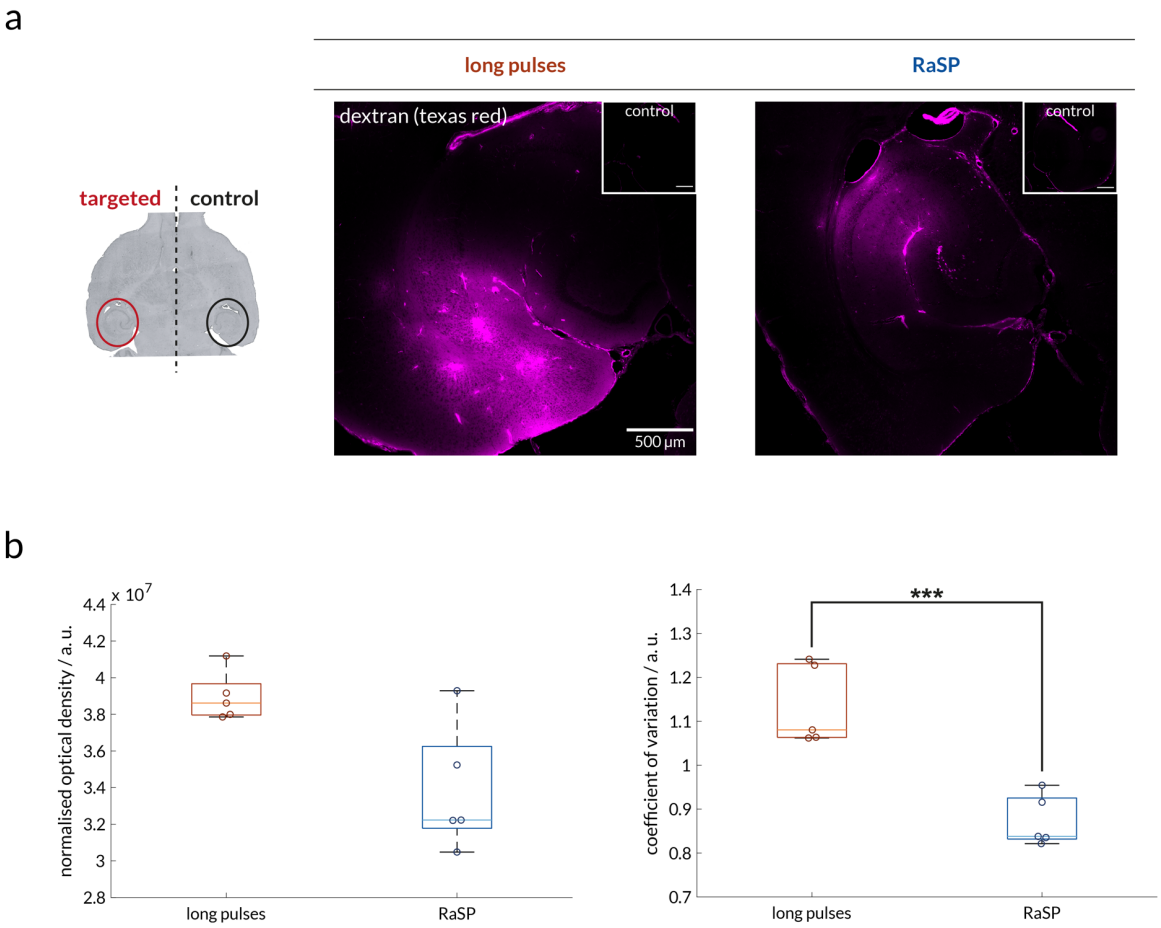


Figure 4.2: **a)** Representative fluorescence microscopy images obtained after delivering a Texas Red-labelled 3 kDa dextran across the BBB to the left hippocampus using long pulse and RaSP sequences. No evidence of delivery is observed in the right hippocampus (non-sonicated control; insets) in all experiments. **b)** Calculated normalised optical density (NOD; a measure of the dose delivered) and coefficient of variation (COV; a measure of the distribution heterogeneity). No difference in the NOD was observed, but there was a significant difference in the COV (n = 5 for each pulse sequence; $p < 0.001$). All quantitative analysis was conducted by S. Morse (PhD student, NSB Lab).

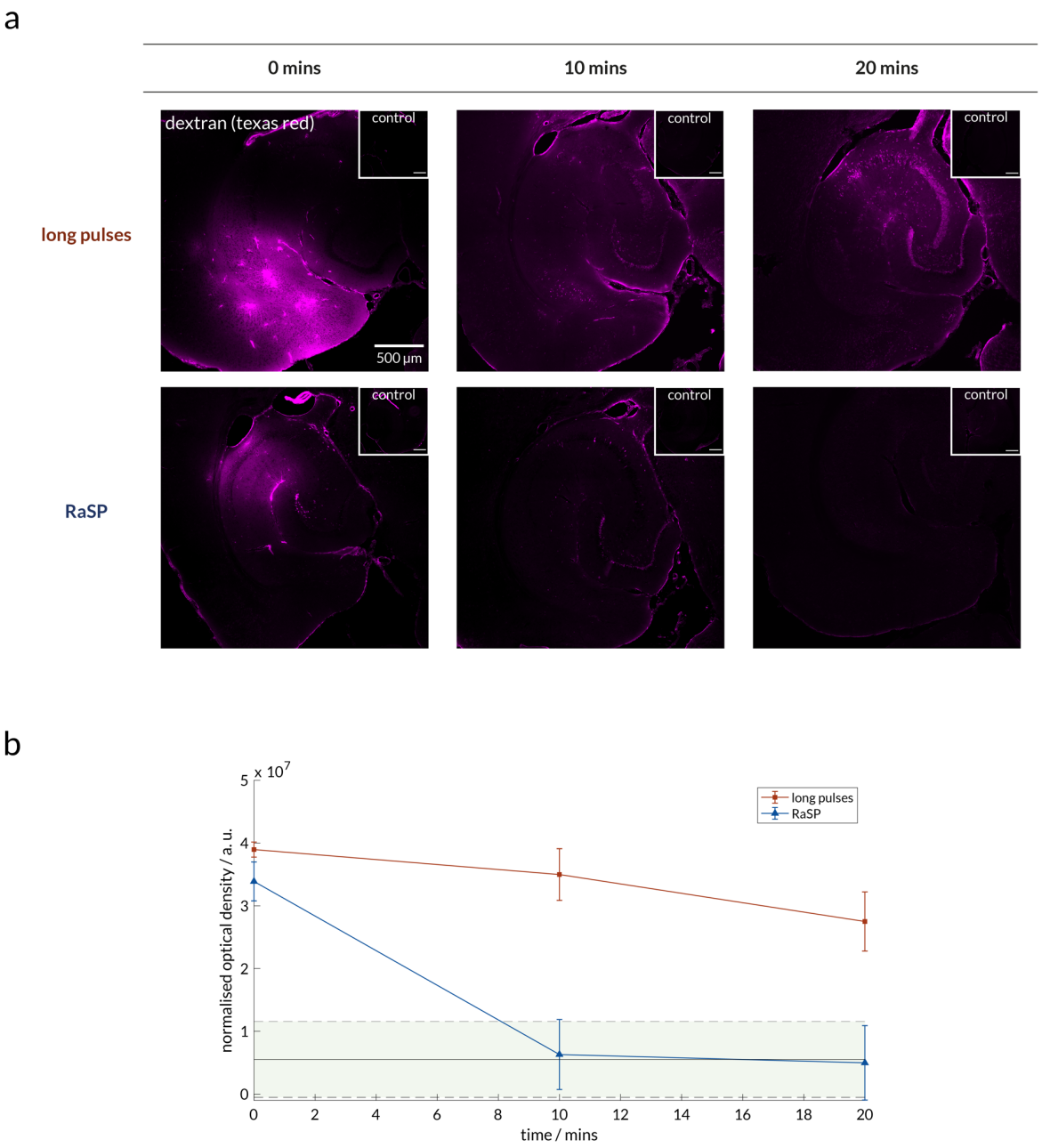


Figure 4.3: **a)** Representative fluorescence microscopy images of the left hippocampus obtained after injecting a Texas Red-labelled 3 kDa dextran 0, 10 or 20 mins after ultrasound-mediated BBB opening using long pulse and RaSP sequences. No evidence of the 3 kDa dextran is seen in the right hippocampus (non-sonicated control; insets) at all time-points. **b)** Calculated normalised optical density at all time-points (n = 3 for each time-point). With RaSP sequences, the BBB closes within 10 mins. The shaded region is the mean normalised optical density ± standard deviation of control non-sonicated mice (n = 3). All quantitative analysis was conducted by S. Morse (PhD student, NSB Lab).

4.3.2 Delivering Metal Salphens and Salnaphs across the BBB using Ultrasound

To date, the detection of small molecules or NPs that have been delivered across the BBB using focused ultrasound *in vivo* has been done *via* fluorescence- or MRI-based methods.[85,86,100,308] With the exception of platinum salphen **1**, our metal salphens and salnaphs are not intrinsically fluorescent and are not MRI-active. Whilst complexes **2-4** could be detected by conjugating a fluorescent or MRI-active tag to their structures, this has the potential to change their interaction with Aβ; for instance, many fluorophores are composed of aromatic, planar scaffolds, which could result in additional π-π stacking interactions with Aβ. Alternatively, the addition of a bulky fluorescent or MRI tag could prevent the complexes from interacting efficiently with the Aβ N-terminal binding site and reduce their activity. As a consequence of this, an alternative method of detection was employed in this work, which takes advantage of the presence of metal centres in all of the synthesised compounds: laser ablation inductively-coupled plasma mass spectrometry (LA-ICP-MS). LA-ICP-MS is a method used for the elemental analysis of solid samples.[309] A solid sample is first placed into an ablation cell, where it is ablated and vaporised by a pulsed laser. The aerosol generated is transferred into an inductively-coupled plasma source and the ions formed are analysed in a mass spectrometer. Ablation across the sample allows 2D element distribution maps to be produced.

As a proof-of-concept, platinum complex **1** was delivered across the BBB to the left hippocampus using focused ultrasound in C57BL/6J mice (RaSP; frequency: 1 MHz, peak negative pressure: 350 kPa, pulse length: 0.005 ms, PRF: 1.25 kHz, burst length: 10 ms, BRF: 0.5 Hz, sonication duration: 250 s). Complex **1** is weakly emissive at 580 nm when excited at 445 nm; thus, in an attempt to locate the site of BBB opening prior to LA-ICP-MS analysis, brain sections were imaged on a fluorescence microscope using a GFP filter set (excitation wavelength: 470 nm, excitation filter: 470/40 nm, emission filter: 525/50 nm). A representative fluorescence image that was obtained is shown in Appendix: Figure 9.9, in which little evidence of the presence of complex **1** in the brain was observed. This result is most likely due to the weak emission properties of complex **1** as clear evidence of its presence in the brain was obtained when the same sections were analysed *via* LA-ICP-MS.

All LA-ICP-MS runs were conducted with Mr. B. Sampson (Imperial College London). Brain samples were sectioned into 30 µm sections and ablated using a spot size of 65 µm. Figure 4.4 shows a representative Pt195 distribution map obtained from an experiment in which the ultrasound-mediated delivery of complex **1** across the BBB was attempted. Element distribution maps were plotted using MATLAB and the Pt195 map was overlaid on the P31 map for clarity. Clear Pt195 signal, which corresponds to complex **1**, was observed in the left hippocampus, whilst no signal was observed in the right hippocampus. This

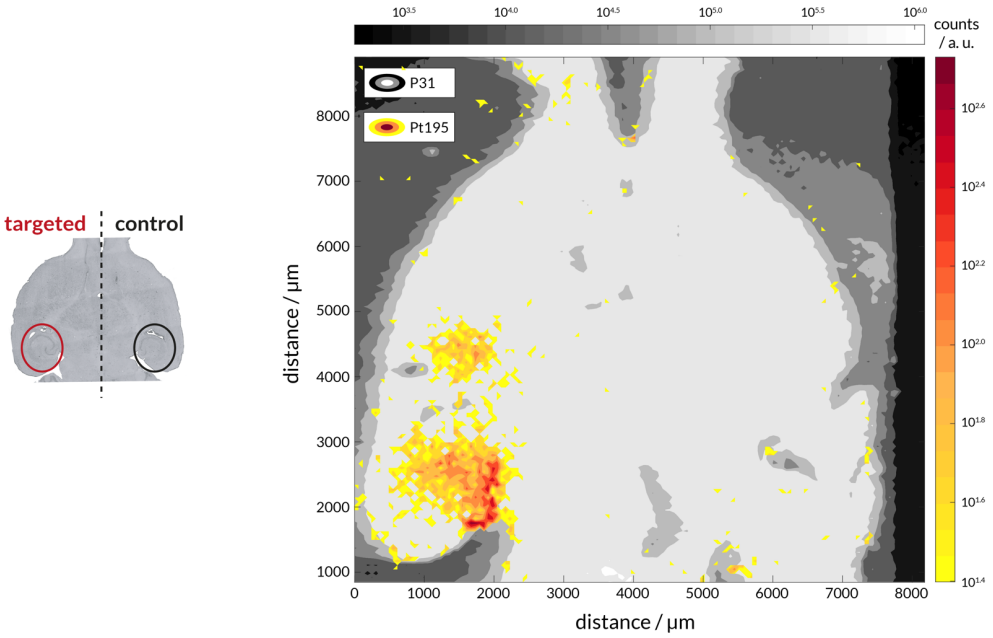


Figure 4.4: Successful delivery of platinum salphen **1** across the BBB to the left hippocampus. Element distribution map for Pt195 (yellow/red) is overlaid on P31 map (grey; provides brain outline) for clarity. No evidence of complex **1** is detected in the right hippocampus (control), indicating that it does not cross the BBB by itself. LA-ICP-MS experiments were run with Mr. B. Sampson (Imperial College London).

shows that complex **1** does not cross the BBB by itself, but it can be delivered into the brain using focused ultrasound and microbubbles.

To determine whether we could use the same ultrasound parameters to deliver cobalt complexes **3** and **4** across the BBB, the same protocols as above were used, with the exception that a Texas Red-labelled 3 kDa dextran was co-injected with complex **4c** to allow for easy identification of the site of BBB opening. Due to the difference in size between the 3 kDa dextran and complexes **3** and **4** (~300 to 400 Da), experimental conditions that are able to deliver the 3 kDa dextran to the brain should also result in successful delivery of our complexes. Brain sections obtained from the co-delivery of Texas Red-labelled 3 kDa dextran and complex **4c** were first imaged in the Texas Red channel to identify the presence of BBB opening. Sections positive for BBB opening were then analysed using LA-ICP-MS. The detection of cobalt complexes **3** and **4** in the brain using LA-ICP-MS is more challenging than for complex **1** as brain tissue itself contains trace concentrations of cobalt.[310] Nevertheless, as shown in Figure 4.5, good agreement is observed between the optical image (corresponding to the 3 kDa dextran) and Co59 distribution map (corresponding to complex **4c**), indicating that both the 3 kDa dextran and complex **4c** can be delivered across the BBB under the ultrasound parameters used. The lack of signal observed in the right hippocampus regions in both images indicates that neither molecule is able to cross the BBB by itself.

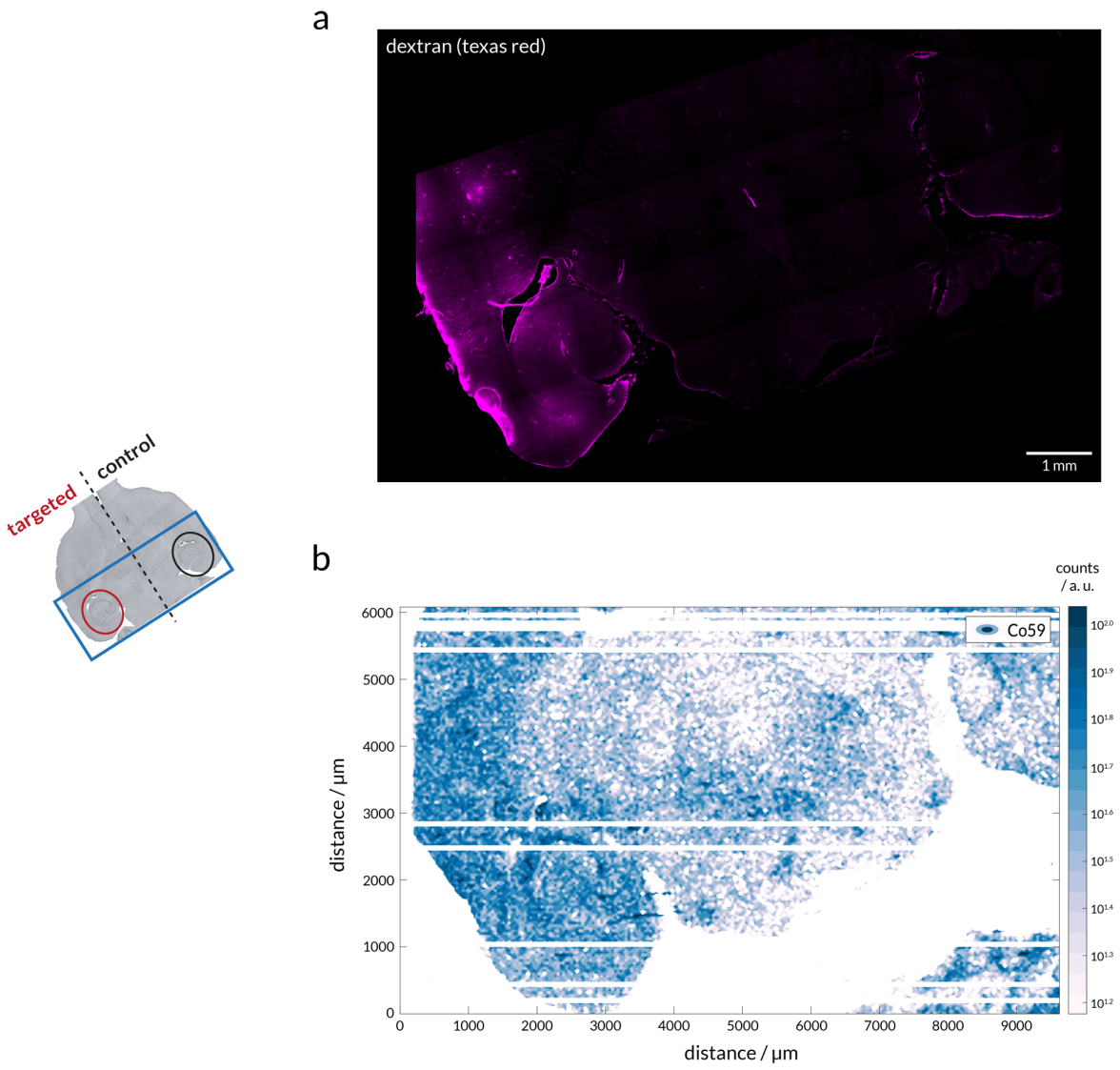


Figure 4.5: **a)** Fluorescence microscopy image of successful ultrasound-mediated BBB opening in the left hippocampus, detected by co-injecting a Texas Red-labelled 3 kDa dextran (purple). **b)** Element distribution map for Co59 obtained after delivering cobalt complex **4c** across the BBB to the left hippocampus using ultrasound. Missing lines are due to a software malfunction that took place during the LA-ICP-MS run. LA-ICP-MS runs were conducted with Mr. B. Sampson (Imperial College London).

4.3.3 Safety of Repeated Treatments

Patients with Alzheimer's disease typically live for eight to ten years after diagnosis and any potential treatment is therefore likely to be required over an extended period of time.[170] Consequently, we began by investigating the safety of delivering our cobalt complexes across the BBB using ultrasound over a five week period in wild type C57BL/6J mice before moving to studies in disease models. As discussed in Chapter 3, the difference in inhibitory activity against Aβ aggregation between complexes **3a** to **3e** and **4a** to **4e** was found to be minimal; thus, for these initial preliminary studies, cobalt salnaph **4b** was used as it is the most stable in aqueous solution and is therefore easiest to handle for *in vivo* applications. The treatment schedule followed is shown in Figure 4.6. Briefly, wild type C57BL/6J mice were treated once a week for four weeks at a complex **4b** concentration of 30 mg/kg or 23 mg/kg (n = 2 for each complex **4b** dose). The body weight and behaviour of the mice were closely monitored over a five week period. At the end-point of the study, brains were stained with H&E following the same protocols as those described in Chapter 2 in order to check for any signs of tissue damage on a microscopic level.

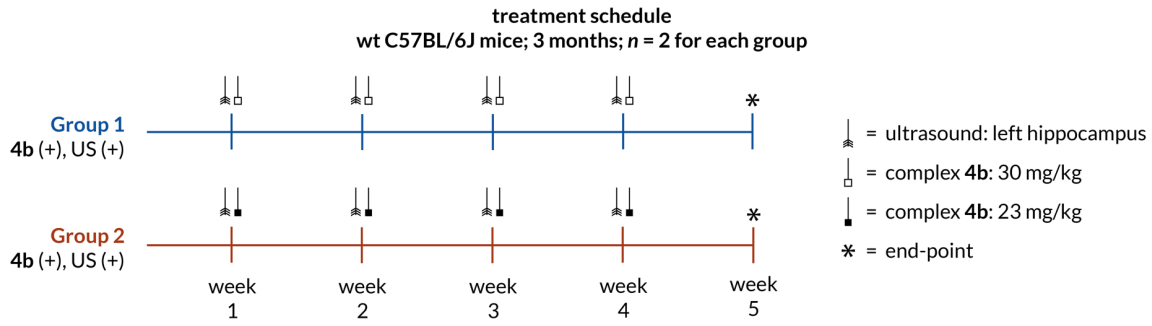


Figure 4.6: Summary of treatment schedule and treatment conditions. Wild type C57BL/6J mice were treated with ultrasound (US) and complex **4b** at either 30 mg/kg or 23 mg/kg once a week for four weeks (n = 2 for each group). Body weight and behaviour were monitored every week in accordance with Home Office regulations and institutional guidelines.

As shown in Figure 4.7, no adverse changes in body weight were observed from weekly ultrasound + complex **4b** treatments at either 30 mg/kg or 20 mg/kg dosages over a five week period. In addition to this, no behavioural changes were detected, suggesting that this treatment paradigm was well-tolerated. No signs of tissue damage in H&E-stained sections were observed, which is in line with our previous studies using RaSP sequences to disrupt the BBB.[86]

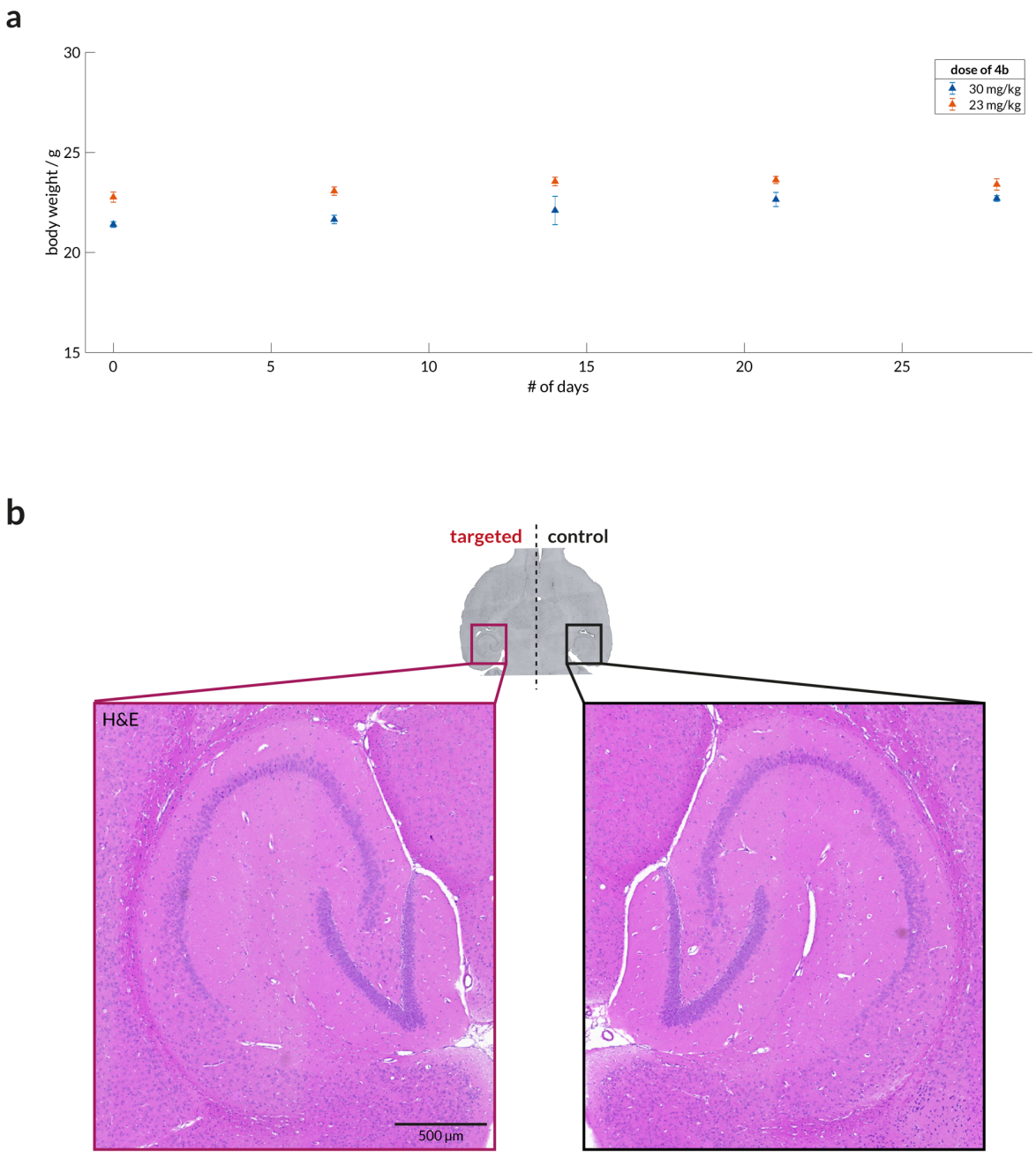


Figure 4.7: **a)** No signs of weight loss were observed when complex **4b** (30 mg/kg or 23 mg/kg; *n* = 2 for each dose) was delivered across the BBB in C57BL/6J mice. Treatment was conducted on days 0, 7, 14 and 21. **b)** Representative example of H&E staining. No differences were observed between the targeted and control regions.

Due to time constraints, a 30 mg/kg dose of complex **4b** administered on a weekly basis was used for all subsequent animal studies. However, a wider concentration range for complex **4b**, as well as different treatment times and frequencies, should be tested in the future as this could lead to improved efficacy. Ideally, these studies should also be repeated in relevant mouse models of disease.

4.3.4 Assessing Efficacy in an Alzheimer's Disease Mouse Model

To assess the therapeutic efficacy of cobalt complex **4b** *in vivo*, a series of experiments were conducted in 5xFAD mice kindly supplied by Dr. M. Sastre (Imperial College London). The 5xFAD mouse model is a transgenic mouse model of Alzheimer's disease that expresses mutant human amyloid precursor protein (APP) and presenilin 1 (PSEN1), both of which are key proteins in the Aβ pathway.[311] It contains a total of five Alzheimer's disease-associated mutations: K670N/M671L (Swedish), I716V (Florida), V717I (London) mutations in APP and M146L and L286V mutations in PSEN1.[311] 5xFAD mice show age-dependent amyloid plaque formation in the hippocampus, cortex, thalamus and spinal cord regions, making them useful models of amyloid pathology.[311]

In this preliminary study, a total of n = 9 transgenic 5xFAD mice were used, split into three treatment groups (Figure 4.8): no treatment (Group 1), ultrasound only (Group 2) and ultrasound + complex **4b** (Group 3). As a starting point, all mice were treated on a weekly basis for a period of three weeks and ultrasound was focused solely on the left hippocampus where applied. This treatment frequency and study length was chosen based on the 'safe' treatment paradigm established in the previous section, though future studies will need to optimise this. Following the end-point of the study, the amyloid burden in the brain was compared between treatment groups using histological and immunohistochemical methods.

Staining for Amyloid Beta: Thioflavin-S and MOAB-2

To stain for Aβ in the brain post-mortem, two different stains were used: thioflavin-S (ThS) and anti-beta amyloid antibody (MOAB-2). ThS is a derivative of ThT used in the *in vitro* assays presented in Chapter 3 and stains for the presence of Aβ fibrils.[312,313] ThS has been widely used for staining Aβ in cell culture and in tissues, whilst ThT is mainly used for *in vitro* detection of Aβ. The reason for this choice appears to be historic. ThS staining of tissue sections is simple to perform and involves incubating the sections in a 1% (w/v) solution of ThS. Sections are then imaged in the Alexa Fluor 488 channel, with any Aβ fibrils appearing as bright dots (Figure 4.9).

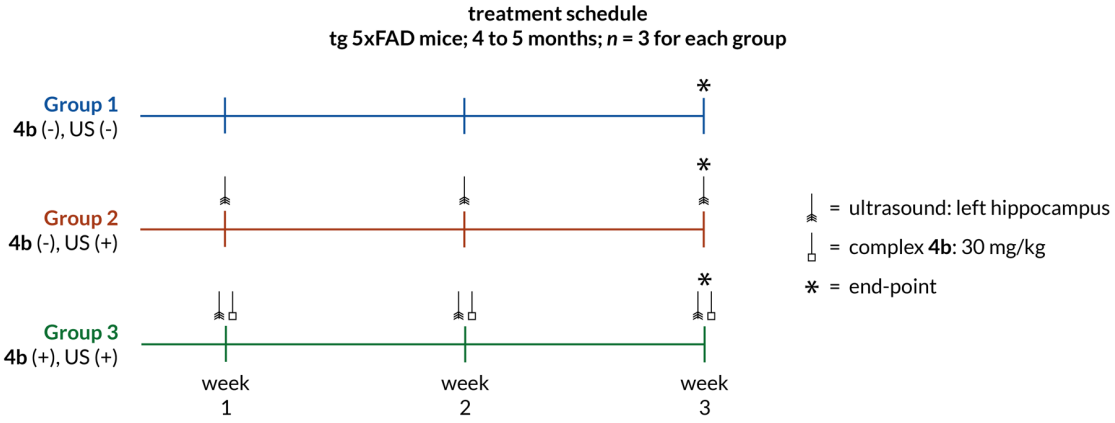


Figure 4.8: Summary of treatment schedule and treatment conditions. A total of *n* = 9 transgenic 5xFAD mice were used in this study, *n* = 3 mice per group. Group 1 received no treatment, Group 2 received only ultrasound treatment and Group 3 received both complex **4b** and ultrasound treatment. The dose of cobalt complex **4b** used was 30 mg/kg.

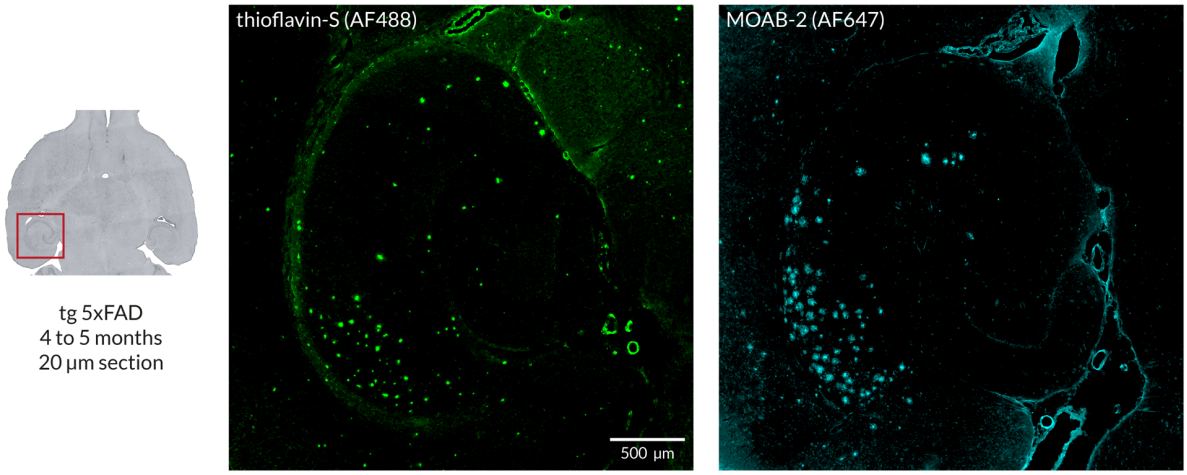


Figure 4.9: Examples of successful Thioflavin-S (green) and MOAB-2 (cyan) staining in transgenic 5xFAD mice. Thioflavin-S is a dye which stains for Aβ fibrils, whilst MOAB-2 is an antibody which stains for all forms of Aβ. The left hippocampal region is shown in both images.

In contrast to ThS, MOAB-2 is an antibody which stains for all forms of Aβ, including unaggregated, oligomeric and fibrillar Aβ.[313] Immunohistochemical staining methods are either direct or indirect (Figure 4.10). The former method involves the use of a single labelled antibody that binds to the antigen of interest and is itself detected. In contrast, the latter method involves the use of two antibodies: a primary antibody (1° Ab) that binds to the antigen of interest and a labelled secondary antibody (2° Ab) that binds to the primary antibody. The secondary antibody is always raised in a different host species to the species in which the primary antibody was raised in order to minimise non-specific staining. Whilst indirect immunohistochemical methods are more technically challenging to perform, they are more widely used as they are more sensitive than direct methods. This is because multiple secondary antibodies are able to bind to a single primary antibody, leading to an amplification of the resulting signal.[314] As a consequence, we decided to follow indirect immunofluorescence staining protocols in this study and employed a combination of mouse MOAB-2 (1° Ab), followed by goat anti-mouse IgG Alexa Fluor 647 (2° Ab).

A typical workflow for indirect immunofluorescence staining is shown in Figure 4.10. The tissue sections are first fixed with a fixative such as 4% paraformaldehyde in order to preserve cellular structure and immobilise the antigens.[314] If detecting intracellular targets, the tissue is then permeabilised with a dilute solution of Triton-X, a detergent which acts to solubilise the cellular membrane so that the primary antibody is able to access the cell interior. Next, the tissue is blocked to prevent non-specific binding of the primary antibody. The inclusion of a blocking step is crucial in order to achieve a high signal-to-noise ratio and involves incubating the sample in an appropriate blocking buffer.[314] Blocking buffers usually consist of normal serum from the species in which the secondary antibody was raised and/or bovine serum albumin, both of which contain antibodies that will bind to non-specific epitopes in the sample. When applied in a large excess, these serum antibodies should be able to outcompete the primary antibody for any non-specific binding sites, resulting in an improved signal-to-noise ratio. If normal serum is used, it should not be from the species in which the primary antibody was raised as this will be recognised by the secondary antibody and thus, lead to higher background staining.

Following blocking, the primary antibody is applied to the section at an appropriate dilution and incubated: for all primary antibodies used in this study, an overnight incubation was used based on the manufacturer's instructions. After thorough washing, the secondary antibody can then be applied. To minimise any interference from brain autofluorescence, which is typically found in the GFP channel, a far red Alexa Fluor 647-labelled secondary antibody was used in all immunofluorescence staining reported in this section. Stained sections can be imaged on a fluorescence microscope using an appropriate filter set. Figure 4.9 shows a representative image of positive MOAB-2 staining in a transgenic 5xFAD mouse, in which the presence of Aβ in the brain is clearly observed as bright dots.

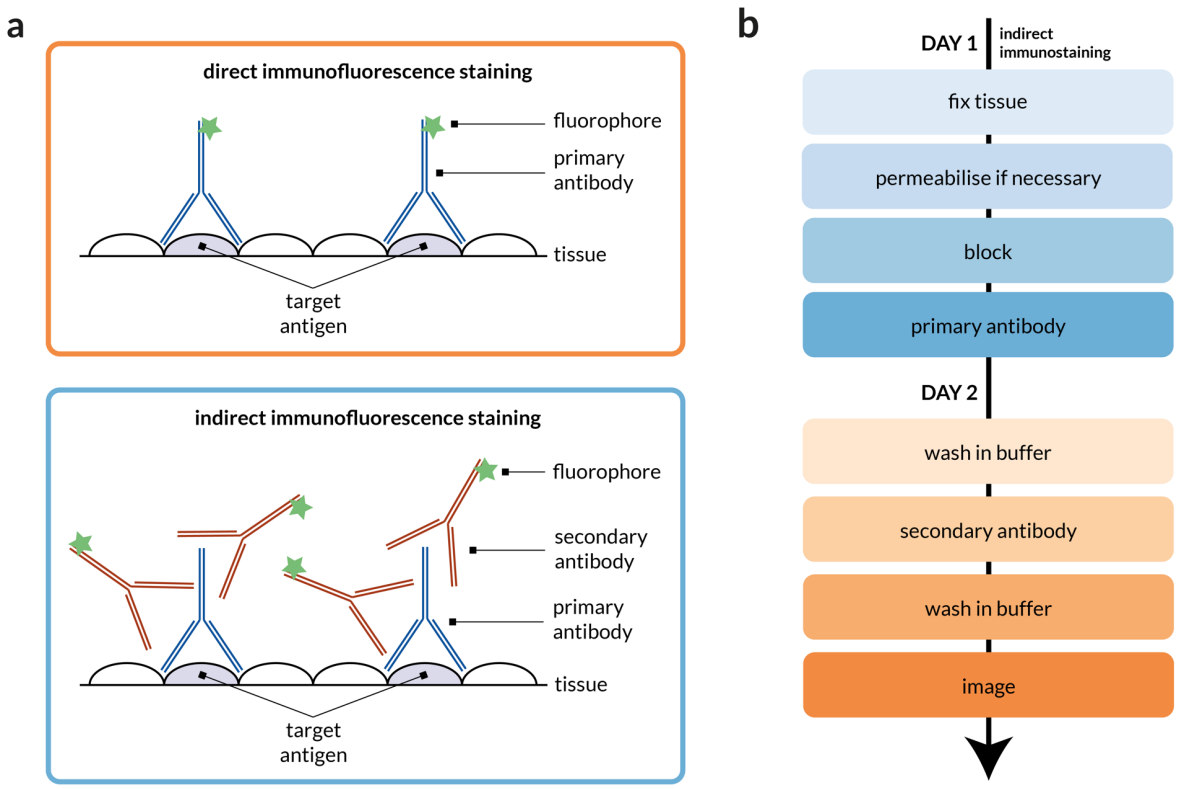


Figure 4.10: **a)** Direct and indirect immunofluorescence staining methods, redrawn from *[313]*. Only one antibody is used in direct methods, whilst two are used in indirect methods. Indirect methods are more complicated to perform, but they are more sensitive than direct methods. **b)** General steps involved in indirect immunohistochemical staining.

Sample Processing Workflow

With our focused ultrasound setup and experimental conditions, we do not typically see BBB opening throughout the entire brain. As a consequence, we first had to locate the exact site of BBB opening in all ultrasound-treated brains (Groups 2 and 3) to allow proper comparison between the treatment groups. We have shown in prior work that minor extravasation of serum albumin from the blood vessels can be observed at t = 0 with the RaSP ultrasound sequences used in this study; albumin staining can therefore be used to detect the site of BBB opening.[86] For each of the ultrasound-treated brains, five sections spanning the hippocampal region were stained for serum albumin using indirect immunofluorescence methods (1° Ab: rabbit anti-mouse serum albumin, 1:100; 2° Ab: donkey anti-rabbit IgG H&L Alexa Fluor 647, 1:200). Sections with BBB opening were identified from fluorescence images and were verified by S. Morse (PhD student, NSB Lab) without prior knowledge of which side was targeted with ultrasound to avoid any bias. An example of this is shown in Figure 4.11, in which positive albumin staining in the left hippocampal region - and thus, BBB opening - can be seen in section **b.**

To avoid any interference between the two amyloid stains, ThS and MOAB-2 staining was conducted on adjacent brain sections, rather than co-staining the same sections. For the ultrasound-treated groups, ten sections from each brain sample around the site of BBB opening were stained with ThS and another ten were stained with MOAB-2 (Figure 4.12). Sections at a similar anatomical level from Group 1 (no treatment) were also stained to allow comparison. Stained sections were then imaged using a fluorescence microscope using appropriate filter sets.

In order to obtain quantitative information from the fluorescence images obtained, we first defined the region of interest - the left hippocampus - using a polygon tool in ImageJ (Figure 4.12). A threshold was then applied to exclude any artefacts and the particle burden, number of particles and particle area were determined using the automated 'Analyse Particles' tool in ImageJ. The particle burden is defined as the percentage of pixels in the defined region of interest that have an intensity greater than the applied threshold, whilst the number of particles and particle area refer to the average number and area of individual particles identified by ImageJ. It should, however, be noted that the latter two measures are likely to be less meaningful than the calculated particle burden as ImageJ is unable to separate out a cluster of individual particles and will count this as one large particle instead. All quantification was repeated at least three times on each brain section and performed blind to avoid bias.

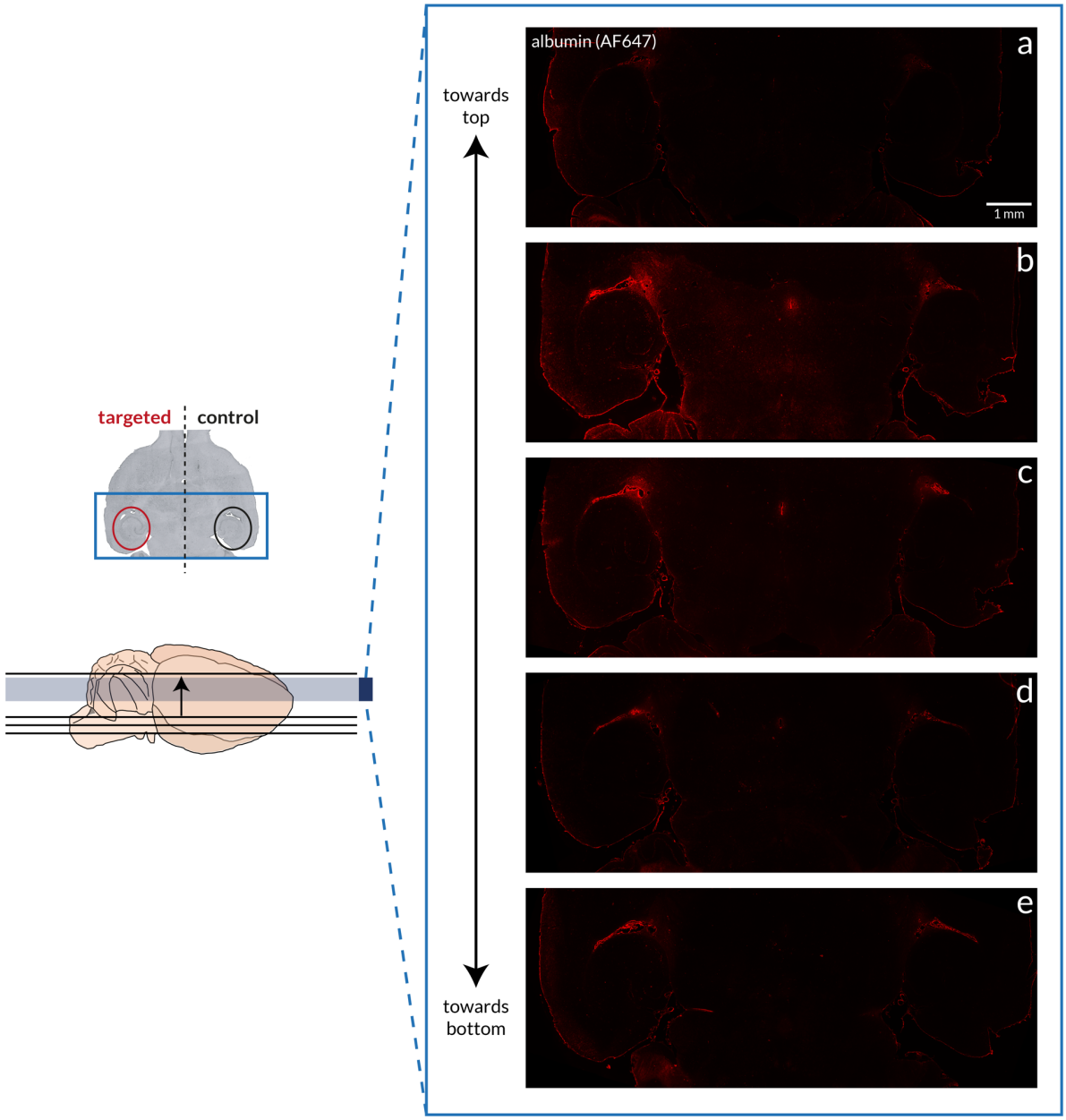


Figure 4.11: Albumin staining across five sections at the hippocampal level. The albumin extravasation seen is directly related to the extent of BBB opening induced by the focused ultrasound and microbubbles.[86] Under the experimental conditions used, the extent of BBB opening differs throughout the brain, with BBB opening observed at the level in which sections **b** and **c** were taken from. Less BBB opening is seen in sections **a, d** and **e**. It should be noted that we do not expect major extravasation of albumin with these ultrasound parameters.[86]

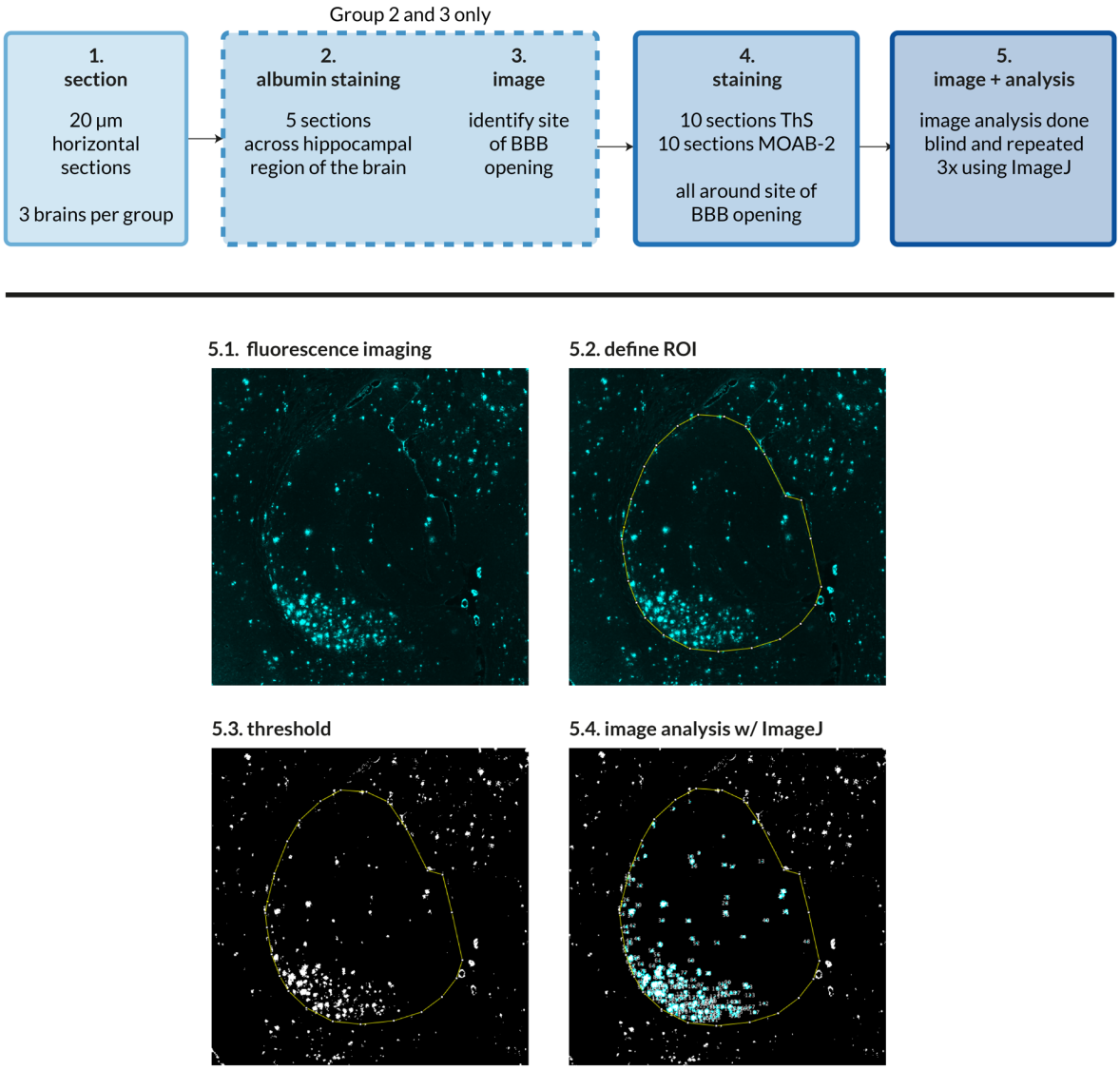


Figure 4.12: **Top:** Sample processing workflow. Brains were sectioned into 20 µm horizontal sections. For ultrasound-treated brains (Groups 2 and 3), five sections across the hippocampal region were stained with albumin to identify the site of BBB opening. Ten sections from each brain around the site of BBB opening were stained with ThS and another ten with MOAB-2. **Bottom:** Image analysis workflow. The region of interest, the left hippocampus, was defined. Images were then thresholded and the particle burden, number of particles and average particle area was calculated automatically using ImageJ. All analysis was conducted blind and repeated three times to prevent bias.

Thioflavin-S and MOAB-2 Staining

In Chapter 3, we showed that octahedral cobalt complex **4b** is able to inhibit the aggregation of monomeric Aβ and prevent fibril formation. It follows that if complex **4b** is able to induce a therapeutic effect *in vivo* at the treatment dose and frequency used in this preliminary animal study, a reduction in the Aβ plaque burden and thus, reduced ThS staining would be observed. In contrast, unlike ThS which only stains Aβ fibrils, MOAB-2 stains all forms of Aβ. If complex **4b** is able to inhibit the aggregation of Aβ *in vivo* under the experimental conditions used, then higher levels of soluble Aβ (*e.g.* monomers and oligomers) would be expected. One of the key clearance mechanisms for Aβ in the brain is enzymatic degradation by metalloproteases such as neprilysin (NEP) and insulin-degrading enzyme (IDE).[315,316] Aβ-degrading enzymes are believed to act primarily on monomeric Aβ and there exists only a few reported examples of enzymes that are able to cleave oligomeric or fibrillar forms of Aβ.[315–318] Consequently, if complex **4b** is able to increase the levels of monomeric Aβ relative to insoluble fibrillar Aβ in the brain when administered *in vivo*, enhanced clearance activity may occur, resulting in reduced MOAB-2 staining.

Representative ThS-stained sections and MOAB-2-stained sections from each treatment group are shown in Figure 4.13 and Figure 4.14. Images shown are from the section that best represents the average particle burden of that brain sample; additional images from each brain sample can be found in Appendix. Quantitative analysis of ten sections per brain sample was carried out to determine the particle burden, number of particles and average particle area following the protocols outlined above. As shown in Figure 4.15, a reduction in the Aβ particle burden and average number of Aβ particles was detected between Group 1 (no treatment) and Groups 2 and 3 (ultrasound only; ultrasound + **4b**) with both ThS and MOAB-2 staining. As discussed at the start of this chapter, focused ultrasound-mediated BBB opening has been demonstrated to lead to reduced Aβ plaque burden *in vivo* in the absence of therapeutic agents, which could explain the differences between Group 1 (no treatment) and Group 2 (ultrasound only).[288,292,298] However, promisingly, the reduction in Aβ burden was greater in Group 3 (ultrasound + **4b**) than in the Group 2 (ultrasound only), suggesting that complex **4b** may be inhibiting Aβ aggregation under the experimental conditions used. No significant changes in the average particle area were detected with complex **4b** using both stains, which could indicate that complex **4b** is unable to disassemble pre-formed amyloid fibrils; however, as stated above, this measure (and the average number of particles) is less reliable than the calculated particle burden as ImageJ cannot separate out clusters of particles in close proximity and will instead treat them as one large particle.

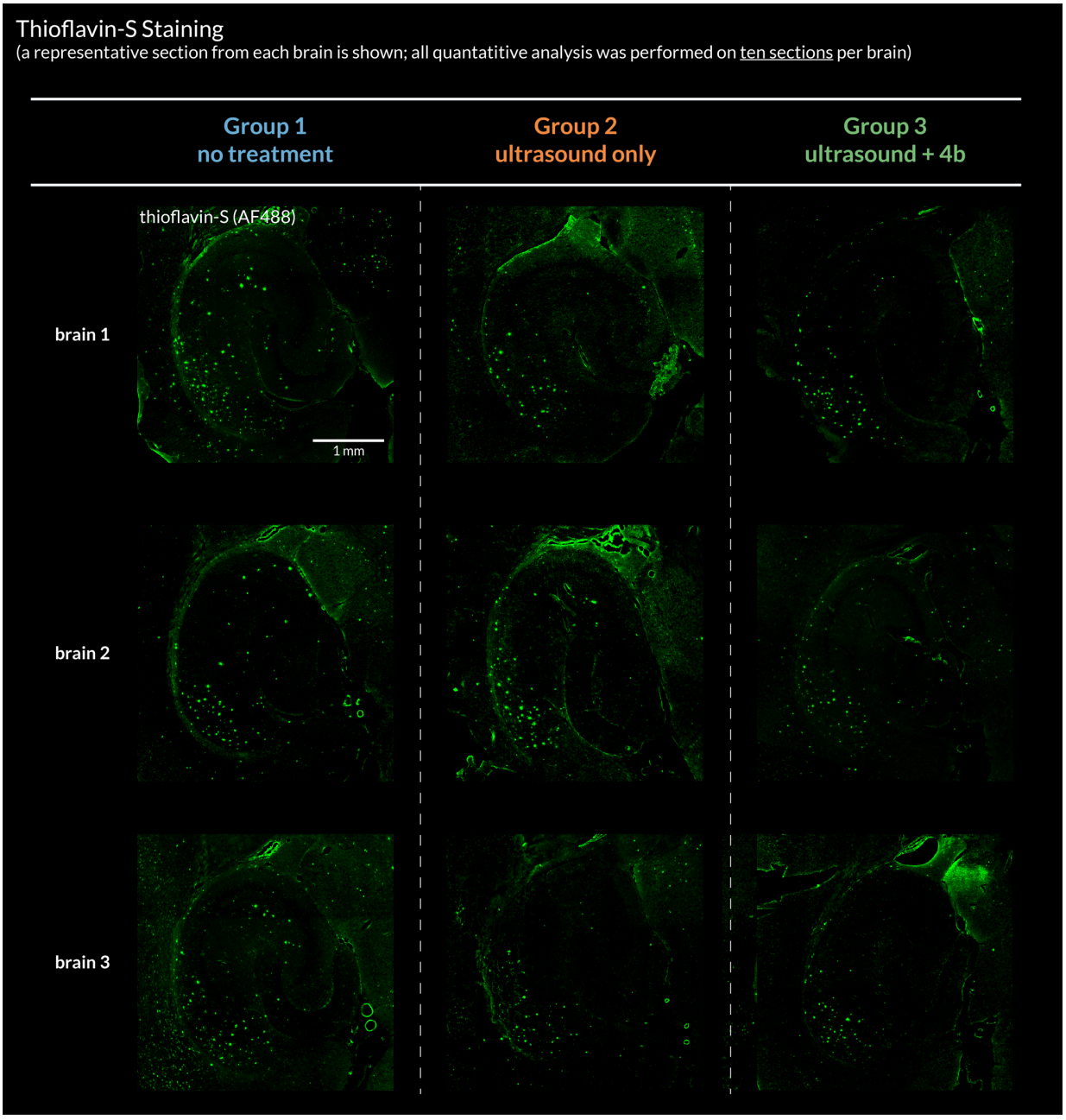


Figure 4.13: Representative ThS-stained sections from each brain studied (n = 3 mice per treatment condition). The image shown is the section that best represents the average plaque burden of that brain sample. All quantitative analysis was conducted on ten sections from each brain. Additional images from each brain can be found in the Appendix.

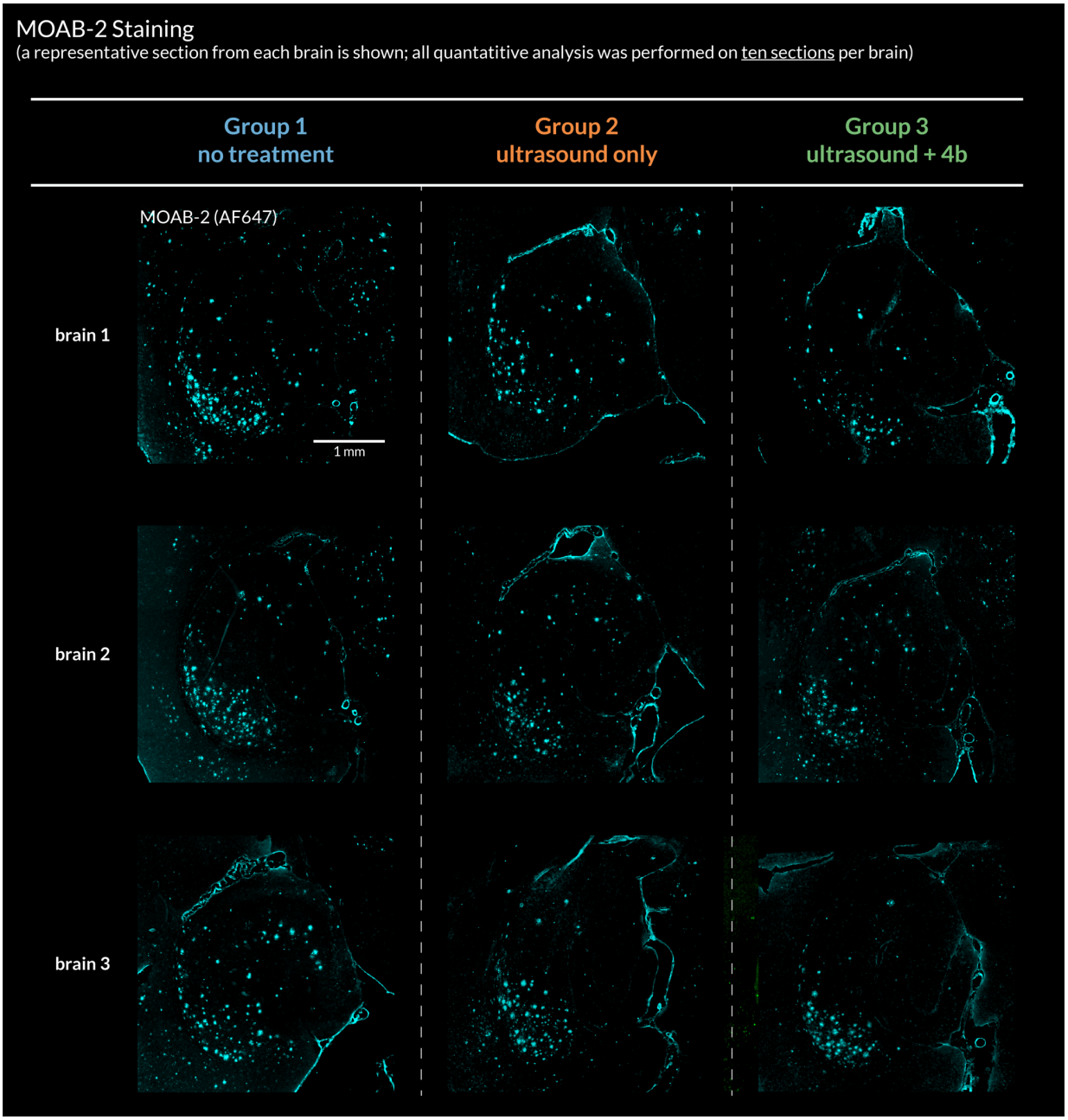


Figure 4.14: Representative MOAB-2-stained sections from each brain studied (n = 3 mice per treatment condition). The image shown is the section that best represents the average particle burden of that brain sample. All quantitative analysis was conducted on ten sections from each brain. Additional images from each brain can be found in the Appendix.

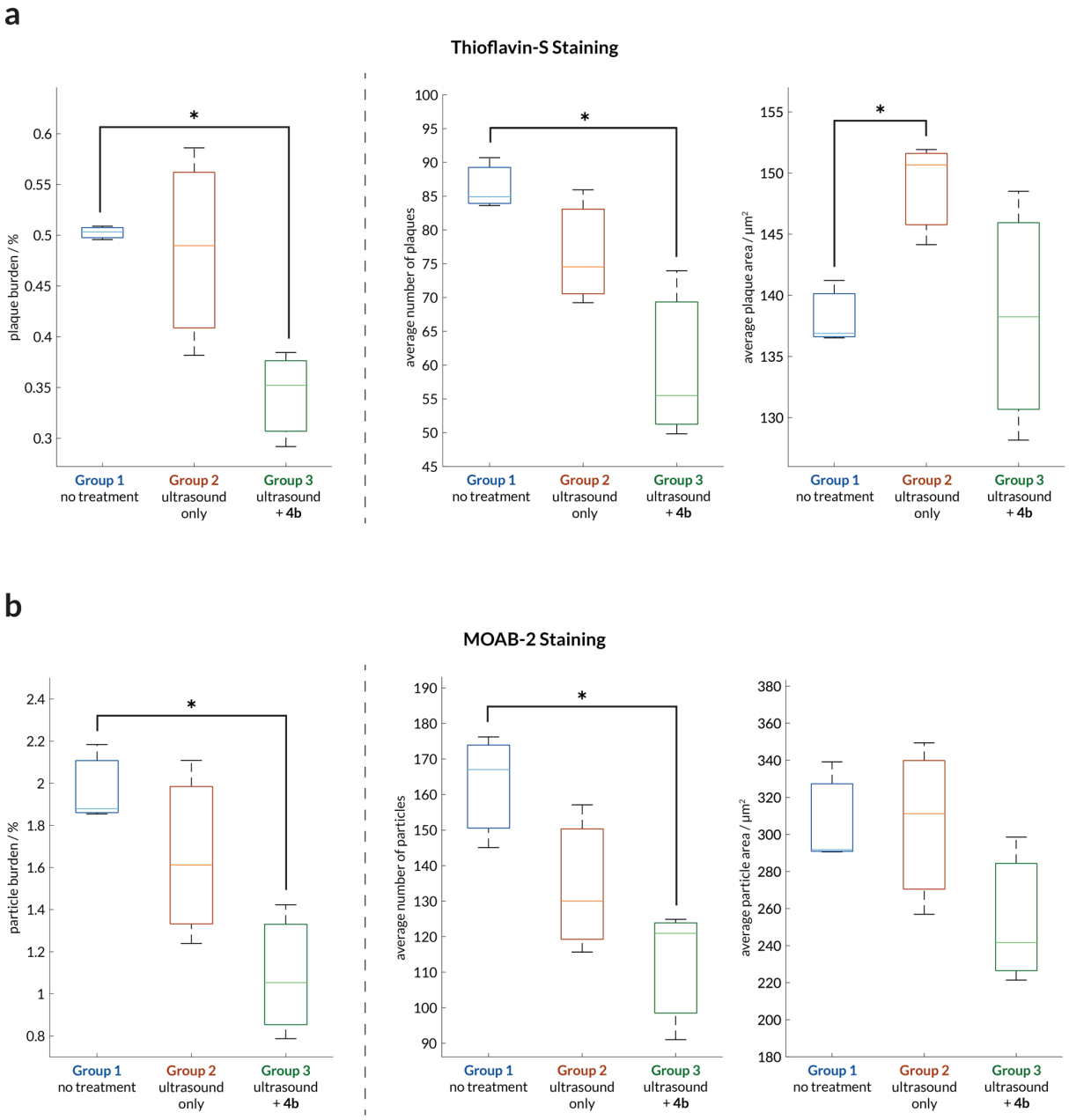


Figure 4.15: Particle burden, number of particles and average particle area determined from brain sections stained with ThS **(a)** and MOAB-2 **(b)**. A reduction in the particle burden and number of particles ($p < 0.05$) was observed between Group 1 (no treatment) and Group 3 (ultrasound + **4b**). Quantitative analysis was conducted blind and repeated three times to minimise errors ($n = 3$ mice for each treatment condition; 10 sections per brain).

4.4 CONCLUSIONS AND FUTURE DIRECTIONS

In Chapter 3, a series of metal salphens and salnaphs were reported as potential inhibitors of Aβ aggregation *in vitro*. Through a combination of peptide assays, spectroscopic studies and cytotoxicity experiments, we demonstrated that octahedral cobalt complexes **3** and **4** are able to inhibit the aggregation of monomeric Aβ *in vitro* and are non-cytotoxic. In this chapter, we sought to extend this work further and obtain preliminary data with our cobalt complexes in an Alzheimer's disease mouse model. To our knowledge, this represents the first time that octahedral complexes targeted to the N-terminal of Aβ have been tested *in vivo* for the treatment of Alzheimer's disease; in fact, this is only the second time that a metal complex - of any geometry - has been tested *in vivo* for this application.

Before conducting studies in an Alzheimer's disease mouse model, we first attempted to improve the safety and efficiency of ultrasound-mediated BBB opening by switching to a series of short microsecond ultrasound pulses, rather than using the long millisecond pulses typically used for BBB opening. Experiments conducted with S. Morse, Dr. A. Pouliopoulos, M. Copping and J. Lin (PhD and MRes students, NSB Lab) demonstrated that the use of RaSP sequences leads to more homogeneous drug delivery within the targeted region, reduced extravasation of serum proteins from the bloodstream into the brain and less tissue damage.[86] The permeability of the BBB was also found to remain disrupted for a much shorter time when RaSP sequences were used, reducing the chance of other blood-borne substances entering the brain.[86] Due to the improved safety and efficiency of ultrasound-mediated drug delivery to the brain obtained with RaSP sequences, these sequences were used for all subsequent *in vivo* studies.

Initially, we showed that we could successfully deliver our metal complexes across the BBB with RaSP sequences using LA-ICP-MS. We then assessed the safety of delivering our metal complexes across the BBB using ultrasound over an extended period of time by treating a group of wild type C57BL/6J mice every week for four weeks. Cobalt complex **4b** was chosen for *in vivo* studies as it is the most stable of the cobalt complexes synthesised and thus, easiest to handle. No changes in behaviour, body weight or tissue morphology were observed in the C57BL/6J mice treated, indicating that the repeated delivery of complex **4b** to the brain using RaSP sequences was well-tolerated. Next, we moved onto conducting a preliminary efficacy study in transgenic 5xFAD mice. 5xFAD mice were split into three treatment groups (no treatment, ultrasound only and ultrasound + complex **4b**) and were treated every week for three weeks. At the end-point of the study, the amyloid burden in the ultrasound-targeted region, the left hippocampus, was quantified using histological and immunohistochemical methods. The initial data collected suggests that complex **4b** may be exerting therapeutic effects under the experimental conditions used, with a reduction in Aβ burden observed between the 'no treatment' control and 'ultrasound + complex **4b**' group.

Prior studies have reported that focused ultrasound-mediated BBB opening can induce reductions in Aβ plaque burden by itself through activation of glial cells; in the preliminary study presented here, whilst a slight reduction in Aβ burden is indeed detected in the 'ultrasound only' group, the reduction is greater in the 'ultrasound + complex **4b**' group, indicating that the combined use of focused ultrasound-mediated BBB opening and complex **4b** may provide additive effects.[288,292,298]

The main limitations of our preliminary *in vivo* study to date are: 1) sample size and 2) a lack of a control 'drug only' group. Due to time constraints and a lack of available age-matched transgenic 5xFAD mice, the treatment groups that were used only contained three mice each; thus, whilst our initial data is promising, it is difficult to draw any real conclusions about the therapeutic efficacy of complex **4b** at this point in time. Future work should seek to expand the sample size of the study to allow for more robust statistical analyses to be conducted. In addition to this, we have been unable to include a fourth treatment group in which mice were administered complex **4b** in the absence of focused ultrasound-mediated BBB opening. Whilst the LA-ICP-MS data presented suggests that the synthesised metal complexes show poor BBB penetration in the absence of focused ultrasound and microbubbles, these analyses were conducted approximately 5 minutes after a single administration of the complex. Weekly exposure to the complexes as was done in our preliminary *in vivo* study may result in the complexes crossing the BBB - albeit at low concentrations - and could produce therapeutic effects. The inclusion of a 'complex **4b** only' group is therefore needed so that this possibility can be investigated; these experiments are currently ongoing. As well as this, optimising study parameters such as the treatment frequency, duration and complex dosage should be done as this could lead to more significant therapeutic effects being observed.

In the longer term, investigating the biodistribution of the complexes when administered *in vivo*, as well as the fate of the complexes after binding to Aβ in the brain would be crucial. Moreover, if reductions in Aβ plaque burden are consistently observed with complex **4b** *in vivo*, longitudinal behavioural studies should be conducted to assess if it has any effects on memory function. Combining complex **4b** with existing therapeutic agents would also be interesting to explore; for instance, given that complex **4b** is hypothesised to prevent Aβ aggregation by binding to extracellular Aβ, co-administering complex **4b** with a β-secretase 1 (BACE1) inhibitor, which works to prevent Aβ production, could lead to synergistic effects being achieved.

5 CONCLUSIONS

The BBB is one of the biggest obstacles for the effective treatment of brain diseases, preventing 98% of small molecule drugs from entering the brain.[48] As of now, the use of focused ultrasound and microbubbles is the only method which is able to disrupt the BBB in a manner that is non-invasive, targeted and reversible.[78] The application of ultrasound-mediated drug delivery methods allows for more sophisticated therapeutics to be developed as traditional chemical design rules (*e.g.* small size, moderately lipophilic) do not need to be followed in order to achieve BBB penetration.[51] In this thesis, we have developed two different systems to take advantage of this technology - nanoparticles as delivery platforms for combination therapies and metal complexes as inhibitors of Aβ aggregation for the treatment of Alzheimer's disease - and we have evaluated them *in vitro* and *in vivo* using focused ultrasound.

In Chapter 2, fluorescently-labelled DNA-coated Au NPs of different sizes were synthesised and characterised. We showed that we were able to deliver these NPs across the BBB using focused ultrasound and that the DNA-coated NPs remained intact upon delivery. The size-threshold of ultrasound-mediated delivery was also investigated, with smaller diameter NPs being delivered more efficiently to the brain than larger diameter NPs using this technology. This supports prior proposals that ultrasound-mediated BBB opening primarily occurs through a widening of the tight junctions between adjacent endothelial cells.[92] NP systems loaded with therapeutic agents have been developed in collaboration with Dr. A. Torres-Huerta (Postdoc, Vilar Group) and ongoing work is focused on evaluating their efficacy *in vitro* and *in vivo*.

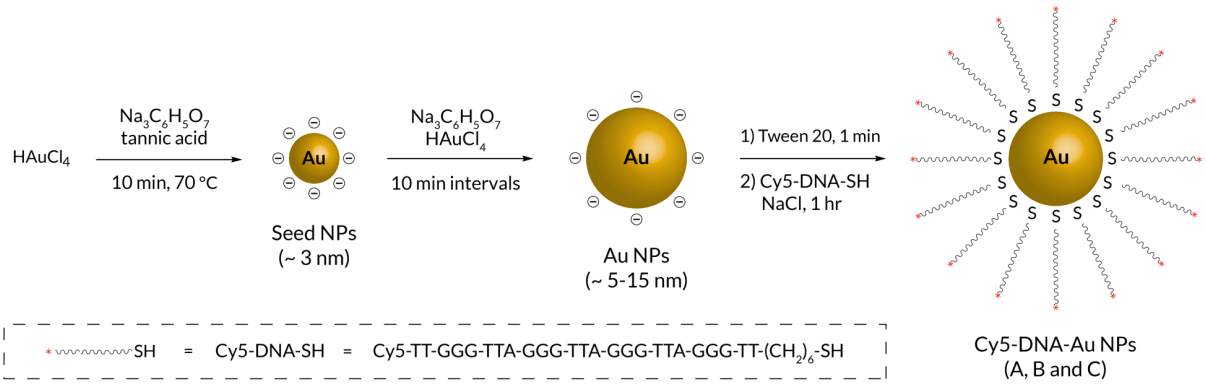
In Chapter 3, a series of metal salphens and salnaphs were investigated as potential inhibitors of Aβ aggregation for the treatment of Alzheimer's disease. The aggregation of the Aβ peptide in the extracellular space is one of the key pathological hallmarks of Alzheimer's disease and is believed to play a central role in disease progression. Studies have shown that Aβ contains a high affinity metal ion binding site that is able to modulate Aβ aggregation, and as a consequence, this site has been proposed as a potential therapeutic target.[217–221] To date, there have only been a handful of compounds developed to target this site, most of which are platinum complexes with planar, aromatic ligands.[246,250–252] To expand on this work further, we investigated a family of metal salphens and salnaphs for their ability to inhibit Aβ aggregation. Using the Thioflavin-T assay, we showed that all of the complexes studied are able to prevent Aβ aggregation, with greater inhibitory activity against Aβ aggregation observed for octahedral cobalt complexes **3** and **4** compared to square planar derivatives **1** and **2**. Similar to the binding mode proposed for the octahedral cobalt(III) Schiff base complexes developed by Heffern *et al.* and Iscen *et al.*, we hypothesised

that complexes **3** and **4** are able to coordinate to the histidine residues of Aβ *via* dissociative ligand exchange at the axial positions.[250,253] Spectroscopic experiments were carried out to probe the binding of complexes **1** to **4** to Aβ, which provided evidence that complexes **3** and **4** are able to coordinate to His6 of Aβ. In addition to this, we showed that complexes **3** and **4** show minimal cytotoxic effects *in vitro*, with IC50s > 100 μM being obtained in human cell lines (SH-SY5Y and PC3).

In Chapter 4, we sought to evaluate cobalt complexes **3** and **4** *in vivo* in an Alzheimer's disease mouse model. We first demonstrated that we can deliver these complexes across the BBB *in vivo* with focused ultrasound and that doing so on a weekly basis over a period of five weeks is well-tolerated in mice. A preliminary efficacy study in an Alzheimer's disease mouse model (5xFAD) was then carried out, consisting of three treatment groups: no treatment, ultrasound only and ultrasound + complex **4b**. The Aβ burden of the brains was compared between treatment groups using histological and immunohistochemical methods post-mortem. In spite of the small sample size used in our preliminary study, the results obtained thus far are promising, with a reduction in Aβ burden detected between the 'no treatment' and 'ultrasound + complex **4b**' groups. Ongoing work aims to expand this *in vivo* study further and increase the sample size, as well as include a fourth 'complex **4b** only' control group.

6.1 SYNTHESIS OF DNA-COATED GOLD NANOPARTICLES

Unless otherwise stated, all reagents were purchased from commercial suppliers and used without further purification. Ultrapure water was used in all reactions and all glassware was washed thoroughly with *aqua regia* (1:3 HNO_3:HCl).



Au NPs of different sizes were synthesised following seeded growth protocols adapted from Piella *et al.*[130] Briefly, a solution of sodium citrate (2.2 mM, 25 mL) and tannic acid (2.5 mM, 17 µL) was adjusted to pH 10 with K_2CO_3 (150 mM, ~170 µL) and heated to 70 °C with stirring. $HAuCl_4$ (10 mM, 410 µL) was then added, resulting in a colour change from colourless to pink. Stirring at 70 °C for a further 10 mins resulted in a solution of seed gold nanoparticles (7 x 10^{13} NPs/mL).

To grow larger nanoparticles, the seed solution was immediately diluted by removing a third of the solution volume and replacing with sodium citrate (2.2 mM). Two injections of $HAuCl_4$ (10 mM, 200 µL) were added on a time interval of 10 mins before diluting the reaction as before. Further injections and dilutions were carried out until the nanoparticles reached the desired size.

6.1.1 Surface Functionalisation with Oligonucleotides

Au NPs were functionalised with fluorescently-tagged oligonucleotides following protocols adapted from Li *et al.*[134] Since oligonucleotides typically used for gene therapies are 20-25 bases in length, a 25 base

oligonucleotide sequence was chosen for this study: Cy5-TT-GGG-TTA-GGG-TTA-GGG-TTA-GGG-TT-$(CH_2)_6$-SH (Cy5-DNA-SH).[108] The oligonucleotide had a thiol modifier on the 3' end to allow it to bind to the gold nanoparticle surface and a Cy5 modifier on the 5' end to allow for tracking after delivery across the BBB *in vivo*.

Before use, tris(2-carboxyethyl)phosphine) (TCEP) was added to Cy5-DNA-SH in a 100x excess and the mixture was incubated for 1 hr at 25 °C. 1 wt% Tween 20 (10 µL) was added to the Au NPs (50 nM, 1.15 mL) and the mixture was stirred for 1 min. Cy5-DNA-SH (50 µM) was added at a volume that allowed for 100 oligonucleotide strands present per Au NP. NaCl (5 M) was then added until its final concentration in the mixture reached 800 mM. The solution was incubated for 1 hr at 25 °C with gentle agitation and then centrifuged at 30,000 rpm (∼55,000 x g) for 45 mins at 15 °C. The supernatant was removed and the nanoparticles were redispersed in 500 µL of phosphate-buffered saline (pH 7.4; 137 mM NaCl, 2.7 mM KCl, 8 mM Na_2HPO_4 and 2 mM KH_2PO_4) with 0.1% Tween 20 (PBST). This centrifugation process was repeated at least 3x to ensure thorough washing of the nanoparticles. All nanoparticle solutions were stored at 4 °C, kept away from light and were used within 2 weeks.

6.2 CHARACTERISATION OF DNA-COATED GOLD NANOPARTICLES

6.2.1 UV-Vis Spectroscopy

Absorbance spectra were recorded on a Perkin Elmer Lambda 25 UV-Vis Spectrometer, scanning between 400 to 700 nm. The concentrations of all Au NP solutions were determined using the method reported by Haiss *et al*.[136]

6.2.2 Transmission Electron Microscopy

Synthesised nanoparticles were imaged using a JEOL JEM-2100Plus transmission electron microscope. 10 µL of Au NP solution was drop-casted onto a carbon-coated grid and left to dry for 18 hrs before imaging. Images were taken at 60,000-120,000x magnification. The average particle size and size distribution were determined using ImageJ by counting at least 100 Au NPs.

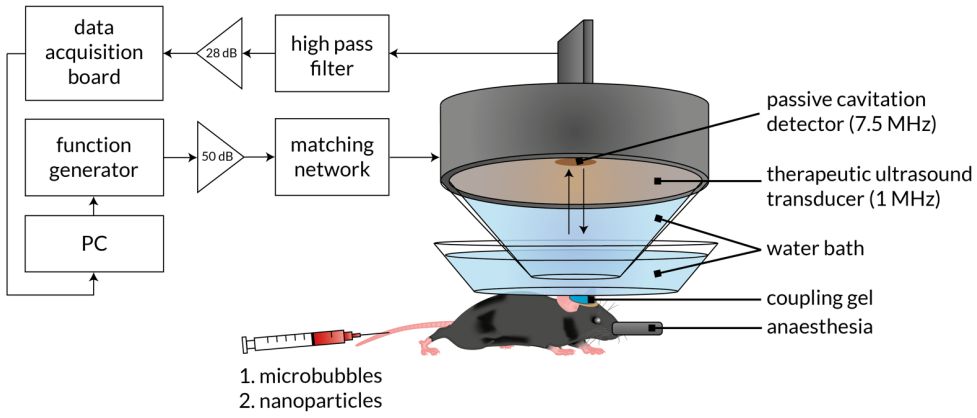
6.2.3 Dynamic Light Scattering and Electrophoretic Light Scattering

Hydrodynamic diameters and zeta potentials of Au NP solutions were recorded on a Malvern Zetasizer Nano ZS instrument in Malvern DTS1070 folded capillary zeta cells. All solutions were filtered through a 0.45 µM syringe filter prior to analysis and were measured at 25 °C. Reported values are the mean ± standard deviation of three separate batches of nanoparticles.

6.2.4 Determination of Oligonucleotide Loading

Mercaptoethanol was added to a solution of Cy5-DNA-Au NPs dispersed in PBST until it reached a final concentration of 20 mM. After stirring the solution at 25 °C for 48 hrs, the mixture was centrifuged at ~55,000 x g for 45 mins and the supernatant (containing the displaced oligonucleotides) was separated. The fluorescence of the displaced Cy5-oligonucleotides was measured on a Cary Eclipse Fluorescence Spectrophotometer and compared to a standard curve; samples were excited at 656 nm and were scanned from 660 to 760 nm. The concentration of fluorescent oligonucleotides was divided by the initial Au NP concentration to give the number of oligonucleotides attached per nanoparticle.

6.3 ULTRASOUND-MEDIATED DELIVERY OF NANOPARTICLES INTO THE BRAIN



Ultrasound pulses were emitted from a Sonic Concepts single-element, spherical-segment focused ultrasound transducer (centre frequency: 1 MHz, active diameter: 90 mm, geometric focus: 77 mm) driven by an Agilent Technologies 33500B function generator through a Precision Acoustics 50 dB power amplifier.

The lateral, elevational and axial full width at half maximum (FWHM) at the focus were 2 mm, 1 mm and 20 mm respectively. Microbubble emissions were captured using an Olympus Industrial focused passive cavitation detector (centre frequency: 7.5 MHz, focal length: 76.2 mm) aligned co-axially with the FUS transducer, filtered using a Mini Circuits 3-30 MHz band-pass filter, amplified with a Stanford Research Systems 28 dB pre-amplifier and then recorded with a Pico Technology Picoscope 3205A 8-bit oscilloscope sampling at 250 MHz. Transducers were mounted onto a 3D positioning system to allow targeting of the desired region.

Before *in vivo* experiments, pressure amplitudes were measured using a Precision Acoustics needle hydrophone (diameter: 0.2 mm) in a degassed water tank. Peak-positive and peak-negative values were attenuated by 11% to correct for skull attenuation.[86]

6.3.1 Delivery of DNA-coated Gold Nanoparticles across the BBB

All animal procedures were performed following Home Office regulations and institutional guidelines. Eighteen female wild-type C57BL/6J mice (8-10 weeks old, 19.2 ± 0.95 g) were used in total. Mice were anaesthetised with 98% O_2/2% isoflurane and maintained under anaesthesia for the duration of the experiment. The fur from the head of each mouse was removed using an electric clipper and depilatory cream to reduce any potential interferences from trapped air bubbles. The mouse was then positioned and immobilised using a stereotaxic frame.

The left thalamus of the brain was targeted using a reported method, in which a metal cross is placed on top of the skull in alignment with the lambdoid and sagittal sutures.[141] A 2D raster scan of the cross was generated using the transducer in pulse-echo mode and used to position the transducer 1 mm laterally from the sagittal suture and 0.5 mm above the lambdoid suture. The right thalamus was used as the control.

The left thalamus was sonicated using conventional therapeutic ultrasound sequences (frequency: 1 MHz, peak-negative pressure: 530 kPa, pulse length: 10,000 cycles, pulse repetition frequency: 0.5 Hz, sonication duration: 250 s). After five pulses, SonoVue microbubbles (100 µL, 5 µL/g) were administered intravenously into the mouse *via* a tail vein catheter, followed by Cy5-DNA-Au NPs **A**, **B** or **C** (100 µL, 500 nM). Following sonication, mice were sacrificed and transcardially perfused with 20 mL ice-cold phosphate-buffered saline (pH 7.4; 137 mM NaCl, 2.7 mM KCl, 8 mM Na_2HPO_4 and 2 mM KH_2PO_4) with added heparin (10 units/mL) to reduce blood coagulation. Once the blood was cleared, mice were fixed with

20 mL ice-cold 10% formalin solution. Brains were extracted and submerged in 10 mL 10% formalin solution at 4 °C overnight.

6.3.2 Fluorescence Microscopy

Mouse brains were cryoprotected by immersing them in sucrose solutions of increasing concentration at 4 °C: 15% (w/v) sucrose solution for 6 hrs, followed by immersion in a 30% (w/v) sucrose solution overnight. Cryoprotected brains were sectioned into 30 or 15 µm horizontal sections on a Thermo Scientific CryoStar NX70 Cryostat and imaged using a Zeiss Axio Observer Inverted Widefield microscope. Images of the left (sonicated) and right (non-sonicated control) thalamus were taken using a 10x objective in both the bright-field and Cy5 (excitation wavelength: 640 nm, excitation filter: 640/30 nm, emission filter: 690/50 nm) channels to detect the presence of Cy5-DNA-Au NPs in the brain.

Fluorescence images of five sections from each brain were used to calculate the normalised optical density (NOD) – the average fluorescence in the targeted region normalised by the control – to give an indication of the amount of Cy5-DNA-Au NPs delivered. Quantification was done using an in-house MATLAB script written by S. Morse (PhD student, NSB Lab). Briefly, regions of interest were selected using MATLAB and any artefacts such as folds were manually segmented and omitted from the calculation. To exclude brain autofluoresence, a threshold of twice the standard deviation of the intensity of the control region was employed. Pixel intensities above this threshold were summed in the targeted and control regions and the NOD was obtained by subtracting the value obtained for the targeted region by that of the control region. A two-sided Student's *t*-test was performed to assess statistical significance, taking $p < 0.05$ to be significant.

6.3.3 Assessing Safety with H&E Staining

Following sonication, brains were extracted, paraffin-embedded and cut into 5 µm sections by the UCL IQPath laboratory ($n = 3$). Eight brain sections covering the entirety of the focal volume were then stained with haematoxylin and eosin (H&E) following standard procedures. Briefly, slides were first cleared by submerging in Histo-Clear II for 5 mins and then again for 10 mins. Sections were then hydrated in water and immersed in Harris Haematoxylin solution for 5 mins. Following rinsing with tap water, slides were dipped 3x in 1% acid-alcohol solution (1% HCl in 70% ethanol) and rinsed. Sections were then dipped in Eosin Y for 50 secs and rinsed with water again. Stained slides were dehydrated by placing in 90%

ethanol for 30 secs, followed by 100% ethanol for 30 secs and then left in Histo-Clear II until mounting. Slides were mounted with DPX, coverslipped and imaged using a Zeiss Axio Observer Inverted Widefield microscope.

7 METHODS - METAL COMPLEXES FOR ALZHEIMER'S DISEASE

7.1 SYNTHESIS OF METAL COMPLEXES

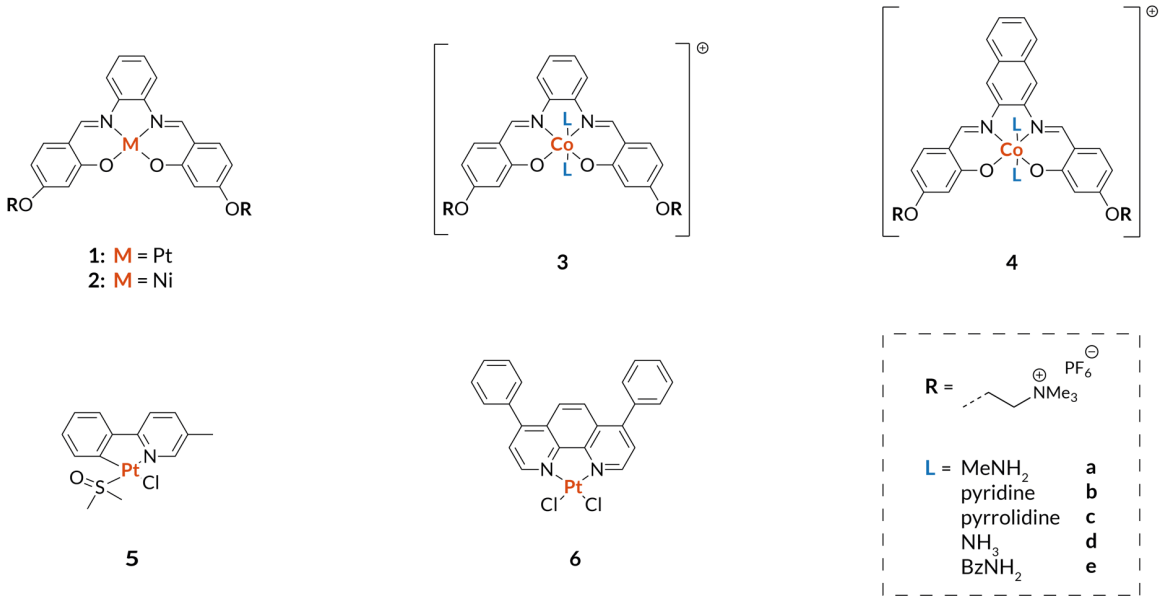
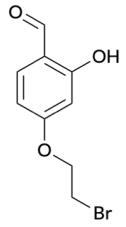


Figure 7.1: Structures of the metal complexes used in this study. Metal salphens **1** and **2** were synthesised by Dr. V. Rakers (PhD student, Vilar Group), whilst cobalt salphens **3a-e** were synthesised by C. Ruehl (PhD student, Vilar Group).[257,258] Complexes **5** and **6** were used as controls and synthesised based on literature protocols.[248,319–321]

Unless otherwise stated, all reagents were purchased from commercial suppliers and used without further purification. Elemental analyses (C, H, N) are reported as the average of two independent measurements and were obtained by Mr. A. Dickerson (University of Cambridge). ^{1}H NMR spectra were recorded on a 400 MHz Bruker Avance III HD NMR spectrometer at 298 K. Chemical shifts are given in parts per million (ppm, δ) and are reported relative to TMS and referenced to the residual deuterated solvent. Splitting patterns are designated as s for singlet, d for doublet, t for triplet and m for multiplet. High-resolution electrospray ionisation (ES) mass spectra were obtained on a Waters LCT Premier (ES-TOF)/Acquity i-Class spectrometer by Dr. L. Haigh (Imperial College London).

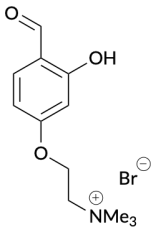
7.1.1 4-(2-bromoethoxy)-2-hydroxybenzaldehyde



4-(2-bromoethoxy)-2-hydroxybenzaldehyde was synthesised via a modified procedure reported by Oliveri *et al.*[260] 1,2-dibromoethane (7.03 mL, 81.6 mmol) was added to 2,4-dihydroxybenzaldehyde (11.3 g, 81.6 mmol) and potassium carbonate (5.6 g, 40.8 mmol) in anhydrous acetone (300 mL). The mixture was heated under reflux for 72 hrs under nitrogen, resulting in the formation of a pink suspension. The solid precipitate was filtered off under suction, leaving an orange-brown filtrate. The filtrate was concentrated and purified by column chromatography (silica gel; hexane:ethyl acetate, 90:10) to give 4-(2-bromoethoxy)-2-hydroxybenzaldehyde as a white solid (2.51 g, 10.2 mmol, 13%).

^{1}H NMR (400 MHz, $CDCl_3$) δ 11.02 (s, 1H, -OH), 10.03 (s, 1H, -CHO), 7.64 (d, *J* = 8.7 Hz, 1H, Ar-H), 6.60 (dd, *J* = 8.6, 2.3 Hz, 1H, Ar-H), 6.51 (d, *J* = 2.4 Hz, 1H, Ar-H), 4.39 (t, *J* = 6.2 Hz, 2H, -O-CH_2-), 3.82 (t, *J* = 6.1 Hz, 2H, –CH_2-Br); ^{13}C NMR (101 MHz, DMSO-d_6) δ 191.0, 164.5, 163.0, 132.2, 116.6, 107.6, 101.5, 68.1, 31.0.

7.1.2 4-(4-formyl-3-hydroxyphenoxy)-*N*,*N*,*N*-trimethylethan-1-ammonium bromide

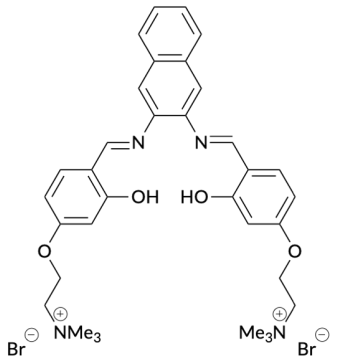


4-(4-formyl-3-hydroxyphenoxy)-*N*,*N*,*N*-trimethylethan-1-ammonium bromide was synthesised via a procedure reported by Rakers *et al.*[257] Briefly, 4-(2-bromoethoxy)-2-hydroxybenzaldehyde (1.07 g, 4.3 mmol) was first dissolved in a 4.2 M ethanolic solution of trimethylamine (50 mL) to give a yellow solution. After heating the mixture at 50 °C for 18 hrs, the solvent was removed to give a yellow-orange solid. Washing

with chloroform (3 x 20 mL) resulted in the isolation of the desired product as a pale yellow solid (1.02 g, 3.3 mmol, 76%).

^{1}H NMR (400 MHz, DMSO-d_6) δ 11.06 (s, 1H, -OH), 10.05 (s, 1H, -CHO), 7.67 (d, *J* = 8.7 Hz, 1H, Ar-H), 6.63 (dd, *J* = 8.7, 2.3 Hz, 1H, Ar-H), 6.56 (d, *J* = 2.3 Hz, 1H, Ar-H), 4.53 (t, *J* = 4.6 Hz, 2H, -O-CH_2-), 3.85 (t, *J* = 4.6 Hz, 2H, -CH_2-NMe_3), 3.18 (s, 9H, -$(CH_3)_3$); ^{13}C NMR (101 MHz, DMSO-d_6) δ 191.2, 163.9, 162.9, 132.2, 116.8, 107.7, 101.8, 63.9, 62.0, 53.1; MS (ES^+) *m/z* 224.1291 ($[M+H]^+$, 100%), where M = $C_{12}H_{18}NO_3$.

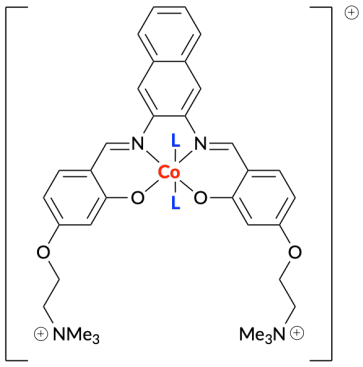
7.1.3 Salnaph Ligand



4-(4-formyl-3-hydroxyphenoxy)-*N*,*N*,*N*-trimethylethan-1-ammonium bromide (500 mg, 1.64 mmol) and 2,3-diaminonaphthalene (130 mg, 0.82 mmol) in ethanol (15 mL) was heated under reflux for 5 hrs under nitrogen, resulting in the formation of a yellow precipitate. The yellow precipitate was isolated via filtration and washed with ethyl acetate, DCM and diethyl ether (3 x 5 mL) to give the desired product as a bright yellow solid (478 mg, 0.65 mmol, 80%).

^{1}H NMR (400 MHz, DMSO-d_6) δ 13.52 (s, 2H, -OH), 9.02 (s, 2H, -N=CH-), 7.97 – 7.90 (m, 4H, Ar-H), 7.67 (d, *J* = 8.6 Hz, 2H, Ar-H), 7.52 (dd, *J* = 6.2, 3.4 Hz, 2H, Ar-H), 6.68 – 6.58 (m, 4H, Ar-H), 4.56 (t, *J* = 4.7 Hz, 4H, -O-CH_2-), 3.85 (t, *J* = 4.8 Hz, 4H, -CH_2-NMe_3), 3.22 (s, 18H, -$(CH_3)_3$); ^{13}C NMR (101 MHz, DMSO-d_6) δ 163.5, 163.1, 161.9, 141.8, 134.8, 132.2, 127.6, 126.2, 116.4, 113.9, 107.3, 101.8, 63.9, 61.9, 53.1; MS (ES^+) *m/z* 285.1594 ($[M+2H]^{2+}$, 100%), where M = $C_{34}H_{42}N_4O_4^{2+}$.

7.1.4 Cobalt Salnaph Complexes (4a-4e)



Cobalt salnaph complexes with different axial ligands were synthesised via the same general procedure. Briefly, cobalt (II) acetate tetrahydrate (17 mg, 0.07 mmol) was added to a solution of salnaph ligand (50 mg, 0.07 mmol, 1 eq.) in methanol (10 mL), resulting in a colour change from yellow to dark red. The desired axial ligand (0.70 mmol, 10 eq.) was added and the mixture was stirred for 5 hr in air. NH_4PF_6 (> 10 eq.) was then added, resulting in the formation of a precipitate which was separated via centrifugation and washed with water (3 x 5 mL) and DCM (3 x 5 mL) to give the desired product.

4a: L = methylamine

Yellow-orange solid, 74 mg, 0.07 mmol, 96%.

Elem. Anal. Found: C, 36.6; H, 4.39; N, 7.48. $C_{36}H_{49}CoN_6O_4P_3F_{18}.3H_2O$ requires C, 36.72; H, 4.71; Co, 5.00; F, 29.04; N = 7.14; O, 9.51; P, 7.89%; ^{1}H NMR (400 MHz, DMSO-d_6) δ 8.99 (s, 2H, -N=C<u>H</u>-), 8.85 (s, 2H, Ar-<u>H</u>), 8.03 – 7.95 (m, 2H, Ar-<u>H</u>), 7.61 (m, 4H, Ar-<u>H</u>), 6.76 (s, 2H, Ar-<u>H</u>), 6.43 (d, *J* = 8.9 Hz, 2H, Ar-<u>H</u>), 4.55 (br, 4H, -O-C<u>H$_2$</u>-), 3.83 (br, 4H, -C<u>H$_2$</u>-NMe$_3$), 3.71 – 3.65 (m, 4H, -N<u>H$_2$</u>CH$_3$), 3.21 (s, 18H, -(C<u>H$_3$</u>)$_3$), 1.40 (t, *J* = 6.4 Hz, 6H, -NH$_2$C<u>H$_3$</u>); MS (ES$^+$) *m/z* 417.1392 ([M+PF_6^-+2H]$^{2+}$, 45%), 367.1545 ([M+2Na]$^{2+}$, 100%), where M = $C_{36}H_{49}CoN_6O_4^{3+}$.

4b: L = pyridine

Dark red solid, 63 mg, 0.05 mmol, 74%.

Elem. Anal. Found: C, 41.75; H, 4.13; N, 6.45. $C_{44}H_{50}CoN_6O_4P_3F_{18}.3H_2O$ requires C, 41.46; H, 4.43; Co, 4.62; F, 26.83; N = 6.59; O, 8.79; P, 7.29%; ^{1}H NMR (400 MHz, DMSO-d_6) δ 9.07 (s, 2H, -N=C<u>H</u>-), 8.84 (s, 2H, Ar-<u>H</u>), 8.06 – 7.96 (m, 6H, Ar-<u>H</u>), 7.90 – 7.81 (m, 2H, Ar-<u>H</u>), 7.64 (dd, *J* = 6.3, 3.1 Hz, 2H, Ar-<u>H</u>),

7.51 (d, *J* = 9.1 Hz, 2H, Ar-H), 7.36 (m, 4H, Ar-H), 6.88 (s, 2H, Ar-H), 6.39 (d, *J* = 9.1 Hz, 2H, Ar-H), 4.54 (t, 4H, -O-CH$_2$-), 3.81 (t, 4H, -CH$_2$-NMe$_3$), 3.19 (s, 18H, -(CH$_3$)$_3$); MS (ES$^+$) *m/z* 465.1379 ([M+PF$_6^-$+2H]$^{2+}$, 70%), 415.1526 ([M+2Na]$^{2+}$, 100%), where M = $C_{44}H_{50}CoN_6O_4^{3+}$.

4c: L = pyrrolidine

Yellow-orange solid, 65 mg, 0.05 mmol, 79%.

Elem. Anal. Found: C, 41.68; H, 4.75; N, 6.87. $C_{42}H_{58}CoN_6O_4P_3F_{18}$ requires C, 41.87; H, 4.85; Co, 4.89; F, 28.38; N = 6.98; O, 5.38; P, 7.71%; ^{1}H NMR (400 MHz, DMSO-d$_6$) δ 9.04 (s, 2H, -N=CH-), 8.93 (s, 2H, Ar-H), 8.01 (m, 2H, Ar-H), 7.67-7.59 (m, 4H, Ar-H), 6.81 (d, *J* = 2.4 Hz, 2H, Ar-H), 6.45 (dd, *J* = 8.8 Hz, 2.4 Hz, 2H, Ar-H), 4.56 (s, 4H, -O-CH$_2$-), 4.45 (s, 4H, -NH-), 3.83 (s, 4H, -CH$_2$-NMe$_3$), 3.21 (s, 18H, -(CH$_3$)$_3$), 2.19 (m, 4H, -NH-CH$_2$-), 1.96 (m, 4H, -NH-CH$_2$-), 1.34 (br, 6H, -NH-CH$_2$-CH$_2$-); MS (ES$^+$) *m/z* 407.2071 ([M+2Na]$^{2+}$, 100%), where M = $C_{42}H_{58}CoN_6O_4^{3+}$.

4d: L = ammonia

Yellow-orange solid, 56 mg, 0.05 mmol, 75%.

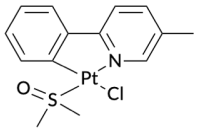
Elem. Anal. Found: C, 37.12; H, 4.18; N, 7.56. $C_{34}H_{46}CoN_6O_4P_3F_{18}$ requires C, 37.24; H, 4.23; Co, 5.37; F, 31.18; N = 7.66; O, 5.84; P, 8.47%; ^{1}H NMR (400 MHz, DMSO-d$_6$) δ 8.92 (s, 2H, -N=CH-), 8.82 (s, 2H, Ar-H), 7.99-7.96 (m, 2H, Ar-H), 7.61-7.57 (m, 4H, Ar-H), 6.69 (d, *J* = 2.2 Hz, 2H, Ar-H), 6.42-6.39 (m, 2H, Ar-H), 4.53 (s, 4H, -O-CH$_2$-), 3.82 (s, 4H, -CH$_2$-NMe$_3$), 3.20 (s, 18H, -(CH$_3$)$_3$), 2.77 (s, 6H, -NH$_3$); MS (ES$^+$) *m/z* 403.1255 ([M+PF$_6^-$+2H]$^{2+}$, 35%), 353.1585 ([M+2Na]$^{2+}$, 100%), where M = $C_{34}H_{46}CoN_6O_4^{3+}$.

4e: L = benzylamine

Brown solid, 81 mg, 0.06 mmol, 92%.

Elem. Anal. Found: C, 44.58; H, 4.58; N, 6.35. $C_{48}H_{58}CoN_6O_4P_3F_{18}.H_2O$ requires C, 44.52; H, 4.67; Co, 4.55; F, 26.41; N = 6.49; O, 6.18; P, 7.18%; ^{1}H NMR (400 MHz, DMSO-d$_6$) δ 8.92 (s, 2H, -N=CH-), 8.80 (s, 2H, Ar-H), 7.98 (s, 2H, Ar-H), 7.67-7.56 (m, 4H, Ar-H), 7.14 (s, 6H, Ar-H), 6.99 (s, 4H, Ar-H), 6.92 (s, 2H, Ar-H), 6.45 (d, *J* = 8.7 Hz, 2H, Ar-H), 4.57 (s, 4H, -O-CH$_2$-), 3.86 (m, 8H, -CH$_2$-NMe$_3$, -NH$_2$-CH$_2$-), 3.21 (s, 18H, -(CH$_3$)$_3$); MS (ES$^+$) *m/z* 443.1873 ([M+2Na]$^{2+}$, 100%), 280.4556 ([M+3H]$^{3+}$, 80%), where M = $C_{48}H_{58}CoN_6O_4^{3+}$.

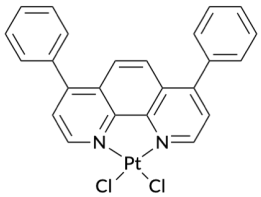
7.1.5 [Pt(5-methyl-2-phenylpyridine)(DMSO)Cl] (5)



First, 5-methyl-2-phenylpyridine was synthesised by adding phenylboronic acid (357 mg, 3.00 mmol) to 2-bromo-5-methylpyridine (351 mg, 2.04 mmol), K_2CO_3 (552 mg, 4.00 mmol) and $Pd(OAc)_2$ (6.91 mg, 0.031 mmol) in water (8 mL) and ethanol (24 mL).[319] The mixture was stirred at 80 °C in air for 30 mins, resulting in a dark brown solution. Brine (20 mL) was added and the solution was extracted with EtOAc (3 x 15 mL). The organic layers were concentrated to give 5-methyl-2-phenylpyridine as a cream solid (329 mg, 1.94 mmol, 95%). [Pt(5-methyl-2-phenylpyridine)(DMSO)Cl] was synthesised by adding K_2PtCl_4 (125 mg, 0.30 mmol) in water (1.25 mL) to a degassed solution of 5-methyl-2-phenylpyridine (50 mg, 0.30 mmol) in 2-ethoxyethanol (3.75 mL).[320] The mixture was heated at 60 °C for 24 hrs under nitrogen, resulting in a dark yellow-brown solution. Water (15 mL) was added to the reaction mixture until a green-brown solid precipitated. This solid was filtered, washed with ethanol (3 x 10 mL) and then dissolved in DMSO (2 mL) to give a dark brown solution. Addition of water (15 mL) gave a light grey solution. The mixture was filtered and dried to give the product as grey flakes (71.6 mg, 0.15 mmol, 50%).

Elem. Anal. Found: C, 35.43; H, 3.21; N, 2.82. $C_{14}H_{16}ClNOPtS$ requires C, 35.26; H, 3.38; Cl, 7.43; N, 2.94; O, 3.35; Pt, 40.91; S, 6.72%; ^{1}H NMR (400 MHz, $CDCl_3$) δ 9.43 (s, 1H, Ar-H), 8.34 (dd, 1H, Ar-H), 7.67 (dd, 1H, Ar-H), 7.63 (d, 1H, Ar-H), 7.48 (dd, 1H, Ar-H), 7.22-7.16 (m, 2H, Ar-H), 3.65 (s, 6H, -S-(CH_3)$_2$), 2.42 (s, 3H, CH_3).

7.1.6 [Pt(4,7-diphenyl-1,10-phenanthroline)Cl_2] (6)



[Pt(4,7-diphenyl-1,10-phenanthroline)Cl_2] was synthesised following protocols adapted from Shahabadi *et al.* and Wang *et al.*[248,321] K_2PtCl_4 (50.0 mg, 0.12 mmol) was first added to a solution of DMSO (25 mL)

in water (0.5 mL). The solution was stirred for 3 hrs at room temperature until white crystals precipitated. The crystals were isolated, washed with water, ethanol and diethyl ether (3 x 5 mL), and then dried to give $Pt(DMSO)_2Cl_2$ as white needles (35.6 mg, 0.084 mmol, 70%). $Pt(DMSO)_2Cl_2$ (35.0 mg, 0.083 mmol) was added to 4,7-diphenyl-1,10-phenanthroline (27.6 mg, 0.083 mmol) in methanol (4.5 mL). The mixture was heated under reflux for 3 hrs, resulting in the formation of a yellow precipitate. The solid was isolated, washed with methanol and diethyl ether (3 x 5 mL), and then dried to give the desired product as a yellow solid (42 mg, 0.070 mmol, 85%).

Elem. Anal. Found: C, 48.66; H, 2.63; N, 4.69. $C_{24}H_{16}Cl_2N_2Pt$ requires C, 48.17; H, 2.70; Cl, 11.85; N, 4.68%; ^{1}H NMR (400 MHz, DMSO-d_6) δ 9.51 (d, *J* = 5.7 Hz, 2H, Ar-H), 8.11 (s, 2H, Ar-H), 8.09 (d, *J* = 5.7 Hz, 2H, Ar-H), 7.77-7.66 (m, 10H, Ar-H).

7.1.7 Stability of Cobalt Salnaphs in Aqueous Solution

The NMR spectra of each complex (500 μM) were recorded at 0, 2, 4, 8, 24 and 48 hrs in 1:9 D_2O:phosphate-buffered saline (pH 7.4; 137 mM NaCl, 2.7 mM KCl, 8 mM Na_2HPO_4 and 2 mM KH_2PO_4) by Mr. P. Haycock using standard water suppression techniques. The ratio of complex with axial ligands:complex without axial ligands was determined by comparing the integrals of the relevant peaks and used to calculate the abundance of each species over time.

7.2 PREPARATION OF AMYLOID BETA PEPTIDE

All amyloid beta peptides (Aβ1-42, Aβ1-28, H6R Aβ1-28 or Aβ1-16) were bought from Cambridge Research Biochemicals and treated with 10% (w/v) NH_4OH to remove any aggregates following reported protocols.[265] Briefly, 1 mg of lyophilised peptide was dissolved in 200 μL of NH_4OH, incubated at 25 °C for 10 mins, sonicated for 5 mins and then aliquoted into known amounts. The NH_4OH was removed by lyophilisation to give a fluffy white solid. The dry peptide was stored at -80 °C and each aliquot was used only once. Before use, peptide aliquots were dissolved in 60 mM NaOH to a stock concentration of 200 μM and then diluted to the desired concentration with phosphate-buffered saline (pH 7.4; 137 mM NaCl, 2.7 mM KCl, 8 mM Na_2HPO_4 and 2 mM KH_2PO_4). Peptide concentrations were determined by UV-Vis spectroscopy using an extinction coefficient of 1490 cm^{-1} M^{-1} at 280 nm.[322,323]

	Peptide Sequence
Aβ1-16	DAEFRHDSGYEVHHQK
Aβ1-28	DAEFRHDSGYEVHHQKLVFFAEDVGSNK
H6R Aβ1-28	DAEFR**R**DSGYEVHHQKLVFFAEDVGSNK
Aβ1-42	DAEFRHDSGYEVHHQKLVFFAEDVGSNKGAIIGLMVGGVVIA

Table 7.1: Peptide sequences used.

7.3 IN VITRO EXPERIMENTS

7.3.1 Thioflavin-T Assay

Complexes were dissolved in DMSO:phosphate-buffered saline (pH 7.4; 137 mM NaCl, 2.7 mM KCl, 8 mM Na_2HPO_4 and 2 mM KH_2PO_4) to give stock solutions of the required concentrations. The final percentage of DMSO was 1% in all cases. The metal complex (20 μL) was added to Aβ1-42 (10 μL, 20 μM) and ThT (10 μL, 80 μM). The final concentrations of ThT and Aβ1-42 were 20 μM and 5 μM respectively, and final [Aβ1-42]:[complex] ratios were 1:0.2, 1:0.1, 1:0.07, 1:0.05 and 1:0.04. Samples were incubated at 37 °C with shaking every 5 mins for 10 secs in a 384 well-plate. After each round of shaking, the fluorescence emission at 485 nm when excited at 442 nm was recorded using a Perkin Elmer EnVision plate reader. All samples were run in triplicate and a positive (10 μM of complex **5** or **6**) and negative (no complex) control was included in every run. The emission values recorded for Aβ1-42 by itself over time were fitted to a sigmoidal curve using MATLAB and the values at the end-point were used to calculate the % inhibition values. For all complexes, the data reported is the mean ± standard deviation of three independent experiments.

7.3.2 Transmission Electron Microscopy

A solution of 10 μM Aβ1-42 was incubated with 10 μM complex for 48 hrs at 37 °C. 5 μL of the mixture was drop-casted onto a carbon-coated grid and then negatively-stained with 5 μL of uranyl acetate. Images were acquired by Dr. J. Barrit (Imperial College London) on a Tecnai Spirit TWIN TEM microscope at 52,000x magnification and with -2 micron defocus. All grid screening was conducted blind to avoid bias.

7.3.3 Fluorescence Spectroscopy

A solution of 150 μM Aβ1-16 in phosphate-buffered saline (pH 7.4; 137 mM NaCl, 2.7 mM KCl, 8 mM Na_2HPO_4 and 2 mM KH_2PO_4) was titrated with increasing concentrations of metal complexes (11.3 μM to 112.5 μM; 0 to 0.75 eq.) After each addition, the fluorescence emission between 285-400 nm was recorded using a Cary Eclipse Fluorescence Spectrophotometer using an excitation wavelength of 280 nm. Emission values at 310 nm (λ_{max}) were normalised to the emission recorded for Aβ1-16 without any complex added. All samples were measured in triplicate, with cisplatin included as a negative control.

7.3.4 ^{1}H NMR Spectroscopy of Aβ

^{1}H NMR spectroscopy was run with the wild-type (WT) Aβ1-28 peptide (DAEFRHDSGYEVHHQKLVFFAEDVGSNK) and the H6R point-mutated peptide (DAEFR**R**DSGYEVHHQKLVFFAEDVGSNK). Samples of WT Aβ1-28 or H6R Aβ1-28 (100 μM) in 1:9 D_2O:phosphate-buffered saline (pH 7.4; 137 mM NaCl, 2.7 mM KCl, 8 mM Na_2HPO_4 and 2 mM KH_2PO_4) were incubated at 37 °C in the presence and absence of metal complex (100 μM). ^{1}H NMR spectra were recorded at various time-points (t = 0 to 24 hr) on a 600 MHz Bruker Avance III HD NMR spectrometer at 298 K using standard water suppression techniques.

7.3.5 Circular Dichroism

Solutions of Aβ1-42 (20 μM) in phosphate-buffered saline (pH 7.4; 137 mM NaCl, 2.7 mM KCl, 8 mM Na_2HPO_4 and 2 mM KH_2PO_4) were incubated at 37 °C for 48 hrs in the presence or absence of metal complex (20 μM). Circular dichroism spectra were recorded in 1 cm quartz cuvettes on a JASCO J-810 circular dichroism spectrophotometer. Spectra were collected between 200 to 260 nm and the data was averaged over two independent experiments.

7.4 CELLULAR STUDIES

Human neuroblastoma (SH-SY5Y) and prostate cancer (PC3) cells were cultured in Dulbecco's Modified Eagle Medium (DMEM) supplemented with F-12 nutrient mix and 10% foetal calf serum (FBS) at 37 °C

and 5% CO_2. Before each assay, cells were seeded at an appropriate density in a 96-well plate (SH-SY5Y: 2,500 cells/well; PC3: 5,000 cells/well) and incubated for 24 hrs.

7.4.1 Cytotoxicity of Complexes

SH-SY5Y cells were incubated with differing concentrations of complex (20, 10, 5, 2.5, 1.25, 0.625 μM) for 24 hrs. Cytotoxicity was evaluated using a colorimetric assay following manufacturer's protocols (CellTiter 96 Aqueous One Solution Cell Proliferation Assay): 2 mL of [3-(4,5-dimethylthiazol-2-yl)-5-(3-carboxymethoxyphenyl)-2-(4-sulphophenyl)-2*H*-tetrazolium, inner salt] (MTS) was first mixed with 100 μL of phenazine methosulphate (PMS). 20 μL of the MTS/PMS mixture was then added to each well and the plate was incubated for 2 hrs. The absorbance at 492 nm was recorded using a Thermo Scientific Varioskan LUX multimode microplate reader. Wells containing MTS/PMS in media (no cells) were used as a blank and their average absorbance was subtracted from all sample wells. All data is reported as the mean ± standard deviation of three independent experiments.

7.4.2 Cytotoxicity of 4b

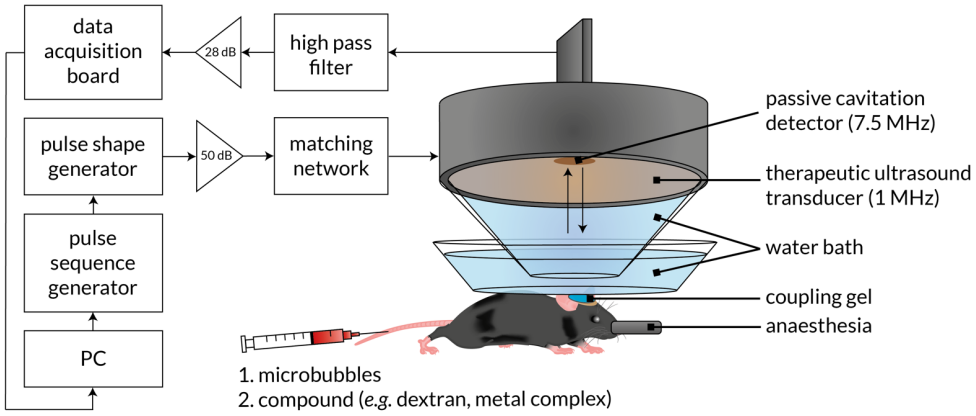
SH-SY5Y and PC3 cells were incubated with differing concentrations of complex (100, 50, 25, 12.5, 6.25, 3.125 μM) for 24 hrs. Cytotoxicity was evaluated using a colorimetric assay as described previously, with the exception that media was removed from all wells and replaced with MTS/PMS-containing media to avoid any interference from the added complexes. Plates were then incubated for 2 hrs (SH-SY5Y) or 3 hrs (PC3). The absorbance at 492 nm was recorded using a Thermo Scientific Varioskan LUX multimode microplate reader. Wells containing MTS/PMS in media (no cells) were used as a blank and their average absorbance was subtracted from all sample wells. All data is reported as the mean ± standard deviation of three independent experiments.

7.4.3 Cytotoxicity of Aβ1-42

Aβ1-42 was either pre-incubated in a shaking incubator at 37 °C for 24 hrs or freshly dissolved in sterile phosphate-buffered saline (pH 7.4; 137 mM NaCl, 2.7 mM KCl, 8 mM Na_2HPO_4 and 2 mM KH_2PO_4). SH-SY5Y cells were incubated with differing concentrations of Aβ1-42 (15, 12, 10, 8, 5 μM) for 4, 24 or 48 hrs.

Cytotoxicity was evaluated using the MTS assay as above. All data is reported as the mean ± standard deviation of three independent experiments.

8.1 ULTRASOUND SETUP



Ultrasound pulses were emitted from a Sonic Concepts single-element, spherical-segment focused ultrasound transducer (centre frequency: 1 MHz, active diameter: 90 mm, geometric focus: 77 mm) driven by Agilent Technologies 33500B function generators through a Precision Acoustics 50 dB power amplifier. The lateral, elevational and axial full width at half maximum (FWHM) at the focus were 2 mm, 1 mm and 20 mm respectively. Microbubble emissions were captured using an Olympus Industrial focused passive cavitation detector (centre frequency: 7.5 MHz, focal length: 76.2 mm) aligned co-axially with the FUS transducer, filtered using a Mini Circuits 3-30 MHz band-pass filter, amplified with a Stanford Research Systems 28 dB pre-amplifier and then recorded with a Pico Technology Picoscope 3205A 8-bit oscilloscope sampling at 250 MHz. Transducers were mounted onto a 3D positioning system to allow targeting of the desired region; in all experiments, the left hippocampus of the brain was targeted by positioning the transducer 3 mm laterally from the sagittal suture and 0.5 mm above the lambdoid suture. The right hippocampus was used as the control. This ultrasound setup was used for all *in vivo* experiments reported in Chapter 4.

Before *in vivo* experiments, pressure amplitudes were measured using a Precision Acoustics needle hydrophone (diameter: 0.2 mm) in a degassed water tank. Peak-positive and peak-negative values were attenuated by 11% to correct for skull attenuation.[86]

8.2 RAPID SHORT PULSE SEQUENCES

In vivo experiments conducted for the RaSP study were done with S. Morse, Dr. A. Pouliopoulos, M. Copping and J. Lin (PhD and MRes students, NSB Lab). All quantitative analysis was performed by S. Morse. The mouse was sonicated using long pulse or rapid short pulse sequences (long pulses = frequency: 1 MHz, peak-negative pressure: 350 kPa, pulse length: 10,000 cycles, pulse repetition frequency: 0.5 Hz, sonication duration: 250 s; RaSP = frequency: 1 MHz, peak-negative pressure: 350 kPa, pulse length: 5 cycles, pulse repetition frequency: 1.25 kHz, burst length: 10 ms, burst repetition frequency: 0.5 Hz, sonication duration: 250 s). After five pulses, SonoVue microbubbles (100 µL, 5 µL/g) were administered over a period of approximately half a minute. As soon as the microbubbles had been injected, Texas Red-labelled 3 kDa dextran (100 µL, 2 mg) was administered intravenously into the mouse *via* a tail vein catheter at 0, 10 or 20 mins following ultrasound exposure (n = 5 for each pulse sequence at t = 0 mins; n = 3 for each pulse sequence at t = 10 and 20 mins). Following sonication, mice were sacrificed and transcardially perfused with 20 mL ice-cold phosphate-buffered saline (pH 7.4; 137 mM NaCl, 2.7 mM KCl, 8 mM Na_2HPO_4 and 2 mM KH_2PO_4) with added heparin (10 units/mL) to reduce blood coagulation. Once the blood was cleared, mice were fixed with 20 mL ice-cold 10% formalin solution. Brains were extracted, submerged in 10 mL 10% formalin solution at 4 °C overnight and then cryoprotected by immersing in 15% sucrose for 6 hrs, followed by 30% sucrose overnight. The normalised optical density (NOD), the average fluorescence intensity in the targeted region, and the coefficient of variation, the ratio of the standard deviation to the mean fluorescence pixel intensity in the targeted region, was calculated from fluorescence images by S. Morse (PhD student, NSB Lab).

8.3 LASER ABLATION INDUCTIVELY COUPLED PLASMA MASS SPECTROMETRY

The ultrasound setup and general animal procedures are identical to those reported above. The mouse was sonicated using RaSP ultrasound pulses (frequency: 1 MHz, peak-negative pressure: 350 kPa, pulse length: 5 cycles, pulse repetition frequency: 1.25 kHz, burst length: 10 ms, burst repetition frequency: 0.5 Hz, sonication duration: 250 s). After five pulses, SonoVue microbubbles (100 µL, 5 µL/g) were administered over a period of approximately half a minute. For experiments with complex **1**, complex **1** (5 µL, 10 mM) was then administered intravenously into the mouse *via* a tail vein catheter. Following sonication, mice were sacrificed and transcardially perfused with 20 mL ice-cold phosphate-buffered saline (pH 7.4; 137 mM NaCl, 2.7 mM KCl, 8 mM Na_2HPO_4 and 2 mM KH_2PO_4) with added heparin (10 units/mL) to reduce blood

coagulation. Once the blood was cleared, mice were fixed with 20 mL ice-cold 10% formalin solution. Brains were extracted, submerged in 10 mL 10% formalin solution at 4 °C overnight and then cryoprotected by immersing in 15% sucrose for 6 hrs, followed by 30% sucrose overnight. Cryoprotected brains were sectioned into 30 µm sections and imaged using a Zeiss Axio Observer Inverted Widefield microscope in the GFP channel (excitation wavelength: 470 nm, excitation filter: 470/40 nm, emission filter: 525/50 nm) prior to LA-ICP-MS.

For experiments with complex **4c**, the same experimental procedure as above was followed, except that Texas Red-labelled 3 kDa dextran (100 µL, 0.6 mg) and complex **4c** (5 µL, 10 mM) were mixed and administered intravenously into the mouse *via* a tail vein catheter. Prior to LA-ICP-MS, brain sections were imaged using a Zeiss Axio Observer Inverted Widefield microscope in the Texas Red channel (excitation wavelength: 575 nm, excitation filter: 562/40 nm, emission filter: 624/40 nm) to detect the presence of Texas Red-labelled 3 kDa dextran and thus, the site of BBB disruption.

8.3.1 LA-ICP-MS

Brain sections showing BBB disruption were analysed using LA-ICP-MS with Mr. B. Sampson (Imperial College London) using an Agilent 7900 quadrupole-based inductively coupled plasma mass spectrometer coupled to a New Wave UP213 laser ablation system. Laser ablation was performed using a focused laser beam in scanning mode with a series of ~65 lines of ~10 mm long, giving a total ablated area of approximately 10 mm x 10 mm. The spot size used was 65 µm. Distribution maps of the isotopes of interest were plotted using MATLAB.

8.4 SAFETY OF REPEATED TREATMENTS

Cobalt salnaph **4b** at two different concentrations (30 mg/kg and 23 mg/kg) was delivered to the left hippocampus of wild-type C57BL/6J mice (n = 2) once a week for four weeks (Figure 8.1). The body weight and behaviour of the treated mice were closely monitored according to standard procedures.

The left hippocampus of the mouse was sonicated using ultrasound pulses (frequency: 1 MHz, peak-negative pressure: 350 kPa, pulse length: 5 cycles, pulse repetition frequency: 1.25 kHz, burst length: 10 ms, burst repetition frequency: 0.5 Hz, sonication duration: 250 s). After five pulses, SonoVue microbubbles (100 µL, 5 µL/g) were administered *via* a tail vein catheter, followed by cobalt salnaph **4b** (100 µL, 30 or 23 mg/kg).

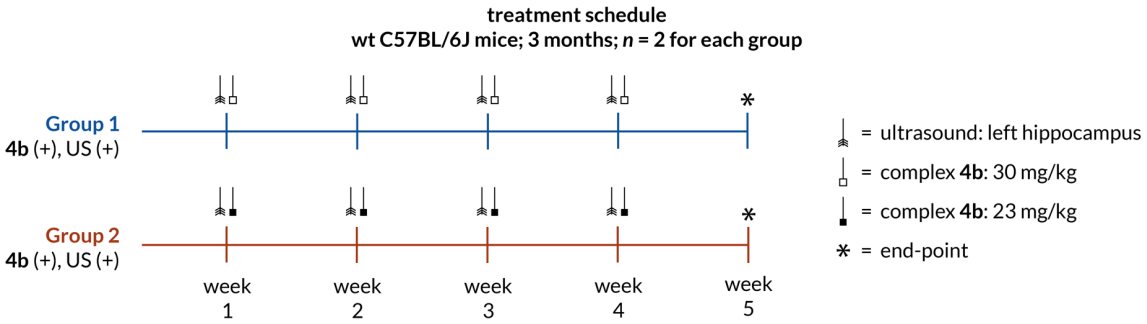


Figure 8.1: Summary of treatment schedule and treatment conditions. Wild-type C57BL/6J mice were treated with ultrasound and cobalt salnaph **4b** at either 30 mg/kg or 23 mg/kg once a week for four weeks (n = 2 mice per group). Body weight was recorded every week.

At the treatment end-point, mice were sacrificed and transcardially perfused with 20 mL ice-cold phosphate-buffered saline (pH 7.4; 137 mM NaCl, 2.7 mM KCl, 8 mM Na_2HPO_4 and 2 mM KH_2PO_4) with added heparin (10 units/mL). Once the blood was cleared, mice were fixed with 20 mL ice-cold 10% formalin solution. Brains were extracted and submerged in 10 mL 10% formalin solution at 4 °C. To assess safety, brains were paraffin-embedded and stained with H&E by the UCL IQPath laboratories.

8.5 PRELIMINARY STUDY IN 5XFAD MICE

Transgenic 5xFAD mice (n = 9, 4 to 5 months) were kindly provided by Dr. M. Sastre (Imperial College London). Mice were split into three treatment groups: Group 1 (no treatment), Group 2 (ultrasound only) and Group 3 (ultrasound + complex **4b**). Mice were treated once a week for three weeks and were monitored for any changes in behaviour or weight loss according to standard procedures (Figure 8.2).

The left hippocampus of the mouse was sonicated using ultrasound pulses (frequency: 1 MHz, peak-negative pressure: 350 kPa, pulse length: 5 cycles, pulse repetition frequency: 1.25 kHz, burst length: 10 ms, burst repetition frequency: 0.5 Hz, sonication duration: 250 s). After five pulses, SonoVue microbubbles (100 µL, 5 µL/g) were administered *via* a tail vein catheter, followed by cobalt salnaph **4b** (100 µL, 30 mg/kg).

At the treatment end-point, mice were sacrificed and transcardially perfused with 20 mL ice-cold phosphate-buffered saline (pH 7.4; 137 mM NaCl, 2.7 mM KCl, 8 mM Na_2HPO_4 and 2 mM KH_2PO_4) with added heparin (10 units/mL). Once the blood was cleared, mice were fixed with 20 mL ice-cold 10% formalin solution. Brains were extracted, submerged in 10 mL 10% formalin solution at 4 °C overnight and then

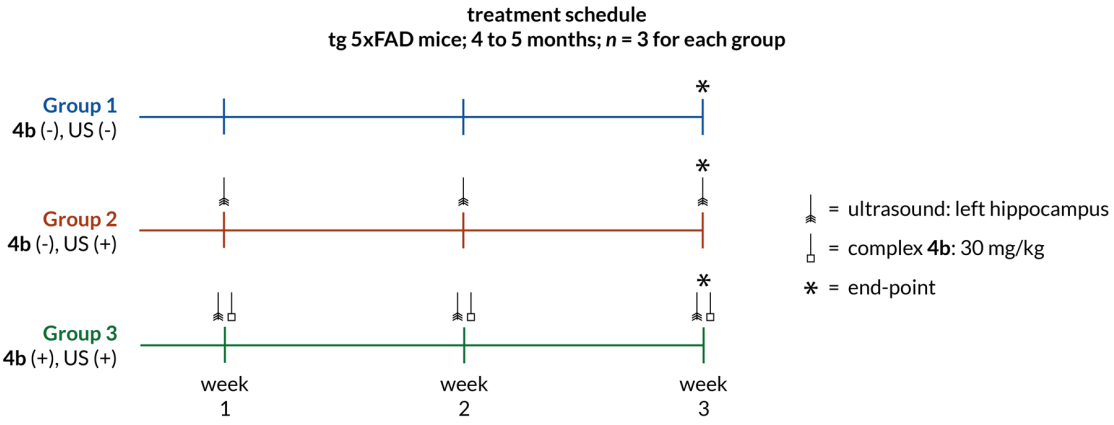


Figure 8.2: Summary of treatment schedule and treatment conditions. A total of *n* = 9 transgenic 5xFAD mice were used in this study, *n* = 3 mice per group.

cryoprotected by immersing in 15% sucrose for 6 hrs, followed by 30% sucrose overnight. Samples were cryosectioned into 20 µm sections, allowed to air-dry and then stained for albumin or amyloid beta (*via* ThS or MOAB-2 staining). Fluorescence images were analysed using ImageJ as described below.

8.5.1 Albumin Staining

Brain sections (20 µm) covering the entirety of the focal volume were stained for albumin to locate the site of BBB opening in Groups 2 and 3. Slides were first washed with tris-buffered saline (TBS) for 2 x 5 mins and then blocked with a TBS solution containing 1% bovine serum albumin (BSA), 0.1% Triton X and 5% normal goat serum for 1 hr. The primary antibody, rabbit anti-mouse serum albumin, was diluted 1:100 in TBS containing 0.01% Triton X and 0.1% BSA and applied to the sections for 18 hrs at 4 °C. After washing thoroughly with TBS, the secondary antibody, goat anti-rabbit IgG Alexa Fluor 647, was diluted 1:200 in TBS containing 0.01% Triton X and 0.1% BSA and applied to the slides for 2 hrs at 25 °C. Slides were washed with TBS for 3 x 5 mins, stored overnight in the fridge and then imaged on a fluorescence microscope in the Alexa Fluor 647 channel (excitation wavelength: 640 nm, excitation filter: 640/30 nm, emission filter: 690/50 nm).

8.5.2 Thioflavin-S Staining

Ten sections from each brain around the site of BBB opening were stained with ThS. Brain sections were incubated in a filtered solution of 1% (w/v) ThS in 70% ethanol for 10 min at 25 °C, washed with 70% ethanol for 3 x 5 mins and then washed with phosphate-buffered saline (pH 7.4; 137 mM NaCl, 2.7 mM KCl, 8 mM Na_2HPO_4 and 2 mM KH_2PO_4) for 5 mins. Stained sections were imaged on a fluorescence microscope in the Alexa Fluor 488 channel (excitation wavelength: 470 nm, excitation filter: 470/40 nm, emission filter: 525/50 nm).

8.5.3 MOAB-2 Staining

Ten sections from each brain around the site of BBB opening were stained with MOAB-2. Brain sections were washed with TBS for 3 x 5 mins and then blocked using a TBS solution containing 1% BSA and 0.1% Triton X for 1 hr. A solution of mouse anti-beta amyloid antibody MOAB-2 (1:200) was prepared in TBS with 0.1% BSA and 0.01% Triton X and applied to the sections overnight at 4 °C. After washing with TBS for 3 x 5 mins, sections were incubated with a solution of goat anti-mouse IgG Alexa Fluor 647 (1:500) in TBS with 0.1% BSA and 0.01% Triton X for 2 hrs at 25 °C. Slides were washed with TBS for 3 x 5 mins, stored overnight in the fridge and then imaged on a fluorescence microscope in the Alexa Fluor 647 channel (excitation wavelength: 640 nm, excitation filter: 640/30 nm, emission filter: 690/50 nm).

8.5.4 Image Analysis: ThS & MOAB-2 Staining

A total of ten sections stained with ThS and ten sections stained with MOAB-2 were analysed to assess the amyloid burden. The region of interest, the left hippocampus, was first selected using ImageJ and any artefacts (*e.g.* tissue folds) were removed. Images were then thresholded and the percentage area (the percentage of pixels in the defined ROI that have an intensity greater than the applied threshold), number of particles and average particle size were determined using the automated 'Analyse Particles' function in ImageJ. The same threshold was used for all images and all analysis was done blind and repeated three times to prevent bias. To assess statistical significance, unpaired Student *t*-tests were performed between treatment groups ($p < 0.05$).

BIBLIOGRAPHY

(1) C. D. Arvanitis, G. B. Ferraro and R. K. Jain, *Nat. Rev. Cancer*, 2019, **20**, 26–41 (cit. on pp. 21, 23).

(2) J. Fenstermacher, P. Gross, N. Sposito, V. Acuff, S. Pettersen and K. Gruber, *Ann. N. Y. Acad. Sci.*, 1988, **529**, 21–30 (cit. on p. 21).

(3) B. L. Coomber and P. A. Stewart, *Microvasc. Res.*, 1985, **30**, 99–115 (cit. on p. 21).

(4) N. J. Abbott, *J. Anat.*, 2002, **200**, 629–638 (cit. on pp. 22, 24, 25).

(5) L. Xu, A. Nirwane and Y. Yao, *Stroke Vasc. Neurol.*, 2019, **4**, 78–82 (cit. on p. 22).

(6) Z. L. Chen, Y. Yao, E. H. Norris, A. Kruyer, O. Jno-Charles, A. Akhmerov and S. Strickland, *J. Cell Biol.*, 2013, **202**, 381–395 (cit. on p. 22).

(7) D. B. Gould et al., *Science*, 2005, **308**, 1167–1171 (cit. on p. 22).

(8) D. Bonkowski, V. Katyshev, R. D. Balabanov, A. Borisov and P. Dore-Duffy, *Fluids Barriers CNS*, 2011, **8**, 8 (cit. on p. 22).

(9) R. Daneman, L. Zhou, A. A. Kebede and B. A. Barres, *Nature*, 2010, **468**, 562–566 (cit. on p. 22).

(10) A. Armulik et al., *Nature*, 2010, **468**, 557–561 (cit. on p. 22).

(11) R. D. Bell, E. A. Winkler, A. P. Sagare, I. Singh, B. LaRue, R. Deane and B. V. Zlokovic, *Neuron*, 2010, **68**, 409–427 (cit. on p. 22).

(12) A. Reyahi, A. M. Nik, M. Ghiami, A. Gritli-Linde, F. Pontén, B. R. Johansson and P. Carlsson, *Dev. Cell*, 2015, **34**, 19–32 (cit. on p. 22).

(13) C. García-Cáceres et al., *Cell*, 2016, **166**, 867–880 (cit. on p. 22).

(14) H. Kubotera, H. Ikeshima-Kataoka, Y. Hatashita, A. L. Allegra Mascaro, F. S. Pavone and T. Inoue, *Sci. Rep.*, 2019, **9**, 1263 (cit. on p. 22).

(15) Y. Chen and R. A. Swanson, *J. Cereb. Blood Flow Metab.*, 2003, **23**, 137–149 (cit. on p. 22).

(16) N. J. Maragakis and J. D. Rothstein, *Nat. Clin. Pract. Neurol.*, 2006, **2**, 679–689 (cit. on p. 22).

(17) M. Zonta, M. C. Angulo, S. Gobbo, B. Rosengarten, K. A. Hossmann, T. Pozzan and G. Carmignoto, *Nat. Neurosci.*, 2003, **6**, 43–50 (cit. on p. 22).

(18) T. Takano, G. F. Tian, W. Peng, N. Lou, W. Libionka, X. Han and M. Nedergaard, *Nat. Neurosci.*, 2006, **9**, 260–267 (cit. on p. 22).

(19) O. B. Dimitrijevic, S. M. Stamatovic, R. F. Keep and A. V. Andjelkovic, *J. Cereb. Blood Flow Metab.*, 2006, **26**, 797–810 (cit. on p. 22).

(20) Y. Shigemoto-Mogami, K. Hoshikawa and K. Sato, *Front. Cell. Neurosci.*, 2018, **12**, 494 (cit. on p. 22).

(21) C. Herzog, L. P. Garcia, M. Keatinge, D. Greenald, C. Moritz, F. Peri and L. Herrgen, *Dev.*, 2019, **146**, dev174698 (cit. on p. 22).

(22) N. Levtova, L. M. Healy, C. M. C. Gonczi, B. Stopnicki, M. Blain, T. E. Kennedy, C. S. Moore, J. P. Antel and P. J. Darlington, *J. Neuroimmunol.*, 2017, **310**, 143–149 (cit. on p. 22).

(23) S. Prokop, K. R. Miller and F. L. Heppner, *Acta Neuropathol.*, 2013, **126**, 461–477 (cit. on p. 22).

(24) I. Napoli and H. Neumann, *Exp. Neurol.*, 2010, **225**, 24–28 (cit. on p. 22).

(25) C. M. Long-Smith, A. M. Sullivan and Y. M. Nolan, *Prog. Neurobiol.*, 2009, **89**, 277–287 (cit. on p. 22).

(26) J. Piorntek et al., *FASEB J.*, 2008, **22**, 146–158 (cit. on p. 22).

(27) J. Piontek et al., *Cell. Mol. Life Sci.*, 2011, **68**, 3903–3918 (cit. on p. 22).

(28) H. Wolburg et al., *Acta Neuropathol.*, 2003, **105**, 586–592 (cit. on p. 23).

(29) M. Castro Dias et al., *Fluids Barriers CNS*, 2019, **16**, 30 (cit. on p. 23).

(30) S. Ohtsuki, H. Yamaguchi, Y. Katsukura, T. Asashima and T. Terasaki, *J. Neurochem.*, 2008, **104**, 147–154 (cit. on p. 23).

(31) R. Daneman, L. Zhou, D. Agalliu, J. D. Cahoy, A. Kaushal and B. A. Barres, *PLoS One*, 2010, **5**, ed. T. Ikezu, e13741 (cit. on p. 23).

(32) T. Nitta, M. Hata, S. Gotoh, Y. Seo, H. Sasaki, N. Hashimoto, M. Furuse and S. Tsukita, *J. Cell Biol.*, 2003, **161**, 653–660 (cit. on p. 23).

(33) P. Polakis, *J. Cell Biol.*, 2008, **183**, 371–373 (cit. on p. 23).

(34) M. Saitou, M. Furuse, H. Sasaki, J. D. Schulzke, M. Fromm, H. Takano, T. Noda and S. Tsukita, *Mol. Biol. Cell*, 2000, **11**, ed. W. J. Nelson, 4131–4142 (cit. on p. 23).

(35) T. Hirase, S. Kawashima, E. Y. Wong, T. Ueyama, Y. Rikitake, S. Tsukita, M. Yokoyama and J. M. Staddon, *J. Biol. Chem.*, 2001, **276**, 10423–10431 (cit. on p. 23).

(36) J. K. Walter, C. Rueckert, M. Voss, S. L. Mueller, J. Piontek, K. Gast and I. E. Blasig, *Ann. N. Y. Acad. Sci.*, 2009, **1165**, 19–27 (cit. on p. 23).

(37) I. E. Blasig, C. Bellmann, J. Cording, G. D. Vecchio, D. Zwanziger, O. Huber and R. F. Haseloff, *Antioxidants Redox Signal.*, 2011, **15**, 1195–1219 (cit. on p. 23).

(38) G. Bazzoni, O. M. Martínez-Estrada, F. Orsenigo, M. Cordenonsi, S. Citi and E. Dejana, *J. Biol. Chem.*, 2000, **275**, 20520–20526 (cit. on p. 24).

(39) D. Yeung, J. L. Manias, D. J. Stewart and S. Nag, *Acta Neuropathol.*, 2008, **115**, 635–642 (cit. on p. 24).

(40) M. Giannotta, M. Trani and E. Dejana, *Dev. Cell*, 2013, **26**, 441–454 (cit. on p. 24).

(41) J. M. Halbleib and W. J. Nelson, *Genes Dev.*, 2006, **20**, 3199–3214 (cit. on p. 24).

(42) J. Gavard and S. J. Gutkind, *Nat. Cell Biol.*, 2008, **10**, 883–885 (cit. on p. 24).

(43) W. M. Pardridge, *Mol. Interv.*, 2003, **3**, 90–105 (cit. on p. 24).

(44) C. Cordon-Cardo, J. P. O'Brien, D. Casals, L. Rittman-Grauer, J. L. Biedler, M. R. Melamed and J. R. Bertino, *Proc. Natl. Acad. Sci. U. S. A.*, 1989, **86**, 695–698 (cit. on p. 24).

(45) F. J. Sharom, *Essays Biochem.*, 2011, **50**, ed. F. J. Sharom, 161–178 (cit. on pp. 24, 25).

(46) C. G. Lee et al., *J. Clin. Invest.*, 1998, **101**, 287–288 (cit. on pp. 24, 25).

(47) A. H. Schinkel et al., *Cell*, 1994, **77**, 491–502 (cit. on pp. 24, 25).

(48) W. M. Pardridge, *NeuroRx*, 2005, **2**, 3–14 (cit. on pp. 25, 32, 60, 62, 84, 109).

(49) E. G. Chikhale, K. Y. Ng, P. S. Burton and R. T. Borchardt, *Pharm. Res. An Off. J. Am. Assoc. Pharm. Sci.*, 1994, **11**, 412–419 (cit. on p. 25).

(50) V. A. Levin, *J. Med. Chem.*, 1980, **23**, 682–684 (cit. on p. 25).

(51) C. A. Lipinski, F. Lombardo, B. W. Dominy and P. J. Feeney, *Adv. Drug Deliv. Rev.*, 2001, **46**, 3–26 (cit. on pp. 25, 109).

(52) P. Calias, W. A. Banks, D. Begley, M. Scarpa and P. Dickson, *Pharmacol. Ther.*, 2014, **144**, 114–122 (cit. on p. 25).

(53) A. M. Cook, K. D. Mieure, R. D. Owen, A. B. Pesaturo and J. Hatton, *Pharmacotherapy*, 2009, **29**, 832–845 (cit. on p. 25).

(54) J. K. Chung, E. Brown, B. Crooker, K. J. Palmieri and T. G. McCauley, *PLoS One*, 2016, **11**, ed. M. A. Deli, e0164765 (cit. on p. 27).

(55) X. Q. Chen, J. R. Fawcett, Y. E. Rahman, T. A. Ala and W. H. Frey, *J. Alzheimer's Dis.*, 1998, **1**, 35–44 (cit. on p. 27).

(56) R. G. Thorne, C. R. Emory, T. A. Ala and W. H. Frey, *Brain Res.*, 1995, **692**, 278–282 (cit. on p. 27).

(57) R. G. Thorne, G. J. Pronk, V. Padmanabhan and W. H. Frey, *Neuroscience*, 2004, **127**, 481–496 (cit. on p. 27).

(58) T. Musumeci, A. Bonaccorso and G. Puglisi, *Pharmaceutics*, 2019, **11**, 118 (cit. on p. 27).

(59) H. Wu, K. Hu and X. Jiang, *Expert Opin. Drug Deliv.*, 2008, **5**, 1159–1168 (cit. on p. 27).

(60) R. Langer and J. Folkman, *Nature*, 1976, **263**, 797–800 (cit. on p. 27).

(61) H. Brem et al., *J. Neurosurg.*, 1991, **74**, 441–446 (cit. on p. 27).

(62) L. K. Fung, M. Shin, B. Tyler, H. Brem and W. M. Saltzman, *Pharm. Res.*, 1996, **13**, 671–682 (cit. on p. 27).

(63) S. I. Rapoport, M. Hori and I. Klatzo, *Am. J. Physiol.*, 1972, **223**, 323–331 (cit. on p. 27).

(64) S. I. Rapoport, *Cell. Mol. Neurobiol.*, 2000, **20**, 217–230 (cit. on p. 27).

(65) P. J. Robinson and S. I. Rapoport, *Am. J. Physiol. - Regul. Integr. Comp. Physiol.*, 1987, **253**, R459–R466 (cit. on p. 27).

(66) N. D. Doolittle et al., *Cancer*, 2000, **88**, 637–647 (cit. on p. 27).

(67) J. K. Burkhardt, H. Riina, B. J. Shin, P. Christos, K. Kesavabhotla, C. P. Hofstetter, A. J. Tsiouris and J. A. Boockvar, *World Neurosurg.*, 2012, **77**, 130–134 (cit. on p. 27).

(68) J. A. Boockvar et al., *J. Neurosurg.*, 2011, **114**, 624–632 (cit. on p. 27).

(69) N. Marchi et al., *Epilepsia*, 2007, **48**, 732–742 (cit. on p. 27).

(70) S. I. Rapoport, W. R. Fredericks, K. Ohno and K. D. Pettigrew, *Am. J. Physiol. - Regul. Integr. Comp. Physiol.*, 1980, **7**, 421–431 (cit. on p. 27).

(71) V. Mishra, S. Mahor, A. Rawat, P. N. Gupta, P. Dubey, K. Khatri and S. P. Vyas, *J. Drug Target.*, 2006, **14**, 45–53 (cit. on p. 27).

(72) K. C. Gatter, G. Brown, I. Strowbridge, R. E. Woolston and D. Y. Mason, *J. Clin. Pathol.*, 1983, **36**, 539–545 (cit. on p. 28).

(73) A. Pietrangelo, E. Rocchi, G. Casalgrandi, G. Rigo, A. Ferrari, M. Perini, E. Ventura and G. Cairo, *Gastroenterology*, 1992, **102**, 802–809 (cit. on p. 28).

(74) Z. M. Qian, H. Li, H. Sun and K. Ho, *Pharmacol. Rev.*, 2002, **54**, 561–587 (cit. on p. 28).

(75) N. Jahanshad et al., *Proc. Natl. Acad. Sci. U. S. A.*, 2012, **109**, E851–E859 (cit. on p. 28).

(76) P. A. Seligman, *Prog. Hematol.*, 1983, **13**, 131–147 (cit. on p. 28).

(77) A. R. Jones and E. V. Shusta, *Pharm. Res.*, 2007, **24**, 1759–1771 (cit. on p. 28).

(78) K. Hynynen, N. McDannold, N. Vykhodtseva and F. A. Jolesz, *Radiology*, 2001, **220**, 640–646 (cit. on pp. 28, 109).

(79) S. R. Sirsi and M. A. Borden, *Bubble Sci. Eng. Technol.*, 2009, **1**, 3–17 (cit. on p. 28).

(80) M. Schneider, *Echocardiography*, 1999, **16**, 743–746 (cit. on p. 28).

(81) M. Diez-Silva, M. Dao, J. Han, C.-T. Lim and S. Suresh, *MRS Bull.*, 2010, **35**, 382–388 (cit. on p. 28).

(82) R. E. Apfel, *J. Acoust. Soc. Am.*, 1997, **101**, 1227–1237 (cit. on p. 28).

(83) Z. Izadifar, P. Babyn and D. Chapman, *J. Med. Biol. Eng.*, 2019, **39**, 259–276 (cit. on p. 28).

(84) N. Sheikov, N. McDannold, N. Vykhodtseva, F. Jolesz and K. Hynynen, *Ultrasound Med. Biol.*, 2004, **30**, 979–989 (cit. on pp. 28, 29).

(85) M. Kinoshita, N. McDannold, F. A. Jolesz and K. Hynynen, *Biochem. Biophys. Res. Commun.*, 2006, **340**, 1085–1090 (cit. on pp. 28, 91).

(86) S. V. Morse, A. N. Pouliopoulos, T. G. Chan, M. J. Copping, J. Lin, N. J. Long and J. J. Choi, *Radiology*, 2019, **291**, 459–466 (cit. on pp. 28, 41, 46, 48, 87, 88, 91, 94, 100, 101, 107, 114, 128).

(87) T. G. Chan, S. V. Morse, M. J. Copping, J. J. Choi and R. Vilar, *ChemMedChem*, 2018, **13**, 1311–1314 (cit. on pp. 28, 35, 38, 86).

(88) N. Sheikov, N. McDannold, S. Sharma and K. Hynynen, *Ultrasound Med. Biol.*, 2008, **34**, 1093–1104 (cit. on pp. 28, 29).

(89) J. Park, Y. Zhang, N. Vykhodtseva, F. A. Jolesz and N. J. McDannold, *J. Control. Release*, 2012, **162**, 134–142 (cit. on p. 28).

(90) G. Samiotaki, F. Vlachos, Y. S. Tung and E. E. Konofagou, *Magn. Reson. Med.*, 2012, **67**, 769–777 (cit. on pp. 28, 88).

(91) N. McDannold, C. D. Arvanitis, N. Vykhodtseva and M. S. Livingstone, *Cancer Res.*, 2012, **72**, 3652–3663 (cit. on p. 28).

(92) H. Chen and E. E. Konofagou, *J. Cereb. Blood Flow Metab.*, 2014, **34**, 1197–1204 (cit. on pp. 28, 29, 33, 41, 43, 46, 50, 109).

(93) B. Baseri, J. J. Choi, Y. S. Tung and E. E. Konofagou, *Ultrasound Med. Biol.*, 2010, **36**, 1445–1459 (cit. on pp. 28, 46, 48).

(94) N. McDannold, N. Vykhodtseva and K. Hynynen, *Ultrasound Med. Biol.*, 2008, **34**, 834–840 (cit. on p. 28).

(95) N. McDannold, N. Vykhodtseva and K. Hynynen, *Ultrasound Med. Biol.*, 2008, **34**, 930–937 (cit. on p. 28).

(96) J. J. Choi, K. Selert, Z. Gao, G. Samiotaki, B. Baseri and E. E. Konofagou, *J. Cereb. Blood Flow Metab.*, 2011, **31**, 725–737 (cit. on pp. 28, 86).

(97) J. J. Choi, K. Selert, F. Vlachos, A. Wong and E. E. Konofagou, *Proc. Natl. Acad. Sci. U. S. A.*, 2011, **108**, 16539–16544 (cit. on pp. 28, 86).

(98) F. Y. Yang, W. M. Fu, W. S. Chen, W. L. Yeh and W. L. Lin, *Ultrason. Sonochem.*, 2008, **15**, 636–643 (cit. on p. 28).

(99) M. Aryal, K. Fischer, C. Gentile, S. Gitto, Y. Z. Zhang and N. McDannold, *PLoS One*, 2017, **12**, ed. M. Toborek, e0166061 (cit. on p. 29).

(100) J. J. Choi, S. Wang, Y. S. Tung, B. Morrison and E. E. Konofagou, *Ultrasound Med. Biol.*, 2010, **36**, 58–67 (cit. on pp. 29, 33, 43, 46, 91).

(101) N. Lipsman et al., *Nat. Commun.*, 2018, **9**, 2336 (cit. on p. 30).

(102) A. Abrahao et al., *Nat. Commun.*, 2019, **10**, 4373 (cit. on p. 30).

(103) A. M. Jhaveri and V. P. Torchilin, *Front. Pharmacol.*, 2014, **5 APR**, DOI: 10.3389/fphar.2014.00077 (cit. on p. 31).

(104) J. K. Patra et al., *J. Nanobiotechnology*, 2018, **16**, 71 (cit. on p. 31).

(105) A. S. Chauhan, *Molecules*, 2018, **23**, 938 (cit. on p. 31).

(106) C. E. Probst, P. Zrazhevskiy, V. Bagalkot and X. Gao, *Adv. Drug Deliv. Rev.*, 2013, **65**, 703–718 (cit. on p. 31).

(107) J. I. Cutler, E. Auyeung and C. A. Mirkin, *J. Am. Chem. Soc.*, 2012, **134**, 1376–1391 (cit. on p. 31).

(108) S. A. Jensen et al., *Sci. Transl. Med.*, 2013, **5**, 209ra152–209ra152 (cit. on pp. 31, 32, 34, 43, 112).

(109) G. P. Mitchell, C. A. Mirkin and R. L. Letsinger, *J. Am. Chem. Soc.*, 1999, **121**, 8122–8123 (cit. on pp. 31, 34).

(110) T. A. Taton, C. A. Mirkin and R. L. Letsinger, *Science*, 2000, **289**, 1757–1760 (cit. on p. 31).

(111) N. L. Rosi, D. A. Giljohann, C. S. Thaxton, A. K. Lytton-Jean, M. S. Han and C. A. Mirkin, *Science*, 2006, **312**, 1027–1030 (cit. on pp. 31, 50).

(112) D. Nykypanchuk, M. M. Maye, D. Van Der Lelie and O. Gang, *Nature*, 2008, **451**, 549–552 (cit. on p. 31).

(113) C. H. J. Choi, L. Hao, S. P. Narayan, E. Auyeung and C. A. Mirkin, *Proc. Natl. Acad. Sci. U. S. A.*, 2013, **110**, 7625–7630 (cit. on pp. 31, 32, 38, 50).

(114) X. A. Wu, C. H. J. Choi, C. Zhang, L. Hao and C. A. Mirkin, *J. Am. Chem. Soc.*, 2014, **136**, 7726–7733 (cit. on p. 32).

(115) D. S. Seferos, A. E. Prigodich, D. A. Giljohann, P. C. Patel and C. A. Mirkin, *Nano Lett.*, 2009, **9**, 308–311 (cit. on p. 32).

(116) M. D. Massich, D. A. Giljohann, D. S. Seferos, L. E. Ludlow, C. M. Horvath and C. A. Mirkin, *Mol. Pharm.*, 2009, **6**, 1934–1940 (cit. on p. 32).

(117) A. F. Radovic-Moreno et al., *Proc. Natl. Acad. Sci. U. S. A.*, 2015, **112**, 3892–3897 (cit. on p. 32).

(118) D. Bousmail, L. Amrein, J. J. Fakhoury, H. H. Fakih, J. C. Hsu, L. Panasci and H. F. Sleiman, *Chem. Sci.*, 2017, **8**, 6218–6229 (cit. on p. 32).

(119) O. Van Tellingen, B. Yetkin-Arik, M. C. De Gooijer, P. Wesseling, T. Wurdinger and H. E. De Vries, *Drug Resist. Updat.*, 2015, **19**, 1–12 (cit. on p. 32).

(120) H. Cabral et al., *Nat. Nanotechnol.*, 2011, **6**, 815–823 (cit. on p. 33).

(121) S. T. Reddy, A. J. Van Der Vlies, E. Simeoni, V. Angeli, G. J. Randolph, C. P. O'Neil, L. K. Lee, M. A. Swartz and J. A. Hubbell, *Nat. Biotechnol.*, 2007, **25**, 1159–1164 (cit. on p. 33).

(122) L. Tang et al., *Proc. Natl. Acad. Sci. U. S. A.*, 2014, **111**, 15344–15349 (cit. on p. 33).

(123) J. I. Cutler, D. Zheng, X. Xu, D. A. Giljohann and C. A. Mirkin, *Nano Lett.*, 2010, **10**, 1477–1480 (cit. on p. 34).

(124) J. Polte, R. Erler, A. F. Thünemann, S. Sokolov, T. T. Ahner, K. Rademann, F. Emmerling and R. Kraehnert, *ACS Nano*, 2010, **4**, 1076–1082 (cit. on p. 34).

(125) J. Turkevich, P. C. Stevenson and J. Hillier, *Discuss. Faraday Soc.*, 1951, **11**, 55–75 (cit. on p. 34).

(126) G. FRENS, *Nat. Phys. Sci.*, 1973, **241**, 20–22 (cit. on p. 34).

(127) X. Ji, X. Song, J. Li, Y. Bai, W. Yang and X. Peng, *J. Am. Chem. Soc.*, 2007, **129**, 13939–13948 (cit. on p. 34).

(128) I. Ojea-Jiménez, F. M. Romero, N. G. Bastús, V. Puntes, I. Ojea-Jiménez, F. M. Romero, N. G. Bastús and V. Puntes, *J. Phys. Chem. C*, 2010, **114**, 1800–1804 (cit. on p. 34).

(129) N. R. Jana, L. Gearheart and C. J. Murphy, *Langmuir*, 2001, **17**, 6782–6786 (cit. on pp. 34, 151).

(130) J. Piella, N. G. Bastús and V. Puntes, *Chem. Mater.*, 2016, **28**, 1066–1075 (cit. on pp. 34, 35, 111).

(131) A. M. Alkilany, P. K. Nagaria, C. R. Hexel, T. J. Shaw, C. J. Murphy and M. D. Wyatt, *Small*, 2009, **5**, 701–708 (cit. on p. 34).

(132) H. Y. Ahn, H. E. Lee, K. Jin and K. T. Nam, *J. Mater. Chem. C*, 2013, **1**, 6861–6868 (cit. on p. 34).

(133) T. G. Chan, *MRes Thesis - Imperial College London*, 2016 (cit. on pp. 34, 35, 38, 151).

(134) J. Li et al., *ACS Appl. Mater. Interfaces*, 2014, **6**, 16800–16807 (cit. on pp. 35, 38, 111).

(135) K. E. Fong and L. Y. L. Yung, *Nanoscale*, 2013, **5**, 12043–12071 (cit. on pp. 36, 152).

(136) W. Haiss, N. T. Thanh, J. Aveyard and D. G. Fernig, *Anal. Chem.*, 2007, **79**, 4215–4221 (cit. on pp. 36, 112).

(137) J. Stetefeld, S. A. McKenna and T. R. Patel, *Biophys. Rev.*, 2016, **8**, 409–427 (cit. on p. 37).

(138) M. Kaszuba, J. Corbett, F. M. N. Watson and A. Jones, *Philos. Trans. R. Soc. A Math. Phys. Eng. Sci.*, 2010, **368**, 4439–4451 (cit. on p. 37).

(139) L. M. Demers, C. A. Mirkin, R. C. Mucic, R. A. Reynolds, R. L. Letsinger, R. Elghanian and G. Viswanadham, *Anal. Chem.*, 2000, **72**, 5535–5541 (cit. on pp. 37, 38).

(140) D. A. Giljohann, D. S. Seferos, P. C. Patel, J. E. Millstone, N. L. Rosi and C. A. Mirkin, *Nano Lett.*, 2007, **7**, 3818–3821 (cit. on p. 38).

(141) J. J. Choi, M. Pernot, S. A. Small and E. E. Konofagou, *Ultrasound Med. Biol.*, 2007, **33**, 95–104 (cit. on pp. 41, 114).

(142) J. P. Sundberg and K. A. Silva, *Vet. Pathol.*, 2012, **49**, 142–145 (cit. on p. 42).

(143) S. Morse, *PhD Thesis - Imperial College London*, 2020 (cit. on p. 42).

(144) E. Patricio Rodrigues, T. Francisco de Oliveira and F. Buiochi, Procceedings 24th ABCM Int. Congr. Mech. Eng. ABCM, 2018 (cit. on p. 43).

(145) T. J. Hall, E. L. Madsen, F. Dong, I. R. Medina and G. R. Frank, *Ultrasound Med. Biol.*, 2001, **27**, 1003–1010 (cit. on p. 43).

(146) R. D. Cardiff, C. H. Miller and R. J. Munn, *Cold Spring Harb. Protoc.*, 2014, **2014**, 655–658 (cit. on p. 48).

(147) V. V. Hira, A. L. de Jong, K. Ferro, M. Khurshed, R. J. Molenaar and C. J. Van Noorden, *Acta Histochem.*, 2019, **121**, 125–134 (cit. on p. 48).

(148) E. M. Lewiecki, *Ther. Adv. Chronic Dis.*, 2010, **1**, 115–128 (cit. on p. 50).

(149) M. Gnant et al., *Lancet Oncol.*, 2011, **12**, 631–641 (cit. on p. 50).

(150) P. Clézardin, *Bonekey Rep.*, 2013, **2**, 267 (cit. on p. 50).

(151) P. M. Tricarico, A. Epate, F. Celsi and S. Crovella, *Inflammopharmacology*, 2018, **26**, 285–290 (cit. on p. 50).

(152) R. Ebert et al., *Mol. Cancer*, 2014, **13**, 265 (cit. on p. 50).

(153) H. Shmeeda, Y. Amitay, J. Gorin, D. Tzemach, L. Mak, J. Ogorka, S. Kumar, J. A. Zhang and A. Gabizon, *J. Control. Release*, 2010, **146**, 76–83 (cit. on p. 50).

(154) K. L. Young, A. W. Scott, L. Hao, S. E. Mirkin, G. Liu and C. A. Mirkin, *Nano Lett.*, 2012, **12**, 3867–3871 (cit. on p. 51).

(155) R. Brookmeyer, E. Johnson, K. Ziegler-Graham and H. M. Arrighi, *Alzheimer's Dement.*, 2007, **3**, 186–191 (cit. on p. 53).

(156) T. D. Bird, *Genet. Med.*, 2008, **10**, 231–239 (cit. on p. 53).

(157) E. P. Barykin, V. A. Mitkevich, S. A. Kozin and A. A. Makarov, *Front. Genet.*, 2017, **8**, 58 (cit. on p. 53).

(158) L. M. Bekris, C. E. Yu, T. D. Bird and D. W. Tsuang, *J. Geriatr. Psychiatry Neurol.*, 2010, **23**, 213–227 (cit. on p. 53).

(159) K. G. Yiannopoulou and S. G. Papageorgiou, *Ther. Adv. Neurol. Disord.*, 2013, **6**, 19–33 (cit. on p. 53).

(160) G. Stewart and O. A. Uthman, in *Cochrane Colloq.* Ed. J. S. Birks, John Wiley {\&} Sons, Ltd, Chichester, UK, 2015 (cit. on p. 53).

(161) B. Reisberg, R. Doody, A. Stöffler, F. Schmitt, S. Ferris and H. J. Möbius, *N. Engl. J. Med.*, 2003, **348**, 1333–1341 (cit. on p. 53).

(162) B. Winblad, R. W. Jones, Y. Wirth, A. Stöffler and H. J. Möbius, *Dement. Geriatr. Cogn. Disord.*, 2007, **24**, 20–27 (cit. on p. 53).

(163) J. Birks, *Cochrane Database Syst. Rev.*, 2006, **61**, ed. J. S. Birks, 41–52 (cit. on p. 53).

(164) B. D. Winters and T. J. Bussey, *Eur. J. Neurosci.*, 2005, **21**, 2263–2270 (cit. on p. 53).

(165) A. E. Power, A. Vazdarjanova and J. L. McGaugh, *Neurobiol. Learn. Mem.*, 2003, **80**, 178–193 (cit. on p. 53).

(166) M. M. Boccia, M. G. Blake, G. B. Acosta and C. M. Baratti, *Neurosci. Lett.*, 2003, **345**, 97–100 (cit. on p. 53).

(167) F. H. Epstein, S. A. Lipton and P. A. Rosenberg, *N. Engl. J. Med.*, 1994, **330**, 613–622 (cit. on p. 53).

(168) W. Danysz and C. G. Parsons, *Int. J. Geriatr. Psychiatry*, 2003, **18**, S23–S32 (cit. on p. 53).

(169) P. Raina, P. Santaguida, A. Ismaila, C. Patterson, D. Cowan, M. Levine, L. Booker and M. Oremus, *Ann. Intern. Med.*, 2008, **148**, 379–397 (cit. on p. 53).

(170) J. Cummings, G. Lee, A. Ritter, M. Sabbagh and K. Zhong, *Alzheimer's Dement. Transl. Res. Clin. Interv.*, 2019, **5**, 272–293 (cit. on pp. 53, 56, 94).

(171) G. S. Bloom, *JAMA Neurol.*, 2014, **71**, 505–508 (cit. on p. 53).

(172) L. Pini, M. Pievani, M. Bocchetta, D. Altomare, P. Bosco, E. Cavedo, S. Galluzzi, M. Marizzoni and G. B. Frisoni, *Ageing Res. Rev.*, 2016, **30**, 25–48 (cit. on p. 54).

(173) L. Crews and E. Masliah, *Hum. Mol. Genet.*, 2010, **19**, R12–R20 (cit. on p. 54).

(174) G. G. Glenner and C. W. Wong, *Biochem. Biophys. Res. Commun.*, 1984, **120**, 885–890 (cit. on p. 54).

(175) J. Hardy and D. Allsop, *Trends Pharmacol. Sci.*, 1991, **12**, 383–388 (cit. on pp. 54, 55).

(176) D. J. Selkoe, *Neuron*, 1991, **6**, 487–498 (cit. on pp. 54, 55).

(177) Q. Guo, H. Li, S. S. Gaddam, N. J. Justice, C. S. Robertson and H. Zheng, *J. Biol. Chem.*, 2012, **287**, 2437–2445 (cit. on p. 54).

(178) S. W. Weyer et al., *EMBO J.*, 2011, **30**, 2266–2280 (cit. on p. 54).

(179) X. Zhang and W. Song, *Alzheimer's Res. Ther.*, 2013, **5**, 46 (cit. on p. 54).

(180) H. Cai, Y. Wang, D. McCarthy, H. Wen, D. R. Borchelt, D. L. Price and P. C. Wong, *Nat. Neurosci.*, 2001, **4**, 233–234 (cit. on p. 54).

(181) A. M. Klein, N. W. Kowall and R. J. Ferrante, *Ann. N. Y. Acad. Sci.*, 1999, **893**, 314–320 (cit. on pp. 54, 55).

(182) L. F. Lue et al., *Am. J. Pathol.*, 1999, **155**, 853–862 (cit. on p. 54).

(183) C. A. McLean, R. A. Cherny, F. W. Fraser, S. J. Fuller, M. J. Smith, K. Beyreuther, A. I. Bush and C. L. Masters, *Ann. Neurol.*, 1999, **46**, 860–866 (cit. on p. 54).

(184) J. P. Cleary, D. M. Walsh, J. J. Hofmeister, G. M. Shankar, M. A. Kuskowski, D. J. Selkoe and K. H. Ashe, *Nat. Neurosci.*, 2005, **8**, 79–84 (cit. on p. 54).

(185) S. Lesné, T. K. Ming, L. Kotilinek, R. Kayed, C. G. Glabe, A. Yang, M. Gallagher and K. H. Ashe, *Nature*, 2006, **440**, 352–357 (cit. on p. 54).

(186) M. L. Giuffrida et al., *J. Neurosci.*, 2009, **29**, 10582–10587 (cit. on p. 55).

(187) Y. Gao et al., *Neurobiol. Aging*, 2019, **77**, 154–157 (cit. on p. 55).

(188) T. Jonsson et al., *Nature*, 2012, **488**, 96 (cit. on p. 55).

(189) D. Puzzo, L. Lee, A. Palmeri, G. Calabrese and O. Arancio, *Biochem. Pharmacol.*, 2014, **88**, 450–467 (cit. on p. 55).

(190) J. Götz, J. R. Streffer, D. David, A. Schild, F. Hoerndli, L. Pennanen, P. Kurosinski and F. Chen, *Mol. Psychiatry*, 2004, **9**, 664–683 (cit. on p. 55).

(191) D. Schenk et al., *Nature*, 1999, **400**, 173–177 (cit. on p. 55).

(192) F. Bard et al., *Nat. Med.*, 2000, **6**, 916–919 (cit. on pp. 55, 84).

(193) T. J. Esparza, H. Zhao, J. R. Cirrito, N. J. Cairns, R. J. Bateman, D. M. Holtzman and D. L. Brody, *Ann. Neurol.*, 2013, **73**, 104–119 (cit. on p. 56).

(194) H. J. Aizenstein et al., *Arch. Neurol.*, 2008, **65**, 1509–1517 (cit. on p. 56).

(195) K. M. Rodrigue, K. M. Kennedy, M. D. Devous, J. R. Rieck, A. C. Hebrank, R. Diaz-Arrastia, D. Mathews and D. C. Park, *Neurology*, 2012, **78**, 387–395 (cit. on p. 56).

(196) P. Delaère, C. Duyckaerts, C. Masters, K. Beyreuther, F. Piette and J. J. Hauw, *Neurosci. Lett.*, 1990, **116**, 87–93 (cit. on p. 56).

(197) M. Gold et al., *Dement. Geriatr. Cogn. Disord.*, 2010, **30**, 131–146 (cit. on p. 56).

(198) R. S. Doody et al., *N. Engl. J. Med.*, 2013, **369**, 341–350 (cit. on p. 56).

(199) Bellus Health, *Open-Label Extension of the Phase III Study With Tramiprosate (3APS) in Patients With Mild to Moderate Alzheimer's Disease*, 2007 (cit. on p. 56).

(200) S. Salloway et al., *Neurology*, 2011, **77**, 1253–1262 (cit. on p. 56).

(201) Pfizer, *Study Evaluating The Efficacy And Safety Of Bapineuzumab In Alzheimer Disease Patients*, 2008 (cit. on p. 56).

(202) Eli Lilly, *A Study of Solanezumab (LY2062430) in Participants With Prodromal Alzheimer's Disease (ExpeditionPRO)*, 2019 (cit. on p. 56).

(203) B. Lawlor et al., *PLoS Med.*, 2018, **15**, ed. C. Brayne, e1002660 (cit. on p. 56).

(204) E. Shokri-Kojori et al., *Proc. Natl. Acad. Sci. U. S. A.*, 2018, **115**, 4483–4488 (cit. on pp. 56, 85).

(205) R. F. Itzhaki and R. Lathe, *J. Alzheimer's Dis.*, 2018, **64**, 363–366 (cit. on p. 56).

(206) S. S. Dominy et al., *Sci. Adv.*, 2019, **5**, eaau3333 (cit. on p. 56).

(207) R. B. Maccioni, G. Farías, I. Morales and L. Navarrete, *Arch. Med. Res.*, 2010, **41**, 226–231 (cit. on p. 56).

(208) D. J. Bonda, H. G. Lee, J. A. Blair, X. Zhu, G. Perry and M. A. Smith, *Metallomics*, 2011, **3**, 267–270 (cit. on p. 56).

(209) A. Q. Truong-Tran, J. Carter, R. E. Ruffin and P. D. Zalewski, *BioMetals*, 2001, **14**, 315–330 (cit. on p. 57).

(210) I. F. Scheiber, J. F. Mercer and R. Dringen, *Prog. Neurobiol.*, 2014, **116**, 33–57 (cit. on p. 57).

(211) R. J. Ward, F. A. Zucca, J. H. Duyn, R. R. Crichton and L. Zecca, *Lancet Neurol.*, 2014, **13**, 1045–1060 (cit. on p. 57).

(212) M. A. Deibel, W. D. Ehmann and W. R. Markesbery, *J. Neurol. Sci.*, 1996, **143**, 137–142 (cit. on p. 57).

(213) M. A. Lovell, J. D. Robertson, W. J. Teesdale, J. L. Campbell and W. R. Markesbery, *J. Neurol. Sci.*, 1998, **158**, 47–52 (cit. on p. 57).

(214) L. M. Miller, Q. Wang, T. P. Telivala, R. J. Smith, A. Lanzirotti and J. Miklossy, *J. Struct. Biol.*, 2006, **155**, 30–37 (cit. on p. 57).

(215) J. Dong, C. S. Atwood, V. E. Anderson, S. L. Siedlak, M. A. Smith, G. Perry and P. R. Carey, *Biochemistry*, 2003, **42**, 2768–2773 (cit. on p. 57).

(216) M. W. Bourassa, A. C. Leskovjan, R. V. Tappero, E. R. Farquhar, C. A. Colton, W. E. Van Nostrand and L. M. Miller, *Biomed. Spectrosc. Imaging*, 2013, **2**, 129–139 (cit. on p. 57).

(217) C. Hureau, V. Balland, Y. Coppel, P. L. Solari, E. Fonda and P. Faller, *J. Biol. Inorg. Chem.*, 2009, **14**, 995–1000 (cit. on pp. 57, 109).

(218) T. R. Young, A. Kirchner, A. G. Wedd and Z. Xiao, *Metallomics*, 2014, **6**, 505–517 (cit. on pp. 57, 109).

(219) N. Yako, T. R. Young, J. M. Cottam Jones, C. A. Hutton, A. G. Wedd and Z. Xiao, *Metallomics*, 2017, **9**, 278–291 (cit. on pp. 57, 58, 109).

(220) C. Hureau and P. Dorlet, *Coord. Chem. Rev.*, 2012, **256**, 2175–2187 (cit. on pp. 57, 109).

(221) B. Alies, H. Eury, C. Bijani, L. Rechignat, P. Faller and C. Hureau, *Inorg. Chem.*, 2011, **50**, 11192–11201 (cit. on pp. 57, 109).

(222) B. Alies, A. Conte-Daban, S. Sayen, F. Collin, I. Kieffer, E. Guillon, P. Faller and C. Hureau, *Inorg. Chem.*, 2016, **55**, 10499–10509 (cit. on p. 57).

(223) F. Bousejra-Elgarah, C. Bijani, Y. Coppel, P. Faller and C. Hureau, *Inorg. Chem.*, 2011, **50**, 9024–9030 (cit. on p. 57).

(224) D. P. Smith, G. D. Ciccotosto, D. J. Tew, M. T. Fodero-Tavoletti, T. Johanssen, C. L. Masters, K. J. Barnham and R. Cappai, *Biochemistry*, 2007, **46**, 2881–2891 (cit. on p. 57).

(225) M. C. Lee, W. C. Yu, Y. H. Shih, C. Y. Chen, Z. H. Guo, S. J. Huang, J. C. Chan and Y. R. Chen, *Sci. Rep.*, 2018, **8**, 4772 (cit. on p. 57).

(226) F. Hane, G. Tran, S. J. Attwood and Z. Leonenko, *PLoS One*, 2013, **8**, ed. I. Sokolov, e59005 (cit. on p. 57).

(227) M. Valko, D. Leibfritz, J. Moncol, M. T. Cronin, M. Mazur and J. Telser, *Int. J. Biochem. Cell Biol.*, 2007, **39**, 44–84 (cit. on p. 58).

(228) R. A. Floyd and J. M. Carney, *Ann. Neurol.*, 1992, **32**, S22–S27 (cit. on p. 58).

(229) T. Rival et al., *Eur. J. Neurosci.*, 2009, **29**, 1335–1347 (cit. on p. 58).

(230) A. C. Mello Filho and R. Meneghini, *BBA - Gene Struct. Expr.*, 1984, **781**, 56–63 (cit. on p. 58).

(231) W. Zheng and A. D. Monnot, *Pharmacol. Ther.*, 2012, **133**, 177–188 (cit. on p. 58).

(232) M. Nakamura, N. Shishido, A. Nunomura, M. A. Smith, G. Perry, Y. Hayashi, K. Nakayama and T. Hayashi, *Biochemistry*, 2007, **46**, 12737–12743 (cit. on p. 58).

(233) S. I. Dikalov, M. P. Vitek and R. P. Mason, *Free Radic. Biol. Med.*, 2004, **36**, 340–347 (cit. on p. 59).

(234) B. J. Tabner, S. Turnbull, O. M. El-Agnaf and D. Allsop, *Free Radic. Biol. Med.*, 2002, **32**, 1076–1083 (cit. on p. 59).

(235) M. Rana and A. K. Sharma, *Metallomics*, 2019, **11**, 64–84 (cit. on p. 59).

(236) D. A. Butterfield, T. Reed, M. Perluigi, C. De Marco, R. Coccia, C. Cini and R. Sultana, *Neurosci. Lett.*, 2006, **397**, 170–173 (cit. on p. 59).

(237) K. Hensley et al., *J. Neurochem.*, 1995, **65**, 2146–2156 (cit. on p. 59).

(238) E. Tamagno et al., *Neurobiol. Dis.*, 2002, **10**, 279–288 (cit. on p. 59).

(239) E. Tamagno et al., *J. Neurochem.*, 2008, **104**, 683–695 (cit. on p. 59).

(240) D. R. McLachlan, T. P. Kruck, W. Kalow, D. F. Andrews, A. J. Dalton, M. Y. Bell and W. L. Smith, *Lancet*, 1991, **337**, 1304–1308 (cit. on p. 60).

(241) L. N. Sheppard and G. J. Kontoghiorghes, *Arzneimittel-Forschung/Drug Res.*, 1993, **43**, 659–662 (cit. on p. 60).

(242) T. Kiss and E. Farkas, *J. Incl. Phenom. Mol. Recognit. Chem.*, 1998, **32**, 385–403 (cit. on p. 60).

(243) D. R. Blake et al., *Qjm*, 1985, **56**, 345–355 (cit. on p. 60).

(244) B. E. Holbein and R. Mira De Orduña, *FEMS Microbiol. Lett.*, 2010, **307**, 19–24 (cit. on p. 60).

(245) D. R. Richardson and P. Ponka, *Am. J. Hematol.*, 1998, **58**, 299–305 (cit. on p. 60).

(246) K. J. Barnham et al., *Proc. Natl. Acad. Sci. U. S. A.*, 2008, **105**, 6813–6818 (cit. on pp. 60, 61, 63, 68, 69, 82, 84, 109).

(247) G. Ma, F. Huang, X. Pu, L. Jia, T. Jiang, L. Li and Y. Liu, *Chem. - A Eur. J.*, 2011, **17**, 11657–11666 (cit. on pp. 60, 63, 73, 74).

(248) X. Wang, X. Wang, C. Zhang, Y. Jiao and Z. Guo, *Chem. Sci.*, 2012, **3**, 1304–1312 (cit. on pp. 60, 117, 122).

(249) I. Sasaki, C. Bijani, S. Ladeira, V. Bourdon, P. Faller and C. Hureau, *Dalt. Trans.*, 2012, **41**, 6404–6407 (cit. on pp. 60, 68, 69, 73, 75, 82, 84).

(250) M. C. Heffern, P. T. Velasco, L. M. Matosziuk, J. L. Coomes, C. Karras, M. A. Ratner, W. L. Klein, A. L. Eckermann and T. J. Meade, *ChemBioChem*, 2014, **15**, 1584–1589 (cit. on pp. 60, 61, 63, 73, 74, 82, 84, 109, 110).

(251) N. A. Vyas, S. N. Ramteke, A. S. Kumbhar, P. P. Kulkarni, V. Jani, U. B. Sonawane, R. R. Joshi, B. Joshi and A. Erxleben, *Eur. J. Med. Chem.*, 2016, **121**, 793–802 (cit. on pp. 60, 61, 109).

(252) G. S. Yellol, J. G. Yellol, V. B. Kenche, X. M. Liu, K. J. Barnham, A. Donaire, C. Janiak and J. Ruiz, *Inorg. Chem.*, 2015, **54**, 470–475 (cit. on pp. 60, 61, 84, 109).

(253) A. Iscen, C. R. Brue, K. F. Roberts, J. Kim, G. C. Schatz and T. J. Meade, *J. Am. Chem. Soc.*, 2019, **141**, 16685–16695 (cit. on pp. 60, 63, 69, 74, 77, 82, 84, 110).

(254) V. B. Kenche et al., *Angew. Chemie - Int. Ed.*, 2013, **52**, 3374–3378 (cit. on pp. 62, 82, 84).

(255) N. Jiang, S. Y. Li, S. S. Xie, Z. R. Li, K. D. Wang, X. B. Wang and L. Y. Kong, *Eur. J. Med. Chem.*, 2014, **87**, 540–551 (cit. on p. 63).

(256) E. Ma, *MSci Thesis - Imperial College London*, 2019 (cit. on p. 63).

(257) V. Rakers, P. Cadinu, J. B. Edel and R. Vilar, *Chem. Sci.*, 2018, **9**, 3459–3469 (cit. on pp. 63, 117, 118).

(258) V. Rakers, *PhD Thesis - Imperial College London*, 2018 (cit. on pp. 63, 117).

(259) C. Ruehl, *PhD Thesis - Imperial College London*, 2020 (cit. on pp. 63, 66, 78).

(260) I. P. Oliveri, S. Failla, A. Colombo, C. Dragonetti, S. Righetto and S. Di Bella, *Dalt. Trans.*, 2014, **43**, 2168–2175 (cit. on pp. 63, 118).

(261) H. Naiki, K. Higuchi, M. Hosokawa and T. Takeda, *Anal. Biochem.*, 1989, **177**, 244–249 (cit. on p. 67).

(262) M. Biancalana and S. Koide, *Biochim. Biophys. Acta - Proteins Proteomics*, 2010, **1804**, 1405–1412 (cit. on p. 67).

(263) W. B. Stine, K. N. Dahlgren, G. A. Krafft and M. J. LaDu, *J. Biol. Chem.*, 2003, **278**, 11612–11622 (cit. on p. 67).

(264) M. Buck, *Q. Rev. Biophys.*, 1998, **31**, 297–355 (cit. on p. 67).

(265) T. M. Ryan et al., *PeerJ*, 2013, **2013**, e73 (cit. on pp. 67, 68, 123).

(266) M. R. Nichols, M. A. Moss, D. K. Reed, S. Cratic-McDaniel, J. H. Hoh and T. L. Rosenberry, *J. Biol. Chem.*, 2005, **280**, 2471–2480 (cit. on p. 67).

(267) P. Frid, S. V. Anisimov and N. Popovic, *Brain Res. Rev.*, 2007, **53**, 135–160 (cit. on p. 70).

(268) L. P. Jameson, N. W. Smith and S. V. Dzyuba, *ACS Chem. Neurosci.*, 2012, **3**, 807–819 (cit. on p. 70).

(269) C. A. Scarff, M. J. Fuller, R. F. Thompson and M. G. Iadaza, *J. Vis. Exp.*, 2018, **2018**, e57199 (cit. on p. 70).

(270) D. Valensin, C. Migliorini, G. Valensin, E. Gaggelli, G. La Penna, H. Kozlowski, C. Gabbiani and L. Messori, *Inorg. Chem.*, 2011, **50**, 6865–6867 (cit. on pp. 73, 75).

(271) N. J. Greenfield, *Nat. Protoc.*, 2007, **1**, 2876–2890 (cit. on pp. 74, 76).

(272) G. Holzwarth and P. Doty, *J. Am. Chem. Soc.*, 1965, **87**, 218–228 (cit. on p. 76).

(273) N. Greenfield and G. D. Fasman, *Biochemistry*, 1969, **8**, 4108–4116 (cit. on p. 76).

(274) S. T. Mutter, M. Turner, R. J. Deeth and J. A. Platts, *ACS Chem. Neurosci.*, 2018, **9**, 2795–2806 (cit. on p. 77).

(275) A. L. Fitzpatrick, L. H. Kuller, O. L. Lopez, C. H. Kawas and W. Jagust, *J. Neurol. Sci.*, 2005, **229-230**, 43–49 (cit. on p. 77).

(276) J. Krishtal, O. Bragina, K. Metsla, P. Palumaa and V. Tõugu, *PLoS One*, 2017, **12**, ed. S. D. Ginsberg, e0186636 (cit. on pp. 77, 78, 81).

(277) T. Oguchi et al., *Front. Aging Neurosci.*, 2017, **9**, 337 (cit. on pp. 77, 78).

(278) P. Sun, H. Ding, M. Liang, X. Li, W. Mo, X. Wang, Y. Liu, R. He and Q. Hua, *Biomed Res. Int.*, 2014, **2014**, 1–11 (cit. on pp. 77, 78, 81).

(279) V. Castelletto et al., *Sci. Rep.*, 2017, **7**, 43637 (cit. on pp. 77, 78, 81).

(280) M. V. Berridge, P. M. Herst and A. S. Tan, in *Biotechnol. Annu. Rev.* 2005, vol. 11, pp. 127–152 (cit. on p. 77).

(281) D. A. Scudiero, R. H. Shoemaker, K. D. Paull, A. Monks, S. Tierney, T. H. Nofziger, M. J. Currens, D. Seniff and M. R. Boyd, *Cancer Res.*, 1988, **48**, 4827–4833 (cit. on p. 77).

(282) M. A. Moss, N. H. Varvel, M. R. Nichols, D. K. Reed and T. L. Rosenberry, *Mol. Pharmacol.*, 2004, **66**, 592–600 (cit. on p. 83).

(283) Y. Zhang, M. Dai and Z. Yuan, *Anal. Methods*, 2018, **10**, 4625–4638 (cit. on p. 83).

(284) A. Chumakov, V. Batalova and Y. Slizhov, AIP Conf. Proc. 2016, vol. 1772, p. 40004 (cit. on p. 83).

(285) M. Manzano and M. Vallet-Regí, *Chem. Commun.*, 2019, **55**, 2731–2740 (cit. on p. 83).

(286) M. A. Chishti et al., *J. Biol. Chem.*, 2001, **276**, 21562–21570 (cit. on p. 84).

(287) J. F. Jordão, C. A. Ayala-Grosso, K. Markham, Y. Huang, R. Chopra, J. A. McLaurin, K. Hynynen and I. Aubert, *PLoS One*, 2010, **5**, e10549 (cit. on p. 84).

(288) J. F. Jordão et al., *Exp. Neurol.*, 2013, **248**, 16–29 (cit. on pp. 84, 85, 103, 108).

(289) J. McLaurin et al., *Nat. Med.*, 2002, **8**, 1263–1269 (cit. on p. 84).

(290) D. M. Wilcock, G. DiCarlo, D. Henderson, J. Jackson, K. Clarke, K. E. Ugen, M. N. Gordon and D. Morgan, *J. Neurosci.*, 2003, **23**, 3745–3751 (cit. on p. 84).

(291) J. A. Nicoll et al., *J. Neuropathol. Exp. Neurol.*, 2006, **65**, 1040–1048 (cit. on p. 85).

(292) G. Leinenga and J. Götz, *Sci. Transl. Med.*, 2015, **7**, 278ra33–278ra33 (cit. on pp. 85, 103, 108).

(293) E. A. Eckman, D. K. Reed and C. B. Eckman, *J. Biol. Chem.*, 2001, **276**, 24540–24548 (cit. on p. 85).

(294) M. Koistinaho et al., *Nat. Med.*, 2004, **10**, 719–726 (cit. on p. 85).

(295) S. D. Mulder, H. M. Nielsen, M. A. Blankenstein, P. Eikelenboom and R. Veerhuis, *Glia*, 2014, **62**, 493–503 (cit. on p. 85).

(296) G. Leinenga and J. Götz, *Front. Neurosci.*, 2018, **12**, 55 (cit. on p. 85).

(297) C. T. Poon, K. Shah, C. Lin, R. Tse, K. K. Kim, S. Mooney, I. Aubert, B. Stefanovic and K. Hynynen, *Sci. Rep.*, 2018, **8**, 14061 (cit. on p. 85).

(298) G. Leinenga, W. K. Koh and J. Götz, *Brain Res. Bull.*, 2019, **153**, 8–14 (cit. on pp. 85, 103, 108).

(299) R. Pandit, G. Leinenga and J. Götz, *Theranostics*, 2019, **9**, 3754–3767 (cit. on p. 85).

(300) P. T. Ly et al., *J. Clin. Invest.*, 2013, **123**, 224–235 (cit. on p. 85).

(301) P. H. Hsu, Y. T. Lin, Y. H. Chung, K. J. Lin, L. Y. Yang, T. C. Yen and H. L. Liu, *Sci. Rep.*, 2018, **8**, 12882 (cit. on p. 85).

(302) C. Lazarus, A. N. Pouliopoulos, M. Tinguely, V. Garbin and J. J. Choi, *J. Acoust. Soc. Am.*, 2017, **142**, 3135–3146 (cit. on p. 87).

(303) A. N. Pouliopoulos, S. Bonaccorsi and J. J. Choi, *Phys. Med. Biol.*, 2014, **59**, 6941–6957 (cit. on p. 87).

(304) A. N. Pouliopoulos, C. Li, M. Tinguely, V. Garbin, M.-X. Tang and J. J. Choi, *J. Acoust. Soc. Am.*, 2016, **140**, 2469–2480 (cit. on p. 87).

(305) Z. I. Kovacsa, S. Kima, N. Jikariaa, F. Qureshia, B. Miloa, B. K. Lewisa, M. Breslera, S. R. Burksa and J. A. Franka, *Proc. Natl. Acad. Sci. U. S. A.*, 2017, **114**, E75–E84 (cit. on p. 88).

(306) D. Shlosberg, M. Benifla, D. Kaufer and A. Friedman, *Nat. Rev. Neurol.*, 2010, **6**, 393–403 (cit. on p. 88).

(307) G. Samiotaki and E. E. Konofagou, *IEEE Trans. Ultrason. Ferroelectr. Freq. Control*, 2013, **60**, 2257–2265 (cit. on p. 88).

(308) M. Kinoshita, N. McDannold, F. A. Jolesz and K. Hynynen, *Proc. Natl. Acad. Sci. U. S. A.*, 2006, **103**, 11719–11723 (cit. on p. 91).

(309) F. A. Orellana, C. G. Gálvez, F. A. Orellana, C. G. Gálvez, M. T. Roldán, C. García-Ruiz, M. T. Roldán and C. García-Ruiz, *TrAC - Trends Anal. Chem.*, 2013, **42**, 1–34 (cit. on p. 91).

(310) A. Höck, U. Demmel, H. Schicha, K. Kasperek and L. E. Feinendegen, *Brain*, 1975, **98**, 49–64 (cit. on p. 92).

(311) H. Oakley et al., *J. Neurosci.*, 2006, **26**, 10129–10140 (cit. on p. 96).

(312) G. Kelényi, *Acta Neuropathol.*, 1967, **7**, 336–348 (cit. on p. 96).

(313) T. Bussière et al., *Am. J. Pathol.*, 2004, **165**, 987–995 (cit. on pp. 96, 98, 99).

(314) J. A. Ramos-Vara, *Vet. Pathol.*, 2005, **42**, 405–426 (cit. on p. 98).

(315) R. E. Llovera, M. De Tullio, L. G. Alonso, M. A. Leissring, S. B. Kaufman, A. E. Roher, G. D. P. Gay, L. Morelli and E. M. Castaño, *J. Biol. Chem.*, 2008, **283**, 17039–17048 (cit. on p. 103).

(316) H. Kanemitsu, T. Tomiyama and H. Mori, *Neurosci. Lett.*, 2003, **350**, 113–116 (cit. on p. 103).

(317) L. Zuroff, D. Daley, K. L. Black and M. Koronyo-Hamaoui, *Cell. Mol. Life Sci.*, 2017, **74**, 2167–2201 (cit. on p. 103).

(318) M. B. de Tullio, L. Morelli and E. M. Castaño, *Prion*, 2008, **2**, 51–56 (cit. on p. 103).

(319) X. Rao, C. Liu, J. Qiu and Z. Jin, *Org. Biomol. Chem.*, 2012, **10**, 7875–7883 (cit. on pp. 117, 122).

(320) N. Godbert, T. Pugliese, I. Aiello, A. Bellusci, A. Crispini and M. Ghedini, *Eur. J. Inorg. Chem.*, 2007, **2007**, 5105–5111 (cit. on pp. 117, 122).

(321) N. Shahabadi and L. Heidari, *Spectrochim. Acta - Part A Mol. Biomol. Spectrosc.*, 2014, **128**, 377–385 (cit. on pp. 117, 122).

(322) C. N. Pace, F. Vajdos, L. Fee, G. Grimsley and T. Gray, *Protein Sci.*, 1995, **4**, 2411–2423 (cit. on p. 123).

(323) B. Zhang-Haagen, R. Biehl, L. Nagel-Steger, A. Radulescu, D. Richter and D. Willbold, *PLoS One*, 2016, **11**, ed. J. Zheng, e0150267 (cit. on p. 123).

APPENDIX

9.6 CHAPTER 2: DNA-COATED NANOPARTICLES FOR BRAIN DISEASES

9.6.1 CTAB-Capped Au NPs

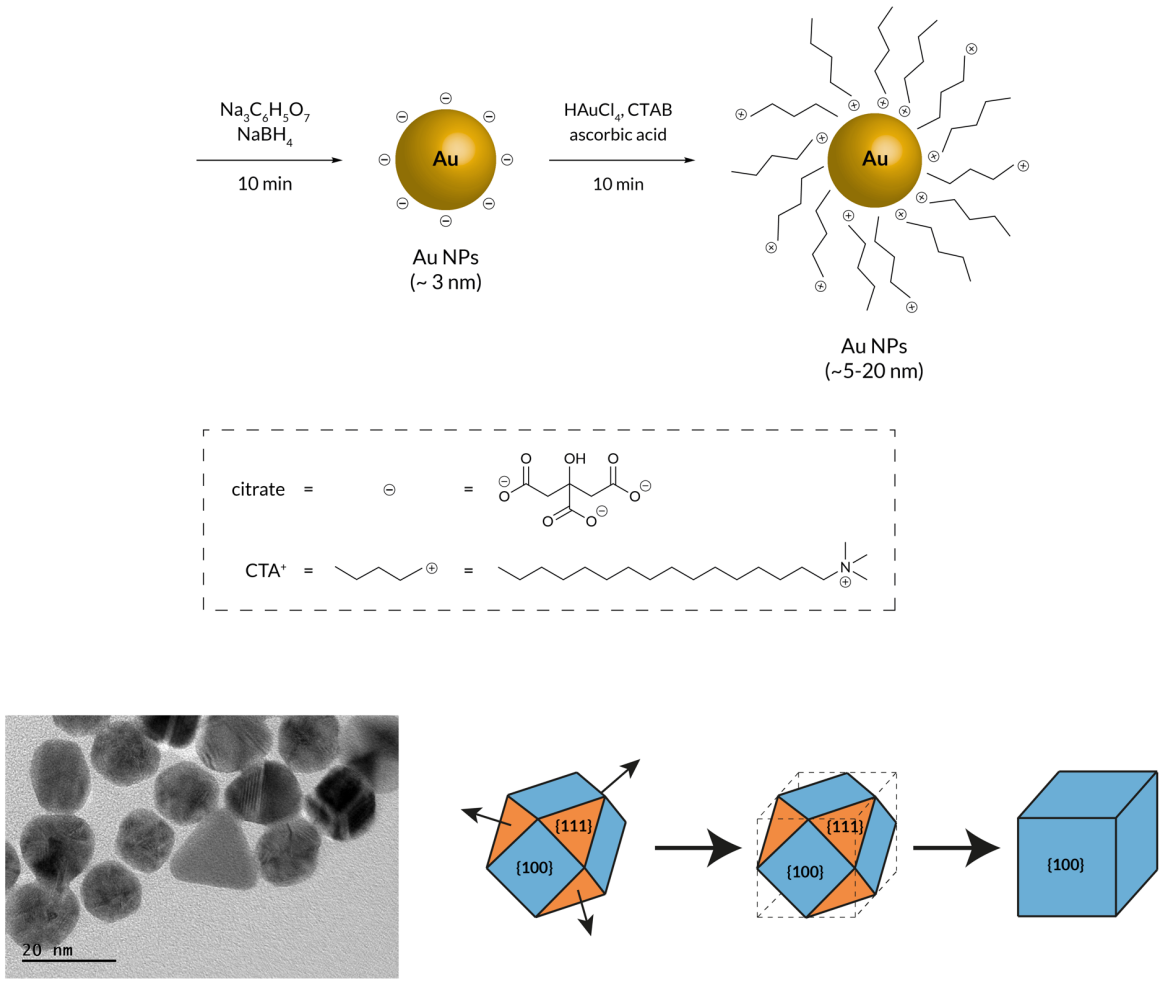


Figure 9.3: **Top:** Synthesis route to CTAB-capped Au NPs.[129] **Bottom:** TEM images of CTAB-capped NPs synthesised (diameter = 19.8 ± 3.1 nm) during MRes work. Non-spherical particles can be seen due to CTAB preferentially binding to the {100} faces.[133]

9.6.2 UV-Vis Spectra of Synthesised Au NPs

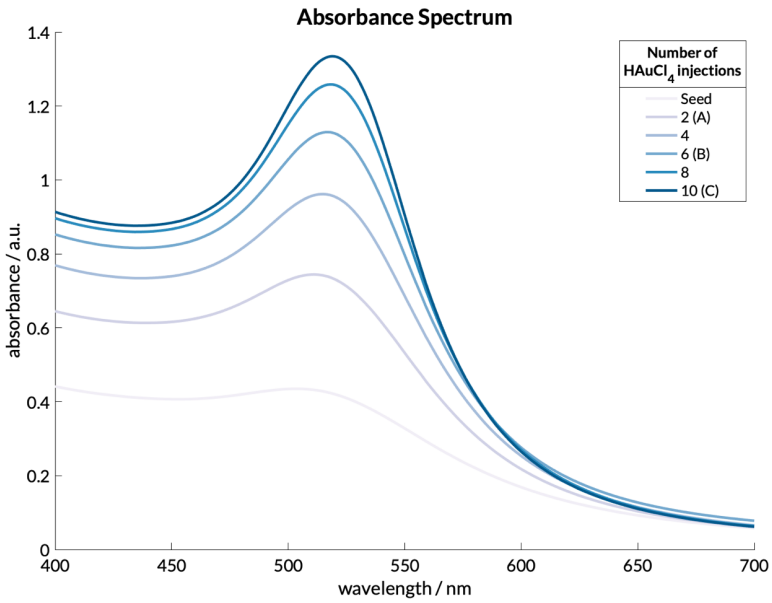


Figure 9.4: Absorbance spectrum of the synthesised Au NPs. An increase in the intensity and wavelength of the absorption band as the NP size is increased is seen.[135]

9.6.3 Emission Intensities of Synthesised Cy5-DNA-Au NPs

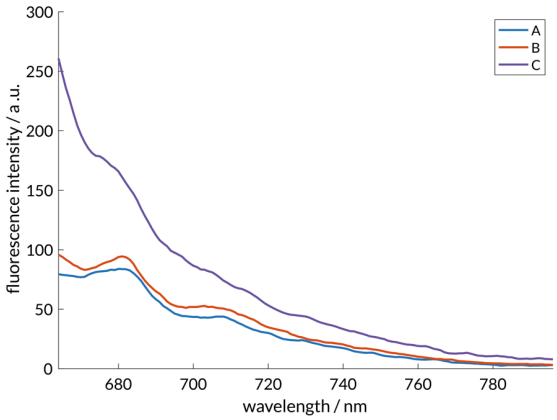


Figure 9.5: Fluorescence emission spectra of Cy5-DNA-Au NPs **A**, **B** and **C**.

9.6.4 Pressure Threshold

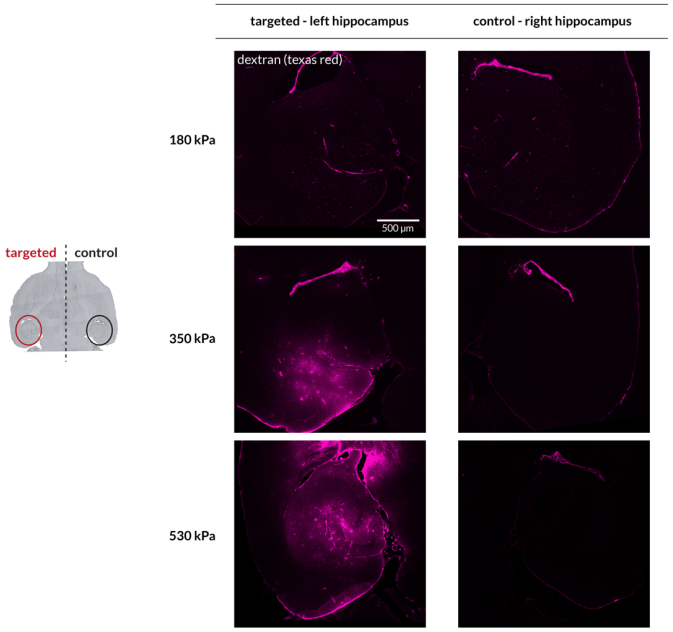


Figure 9.6: Representative images of the delivery of Texas Red-labelled 3 kDa dextran across the BBB at different peak-negative pressures. The pressure threshold was determined to be between 180 and 350 $kPa_{pk\text{-}neg}$. These experiments were conducted with Dr. A. Pouliopoulos and S. Morse (PhD students, NSB Lab).

9.6.5 Cy5-DNA-Au NP Delivery at 350 kPa

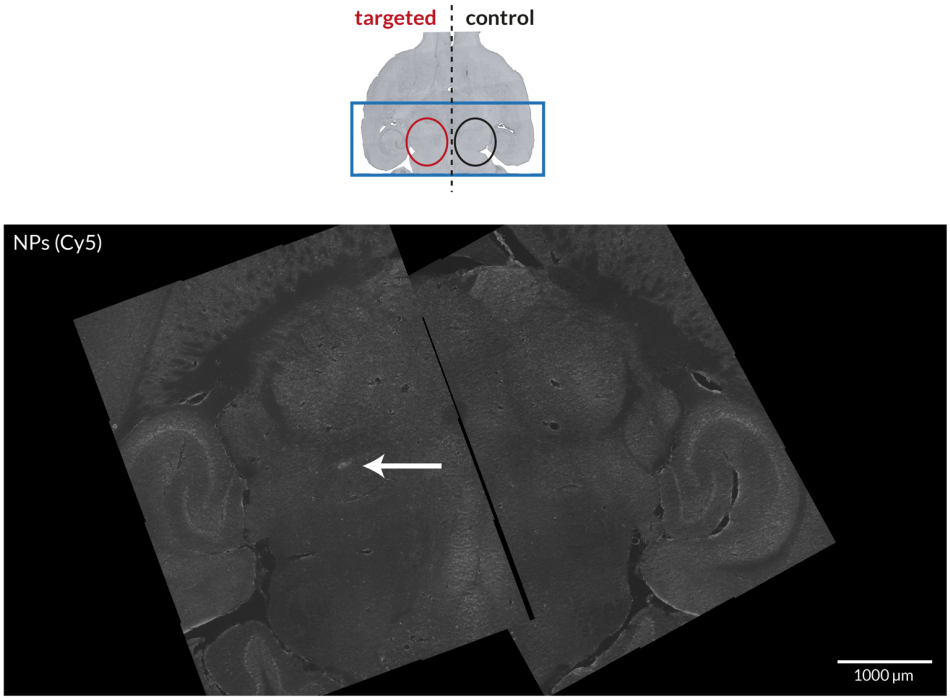


Figure 9.7: Delivery of Cy5-DNA-Au NPs **A** at a peak-negative pressure of 350 kPa. Minimal fluorescence signal in the Cy5 channel is observed, indicating limited delivery of the NPs across the BBB.

9.6.6 H&E Staining

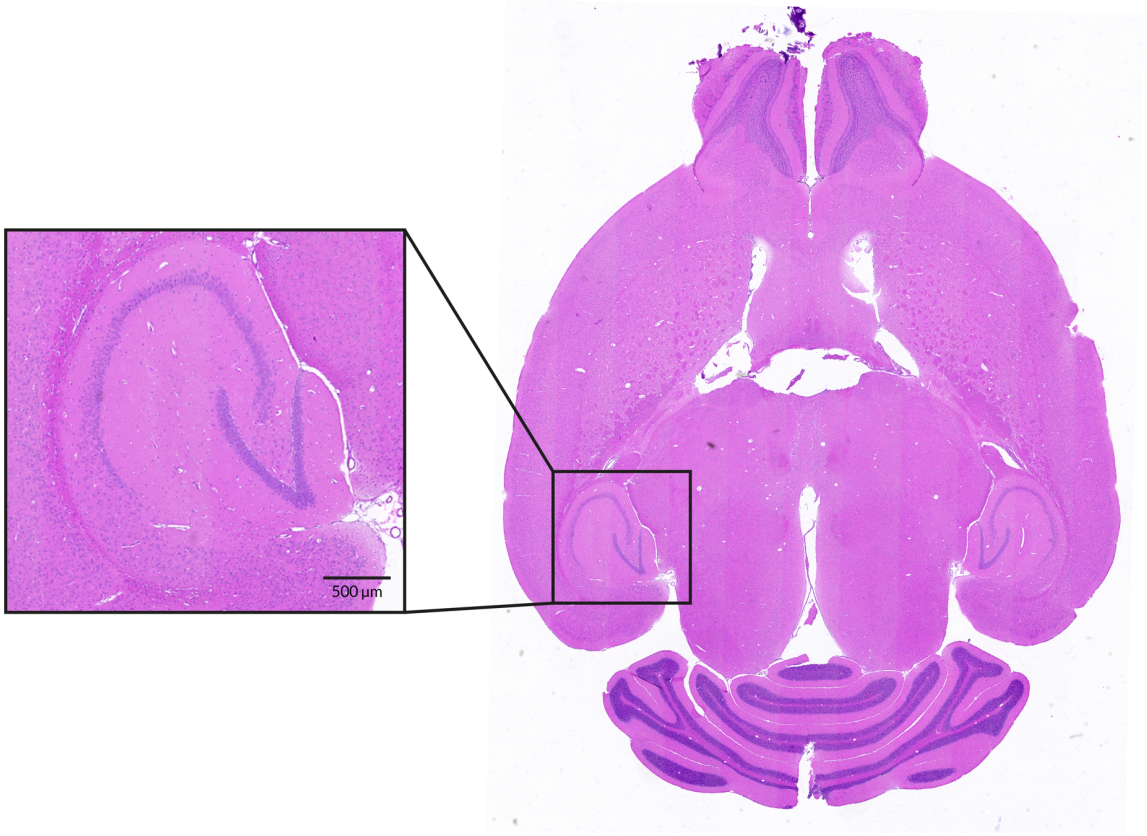


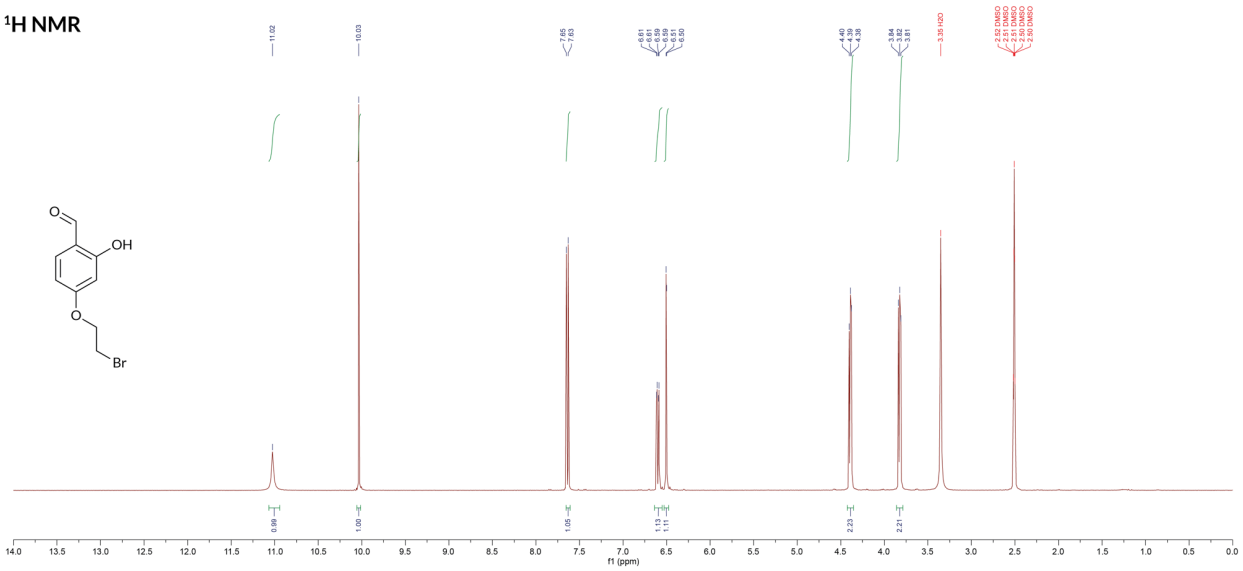
Figure 9.8: Representative image of a H&E-stained section. Haematoxylin stains nuclei blue, whilst eosin stains proteins pink.

9.7 CHAPTER 3: METAL COMPLEXES FOR ALZHEIMER'S DISEASE

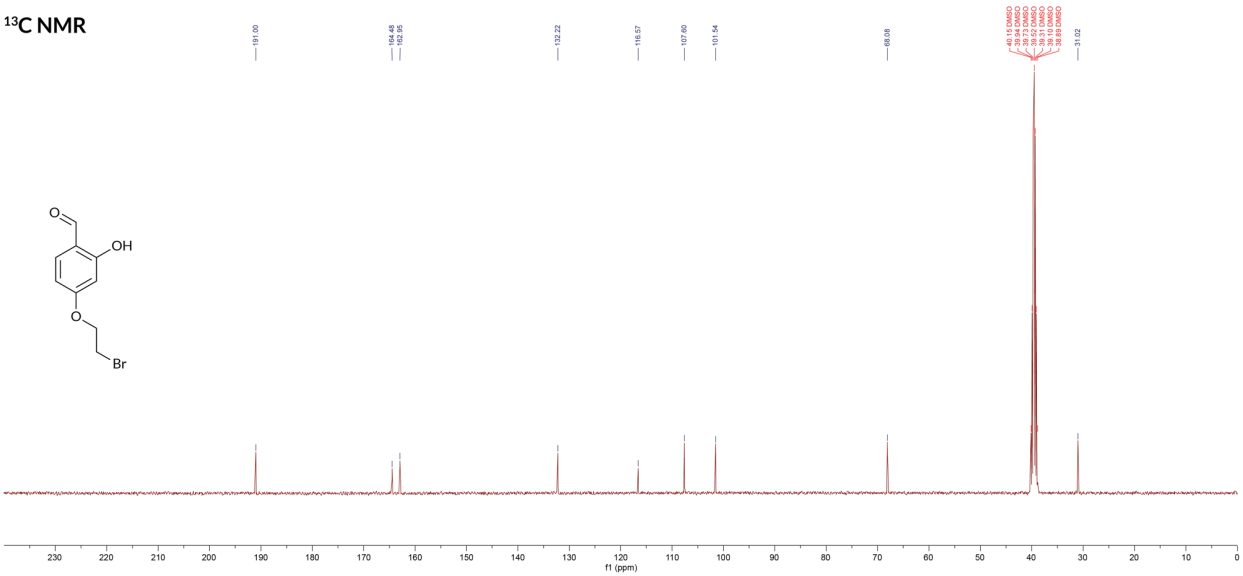
9.7.1 Characterisation Data - Metal Complexes

4-(2-bromoethoxy)-2-hydroxybenzaldehyde

^{1}H NMR

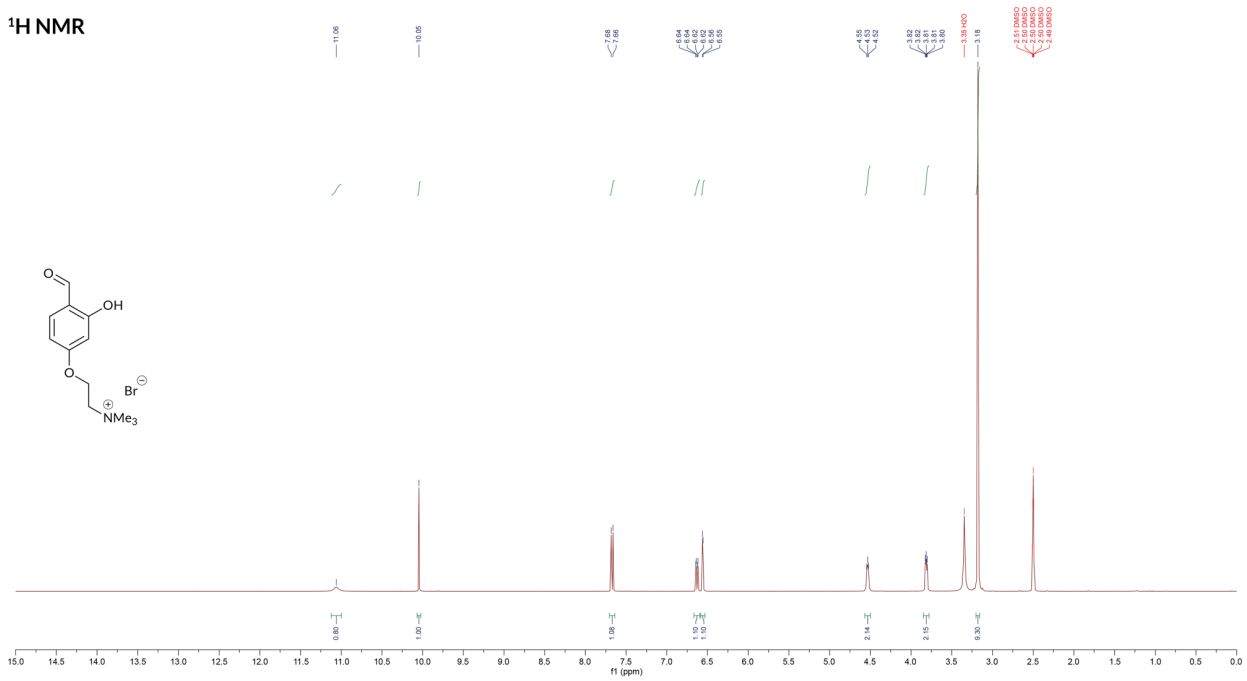


^{13}C NMR

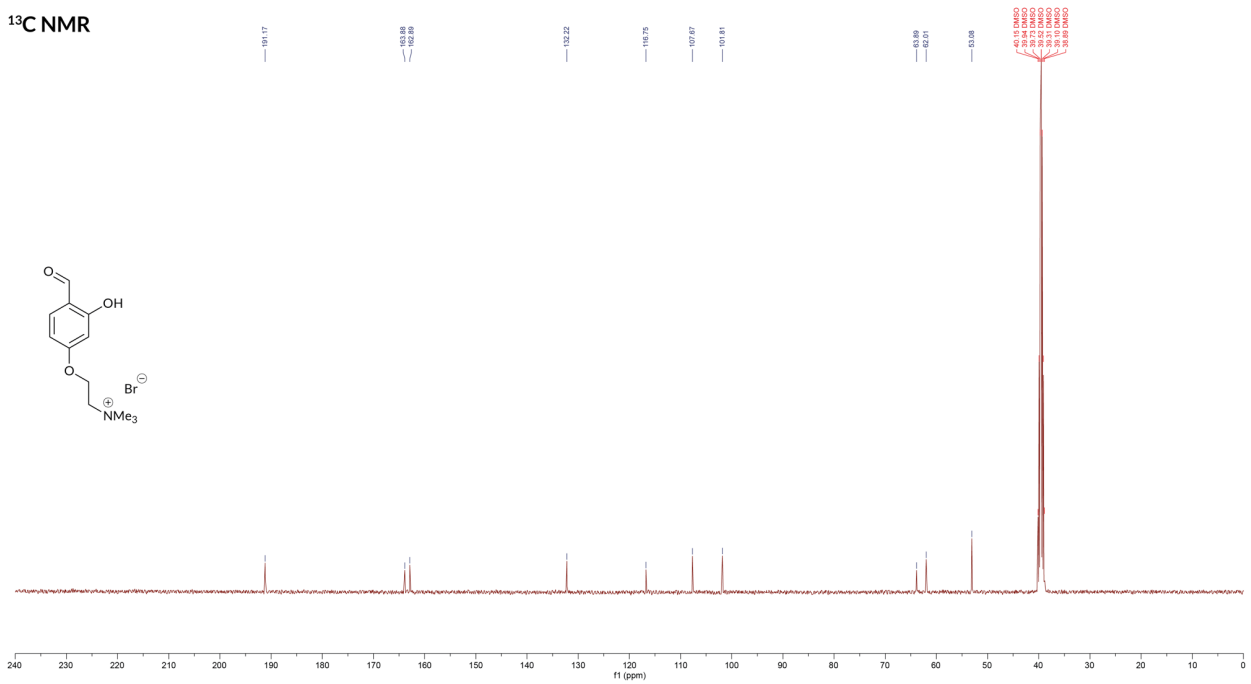


4-(4-formyl-3-hydroxyphenoxy)-*N*,*N*,*N*-trimethylethan-1-ammonium bromide

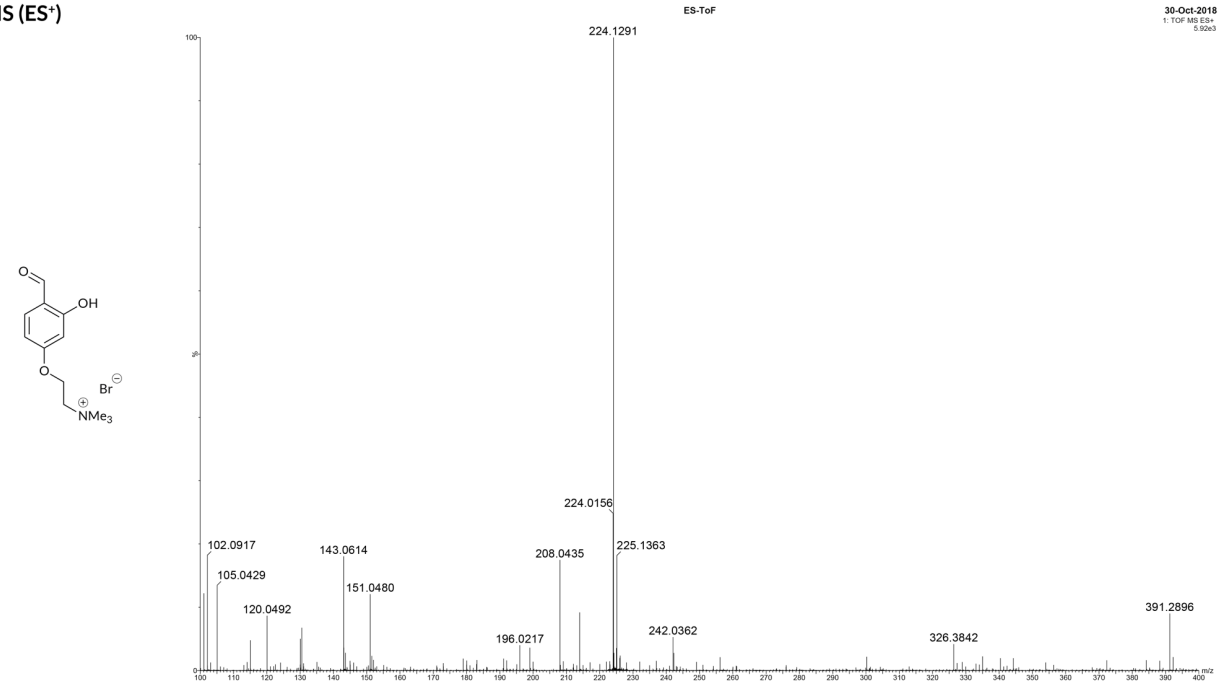
^{1}H NMR



^{13}C NMR

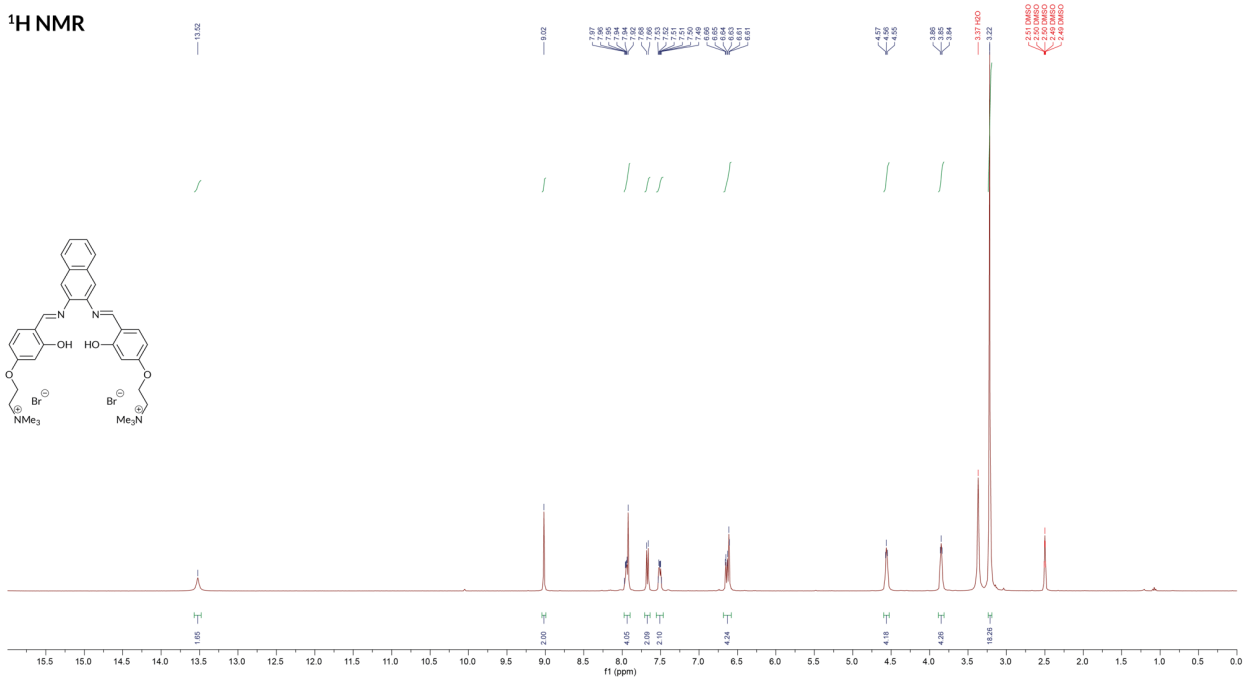


MS (ES$^+$)

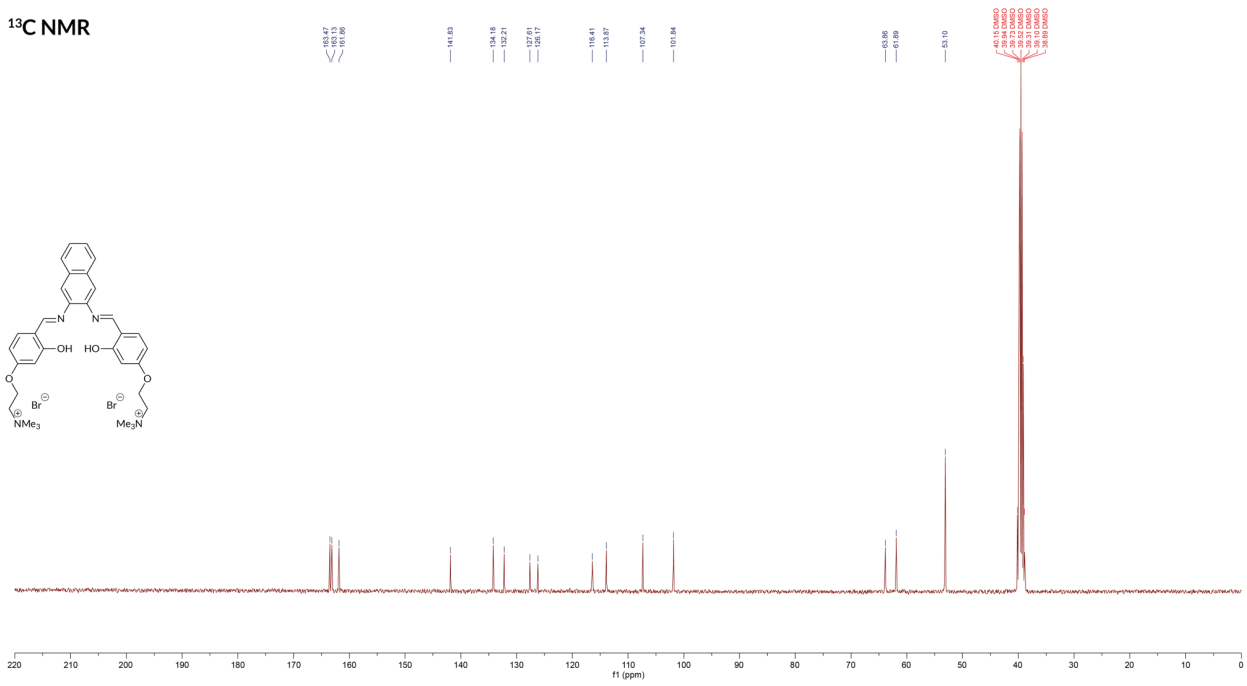


Salnaph Ligand

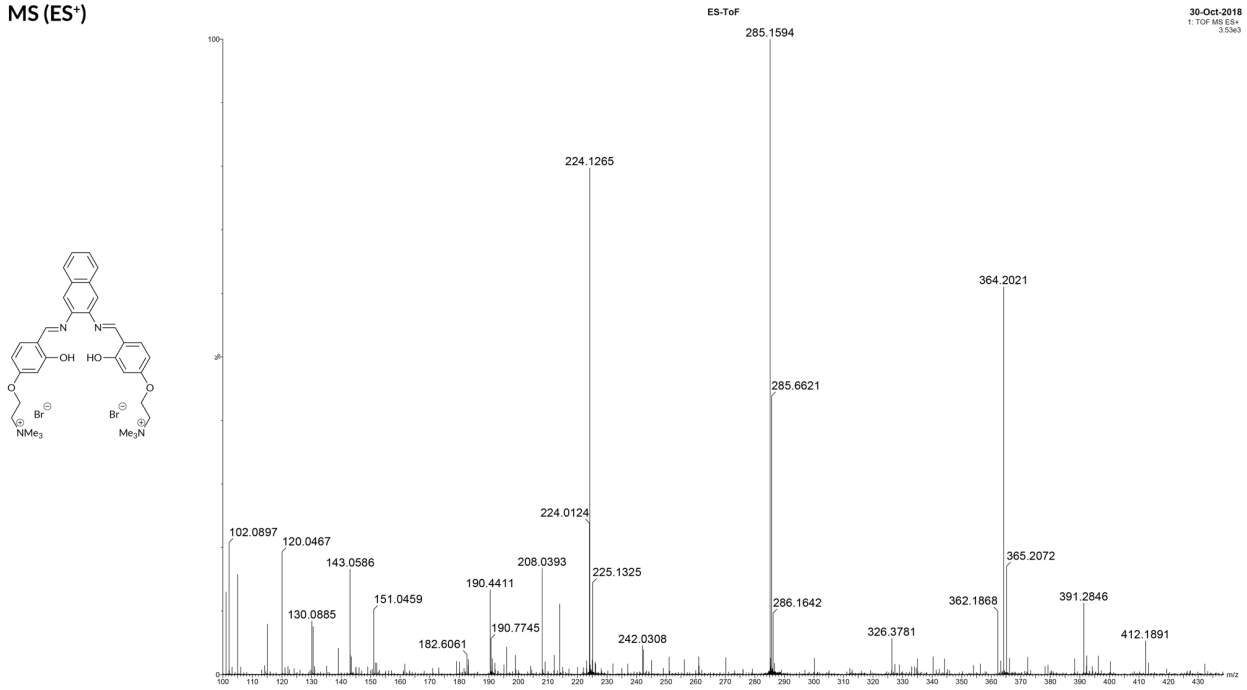
^{1}H NMR



^{13}C NMR

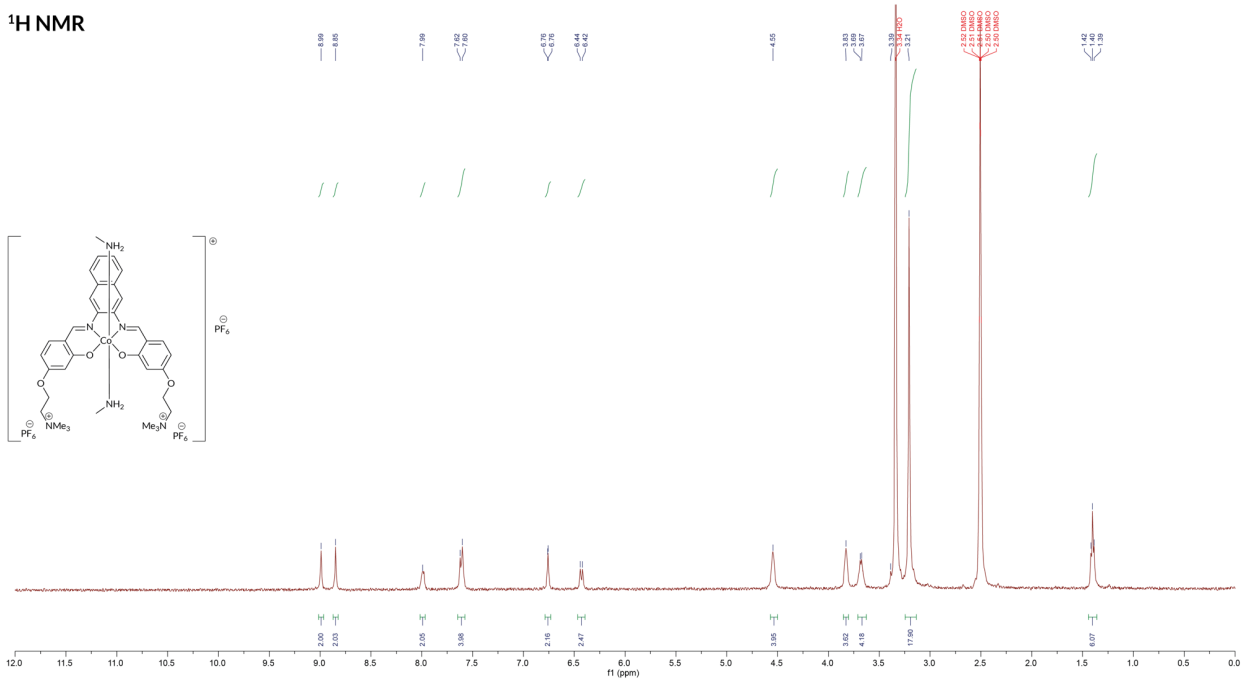

163.47
153.13
151.86
141.83
134.18
132.21
127.61
126.17
116.41
113.67
107.34
101.84
63.86
57.89
53.10
41.15 DMSO
40.73 DMSO
39.73 DMSO
39.31 DMSO
38.91 DMSO
38.50 DMSO
38.10 DMSO
OH
HO
Br
NMe3
Br
Me3N
f1 (ppm)

MS (ES$^+$)

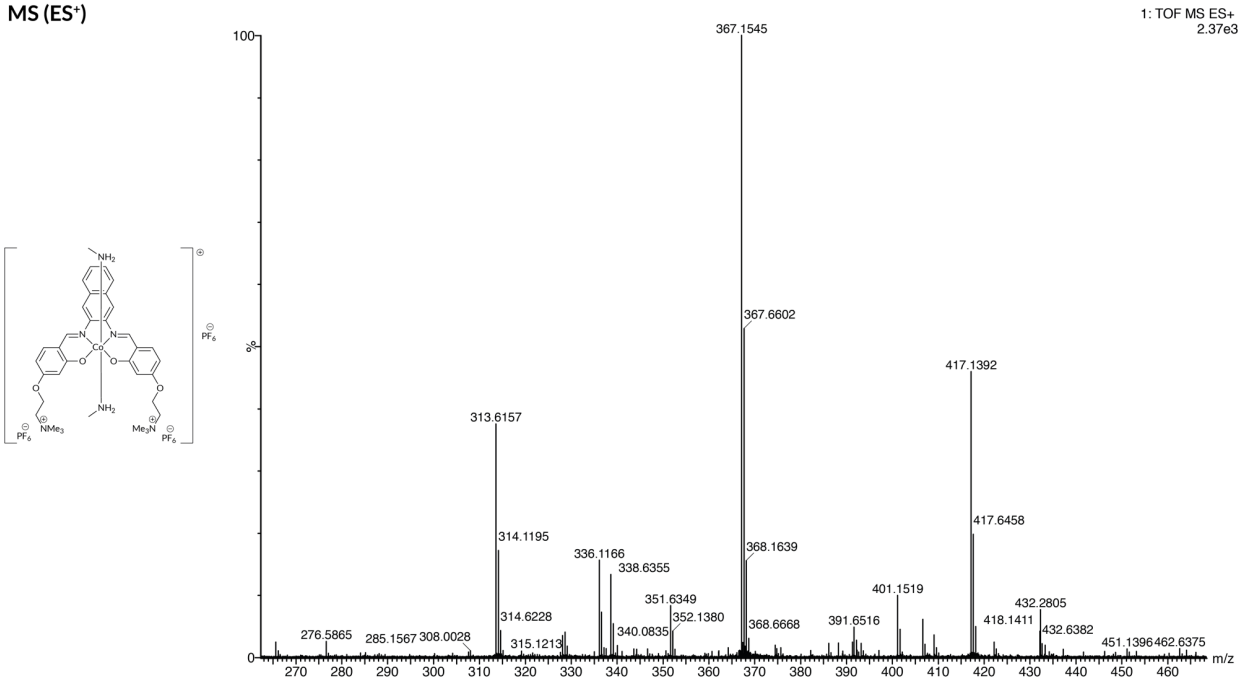

ES-ToF
30-Oct-2018
1: TOF MS ES+
3.53e3
285.1594
224.1265
364.2021
285.6621
224.0124
102.0897
120.0467
143.0586
208.0393
225.1325
190.4411
151.0459
130.0885
190.7745
182.6061
242.0308
286.1642
326.3781
362.1868
365.2072
391.2846
412.1891
%
m/z

Cobalt Salnaph 4a (L = $MeNH_2$)

^{1}H NMR

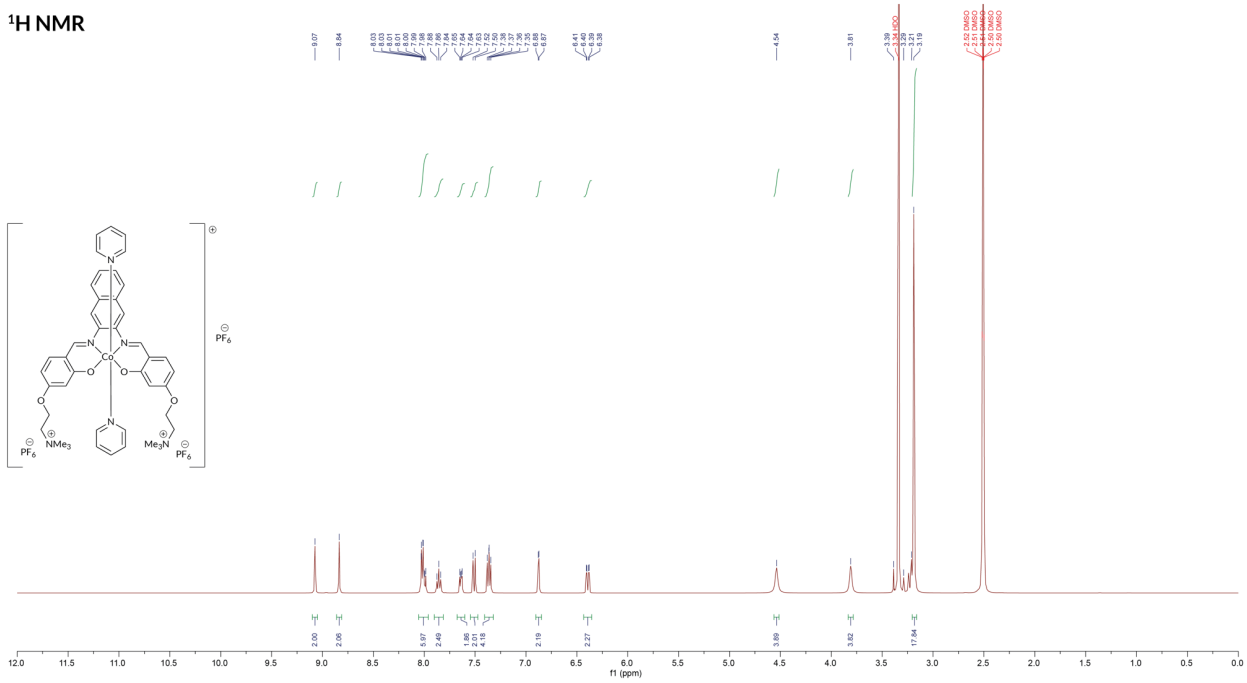


MS (ES$^+$)

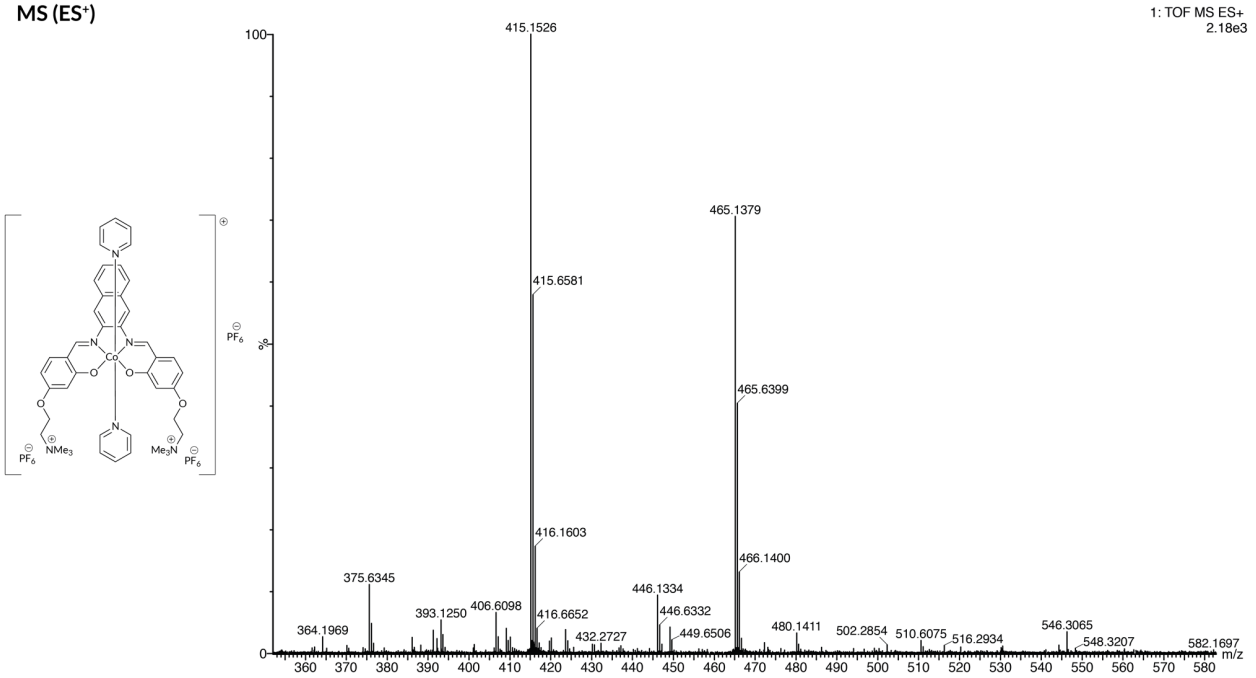


Cobalt Salnaph 4b (L = pyridine)

^{1}H NMR

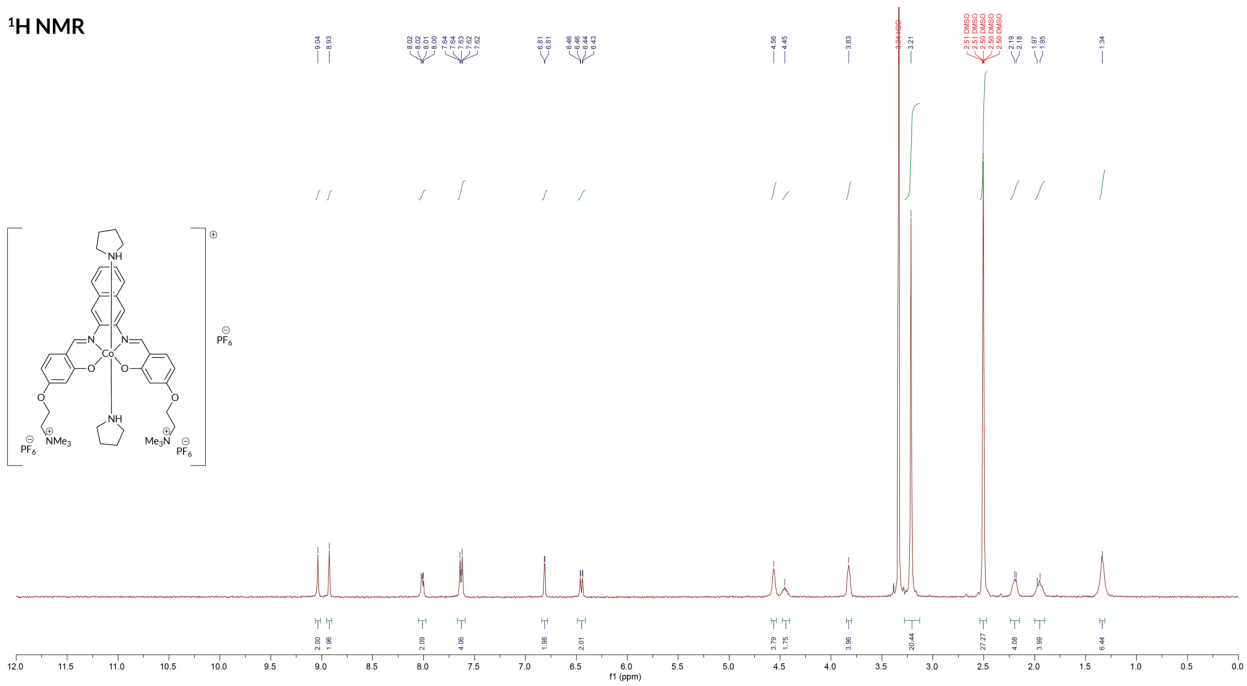


MS (ES$^+$)

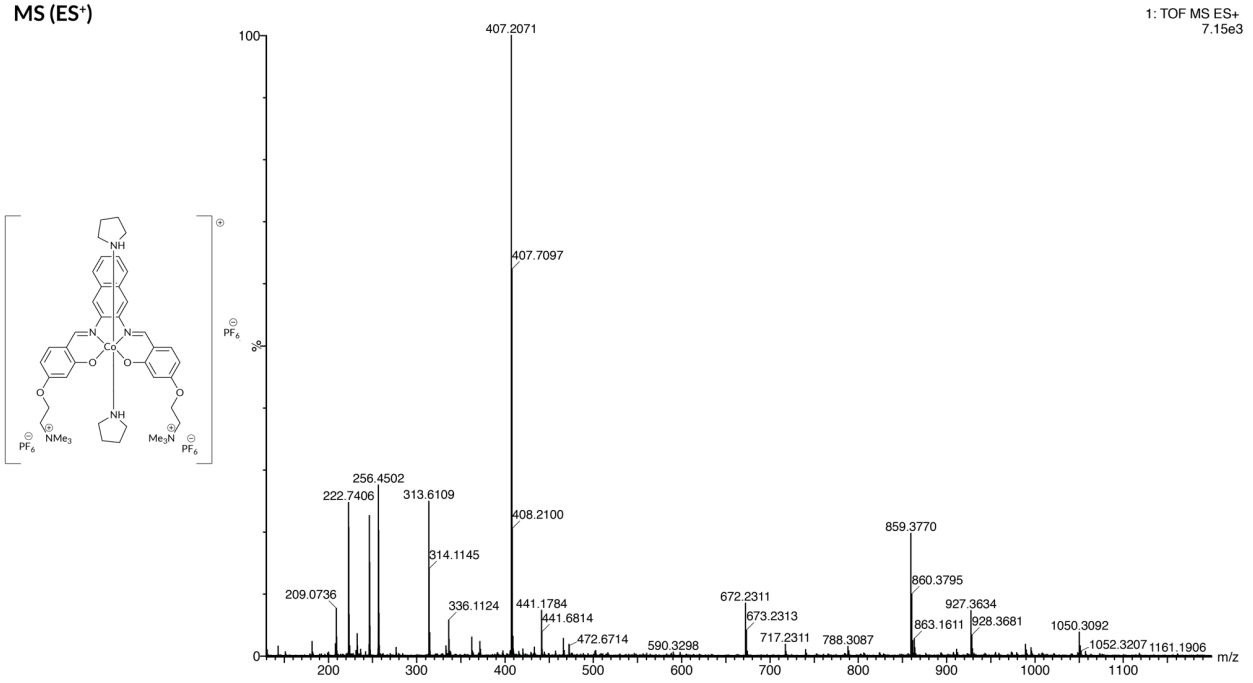


Cobalt Salnaph 4c (L = pyrrolidine)

^{1}H NMR

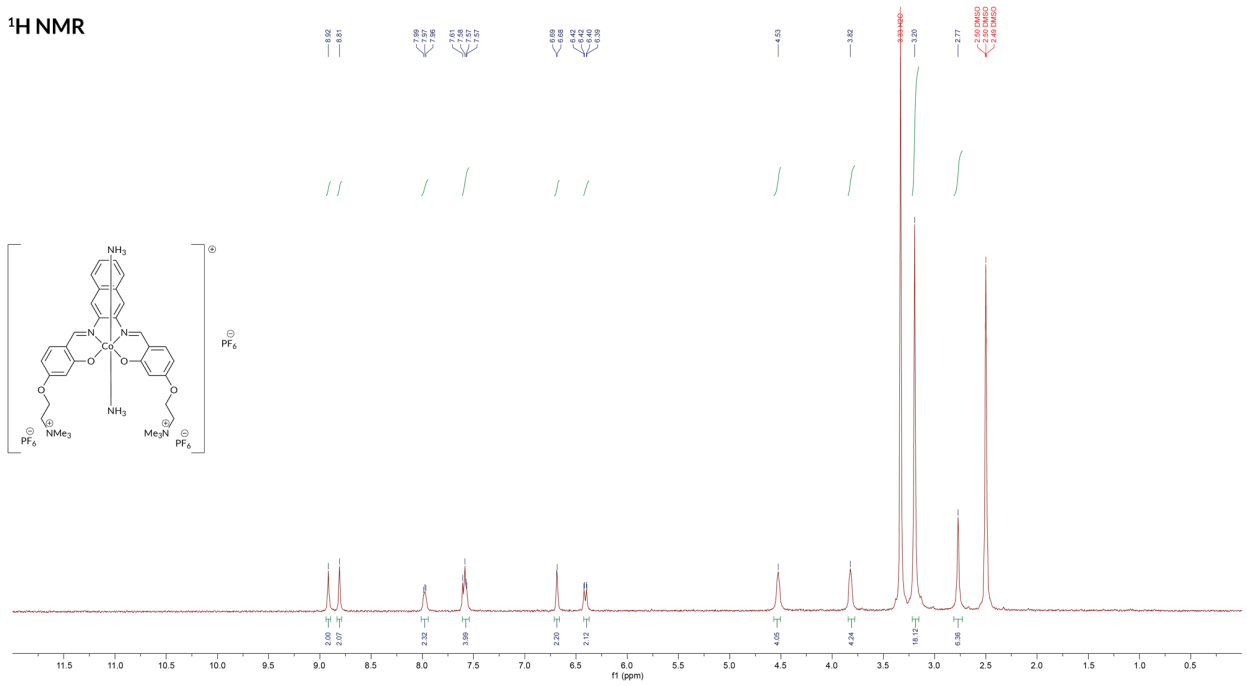


MS (ES$^+$)

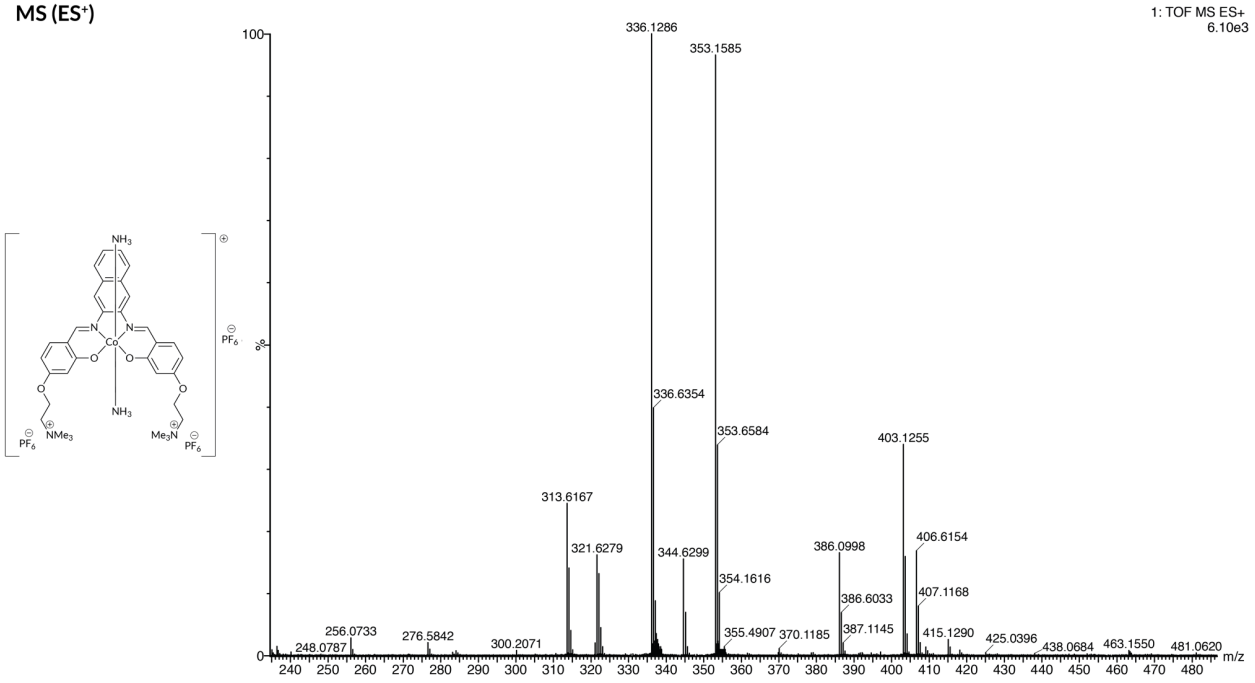


Cobalt Salnaph 4d (L = NH_3)

^{1}H NMR

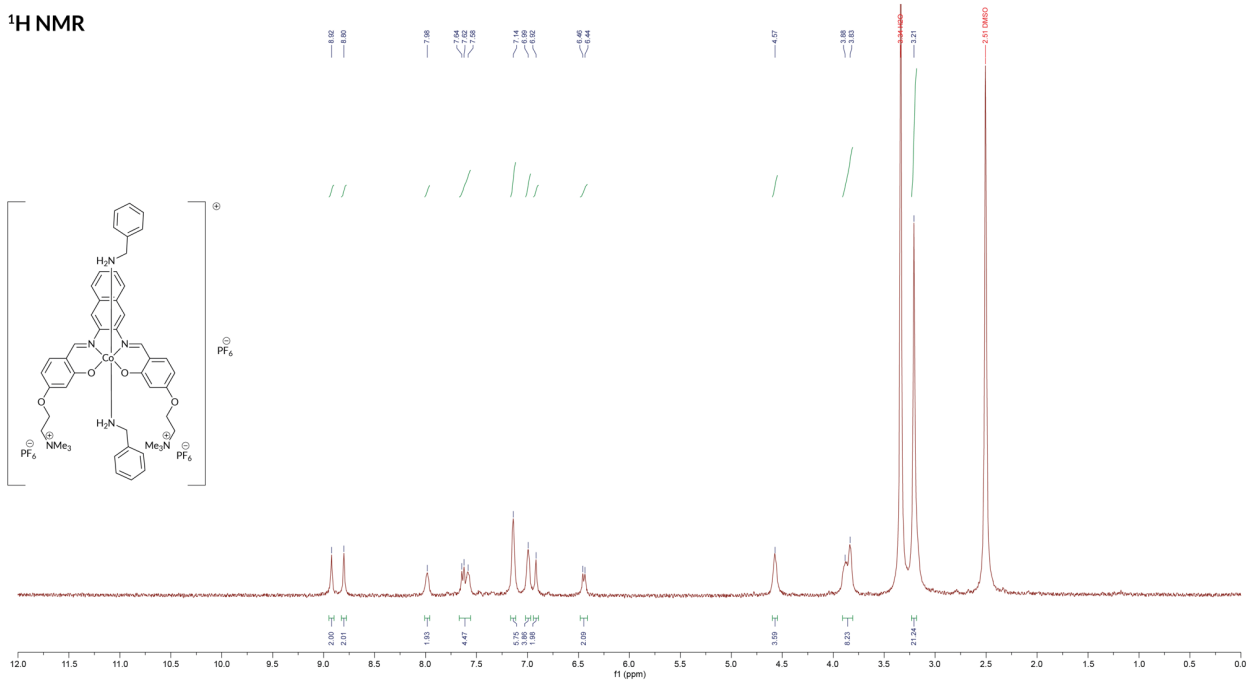


MS (ES$^+$)

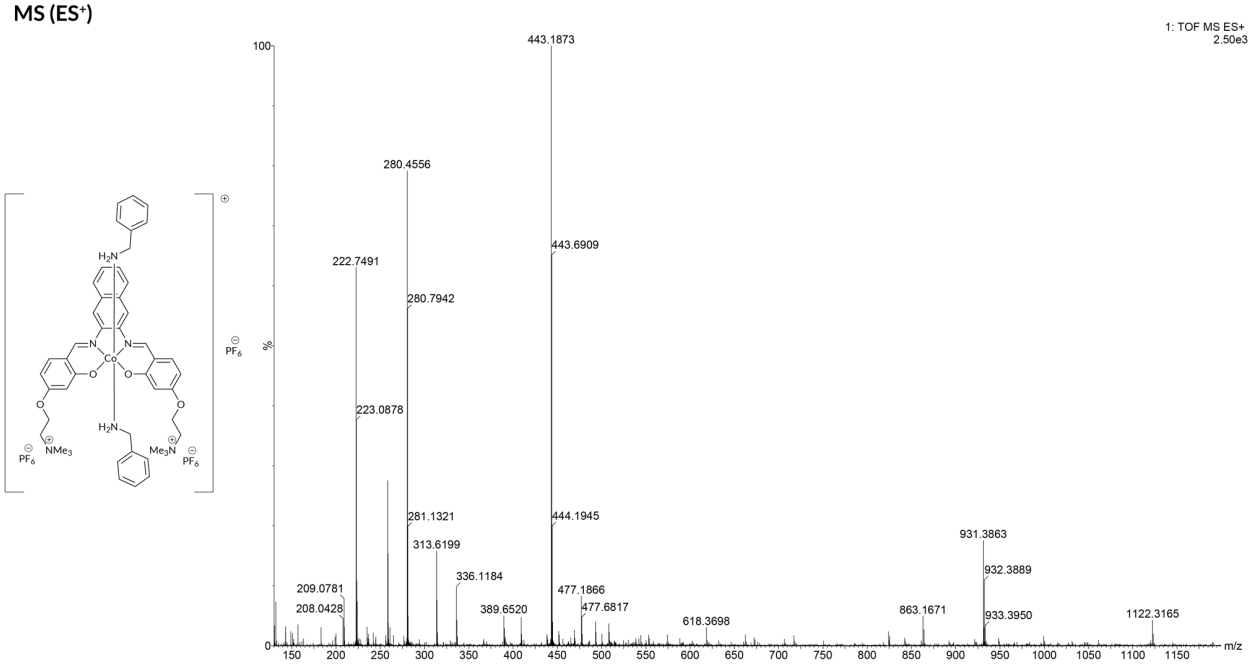


Cobalt Salnaph 4e (L = $BzNH_2$)

^{1}H NMR

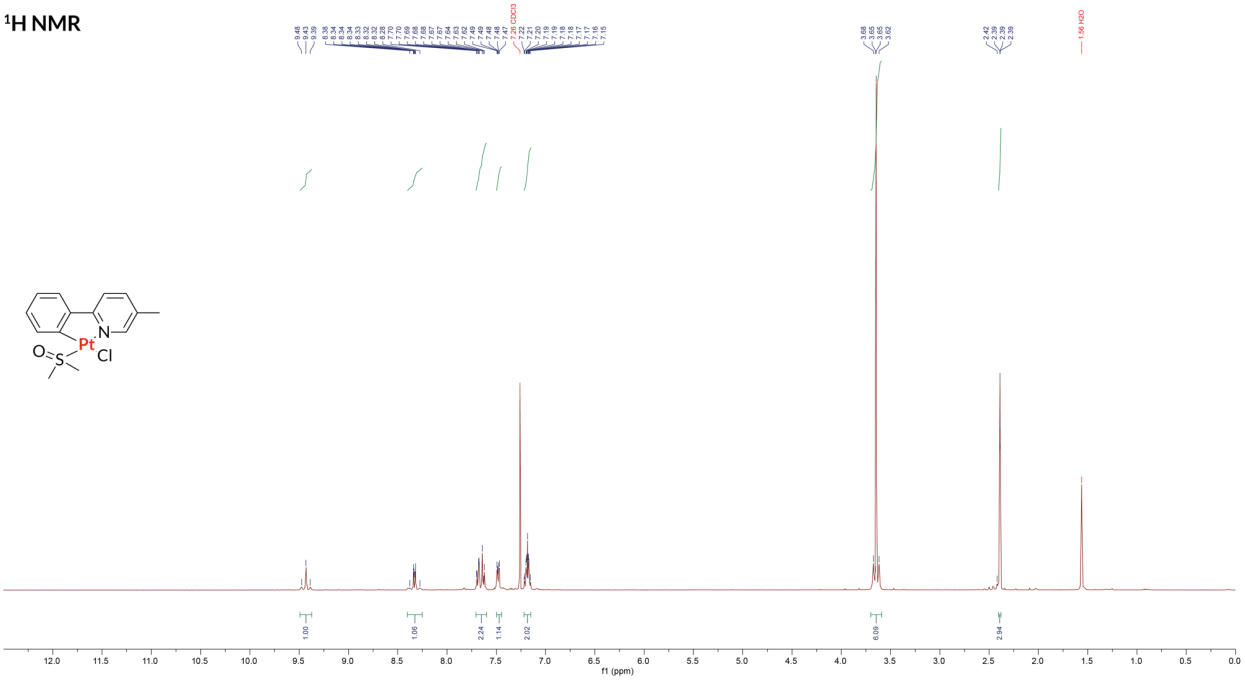


MS (ES$^+$)



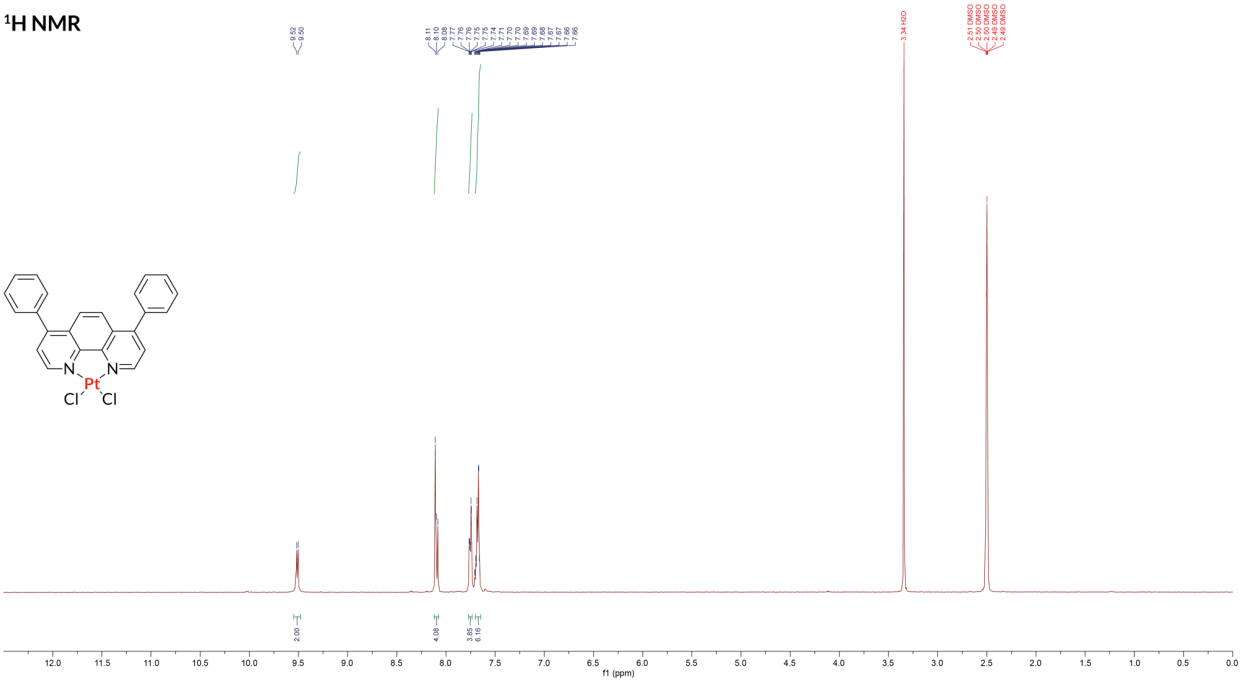
[Pt(5-methyl-2-phenylpyridine)(DMSO)Cl] (5)

^{1}H NMR



[Pt(4,7-diphenyl-1,10-phenanthroline)Cl_2] (6)

^{1}H NMR



9.8 CHAPTER 4: ASSESSING THERAPEUTIC EFFICACY IN VIVO

9.8.1 Delivery of Complex 1 across the BBB using Ultrasound

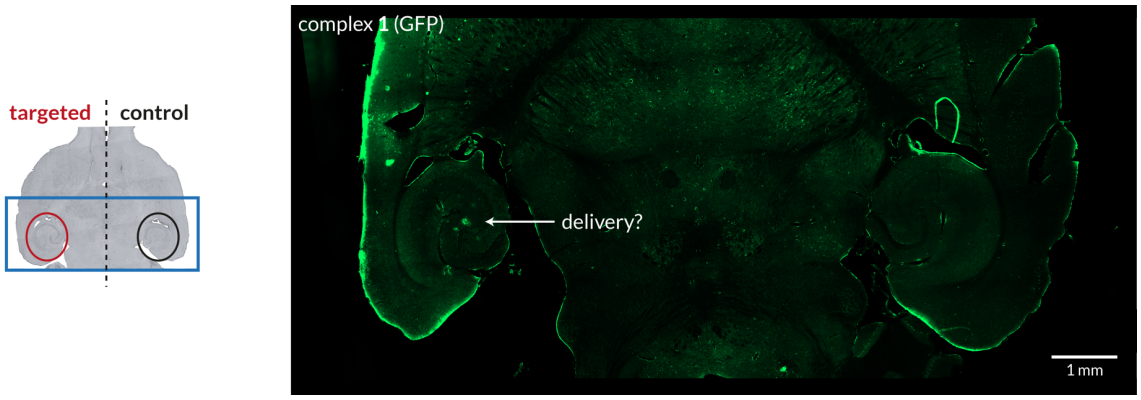
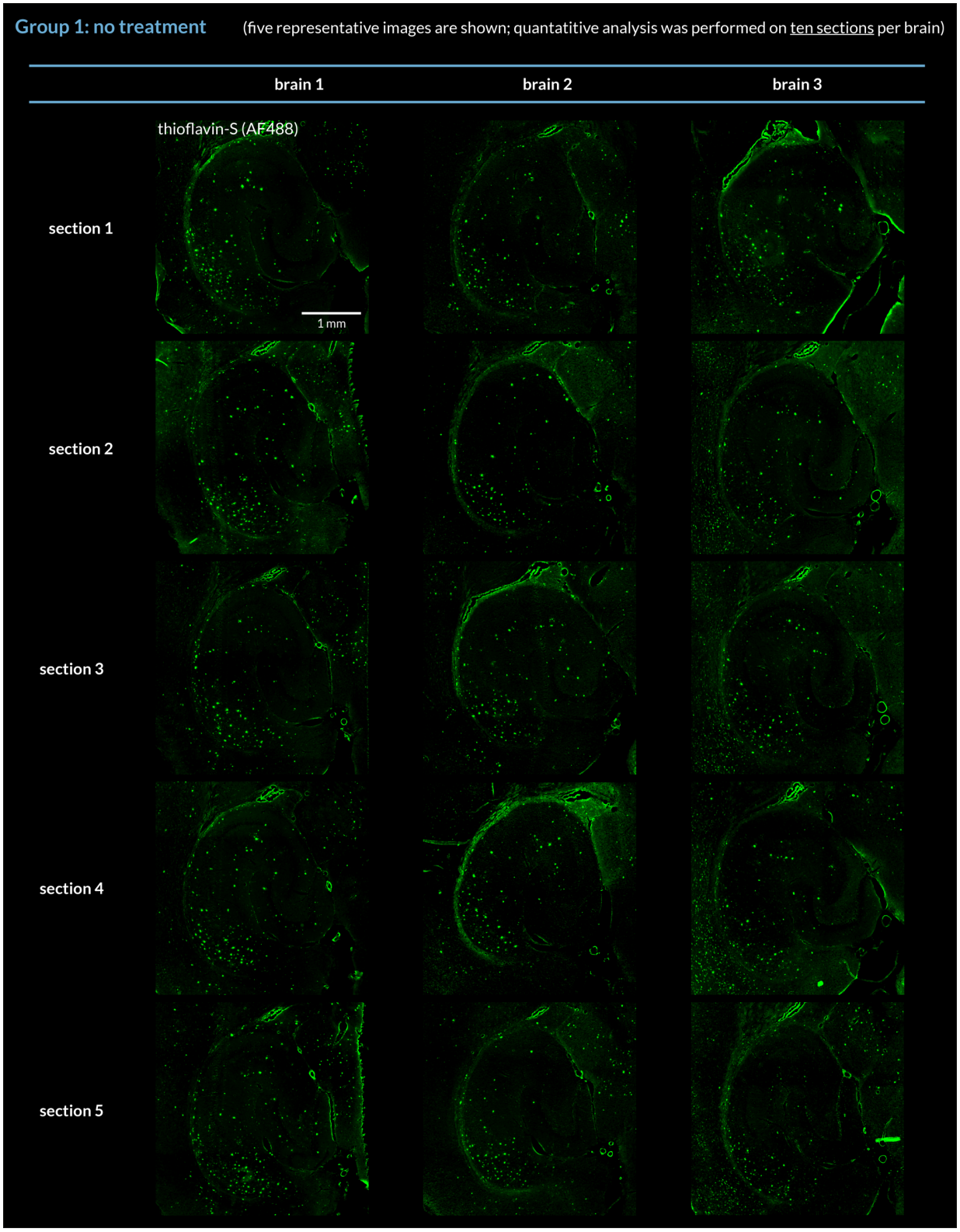
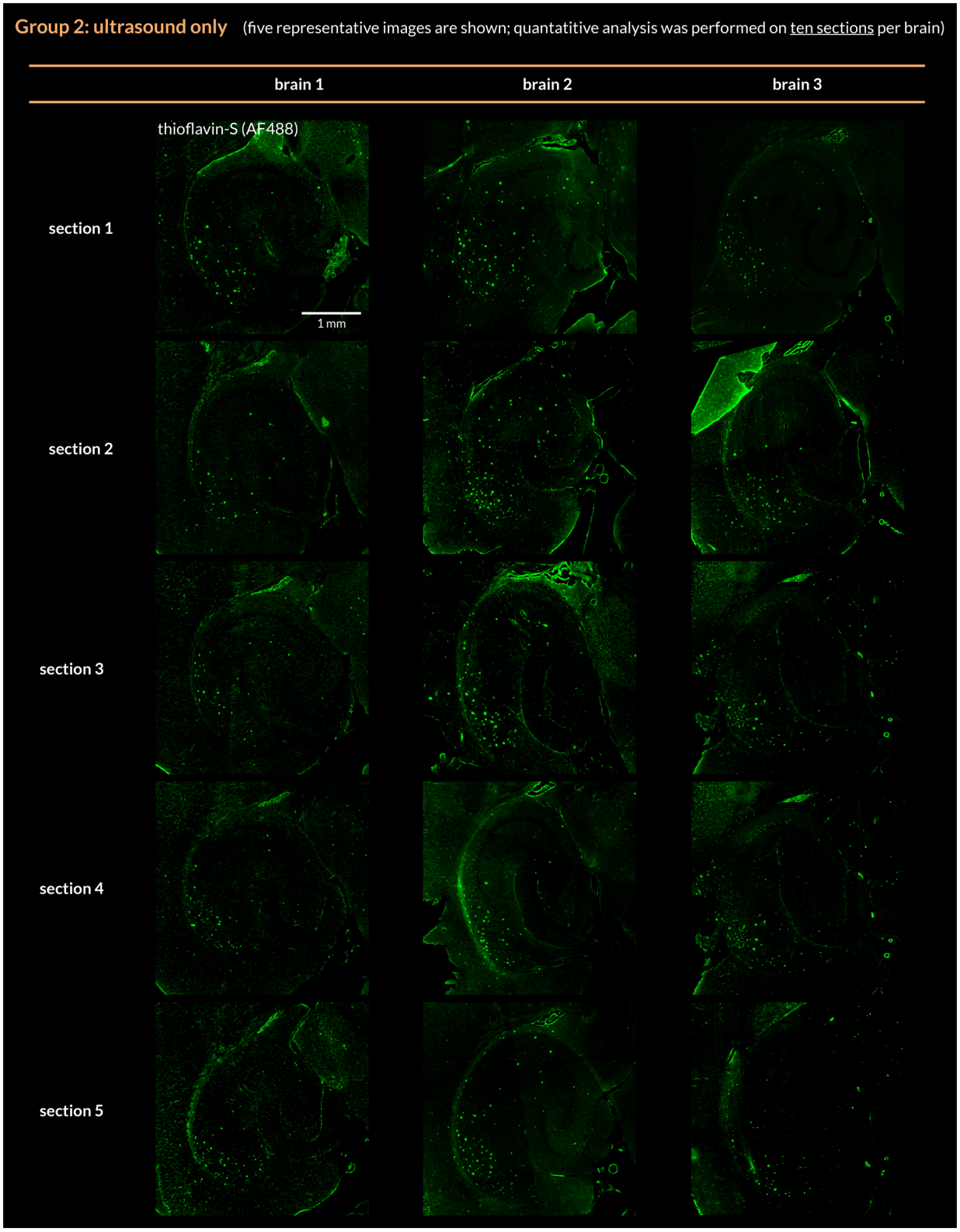


Figure 9.9: Delivery of complex **1** across the BBB using ultrasound (frequency: 1 MHz, peak-negative pressure: 350 kPa, pulse length: 0.005 ms, PRF: 1.25 kHz, burst length: 10 ms, BRF: 0.5 Hz, duration: 250 s). Complex **1** is weakly emissive at 580 nm when excited at 445 nm and thus, sections were imaged in the GFP channel in an attempt to locate the presence of the complex. Little evidence of delivery was observed *via* fluorescence-based methods.

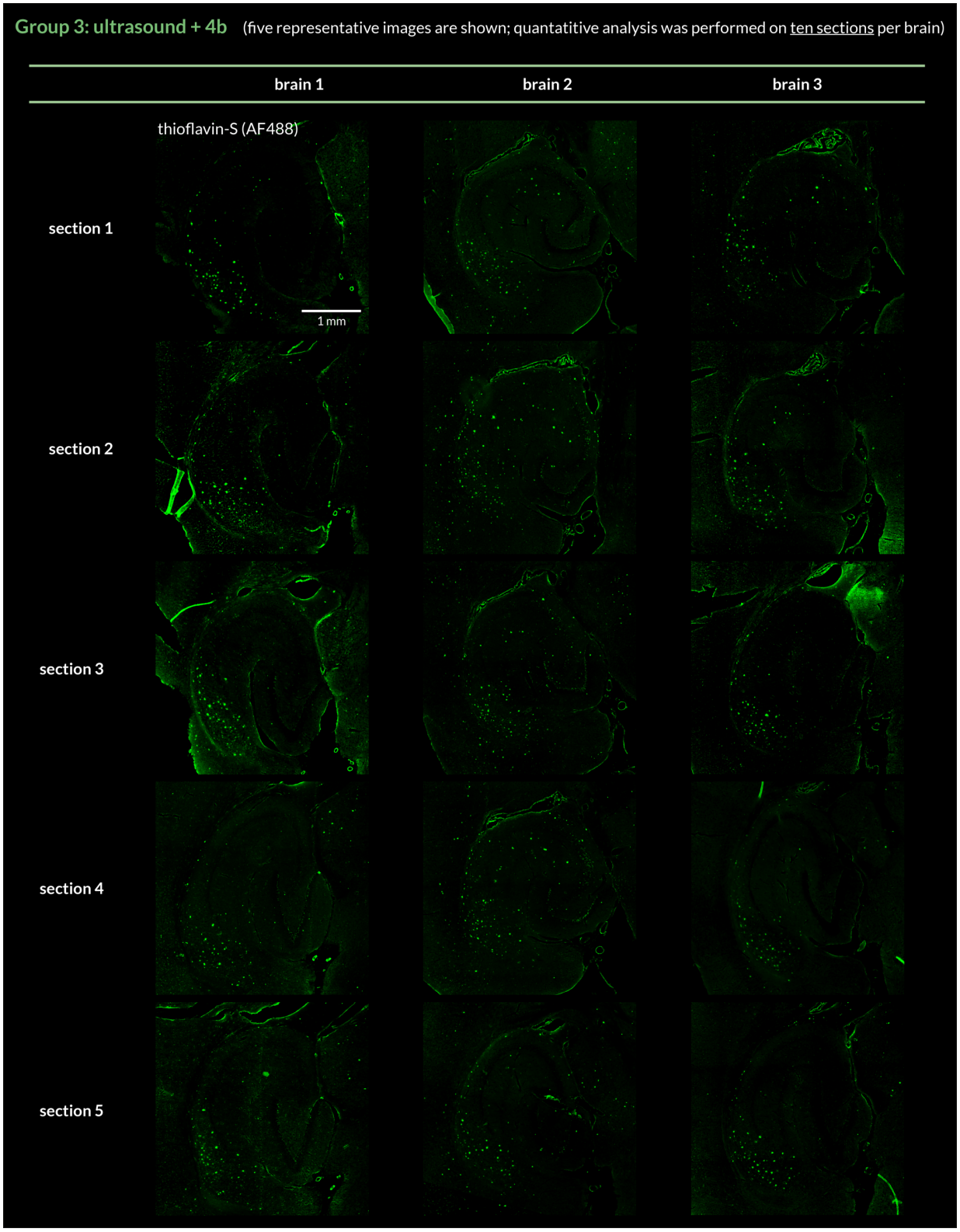
9.8.2 Thioflavin-S Staining: Group 1 (No Treatment)



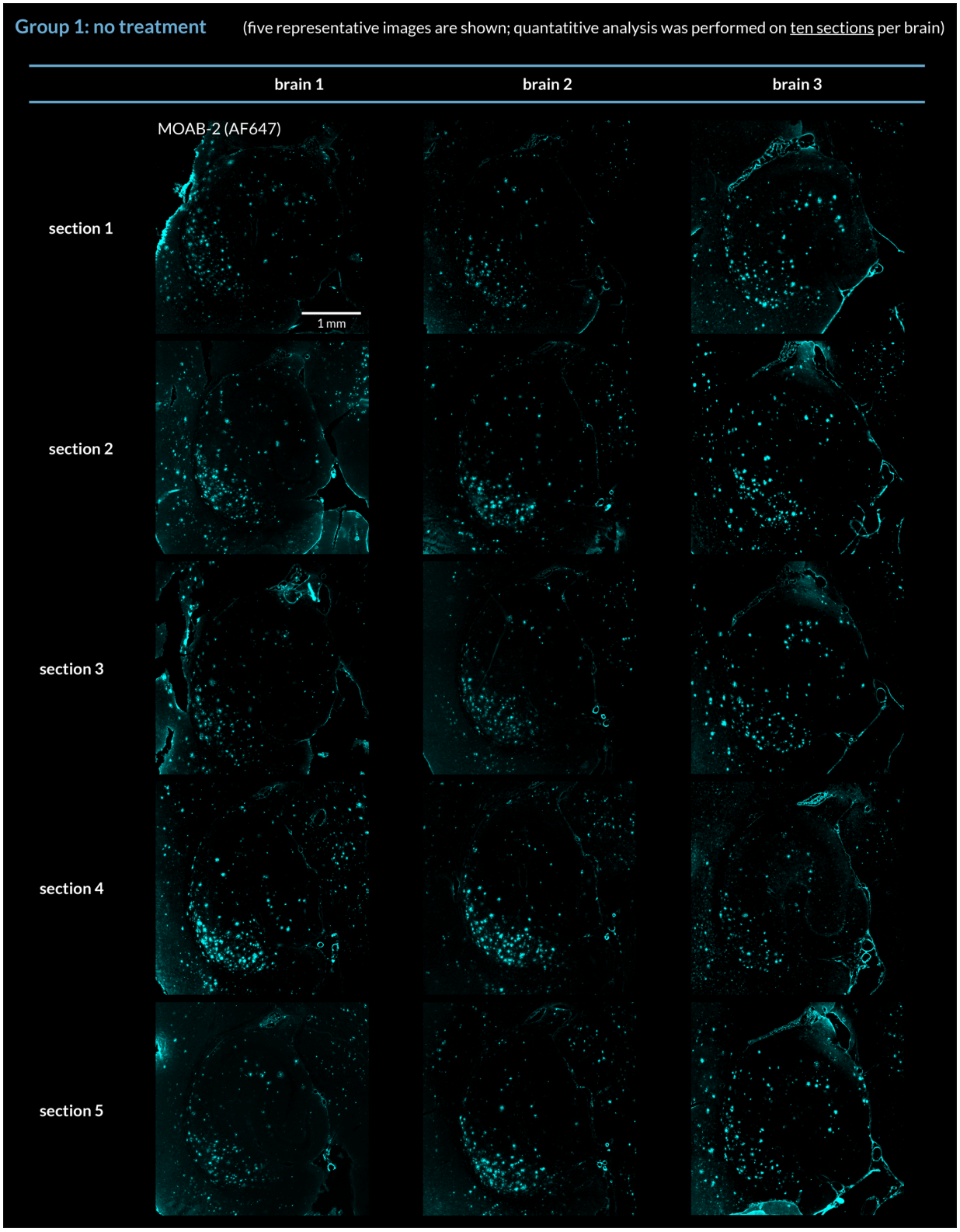
9.8.3 Thioflavin-S Staining: Group 2 (Ultrasound Only)



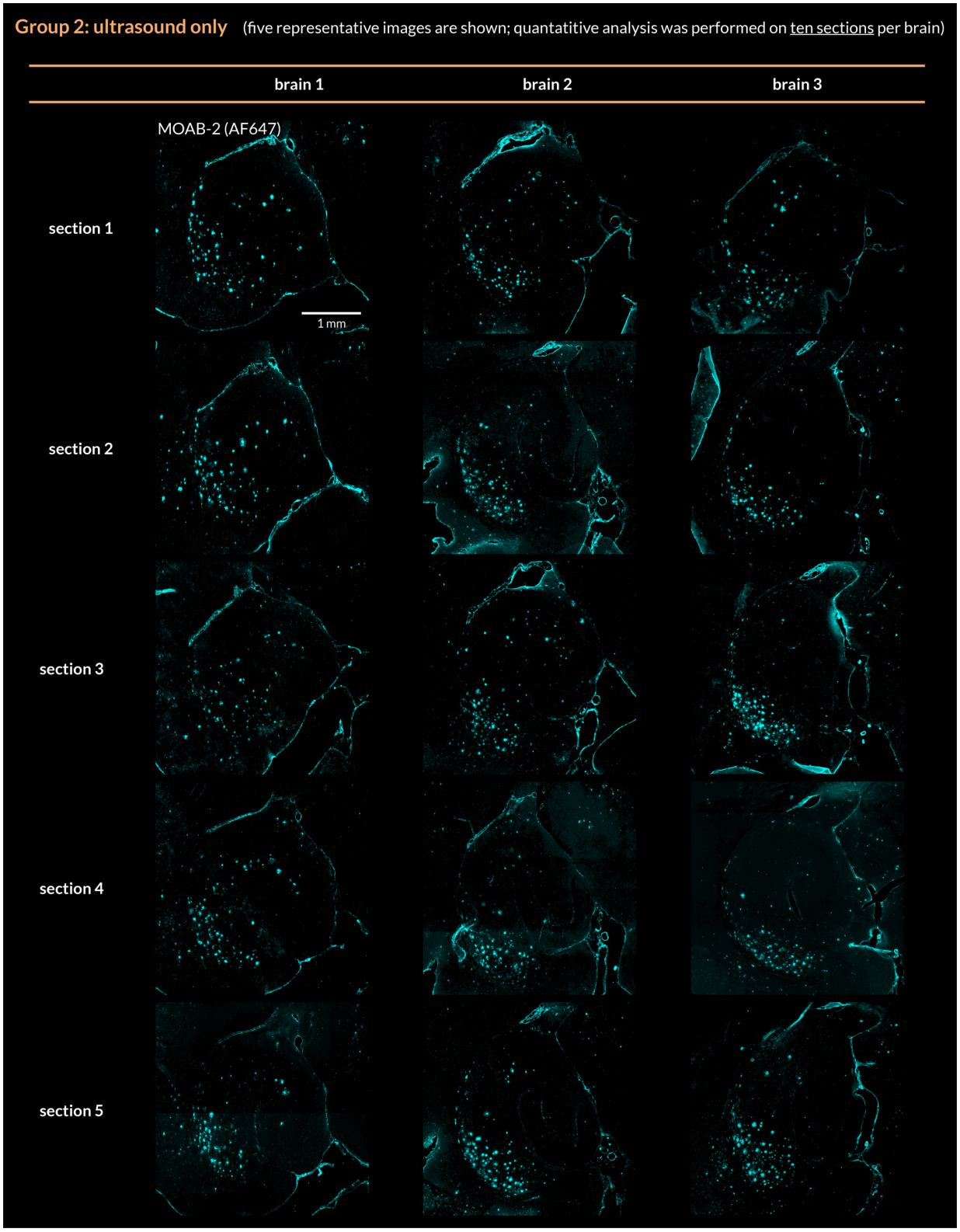
9.8.4 Thioflavin-S Staining: Group 3 (Ultrasound + 4b)



9.8.5 MOAB-2 Staining: Group 1 (No Treatment)



9.8.6 MOAB-2 Staining: Group 2 (Ultrasound Only)



9.8.7 MOAB-2 Staining: Group 3 (Ultrasound + 4b)

